The University of Canterbury

Department of Chemical and Process Engineering

Enhancing Packed Bed Geometry Using Computational Fluid Dynamic Simulations

A thesis submitted in fulfilment of the requirements for a Master of Engineering

21st July 2019

Student: Ben Houlton – 22645989

Supervisors: Professor Conan Fee[1], Associate Professor Matt Watson[1], Dr Fabian Dolamore[1], Dr Hamish Pearson[2]

This report is my own unaided work and was not copied from or written in collaboration with any other person.

[1:] University of Canterbury, [2:] Scion Research

Abstract

This work comprises an investigation into how the efficiency of packed beds can be enhanced by manipulating the geometry of the channel network, without altering the process chemistry. A particular focus is placed on investigating how the morphology of the structures influences the mass transfer properties of a passively transported solute species. This includes the degree of axial dispersion and the breakthrough performance of an adsorption column. Using computational fluid dynamic modelling techniques (the Lattice Boltzmann Method) periodic representations of ordered sphere packing and Triply Periodic Minimal Surface (TPMS) structures were subject to laminar flow conditions to compare the mass transport properties. The model parameters were derived from a proposed novel sorption filter for removal of trace heavy metal contaminants from water sources, although the results are expected to be relevant to many other applications.

A detailed outline of the modelling techniques is given, before addressing the performance of each geometry tested. Initially, traditional packing media (arrangements of spherical particles) were compared with TPMS monolithic structures. After confirming that TPMS structures provide enhanced packed column properties when compared with particle arrangements, additional TPMS and manipulated TPMS structures were considered. Parameters describing the geometry and flow fields within each structure are shown to correlate with chromatographic performance and column breakthrough. The relationships between solid phase distribution and enhanced packed bed performance provide a good basis for further investigations into refining packed bed geometry. The Schwarz Diamond and Double Schoen Gyroid TPMS structures were identified as the best performing of the structures that were modelled. Additionally, several practical suggestions are made to assist with the implementation of these findings, such as the expected dimensions of a real system and the sensitivity of results to operating parameters.

Acknowledgements

I would like to thank my supervisory team at the University of Canterbury for the guidance and support they afforded me while conducting this Masters: Prof. Conan Fee, Associate Prof. Matt Watson, and Dr Fabian Dolamore. You have all assisted me with gaining experience in modelling, conducting research, and in living life.

Additionally I would like to the team at Scion for the external supervision they provided, and allowing me to work with them on this project. Dr Hamish Pearson and Dr Marie Joo Le Guen, it has been a great experience to work with you both.

Many thanks to the Ministry of Business, Innovation, and Employment (MBIE) New Zealand for providing the funding for this project with grant number: C04X1706 - Water and Toxic Metals.

Table of Contents

Nomenclature

The variables used in this thesis are summarized in the table below, and have been expressed using units of Length [L], Mass [M], Time [T], Temperature [K], and Moles [N], or are independent of dimensions entirely.

Roman Symbols		
Symbol	***Description***	
a	Specific surface area	$L^2 L^{-3}$
A_{CS}	Cross sectional area	L^2
A_{flow}	Cross sectional fluid area of a 2D domain	L^2
A_w	Wetted surface area	L^2
a_{pulse}	A constant used to defined the RTD inlet pulse of solute	-
A, B, C	Constants in the Van Deemter Curve equation (chromatography)	-
b_{Lang}	Adsorption equilibrium constant in the Langmuir isotherm	-
b_{pulse}	A constant used to defined the RTD inlet pulse of solute	-
Be	Bejan number: dimensionless pressure drop	-
$\dot{Be}$	Bejan gradient / rate of change of Bejan number	-
c_{CK}	Constant in the Carman-Kozeny correlation	-
c_i	Quadrature point used in the Lattice Boltzmann Method	-
c_{pulse}	A constant used to defined the RTD inlet pulse of solute	-
c_s	Artificial speed of sound in lattice units	-
C	Concentration	$N L^{-3}$
$\hat{C}_{ads}$	Amount of adsorbed solute at a node	N
$\hat{C}_{bulk}$	Amount of solute in the bulk fluid/diffusing through a solid node	N
$\hat{C}_{cap}$	Capacity at one node of the simulation	N
C_0	Inlet concentration	-
C_{CAP}	Molar capacity of the domain available for adsorption to occur	N
C_D	Dimensionless fraction of capacity occupied at breakthrough	-
C_{ads}	Concentration at the solid phase surface	$N L^{-3}$
C_{bulk}	Concentration in the fluid phase	$N L^{-3}$
C_{cap}	Specific capacity of the solid phase	$N L^{-3}$
C_{eq}	Liquid phase concentration in equilibrium with adsorption surface	$N L^{-3}$
C_{max}	Maximum concentration which may occur at the inlet	$N L^{-3}$
$C_{tot-cap}$	Total capacity of specific simulation geometry	N
C_{uptake}	Amount of solute adsorbed at breakthrough	N
$C(f_i)$	Discretised collision term	-
$C(f)$	Collision term in the Lattice Boltzmann Method	-
$C(t)$	Concentration at the inlet as a function of time	$N L^{-3}$
d_{ads}	Maximum depth for adsorption to occur	L
$d_{h,channel}$	Hydraulic diameter using channel based definition	L
$\bar{d}_{h,channel}$	Average hydraulic diameter using channel based definition	L
$d_{h,pore}$	Hydraulic diameter of a pore network	L
d_p	Particle diameter	L

Symbol	*Description*	
d_{pulse}	A constant used to defined the RTD inlet pulse of solute	-
dP/dz	Pressure drop	M L^{-1} T^{-2}
Da	Damköhler number	-
$\widetilde{D}$	Deviated diffusion parameter of solute in fluid	L^2 T^{-1}
D_m	Molecular diffusivity of solute in fluid	L^2 T^{-1}
D_{pipe}	Diameter of a pipe, for determining equivalent hydrodynamic resistance	L
D_{pore}	Pore diffusion coefficient	L^2 T^{-1}
D_{ref}	Reference diffusivity of solute in fluid	L^2 T^{-1}
E	Separation impedance (chromatography)	-
f	The probability density function (LBM Equations)	-
f_{in}	Population of particles incoming to a node during streaming of LBE	-
f_{out}	Population of particles outgoing from a node during streaming of LBE	-
F	Body force	M L T^{-2}
$F_{(h,k,l)}$	Structure factor (X-ray crystallography)	-
$F_i[f]$	Value of the probability density function at equilibrium	-
h	Reduced plate height	-
h_{min}	Minimum reduced plate height	-
h, k, l	Constants in space group definition (Level set equations)	-
$HETP$	Height Equivalent to a Theoretical Plate	L
HRT	Hydraulic residence time	T
k	Permeability / specific column permeability	L^2
k'	Dimensionless for of media permeability	-
k_{ads}	Adsorption rate constant	T^{-1}
k_{des}	Desorption rate constant	N L^{-3} T^{-1}
k_R	Retention factor (chromatography)	-
K_L	Constants of the outer layers in BET isotherm	-
K_S	Constant of the first adsorption layer (BET isotherm)	-
L	Total length of column	L
L_c	Characteristic length of packing media	L
L_i	Representing any length/distance in any units system (i)	-
L_x	Distance between the inlet and outlet slices of a unit cell (axial direction)	L
L_z	Length of the unit cell along the axis of flow	L
m_D	Reference mass in dimensionless form	-
m_l	Reference mass in lattice units	-
m_p	Reference mass in physical units	M
M_w	Molecular weight of the solute species	M N^{-1}
n_{ent}	Number of entry cells used in the periodic simulation	-
n_{lim}	Limiting number of BET isotherm layers	-
n_{surf}	Number of surface nodes available for adsorption to occur	-
N	Number of theoretical plates	-
P	Pressure	M L^{-1} T^{-2}
Pe	Peclet number	-
Pe_{inlet}	Peclet number of the simulation inlet	-
P_{in}	Pressure at the inlet of the unit cell	M L^{-1} T^{-2}
P_{out}	Pressure at the outlet of the unit cell	M L^{-1} T^{-2}

Symbol	*Description*	
P_s	System pressure	M L^{-1} T^{-2}
P_{sat}	Saturation vapour pressure	M L^{-1} T^{-2}
P_{vap}	Vapour pressure within a pore	M L^{-1} T^{-2}
P_w	Wetter perimeter of a 2D domain	L
q_s	Number of available adsorption sites in Langmuir isotherm	-
Q	Volumetric flowrate	L^2 T^{-1}
Q_s	Source or sink term in the advection-diffusion equation	N L^{-3} T^{-1}
r_p	Radius of a packing particle	L
r_{pore}	Radius of a pore	L
r_{rxn}	Rate of reaction	N L^{-3} T^{-1}
R	Universal gas constant	$ML^2T^{-2}K^{-1}$
Re	Reynolds Number	-
R_H	Hydrodynamic resistance of media	-
R_s	Resolution (chromatography)	-
R_x	Resolution of the lattice mesh (nodes in a characteristic length)	-
SA_{ads}	Surface area available for adsorption to occur	L^2
t	Time	T
t_0	Inert solute column elution time (chromatography)	T
t_D	Reference time of the system in dimensionless form	-
t_R	Active solute column elution time (chromatography)	T
t_b	Breakthrough time	T
t_{bt}	Time at which breakthrough occurs	T
t_d	Bed exhaustion / dead time	T
t_i	Representing any time in any units system (i)	-
t_l	Reference time of the system in lattice units	-
t_p	Reference time of the system in physical units	T
$\bar{t}$	Mean elution time for a species passing through a column	T
T	Tortuosity	-
T_K	Temperature	K
u	Velocity	L T^{-1}
u_D	Fluid velocity in dimensionless form	-
u_a	Advection velocity term	L T^{-1}
u_d	Diffusion velocity term	L T^{-1}
u_i	Velocity in the i'th axial direction	L T^{-1}
u_l	Fluid velocity in lattice units	-
u_p	Fluid velocity in physical units	L T^{-1}
u_s	Superficial velocity	L T^{-1}
u_z	Axial velocity component	L T^{-1}
$\bar{u}$	Mean velocity magnitude	L T^{-1}
$\bar{u}_{dev}$	Normalised mean velocity deviation	L T^{-1}
$\bar{u}_s$	Average superficial velocity of the fluid channel	L^3 T^{-1}
$\boldsymbol{u}$	Velocity vector	L T^{-1}
V_D	Dimensionless void volumes (breakthrough performance measure)	-
V_{ads}	Volume of adsorption active material	L^3
V_{cell}	Volume of a unit cell	L^3

Symbol	*Description*	
V_{col}	Total volume of the column observed	L^3
V_{elute}	Volume of fluid passed through the simulation domain at breakthrough	L^3
V_{fluid}	Volume of fluid occupying the unit cell	L^3
V_{lead}	Volume of the non-solid space upstream of the periodic unit cell	L^3
V_m	Molar volume	$L^3\ N^{-1}$
V_p	Volume of a particle	L^3
V_{solid}	Volume of solid occupying the unit cell	L^3
V_{total}	Total volume of the unit cell	L^3
V_{void}	Volume of the void/fluid space	L^3
V_{void}	Volume of the fluid space within a unit cell	L^3
w_i	Width of the base of a chromatogram peak for 'i' (chromatography)	T
x	Pertaining to the axial coordinate system (x-axis)	-
x_D	Reference length of the system in dimensionless form	-
x_l	Reference length of the system in lattice units	-
x_p	Reference length of the system in physical units	L
x_0, y_0, z_0	Coordinates of a particle centre, or the grid system origin point	-
$\boldsymbol{x}$	Lattice Boltzmann Method spatial vector	-
y	Pertaining to the axial coordinate system (y-axis)	-
z	Pertaining to the axial coordinate system (z-axis)	-
z_{bed}	Depth of filtration bed	L
Z_c	A characteristic length used to determine the grids resolution	L

Greek Symbols		
Symbol	***Description***	
α	Separation factor (chromatography)	-
δ	A small increment	-
Δ	A change in the property	-
γ	Surface tension of fluid within a pore	$M\ T^{-2}$
ε	The porosity of the defined domain (void fraction)	-
η_D	Single filter collector diffusion efficiency	-
η_G	Single filter collector gravity efficiency	-
η_I	Single filter collector interception efficiency	-
η_{filter}	Filter collector efficiency	-
θ	Fraction of occupied sites in Langmuir isotherm	-
λ	Filtration coefficient	L^{-1}
μ	Dynamic viscosity	$M\ L^{-1}\ T^{-1}$
ν	Kinematic viscosity	$L^2\ T^{-1}$
ν_D	Kinematic viscosity in dimensionless form	-
ν_l	Lattice kinematic viscosity (lattice units)	-
ν_p	Kinematic viscosity in physical units	$L^2\ T^{-1}$
ξ	Lattice Boltzmann Method velocity in 'i' axis	-
$\boldsymbol{\xi}$	Lattice Boltzmann Method velocity vector	-

Symbol	*Description*	
ρ	Density	M L^{-3}
ρ_D	Density in dimensionless form	-
ρ_l	Density in lattice units	-
ρ_p	Density in physical units	M L^{-3}
σ^2	Standard deviation of the time taken for solute to pass through a column	T
τ	Lattice Boltzmann Method relaxation parameter	-
ϕ	Flow resistance parameters	-
Ψ	Sphericity	-
ω	Collision operator (LBM Equations)	-

Subscripts	
Symbol	***Description***
0	Pertaining to the initial condition or origin
A, B	Different species in a chromatography column
col	Pertaining to a column
CK	'Carman-Kozeny' property
CS	Cross section
D	Properties of the system in dimensionless form
f	Property belonging to a fluid
l	Properties of the system in lattice units
lb	Pertaining to Lattice Boltzmann Method units
m	Molecular property of the solute
max	The maximum instance of the property
min	The minimum instance of the property
p	Properties of the system in physical units
s	'Superficial', of the void space
$total$	The total quantity
$void$	Pertaining to fluid space
w	A 'wetted' property, exposed to fluid interface
x	Pertaining to the axial coordinate system (x-axis)
y	Pertaining to the axial coordinate system (y-axis)
z	Pertaining to the axial coordinate system (z-axis)

Abbreviations	
Symbol	***Description***
1R	A unit cell subject to a single rotation (Miller Index [110])
2R	A unit cell subject to two rotations (Miller Index [111])
ADE	Advection Diffusion Equation
ASTM	American Society for Testing and Materials Standard
BCC	Body-Centred Cubic
BET	Brunauer-Emmet-Taylor
BGK	Bhatnagar-Gross-Krook
CAD	Computer Aided Design
CFD	Computational Fluid Dynamics
CPU	Central Processing Unit
FCC	Face-Centred Cubic
FDM	Fused Deposition Modelling
HETP	Height Equivalent to a Theoretical Plate
HRT	Hydraulic Residence Time
IEC	Ion Exchange Chromatography
ITRI	Industrial Technology and Research Institute
LBE	Lattice Boltzmann Equations
LBM	Lattice Boltzmann Method
LCD	Liquid Crystal Displays
MIP	Molecularly Imprinted Polymers
MOF	Metal Organic Framework
MRT	Multiple Relaxation Time
NS	Navier-Stokes
NTU	Nephelometric Turbidity Units
OS	Operating System
PGD	Primitive-Gyroid-Diamond
RPC	Reversed Phase Chromatography
RTD	Residence Time Distribution
RWPT	Random Walking Particle Tracking
SC	Simple Cubic
SD	Schwarz Diamond
SG	Schoen Gyroid
SP	Schwarz Primitive
SRT	Single Relaxation Time
STA	Sterelithography Apparatus
STL	Stereolithography
TPMS	Triply Periodic Minimal Surface
TRT	Two Relaxation Time
UV	Ultraviolet
VTI	Visual Tool Kit Image
VTK	Visual Tool Kit
WHO	World Health Organisation

Chapter 1 – Introduction

It is known that exposure to heavy metals can cause severe environmental and health problems, and that there are waterways globally and in New Zealand that contain levels of arsenic or other toxic metals above the World Health Organisation (WHO) guidelines[1]. The goal of this work was to assist with the development of a 3D-printable water filter for the extraction of trace heavy metals from contaminated water sources. A Molecularly Imprinted Polymer (MIP) resin developed by Scion's commercial partner is to be incorporated into a printable material that will act as the support matrix and adsorbent medium of the filter. The MIP material is expected to be capable of sequestering metal ions under laminar flow conditions, and behave like an adsorption column. To enhance the performance of the filter, the morphology was optimized through Computational Fluid Dynamics (CFD) studies. The desired outcome of this joint venture between the University of Canterbury, Scion, and the University of Surrey is to produce a filter with enhanced metal adsorption rates, adsorption capacity, and achieve minimised pressure drop while maintaining a sufficient flowrate.

Chapter 2 to comprises a literature review of information relevant to this work, which was centred on designing a packed bed with geometry that produced the most desirable mass transfer characteristics (i.e. dispersion and adsorption properties). Packed beds are used in laboratory and industrial settings to carry out processes including but not limited to: chromatography, distillation, and absorption[2]. Packed beds are favoured for their high interfacial area for processes requiring heterogeneous mass transfer, such as the surface adsorption of the proposed filter. The beds themselves typically consist of a large number of particles or a porous continuous structure (monolith) which divides the space within a column into a solid and fluid phase[3]. Traditionally, spherical particles have been the preferred media for constructing a packed bed, but advances in manufacturing techniques and the capabilities of CFD software enables complex monolithic structures to be investigated. The rapidly improving technologies used in additive manufacturing (such as 3D printing) enables parts as small as 50 µm to be fabricated[4], allowing previously infeasible complex pore networks to be constructed with precision and accuracy. This work builds upon growing interest in the ability to 'design' and create packed beds for improved performance.

It is known that the distribution of solid material within a packed bed can greatly influence the amount of available surface area and induce or limit the quantity of fluid that is able to channel[5] through it. The longstanding use of randomly packed particle beds in industry was a product of convenience, but came at the cost of being able to make precise predictions on the performance of the bed. Empirical relationships were used to describe mass transport and pressure drop observations (such as Darcy's Law[6]), due to the fact that random eddy currents and channelling could not be faithfully recreated by the models of the time. By instead observing ordered structures with three dimensional periodicity, the exact behaviour of the fluid flow and transport phenomena can be recreated, and only requires the

simulation of a small domain. Schure et al.[7] was one of the first to investigate ordered media (arrangements of packed spheres) and show them to have improved chromatographic performance, and Dolamore[8] built upon this by showing that ordered monoliths could outperform ordered particle arrangements. In particular, a family of structures which were nominated to effectively homogenize the fluid flow through them (thus reducing random flow effects) are the Triply Periodic Minimal Surfaces (TPMS) structures, making them of great interest to this work.

While it is possible to manufacture complex ordered structures such as TPMS, assessing the performance of each morphology through experimentation is time consuming and costly. The Lattice Boltzmann Method[9] for CFD was therefore employed to model fluid flow through each structure, and assess the mass transport properties. The use of computational techniques allows for the fast generation of results, and manipulations of the solid phase can be carried out by simply altering model inputs rather than requiring the fabrication of new media. The LBM is favoured in this work over traditional Navier-Stokes equations[10] for its ability to handle complex pore geometries and the readily available parallelisability.

Chapter 3 covers in detail the process of setting up and conducting the LBM and mass transport simulations. The LBM was used to generate a periodic domain representing an infinitely wide column, negating wall effects which disrupt fully developed flow[5,11,12], and the propagation of a passively transported solute was modelled using advection-diffusion equations. An inlet velocity was used to define a converged velocity field, and an inert pulse of solute was introduced to measure the residence time distribution and determine the axial dispersion parameter (the reduced plate height[13,14]). The reduced plate height quantifies the degree of 'band broadening' or axial dispersion (an undesirable phenomenon in column operation) which occurs as a result of the advection and diffusion transport, therefore a low plate height is desirable. A step change in solute concentration was also modelled for both an inert solid phase and surface adsorption case to determine the volume of fluid which could pass through the domain until a breakthrough condition (5% of the inlet concentration) was met. A dimensionless form of the fluid eluted and solid phase capacity occupied at breakthrough were used to generalize the analysis. Each structure was simulated at various flow rates to determine the optimum system parameters, and gauge the pressure drop requirements. The geometric and velocity field parameters for each structure are then related to their mass transport measures, and morphological traits that favour improved performance are identified.

In Chapter 4 the performance of arranged spheres (simple cubic, body-centred cubic, face-centred cubic) are contrasted with the three basic TPMS structures: defined by the Schwarz Primitive (SP), Schoen Gyroid (SG), and Schwarz Diamond (SD) surfaces (collectively known as the PGD family). It was found that there was less axial dispersion occurring in the monolithic TPMS, which when combined with the eluted volume findings confirmed that the TPMS have greater efficiency as packed bed media.

The TPMS also possessed higher porosity, permeability, and specific surface area than the sphere arrangements. From a practical perspective, this infers a greater fluid capacity and adsorption capacity making them even more attractive as a packed column or filter morphology. The Schwarz Diamond structure in particular was found to have the most desirable properties, and has the highest optimum flow rate for reducing axial dispersion. One factor common to all six of the structures observed is that increased tortuosity and homogenisation of the velocity field correlates to desirable mass transport properties, highlighting these as important parameters when designing a packed bed. Another practical limitation of the sphere arrangements is that they are subject to point contacts between particles and thus would be largely unstable in real operation. By combining this work with that done by Dolamore[8] and Schure et al.[7] it was determined that other ordered monolithic packed beds such as TPMS would likely outperform traditional random and ordered particle configurations.

Chapter 5 builds upon the claim that ordered continuous structures produce better chromatographic performance by exploring six additional TPMS structures, as defined by Wohglemuth[15]. Each of the new structures (the IWP, FRD, P2GD, DSG, L, and D' surfaces) differed from the PGD structures as these surfaces separate non-symmetric solid and fluid phases with non-equal porosities. The new structures were also found to have reduced axial dispersion and improved breakthrough performance when compared with sphere arrangements. It was found that TPMS which have a higher specific surface area, such as the L and D' TPMS, are more likely to have higher breakthrough capacities and are thus able to treat greater volumes of fluid. However, these properties are also associated with greater pressure drop requirements, which will impact the cost to operate these structures in a real column. The Double Schoen Gyroid (DSG) is unique in that it separates two distinct fluid phases with an intermediary solid phase, which provides the possibility of printing bi-functional media. The DSG structure also possesses a high specific surface area and thus a high solid-phase capacity, making it competitive with the SD structure.

In Chapter 6 the search for enhanced media was then refined by focusing on the three basic TPMS structures (the PGD family), and applying geometric manipulations to observe their influence on the performance metrics. The work in this chapter describes how re-orienting the solid phase relative to the main axis of flow and modifying the porosity changes mass transfer performance. Previous work by Dolamore et al.[16] had shown that changing the orientation could greatly reduce axial dispersion without changing permeability or the pressure drop requirement. These findings were reproduced in this work by simulating three orientations for each of PGD structures. Dramatic improvements in mass transfer could be obtained by reducing channelling and further homogenising the flow field, which are suspected to reduce mass transfer resistances within the fluid medium[17]. Changes in the orientation were able to alter the velocity field and mass transfer to the adsorptive surface without sacrificing the solid phase capacity, therefore making orientation a critical consideration when designing a packed bed. However, with only limited re-orientation cases observed in this study the results could not be generalized to

determine the optimal orientation of a structure prior to simulation, leaving this as an area for future work. Alternatively, the changes in porosity were systematic and thus could be generalized for exploitation when designing packed bed geometry. In general, higher porosity was related to: reductions in axial dispersion, improved breakthrough performance, and a higher fraction of the solid phase capacity occupied at breakthrough. While the improvements were predictable, they were slight in comparison to those which were obtained from re-orientation. The specific distribution of solid phase material within the unit cell was confirmed to be highly significant in the Stokes flow modelling performed, making the choice and orientation of the packed bed structure highly important. Significant operational improvements could be achieved simply by changing the morphology of a packed bed in any application.

Chapter 7 attempts to summarize all of the findings from the dimensionless analysis performed in the preceding chapters, and relate them to physical systems such as the metal adsorption filter. The dimensionless analysis was performed to allow the relative performance of each structure to be scaled to any physical system, where the operating trade-offs between capacity, flowrate, and pressure drop could be considered in physical units.

The connection between the pore network geometry and the flow characteristics is evident for all of the structures, but is too complicated to reduce to an exact relationship. The mass transfer parameters also display qualitative trends with the geometry and flow parameters. This enabled properties such as the porosity, sphericity, and tortuosity to be used as heuristic indicators of enhanced performance in packed beds (without requiring full simulations). Higher sphericity, high specific surface area and porosity, reduced axial channelling, high tortuosity, and a homogenized velocity field are all associated with more desirable mass transfer characteristics. A prediction was made that a packed bed generated from the DSG structure with an increased porosity would provide improved bed performance. The simulation results highlighted the ability for these relationships to be used as effective guidelines, as the structure was one of the top performing, but the results also addressed the limitations of the relationships as some of the predictions had been overstated. Ultimately, the choice of structure for a real application should be dependent on the requirements of the practical system: high solid phase capacity, high flowrates, low pressure drops, and manufacturing limitations. These results provide a small overview of many monolithic structures and ranks their relative performance in an adsorption filter application. The conclusions about effective mass transport within each structure are not limited to this context, and provide a basis for improving any packed column process with transport phenomena.

To help relate these results to a physical system Chapter 7 briefly addresses many of the considerations not captured by a periodic simulation, such as: the interruption of fully developed flow caused by wall effects, an estimate of the length of unused bed material, and the adsorption model's sensitivity to parameters changes. First, a series of simulations that incorporated bounding walls, thus capturing wall

effects, were used to observe the error in results when compared to the periodic domain. It was determined that a minimum column to unit cell diameter of 30 (which is similar to literature values[12]) would be required to utilize the results of this study without introducing significant errors from wall effects. An assessment of the breakthrough curve development also found that approximately 100 unit cells would be equivalent to the maximum length of unused bed needed at the outlet of a practical column. To investigate whether changes to the process chemistry could influence the relative performance of each structure, a series of simulations with an increased solid phase capacity and adsorption rate constant were performed. The relative performance of the PGD structures was maintained, and the improvements gained from selecting the more favourable SD media were emphasised in the case of the increased adsorption capacity and faster kinetics. While this investigation only provided a limited insight as to the effect of changing process chemistry, it did support the notion that the improved mass transfer ranking of each structure would be maintained in different contexts. The model used in this work could be modified to confirm this for competitive adsorption binding, different reaction schemes, or when considering diffusion deep into the solid phase material.

The complexity of the relationships between bed morphology and mass transfer indicate that there is further scope to study enhanced performance. The set of possible bed morphology solutions is vast and monoliths not constrained to the TPMS family may provide even better performance; it is possible that topological optimisation techniques could be utilised to determine even more optimal media. At the conclusion of this study, the SD and DSG geometries are the recommended structures to be used in an adsorption filter as they possess the best mass transfer properties and show characteristics desirable for an efficient and economical column. The ordered TPMS structures are confirmed to have beneficial properties within the Stokes flow regime, and it is surmised that the benefits should extend into the turbulent regime, but further work is required to confirm this.

Chapter 2 – Literature Review

2.1 Project background

Technological innovation over the past few centuries has both improved quality of life, but also caused unforeseen pollution and detriment to the environment. One issue facing both New Zealand and the world is that of contaminated water sources, which has become an increasingly prevalent issue due to humanity's continued industrialisation. Earth's surface water is subject to pressures from the climate, local environments, and anthropogenic activities. A study conducted by Meybeck identifies that these pressures can cause changes to water systems including but not limited to; sedimentation imbalance, flood regulation, and chemical contamination[18]. It was estimated that as of 2003 less than 17% of surface water was unaffected by human activities.

While the contributing causes of changes in water quality are well documented[19,20,21,22], it is the chemical contamination of water which is of interest in this work. In particular, the increasing amount of heavy metals (copper, cadmium and arsenic) which affects water quality and local ecosystems. In New Zealand alone it is estimated that 10,000 people are currently consuming drinking water that is above the World Health Organisation's recommended safe level of arsenic[1]. As well as the obvious environmental benefits to reducing the levels of heavy metals in water sources, there also exists an economic incentive. The potential for trace metal recovery from wastewater streams from mining and other industrial operations is estimated to amount to a billion dollar industry[23].

This research will contribute to the development of a filter that will be able to selectively remove heavy metal contaminants from water, for the purposes of improving water quality and recovering the metal as a stream of potential revenue. It is proposed that a solid filter can be manufactured using additive manufacturing methods, such as 3D printing, while utilising Molecularly Imprinted Polymers (MIPs) to provide the filter with selective adsorption. The use of affinity adsorption to sequester the metal solute (provided by the MIPs) would allow the filter to be operated by the same principals as a chromatography column, therefore requiring the channel flow to exist in the laminar flow regime. The benefits of using 3D printing for the manufacture of a filter is having the precision and control to create repetitive and ordered internal pore structures, which recent research suggests may have better mass transfer characteristics than traditional packed bed technologies[7,8].

Therefore, it was also an objective of this work to enhance the physical structure of the printed filters. This was achieved by generating multiple designs using Computer Aided Design (CAD) software, and assessing them through computer simulations. Using a specialised branch of CFD known as the Lattice Boltzmann Method (LBM), filter geometries were evaluated for flow characteristics and adsorptive performance. It was hoped that by understanding which parameters have the greatest impact on the filter performance, it would be possible to identify designs which will outperform conventionally

manufactured filters. The parameters that were investigated includes those that are commonly used to assess chromatography columns; dispersion and band broadening, pressure gradients, and adsorption characteristics calculated from breakthrough curves.

The long-term goal of this research is to implement novel filters with Scion's industrial partners to recover toxic metals such as copper, cadmium, and arsenic from wastewater streams. If the technology proves successful then it may be possible to modify the MIP's to target other metal solutes, including precious metals, and open the technology up for further commercialisation. Other potential benefits of this research included the continued promotion of the LBM as an effective CFD tool, and contributions to the growing interest in ordered monolithic columns, which challenges the classical ideas pertaining to packed bed technologies.

2.2 Filtration

Filters are widely used in industry to perform separations on multiphase systems, including the solid-fluid mixtures of interest in this work. A permeable or porous material strains the flow of a fluid and prevents the passage of one or more components from the initial solution. Depending on the desired application, the technology can be applied to particles of sizes spanning several orders of magnitude including: granular material up to several millimetres across, large molecules like proteins, and ions[24]. The solid matter being filtered from solution can be a contaminant species to be removed, or a valuable material to be recovered. Filters perform separations due to physical differences in each phase and may operate by preventing particles from passing through the filter medium, or by forming bonds with particular species within a solution.

The concept of filtration has been used for centuries to purify water. The goal of these early filtration processes was to remove odours and lower the turbidity of drinking water, but over time the technologies have improved and made it possible to soften, purify and disinfect water sources[25]. Typically, larger particles are removed through sedimentation or physical filtration and then smaller contaminants are removed by using filters with smaller pores, diffusion (reverse osmosis), or adsorption principles (selective filter mediums). Filter technology is classified by the size of particles that are able to pass through the filter medium in the permeate phase. Filter technologies are described in detail in Appendix A.1, and include the following classifications for typical filtered particle size ranges; screening (>1 mm), microfiltration (>0.1 μm), ultrafiltration (>10 nm), nanofiltration (>1 nm), and reverse osmosis (<1 nm)[24]. In the case of nanofiltration and reverse osmosis, the molecules are so small that the feed resembles a solution rather than a phase containing discrete particles, and so separation cannot be achieved by size exclusion methods alone. The membranes of specialised filter media used

in these applications utilise diffusion or adsorption mechanisms to assist with the separation[26], as was the case with the proposed filter. Additionally, the concept of depth filters and filter collectors[27] are noted in Appendix A.1, although these concepts are less relevant when utilising MIPs for the adsorbent material.

2.2.1 Filter characteristics

Even when paired with chemical treatment, sand filters commonly used in municipal systems[28] cannot perform sufficient separation for most small contaminants, such as metal ions. Membranes (nanofiltration and reverse osmosis) are one option for the removal of ionic contaminants, and are often characterised by their selectivity, permeability, and flux[29]. The permeability essentially quantifies how easy it is for specific substances to pass through a membrane, and the selectivity relates to the membrane's ability to distinguish between different solutes. Both properties are inherent to the material of the membrane.

While it is important to consider the performance of the filter itself, in the case of water filtration it is also relevant to monitor the quality of the filter permeate (the phase that is able to pass through the filter). Water quality metrics include but are not limited to; turbidity, the water hardness, pH, and the level of organic and inorganic matter[30]. Turbidity measures the cloudiness or the physical appearance of the fluid using Nephelometric Turbidity Units (NTU), and in drinking water is mostly used as an indicator for risk of gastrointestinal diseases[31]. This is because a higher NTU corresponds to more suspended particle matter, which often comprises of organic matter such as phytoplankton. Water hardness is a measure of the multivalence metallic cations in the water (usually Ca^{2+} or Mg^{2+}), but the World Health Organisation[32] (WHO) and independent reviews[33] do not suspect any adverse health effects to be caused by hard water. This work focuses on the concentration of heavy metal elements in water. The levels of heavy metals in contaminated water samples is usually very low, and registers in the parts per million or parts per billion. However even concentrations this low have proven to cause severe health effects both in humans and in other organisms[34,35], therefore it is necessary to lower the concentrations in water streams to below WHO and environmental guidelines. The recommended safe levels of copper, cadmium, and arsenic recommended by the WHO are given in Table 1.

Table 1, Summary of WHO guidelines for safe levels of heavy metals in water[32].

Metal Contaminant	Recommended Safe Limit [µg L^{-1}]	Safe Limit [ppm]
Arsenic	10	0.01
Cadmium	3	0.003
Copper	2,000	2

2.3 Adsorption phenomena

An adsorption process is any reaction where a solid or fluid medium is physicochemically captured at the surface of another solid or fluid[36], and is almost exclusively an exothermic process. Industrially, adsorption processes may be preferred over other separation technologies when there are heat or pressure sensitive species[29], or for their lower energy requirements, high selectivity, lower operating costs, and reusability. When considering any adsorption process it is important to have a thorough understanding of the mechanisms occurring at the molecular level, as they produce the macroscopic phenomena witnessed as adsorption. Possessing appropriate knowledge of the molecular interactions can allow the conditions of the adsorption process to be manipulated for more desirable results (higher selectivity, greater adsorption capacity, rate of adsorption).

The most distinct way to classify adsorption processes involving a solid medium is by whether there is a chemical bond being formed between the adsorbent and adsorbate (chemisorption), or by physical intermolecular forces (physisorption). Chemisorption is typically associated with having a stronger bond between the adsorbate and the adsorbent substrate, but is limited by only being able to form a monolayer of coverage due to the required interaction between surface and adsorbate[37]. Physisorption forms bonds through the intermolecular forces, such as Van Der Waal's forces and electrostatic interactions (such as dipole moments). Due to the nature of these bonds there is the possibility of multiple layered physisorption occurring, with each layer possessing decreasing bond strength. Another potential benefit of physisorption is that the lower bond strengths make it easier to break the bonds to recover adsorbed species.

While it is useful to understand the molecular interactions of adsorption, it is equally useful to model and make predictions about adsorption processes. Important properties such as capacity, selectivity, and the kinetics of the adsorption can be incorporated into models that describe adsorption systems. Some of the most common models include the Langmuir isotherm[38], the BET isotherm[39], and a capillary condensation model developed by Lord Kelvin[40]. The Langmuir isotherm is the simplest model, and only describes monolayer adsorption, while the BET isotherm is more robust and capable of modelling multilayer adsorption. A summary of each of these models can be found in Appendix A.2.

2.3.1 Use of adsorption technologies

Adsorption technology has been widely used in industrial processes and research and development applications for many decades to provide alternative separation processes that can be both less energy intensive and less hazardous[41,42] than alternative technologies such as distillation. In addition, adsorption is reliably used as the principal separation mechanism in many chromatography column designs. Affinity adsorption, ion exchange, and other chromatography techniques are all sorption

processes commonly used in pharmaceuticals, chemical identification and analysis, food processing, and carbon capture[43]. Within a chromatography column the solid phase medium interacts with each solute species with different strengths, causing them to pass through the column at different rates or be retained with different strengths. In other applications, where the adsorption is strong enough, the adsorbed molecules must be cleaved from the adsorbent material to recover the adsorbate or replenish the adsorbent for re-use[36]. Replenishing techniques for adsorption medium can be physical, such as with ultrasonic vibration, thermodynamic manipulation (changing temperature or pressure), or through chemical changes such as altering pH or using a desorbent species with higher binding affinity to displace the original adsorbent[29].

The physical implementation of the adsorption technology has traditionally been through the use of an adsorbent medium, which the mixture undergoing separation comes into contact with. These adsorbent media include crystallographic oxides (including alumina and zeolites[44]), synthetic adsorbents (e.g. polystyrenic materials[45]), and carbonaceous materials (such as activated carbon[46]). Packed beds are commonly used in chromatography columns. More recent innovations have led to the development of new adsorption procedures and functional materials, including activated carbon made from a wide variety of waste materials, molecularly imprinted polymers, and metal organic frameworks.

2.3.2 Treatment of dilute metal contaminants

Current methods for removing heavy metals from water include precipitation, coagulation and flocculation, adsorption, membrane filtration, and electrochemical techniques[47]. A review of heavy metal treatment technologies by Fu et al.[47] determined that precipitation is traditionally the preferred process due to its simplicity and low capital cost, but that it produces unwanted chemical waste in the form of toxic sludge. Therefore there exists an opportunity to explore novel processes, with Fu stating that adsorption has been the most studied alternative. This is supported by the work of Bailey et al.[48] and De Gisi et al.[49], which examine multiple low cost adsorbents for use in water treatment. The materials used as adsorbents include activated carbon made from agricultural wastes[50], marine matter, and fly ash[51], which was found to have a high adsorptive capacity for cadmium and copper. Other adsorbents of interest include seaweed and chitosan.

The processes used to remove heavy metals differs from the treatment methods of other water contaminants because of the tendency for trace metals to exist as ions within the water at low concentrations (ppm levels and below). This makes them more difficult to remove with physical straining due to their ionic size, and less likely to be removed by treatments that target biological contaminants (such as advanced oxidation processes[52]). A review by Barakat[53] on traditional and emerging heavy metal contamination treatment processes found several promising technologies that were limited to only handling certain mixtures of contaminants effectively. A waste stream of both

biological contaminants and trace metals was found to be effectively treated by photocatalysis[53] as it does not produce harmful waste and can handle the complex system. Photocatalysis is a process whereby a semiconductor material activated by light is able to produce the superoxide species O_2^- from simply H_2O and O_2. Then, according to the reaction pathways suggested by Herrmann[54] the superoxide O^{2-} is able to remove contaminants in the water[53].

With waste streams known to be contaminated solely by heavy metals, adsorption and membrane processes are the most widely studied for treatment[53]. One adsorbent that is undergoing development by the Industrial Technology and Research Institute (ITRI) in Taiwan is Green Glass adsorbent material. The Green Glass is refined from discarded Liquid Crystal Displays (LCD) by separating the liquid crystal and Indium for reuse, then processing the glass into a nanoscale adsorbent material[55]. The result is a material that is low cost to produce, has a high adsorption capacity for metal ions in wastewater, and is environmentally friendly.

Metal Organic Frameworks (MOFs) are a relatively modern class of materials that are used for selective separation, such as for the extraction of heavy metals from water[56]. The structure of a MOF (Figure 1), a series of metal ions or clusters suspended in a network of ligands, separates it from other crystalline microporous structures by enabling specific functionality within the pores (if synthesised correctly). There is research to indicate that the pores of a MOF can be modified to selectively bind with heavy metal solutes in a water mixture, with the ability to rapidly and significantly reduce the level of the contaminant in solution[57]. However, MOFs are criticised for their instability over a variety of operating conditions, and ongoing research aims to develop more robust systems. MIPs are another technology with the potential to be developed as adsorbent materials. MIPs are materials that have been created using a template molecule to result in active sites that are tailored for binding with a specific target molecule. The high selectivities that are generally attributed to MIPs is increasing their use for adsorption of high value chemicals or species[58]. The sequestration of heavy metal contaminants using MIPs is proposed to carry out selective adsorption within the filters modelled in this work.

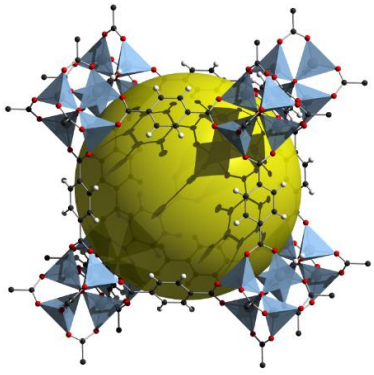

Figure 1. Example of MOF-5[59] unit cell structure, where the yellow sphere represents the volume of the pore (oxygen in red, carbon in black, hydrogen in white, zinc and benzodicarboxylate as tetrahedrons). Sourced from Boehle[60].

2.4 Molecularly Imprinted Polymers (MIPs)

Molecularly Imprinted Polymers are used for applications that require highly selective binding via molecular recognition. Molecular recognition can be found in many naturally occurring processes where specialised structures are only able to 'fit' their target molecules, or very similar species. Natural exemplars of this kind of specialised selectivity include enzymes and hormone receptors[61]. However, these biomolecules are often limited in their applications by the small range of physical conditions they are able to tolerate (pH, temperature), and thus cannot be easily industrialised. Additionally, the extraction of these molecules is often expensive. The goal of MIPs is to develop substances that have selectivity comparable to biomolecules, but can exist over a wide range of conditions, and are inexpensive to synthesise.

2.4.1 MIP fabrication

The concept used for fabricating a molecularly imprinted material is to begin with a target molecule as a template, then to cross-link monomers around the template to create a shell cavity[61]. After the target is arranged within the polymer structure, typically bonded in place by various non-covalent bonds, the target can be extracted through physical and/or chemical means and leave a specifically arranged cavity that will favour bonding with the same molecule again. The cavity will have the same shape, size, and orientation of covalent and non-covalent bonding sites to suit the template molecule[62]. Figure 2 shows a simplified process for fabricating a MIP with cross linking monomers and functional monomers. The final macroscopic size of the MIP material can be achieved by grinding, or by carefully controlling the conditions of the fabrication and precipitation process[63].

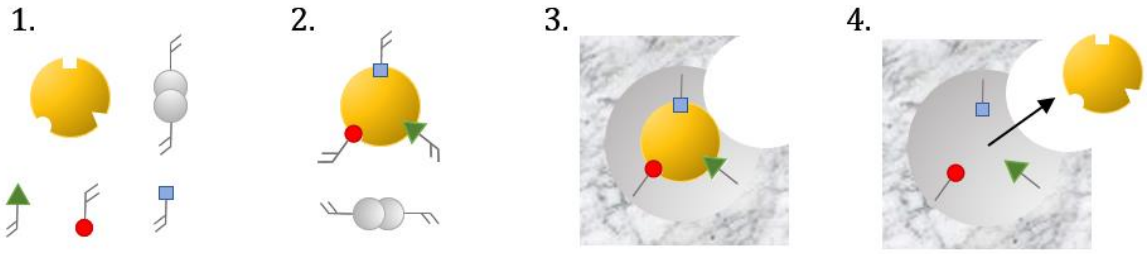

Figure 2. The synthesis process of a MIP. (1) The assembly of functional monomers, cross linkers, and a template molecule. (2) Functional monomers bonding with the target molecule. (3) Polymerization results in a solid structure with target molecule held in the structure by functional monomers. (4) Removing the template molecule to result in a MIP structure.

There is a significant amount of research currently being performed to determine how the fabrication process can affect the selectivity and resilience of MIP materials. Of particular interest when designing

a new MIP is how monomer choice can influence bonding to the template molecule, with Haupt et al. documenting how different monomers provide specific functional groups to bind to target molecules with complimentary functional groups[61]. Other works have assessed the benefits of covalent versus non-covalent bond utilisation[64,65], the method of template removal[62], and the transition states and orientation of the MIPs during fabrication[66]. A review of computational studies of MIPs was able to identify many of the fabrication parameters that influence MIP performance (pressure, temperature, solvent choice), and verified that computational models could predict which monomers would result in effective MIPs for a given target molecule[67]. While there is still plenty of research to bring MIP technology to maturity, it is the general consensus that MIPs may prove to be useful over a range of applications because of their high selectivity and robustness.

2.4.2 MIP applications

The initial motivation to develop MIPs originated from observations of biomolecules such as antibodies, and a desire to replicate their functionality. As such, much of the research into MIPs has been in the field of biotechnology. Many researchers have attempted to make biosensors[65] to recognise organic molecules and upon binding between the target molecule and a MIP site, generate an automated response that can be registered[64]. The energy change from the bond formation is then being harnessed to produce electrochemical and optical (fluorescent) responses. Looking beyond biological applications, MIPs that are fabricated with refined macroscopic geometry were found to be highly effective solid phase sorbents for a range of applications[58]. The geometry could be manipulated to provide a high surface area and increase the access to binding sites, resulting in a material with high capacity and affinity for the target molecule. Irrespective of what the target molecule is, applications for MIPs with these properties include solute concentration, extraction, reaction catalysis, and chromatography[63]. Another important feature of MIPs that is being exploited is the ability for them to distinguish between chiral molecules. If a MIP has a high enough selectivity between stereoisomers, it becomes an attractive candidate for chromatographic separations of enantiomers[68].

In a review of this project scope, it is feasible to utilize a MIP material to effectively remove heavy metal contamination from water sources. The method of fabrication and the selection of monomers used was customized to create a material highly selective for the target metal ions. An enhanced filter geometry could then be implemented to provide solute ions with maximum access to the binding sites. The arrangement of fluid channels to provide enhanced mass transfer was the primary concern of this research, and considerations such as the micro-porosity of the solid phase were not investigated.

2.5 Packed columns

A packed column is a process unit that contains an internal structure with a solid and void space, usually referred to as the packed bed. Packed beds may be defined as a collection of tightly packed particles or a continuous porous structure (monolith) that allows a fluid to flow through the interstitial space[3]. Columns are typically characterised by their void fraction (also known as porosity), pressure drop, and height equivalent to a theoretical plate. Other parameters such as mass and heat transfer coefficients are often related to these using empirical correlations[69]. The geometry within a packed column affords it a high specific surface area, and therefore packed beds are used in processes where it is necessary for a fluid phase to be in contact with a solid phase; such as with catalytic material or surface reaction phenomena. Common applications are those that require good heat or mass transfer characteristics, including; chemical reactors, chromatography, distillation, and absorption[2]. Of particular interest in this work are chromatography columns, due to the similarities between chromatography columns and the proposed 3D printed filter/adsorber.

2.5.1 Porous media and packed beds

A porous structure is defined by a solid matrix with many interconnected void channels through the internal geometry of the medium. The network of void space may be randomly arranged or ordered depending on the fabrication process. Two distinct classes of packed beds are defined by considering an arrangement of individual particles, or a porous continuum such as a monolith, with the difference between them illustrated in Figure 3. The presence of the channels allows fluid to pass through the porous media, but due to the intricacy of these pore networks the flow is heavily restricted and can require large pressure gradients to overcome the resistive forces. Flow through porous structures is often limited to laminar regimes due to low permeability, and highly tortuous flow paths through the solid[70]. These characteristics exist for both monolithic structures and packed beds of particles.

Naturally occurring porous media are almost exclusively characterised by random pore formations, such as naturally occurring monoliths (biological tissues[71] and zeolites[72]) and packed beds (soil and rock formations, or aquifers[73]). Typical synthetically created porous monoliths for use in industry and research have also displayed random pore networks (metal foams[74], ceramics[75], polymer foams[76]), due to the processes which are implemented to create them. However, with innovative manufacturing techniques it is becoming possible to control the internal structure of a porous solid, thus opening up research to optimize the structure of porous media for specific applications.

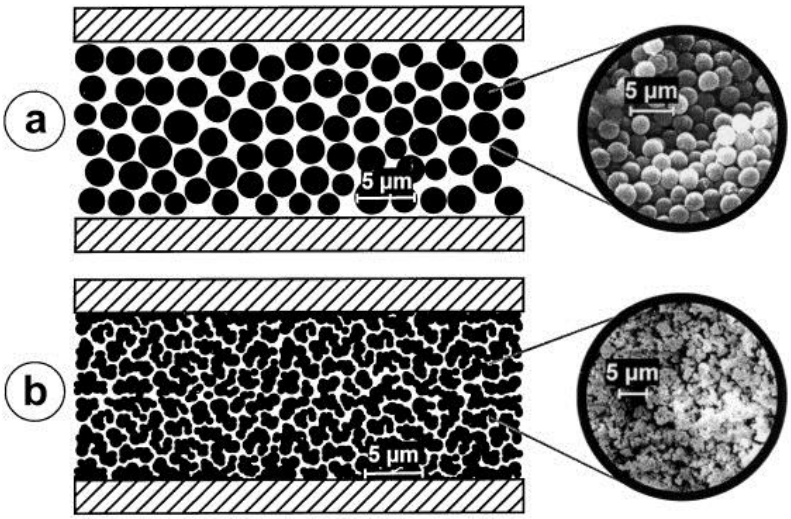

Figure 3, Example of a particle (a) and monolithic (b) packed bed structure with internal porosity (b). Reproduced from[77].

2.5.2 Defining flow characteristics in porous media

2.5.2.1 Porosity and superficial velocity

Porosity (ε) is a basic parameter used to define the ratio of void volume (V_{void}) [L^3] to total volume (V_{total}) [L^3] and can be used to compare the fluid capacity of porous media[78] (Equation [1]). The porosity and other bed properties often influence the permeability and available surface area of a packed bed. There is a trade-off between a low porosity (high amount of solid), which provides more surface area and a greater amount of material for active sites, and a higher porosity (less solid material), which is more permeable to the fluid. Even though it seems intuitively simple to calculate surface area from the porosity, the random or tortuous nature of the channels within porous media often requires this to be found through experimentation or simulation. Only with simple or repetitive structures can the specific surface area be calculated.

Similarly, it is difficult to determine the true velocity at any point within porous media as the flow is seldom uniform within the channels. Instead, the superficial velocity is used. The superficial velocity (u_s) [$L\ T^{-1}$] is much simpler to calculate than the local velocities within the flow channels. It is defined as the volumetric flowrate (Q) [$L^3\ T^{-1}$] divided by the cross sectional area of the column (A_{CS}) [L^2], as shown in Equation [2]. The average superficial velocity within the channels ($\bar{u}_s$) [$L\ T^{-1}$] can then be found by dividing the superficial velocity by the bed porosity (Equation [3]). Further analysis of porous media has historically been done using either empirical equations or with CFD[2, 78]. This is because the complexity and variability of such systems make it difficult to formulate analytical relationships between pressure drop and flowrate.

$$\varepsilon = \frac{V_{void}}{V_{total}} \quad [1]$$

$$u_s = \frac{Q}{A_{CS}} \quad [2]$$

$$\bar{u}_s = \frac{u_s}{\varepsilon} = \frac{Q}{\varepsilon A_{CS}} \quad [3]$$

2.5.2.2 Pressure drop

Some of the earliest research into describing flow in porous media was performed by Henry Darcy, with his experimental results being used to formulate Darcy's Law[6] (Equation [4]). In this form of Darcy's Law, the pressure gradient in the direction of axial flow ($\frac{dP}{dz}$) [M L^{-1} T^{-2}] is related to the superficial velocity, permeability of the solid medium (k) [L^2], and the density (ρ) [M L^{-3}] and kinematic viscosity of the fluid (ν) [L^2 T^{-1}].

$$-\frac{dP}{dz} = u_s \frac{\nu\rho}{k} \quad [4]$$

The permeability of the system is a measure of porous mediums' ability to transmit fluid, and the inverse of the permeability can provide information about the pressure gradient required to achieve a desired channel velocity. However, it is also important to consider that a low permeability suggests a higher pressure gradient is required to achieve the desired flow velocity, which may exceed the compressibility and deformation limits of the medium itself[79]. Therefore the potential for deformation must be considered in all practical scenarios. For all early applications of Darcy's Law, the permeability was determined experimentally and used as a constant parameter, but this assumption only holds for the Stokes flow regime and fluids with constant properties. The Stokes flow regime corresponds to flow with Reynolds numbers (Re) significantly less than one, while laminar flow is thought to occur up to Reynolds numbers of 10 in porous media and packed beds[80]. The Reynolds number for porous systems can be calculated based on the equivalent spherical particle diameter (d_p) [L], the dynamic viscosity of the fluid (μ) [M L^{-1} T^{-1}], fluid density, porosity, and the superficial velocity of the system (Equation [5]). While this is the conventional definition of Reynolds number for porous systems there does exist some discussion about its validity[81], due to the many possible definitions for Re.

$$Re = \frac{d_p u_s \rho_f}{\mu\varepsilon} \quad [5]$$

An alternative equation for relating the pressure drop and flow within a packed bed is Carman-Kozeny equation, which was developed specifically for beds of particles as opposed to porous monolithic structures. The work, initially done by Kozeny and later modified by Carman, replaced the permeability term with a series of parameters that have physical meanings relating to the particles that make up the packed bed. In Equation [6] the particle diameter (d_p), sphericity (Ψ), and a constant (c_{CK}) which usually takes the value 180 or 150 are used[82,83,84]. Sphericity can be calculated using Equation [7], where V_p [L^3] is the volume of solid material and A_w [L^2] is the wetted surface area.

$$-\frac{dP}{dz} = u_s \frac{\nu\rho}{1} \frac{c_{CK}(1-\varepsilon)^2}{\Psi^2 d_p^2 \varepsilon^3} = u_s \frac{c_{CK}\nu\rho}{\Psi^2 d_p^2} \frac{(1-\varepsilon)^2}{\varepsilon^3} \quad [6]$$

$$\Psi = \frac{\left(36\pi V_p\right)^{1/3}}{A_w} \quad [7]$$

The benefit of using the Carman-Kozeny equation is that the constants can be derived from the characteristics of the bed and its constituent particles, removing the need to determine the permeability experimentally. However, the accuracy of the relationship is criticised for limited applicability[85] and it is also only valid for laminar flow regimes. To handle turbulence, the equation can be extended to the Ergun equation[86], which sums the laminar and turbulent regime's contributions to the pressure drop of the separately (Equation [8]). It is important to note that the Ergun equation assumes spherical particles are used, and therefore does not include a sphericity term. Other research has been carried out to modify the correlation to account for non-spherical particles, and have succeeded in better representing experimental results but at the expense of simplicity[87,88]. Many other models for describing the pressure drop exist, and independent reviews of many correlations conclude that there is no universally applicable equation, rather that each model may suit different situations better. Additionally it was noted that many of these models still required constants to be determined experimentally[85,89].

$$-\frac{dP}{dz} = u_s \frac{c_{CK}\nu\rho}{d_p^2} \frac{(1-\varepsilon)^2}{\varepsilon^3} + u_s^2 \frac{1.75\rho}{d_p} \frac{(1-\varepsilon)}{\varepsilon^3} \quad [8]$$

2.5.2.3 Tortuosity

Tortuosity is a measure of the path curvature and pertains to how indirect the flow path between two points is[90,91]. There are many different definitions of tortuosity depending on the application, but for this work the flow tortuosity (T) shall be defined as the ratio of total velocity (u) [L T^{-1}] to axial velocity (u_z) [L T^{-1}] (Equation [9])[92].

$$T = \frac{\Sigma u}{\Sigma u_z} \quad [9]$$

It was thought that this definition of tortuosity could be used as an indicator for channelling[5]. The rationale is: a high amount of channelling would result in the total velocity having less discrepancy with the axial velocity. It would result in a tortuosity value close to one. One of many possible alternative definitions calculates tortuosity as the ratio of diffusion in free space and diffusion in the porous material.

2.5.2.4 Advection and diffusion

To describe a multicomponent fluid, characteristics such as mass and heat dispersion are necessary to fully describe a non-homogeneous system. The goal of this work was to optimize the geometric structure of a packed column to optimize the metal ion adsorption rate and capacity. It was therefore necessary to understand the different aspects of mass transfer occurring within a packed column. Heat transfer phenomena are neglected for this work, as the application of the research is assumed to be isothermal due to low concentrations of metal ion contaminants in water. To further simplify the problem, it was assumed that the velocity field within the packed bed was not affected by the mass transport phenomena of the metal ions. Advection and diffusion equations were used to describe the transport of mass within a fluid system. The transport of material as a result of the bulk flow is described by advection, while diffusion describes transport as a result of concentration gradients and random particle movement[93]. The Advection Diffusion Equation (ADE) to describe the movement of a solute within a fluid is given by Equation [10].

$$\frac{\partial C}{\partial t} = \nabla \cdot (D_m \nabla C) - \nabla \cdot (uC) + Q_s \quad [10]$$

In Equation [10] the partial derivative of a solute's concentration (C) [N L^{-3}] with respect to time is related to three terms; diffusion ($\nabla \cdot (D_m \nabla C)$), advection ($\nabla \cdot (uC)$), and an external term (Q_s). If there is no external cause for a change in concentration, the source/sink term (Q_s) [N L^{-3} T^{-1}] is ignored and the ADE is only dependent on the molecular diffusivity (D_m) [L^2 T^{-1}], concentration, and velocity of the system. The diffusion term can be modelled in accordance with Fick's Law[94], while the advection term ensures that the solute behaves according to momentum of the bulk fluid flow and velocity field[5]. Many packed columns are made of microporous materials, introducing a second tier of diffusion that would occur within the pores. These porous structures often have a greater column capacity, but with the caveat of increased axial dispersion or slower elution of solutes due to the slower diffusion occurring

inside the solid phase. Given that the solutions to the ADE and equations to describe transport phenomena in packed beds and porous systems are non-trivial, research has begun to favour CFD techniques to describe mass and heat transfer.

2.5.3 Random and ordered packing

Another way of defining a column's packing is by its random or repetitious structure of the solid matrix and fluid channels. For packing made up of distinct particles, randomly packed beds comprise of particles loaded into a column without any consideration of their orientation. Thus the channels between them are random and difficult to replicate exactly. Structured packing of particles is possible by carefully orienting each individual particle to fill up a column, but even these configurations may be subject to adjusting during operation and experiencing channelling[95]. Channelling is seen when there is a larger flow channel present in the system that becomes the preferred path for the bulk flow[96]. Synthetic packed beds can be made by either dry packing of particles or slurry packing[97], where the particles are added to the column in a solution or suspension before drying the contents to leave only the packing particles. Slurry packing is known to produce more uniform arrangements[98], but recreating exact geometries from column to column is virtually impossible.

Monoliths generally have a larger porosity than a packed bed, causing them to require smaller pressure gradients and thus making them more attractive for industrial applications. For monolithic porous structures random pore networks can occur naturally[71] or through various fabrication techniques that encourage the formation of void space. However, the random pore networks of these materials still cause them to suffer the same inadequacies as packed beds. Alternatively, the pore channels can be formed through various controlled techniques including 3D printing[99], or the synthesis of Metal Organic Frameworks and artificial zeolites[100]. Figure 4 shows examples of ordered and random packing.

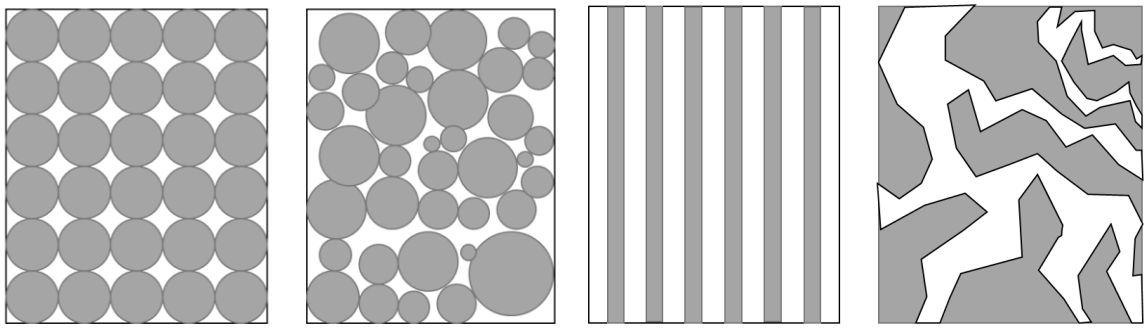

Figure 4, (Left to right) Depiction of: ordered particle parking, random particle packing, ordered monolith pores, random monolith pores. Solid matrix is shown as grey, while flow channels are denoted by white.

Traditionally, porous columns used in research or industry have been randomly packed and thus been difficult to analyse without the use of empirical equations. The random and tortuous nature of the pores results in unpredictable flow phenomena such as eddy diffusion, Dean vortices[101], and flow channelling. All of these phenomena are able to influence the mass flow dispersion within the column and can thus have large effects on processes such as chromatography. The proposed benefits of using ordered packing configurations are a reduction of flow disorder and therefore improved uniformity within the column, reducing dispersion while maintaining sufficient flow rates. This work will seek to build upon this aspiration by investigating highly regular monoliths known as TPMS.

2.5.3.1 Triply periodic minimal surfaces (TPMS)

The optimization of packed bed geometry is an area of research that has been reinvigorated by the advancement of the manufacturing tools available. The enhanced capabilities of CFD simulations and refinement in additive manufacturing capabilities now allow for easier comparison of many different morphologies, and more specifically, ordered packed column structures. Monoliths in particular have been proven to have advantages over traditional packed beds[102,103], although they are typically made from non-microporous materials, thus having low adsorptive capacities. TPMS can be used to segregate distinct void spaces and define monolithic geometries that locally minimise surface area and encourage tortuous flow paths, thereby showing promise for the optimization of packed column performance. Column configurations that minimise axial dispersion are desired.

In order for a surface to be considered minimal it must have a mean curvature of zero, which is a result of every point in the structure existing as a saddle point[104]. They are identified by the Bonnet transformations involved in their Weierstrass–Enneper parameterization[105], which is a parametric set of equations to describe TPMS surfaces using complex numbers. One of the characteristics of TPMS structures is that they have low surface area to volume ratios, thus increasing the likelihood of the structure having a high permeability. Additionally, most basic TPMS structures are not self-intersecting and therefore have smooth surfaces that are desirable for preventing flow obstructions, with the added benefit of being easier that particle packed beds to manufacture with 3D printing technology[106]. Figure 5 displays three common TPMS structures; the Schwartz Primitive (P), Schoen Gyroid (G), and the Schwartz Diamond (D). These particular surfaces (The PGD family)[107] can be described by 'level-set' equations, which are expressed as a set of Cartesian equations in $\mathbb{R}3$. The equations to describe the SP, SG, and SD surfaces are given by Equations [11], [12], and [13] respectively, where (x, y, z) represent coordinates in three dimensional Cartesian space. Many more TPMS structures have been discovered, including some that are combinations of existing TPMS[8,15]. Equations for the SG, SD, and other TPMS are given in Appendix B.

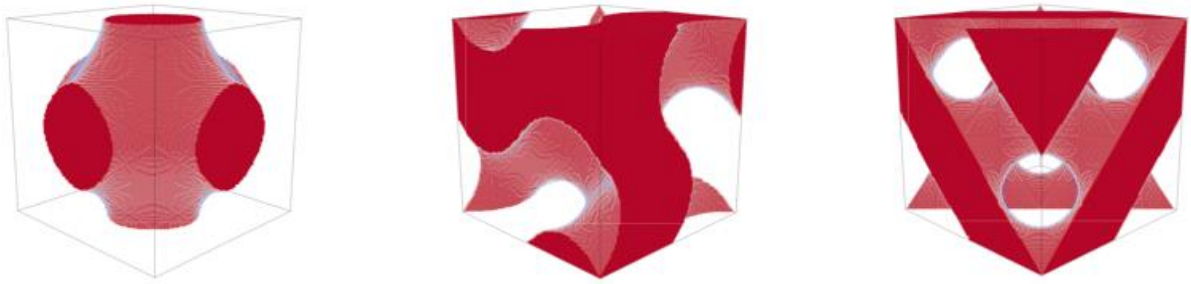

Figure 5, (left to right) Unit cells depicting the SP, SG, and SD TPMS structures.

$$\cos(x) + \cos(y) + \mathrm{coz}(z) = 0 \quad [11]$$

$$sin(x)\,cos(y) + sin(y)\,cos(z) + sin(z)\,cos(x) = 0 \quad [12]$$

$$sin(x)\,sin(y)\,sin(z) + sin(x)\,cos(y)\,cos(z) + cos(x)\,sin(y)\,cos(z) + cos(x)\,cos(y)\,sin(z) = 0 \quad [13]$$

2.5.3.2 Wall effects

Any real packed column requires bounding 'walls' to keep the mobile phase contained. The presence of these walls interrupts the structures of random and ordered packing alike, and can introduce a new contributor to dispersion known as wall effects[5,11,12,]. The most accepted theory for why wall effects occur is because of the change in void fraction near the walls, which encourages preferential channelling. It has been suggested that the negative influence of wall effects can be reduced by extending the packed bed geometry into the wall[7], a feature that is only possible with modern manufacturing techniques. Simulations of packed beds with walls that utilised embedded particles indicated that the wall effects of both random and ordered packing could be reduced with this method[8].

2.5.3.3 Discussion of previous studies

Traditional studies on packed beds indicate that spheres have been the best particle shape for randomly packed beds[108]. The reasoning behind this was due to the efficient packing that can be achieved with spheres, while maintaining a desirable system permeability. A review of chromatography column packing methods was performed by Kirkland et al., who found that traditionally spherical particles (diatomaceous earth, silica) randomly packed through vibration or slurry packing methods were favoured in industry until very recently[109]. To challenge the concept that random packing was the best

performing configuration, Schure et al. conducted a CFD study to compare ordered and random sphere packings[7]. The results of this study indicated that the spheres ordered in the appropriate configuration could have advantages over random packing, such as reduced band broadening in chromatographic simulations. Other numerical studies have begun examining aspects of particle ellipticity[110], particle overlap[99], and orientation[8]. The culmination of these studies indicated that non-spherical particles in certain arrangements appear to achieve better chromatographic performance than spheres. It is noted that there are some trade-offs with using non-spherical shapes, including a high susceptibility to bed deformation and reduced specific adsorption capacity. Another study conducted by Nawada[111] indicated that non-spherical particles possess the potential to outperform spherical particles.

Dolamore[8] investigated the dispersion characteristics of several ordered monolithic structures against ordered and random sphere packing configurations, with particular focus on TPMS structures. The conclusions drawn from this work included:

- Ordered packed beds were able to reduce axial dispersion by normalising flow patterns and reducing eddy dispersion.
- Monolithic structures (TPMS) can show superior performance over packed beds by decreasing band broadening and having higher permeability.
- Changing the unit cell orientation (denoted by Miller indices[112]) with respect to the axial flow direction can improve tortuosity and dispersion without compromising permeability.
- The PGD family of TPMS structures permit geometric manipulation through changes in their level set equations and allow further exploration options to optimize the structures. There exists the opportunity to manipulate monolithic geometry to optimize column performance.
- Further work also supports the conjecture that embedding the walls of a chromatography column with the packing order improves the column efficiency, which is an achievable design aspect when the manufacturing method is 3D printing.

Torquato and Donev investigated the use of minimal surfaces in multifunctional applications and revealed that the resultant materials can be extremal[113,114]. Specifically, they observed how the two void spaces of these structures can be made from materials with opposing but complimentary properties, such as one phase of the bi-continuous structure having a high electrical conductivity, while the other has a high thermal transport efficiency. It is also noted that TPMS structures could be extremal in terms of other transport properties, such as mass. High permeability while maintaining flow symmetry was found in the case of the PGD family[115], with the Schwartz Primitive structure found to have the highest[116]. This research raises the idea that minimising the specific surface area of a porous monolith or TPMS structure may be strongly related to producing higher permeability, which is known to be an important operating parameter for practical chromatography columns.

2.6 Chromatography

Chromatography refers to a family of specific processes that can be used to retrieve or separate different chemical species from a mixture. Chromatography can be used to remove contaminants, retrieve valuable species, or used as an investigative tool to identify the different compounds within a solution[97]. From an industrial perspective chromatography systems may be preferred as they do not require a large investment of energy to perform the separation, and from an analytical standpoint chromatography is coveted for the high selectivity and resolution that can be achieved[117]. Chromatography is always performed by passing a 'mobile phase' (usually a fluid) through a 'stationary phase'. The stationary phase interacts with compounds in the mobile phase; the nature of the interaction is determined by the specific chromatographic techniques being performed. Chromatography can be performed with various combinations of mobile and stationary phase states, but this work will elaborate on liquid-solid chromatography systems (commonly referred to as liquid chromatography). Other chromatography systems include but are not limited to: gas chromatography, high-pressure liquid chromatography, and liquid-liquid chromatography.

2.6.1 Liquid chromatography

Liquid chromatography uses a solid stationary phase and a liquid phase that contains one or multiple solute species to undergo separation. Within the classification of liquid chromatography are five common separation mechanisms; size exclusion, ion exchange chromatography, affinity chromatography, reversed phase chromatography, and hydrophobic interaction. Each mechanism performs a separation based on different operating principals, and are better for separating specific classes of solutes. Therefore it is important to select the appropriate mechanism for any given application. One aspect of operation that all technologies share is that they columns must be operated at low flow rates to satisfy that they are operated within the Stokes Flow regime, with a Reynolds number much lower than one[118]. Under these conditions the optimal chromatographic performance is observed, and the velocity profile scales proportionally to the superficial velocity of the chromatography column. It is also noted that within the Stokes regime the geometry of the stationary phase is able to influence the fluid dispersion[119,120], and thus directly affect column efficiency.

Of the five main liquid chromatography separation mechanisms (discussed in Appendix A.3), only size exclusion performs the separation based on the physical size of the solutes[121]. The other four mechanisms (ion exchange, affinity, reverse phase, and hydrophobic interaction) require non-covalent bond interactions between solutes in the mobile phase and the stationary phase. To remove heavy metal contaminants such as copper from water the best candidates are ion-exchange[122] or affinity chromatography[123], with MIPs belonging to the list of possible affinity media.

2.6.2 Liquid chromatography performance

The performance of a liquid chromatography column can be evaluated using retention, selectivity, resolution, and efficiency. However, before considering each of the metrics, it is important to understand how the results of a chromatographic separation are recorded and reported. A Residence Time Distribution (RTD, Figure 6) shows the relative concentration of each species at the outlet of a chromatography system over time from its initial injection at the entrance of the column[124]. In Figure 6 a typical 'tracer test' is depicted, whereby an instantaneous pulse of a tracer species is introduced to the column (modelled with Dirac Delta function[125]) and the resulting elution is shown by the broader peak after some time has elapsed. The broadening of the peak and a reduced mean concentration is the result of dispersion in the chromatography system. The broadness of the peak also represents the distribution of residence times for molecules of the tracer species within the column.

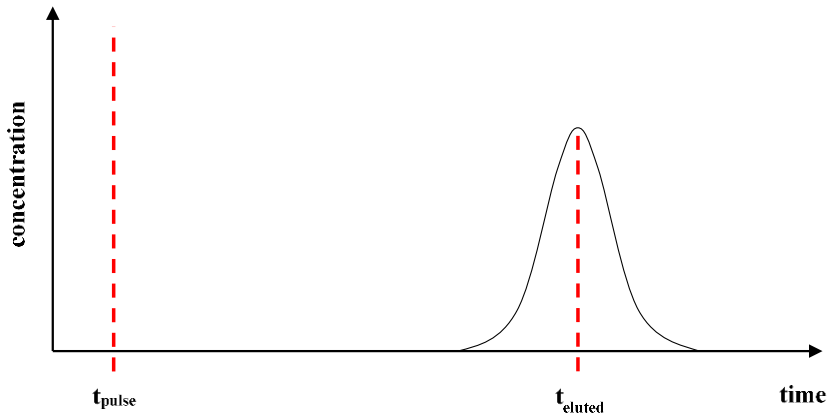

Figure 6, Residence Time Distribution (RTD) of an inert tracer pulse and the corresponding elution concentration profile.

Dispersion is an important concept in chromatography as it is the main cause of non-ideal behaviour, by causing longer elution times and decreasing the concentration of the solute in the eluent. Dispersion occurs through two mechanisms; advection and diffusion. The advection contribution comes from the bulk fluid flow, while the diffusion contribution is from concentration gradients and the random nature of particle movement in solution. In the case of Stokes flow regimes the diffusion may also be contributed to by phenomena similar to Brownian Motion[5].

2.6.2.1 Retention

The retention time of a chromatography column is determined by the amount of time inert tracers and interactive solutes spend inside the chromatographic systems. The retention factor (k_R) is equal to the

ratio between the time it takes for the solvent front, with no affinity for the stationary phase, to elute from the column (t_0) [T], and the time taken for the solute to elute from the column after experiencing interactions with the stationary phase (t_R) [T]. Equation [14] below shows how the retention factor can be calculated from a RTD similar to Figure 7. The selection of exactly when to define t_0 and t_R is at the discretion of the analyst, but must be consistent between the different peaks; whether at the start of the breakthrough curve, at the maximum peak, or any other definition[124]. Retention factors between one and ten are generally regarded as effective when operating a chromatography system.

$$k_R = \frac{t_R - t_0}{t_0} \qquad [14]$$

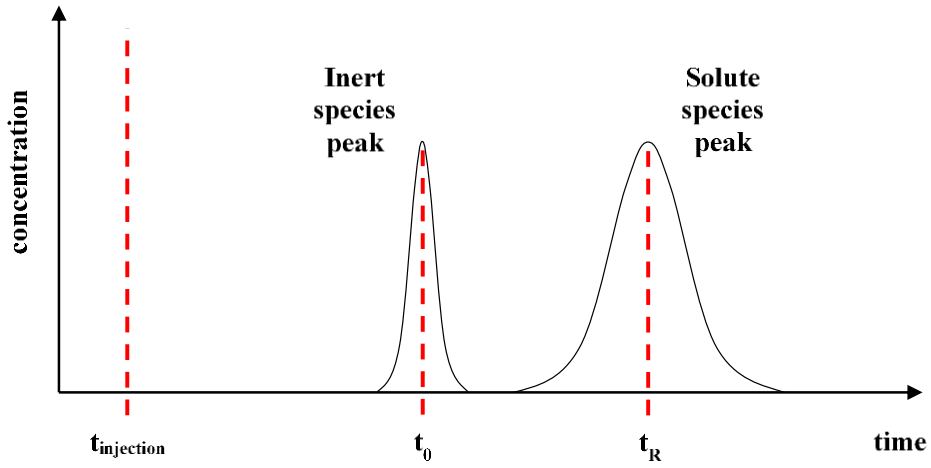

Figure 7, Chromatogram showing the elution of the solvent front (inert) and a solute with affinity for the stationary phase.

2.6.2.2 Selectivity

The selectivity or separation factor (α) in chromatography is used to characterise how distinguishable different solute species are. The selectivity is simply a ratio of the retention factors for multiple species (Equation [15]), and is mostly used to determine the spacing between two peaks (subscripts A and B) in a chromatogram. A higher separation factor is useful for distinguishing peaks, however the effect of band broadening needs to be known too as to assess whether successful separation has occurred. As the context of the metal contaminant filter was considering non-competitive binding with only one solute, the selectivity was not important for this study

$$\alpha = \frac{k_A}{k_B} = \frac{t_{R,A} - t_0}{t_{R,B} - t_0} \qquad [15]$$

2.6.2.3 Efficiency

In chromatography, efficiency is a measure of dispersion. It is used to quantify band broadening of species into Gaussian like distributions[124]. The actual parameter used is the Height Equivalent to a Theoretical Plate ($HETP$) [L], which has been adapted from distillation processes purely for this purpose and is devoid of any physical interpretation[13,14]. Equation [16] shows how the $HETP$ is determined from the axial distance travelled through the column (L_z) [L] and the standard deviation (σ^2) [T] and mean elution time ($\bar{t}$) [T] of a species' RTD within the column. This can then be reduced to a dimensionless form (h) by dividing the $HETP$ by the characteristic length of the system (L_c) [L], as shown in Equation [17].

$$HETP = \frac{\sigma^2 L_z}{\bar{t}^2} \quad [16]$$

$$h = \frac{HETP}{L_c} \quad [17]$$

The mean elution time and standard deviation of any RTD can be determined by software or by manual calculations using the method of moments[125]. The equations for finding the standard deviation (σ^2) and mean (μ) from the RTD curve are shown by Equations [18] and [19] respectively, where C [N L^{-3}] is the concentration and t [T] is time.

$$\mu(t) = \frac{\int_0^\infty Ct\, dt}{\int_0^\infty C\, dt} \quad [18]$$

$$\sigma^2(t) = \frac{\int_0^\infty C(t-\mu)^2\, dt}{\int_0^\infty C\, dt} \quad [19]$$

High chromatographic efficiency corresponds to a low $HETP$ or h, and in the ideal case these would equal zero. A result of zero would occur if the initial pulse of material entering the column, with an hypothetical peak width of zero, experiencing no axial dispersion and thus eluting as a peak with zero width as well. In reality, because the solute passing through the column is not in equilibrium it will experience some degree of dispersion[126]. Therefore it is instead desired to achieve the lowest plate heights possible to improve the operating returns of the column.

2.6.2.4 Resolution

The resolution is perhaps the most important characteristic of a practical chromatography column as it describes the separation achieved between each species. It combines the retention, selectivity, and efficiency terms into one parameter (R_s). The main goal of chromatography is to obtain the optimum resolution in the minimum amount of time. It is desired that baseline separation is achieved; this requires that the peak for each species are fully distinguished and experience no overlap[124]. Otherwise an analyte species may be eluted in conjunction with another analyte species, and make the separation unsuccessful. A resolution greater than 1.5, as defined by Equation [20], is regarded as acceptable separation. In this relationship the width of each peaks base is represented by w_i, where subscripts A and B refer to different species. The resolution may also be represented by the fundamental resolution equation (Equation [21]), which shows how the column resolution is affected by the retention, separation factor, and efficiency. The number of theoretical plates (N) is related to the $HETP$ and the length of the column (L) according to Equation [22], and can be determined using various relationships developed from the RTD curve[127].

$$R_s = \frac{2\left(t_{R,B} - t_{R,A}\right)}{(w_B + w_A)} \quad [20]$$

$$R_s = \left(\frac{1}{4}\sqrt{N}\right)\left(\frac{\alpha - 1}{\alpha}\right)\left(\frac{k}{k+1}\right) \quad [21]$$

$$N = \frac{L}{HETP} \quad [22]$$

Some of the common methods for improving the resolution of a chromatography column include changing the flowrate, changing the length of the column, or changing the time at which the eluent species is introduced[97].

2.6.3 Van Deemter analysis

Within the field of chromatography, J.J. van Deemter developed a relationship between column efficiency and the axial flowrate in the column. Van Deemter was able to identify that the effect of band broadening (column efficiency) was dependent on the flow through the column, and attempted to explain the relationship based on mass transfer resistance and diffusion phenomena[96]. For a fixed column geometry, a Van Deemter curve can be produced to identify the optimum operating flow rate to achieve the minimum amount of dispersion in the column. A typical Van Deemter curve is shown in Figure 8. It is important to note that a Van Deemter curve may be represented with standard parameters

such as flow rate (u) and $HETP$, or with dimensionless variables such as the reduced plate height (h) and the Peclet number (Pe) which is defined by Equation [23]. In this relationship D_m is the molecular diffusion coefficient, L_c is the characteristic length of the geometry, and u is the velocity.

$$Pe = \frac{L_c u}{D_m} \qquad [23]$$

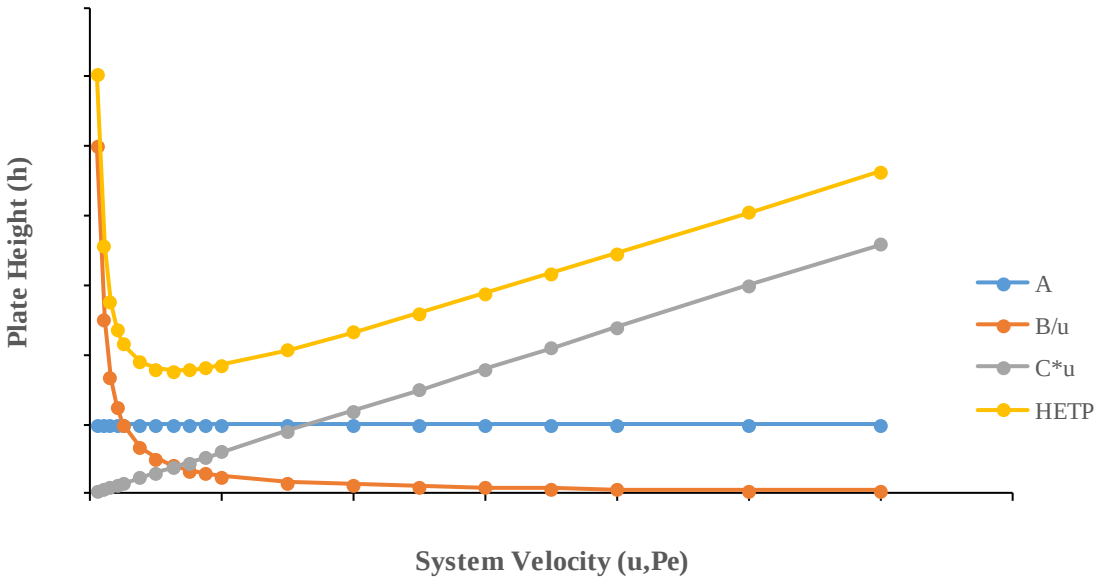

Figure 8, Typical Van Deemter plot showing relationship between system flowrate and plate height. Contributions from each term (A,B,C) shown as well as the cumulative HETP equation.

From Figure 8 it can be seen that the column efficiency has an augmented hyperbolic relationship with the column flow rate. It is also evident that there exists an optimum flow (u or Pe) to operate any given column at so that the maximum efficiency is achieved. For flows below this optimum, it is proposed that diffusion mechanisms increase band broadening, while above these flow rates advection plays a significant role in the dispersion of the solute[126]. Van Deemter proposed a relationship to describe this curve (Equation [24]) by relating the $HETP$ to the flow velocity with three coefficients; A which relates to eddy diffusion, B which accounts for axial diffusion, and C which quantifies the mass transfer resistance in the system[96]. The use of van Deemter plots can be useful to optimise a chromatographic system, as well as to diagnose inefficiency and formulate recommendations for improving performance.

$$HETP = A + \frac{B}{u} + Cu \qquad [24]$$

2.6.3.1 A - Eddy diffusion

The Eddy Diffusion term included in the $HETP$ equation refers to the different path lengths of species passing through the column rather than macroscopic eddies that could be witnessed in the bulk flow of a fluid. If there exists a significant range of path lengths for various particles in the same system it can contribute to decreasing the column efficiency[128], perhaps due to channelling, and may be represented by a high A value in Equation [24]. As it can be seen from Figure 8, the A term is generally regarded to be independent of the system velocity and is instead a result of the flow non-homogeneity caused by the solid medium.

2.6.3.2 B – Axial diffusion

The B term considers the contribution advection has to reduce band broadening and improve column efficiency by muting the effects of molecular diffusion. Molecular diffusion acts to increase the entropy of the system[129], but higher flow rates can be utilised to reduce the impact of the B term. At low velocities, the solute will experience forward and backward diffusion before advection causes it to reach the end of the column, while at higher velocities there is less opportunity for the solute to disperse axially.

2.6.3.3 C – Mass transfer resistance

The C term is used to quantify the mass transfer resistance of a specific system. Several models exist to represent the mass transfer resistance parameter, with the most common considering it as the sum of a dispersive convection effect and an adsorption/desorption effect[17]. The dispersive convection contribution accounts for different channel velocities relative to position near the wall (no-slip boundary) and the centre of the channel. The adsorption/desorption contribution considers how species will elute at different times due to axial dispersion caused by their interaction with the stationary phase. Intuitively, at higher system velocities there will be more dramatic velocity gradients across a channel cross section, leading the mass transfer resistance term to become more detrimental to column efficiency at higher velocities.

2.6.4 Separation impedance

Separation impedance is a useful parameter to use when evaluating column performance because it is able to provide information about the pressure gradient required to operate a column, thus giving a more complete picture of the column performance from a practical perspective. The separation impedance

(E) can be calculated by using Equation [25] to relate it to the column dead time (t_0) [T], pressure drop (ΔP) [M L^{-1} T^{-2}], number of theoretical plates (N), and the mobile phase viscosity (μ)[130]. In this context the dead time of the column refers to the length of time for an inert species to pass through the column (no interaction with the solid phase). The separation impedance can also be related to the reduced plate height (Equation [26]) by using the flow-resistance parameter (ϕ) as defined in Equation [27], where k is the specific column permeability[97]. Lower E values are generally indicative of better column performance.

$$E = \frac{t_0 \Delta P}{N^2 \mu} \quad [25]$$

$$E = h^2 \phi \quad [26]$$

$$\phi = \frac{d^2}{k} \quad [27]$$

2.6.5 Breakthrough Curves

To evaluate a chromatographic process used in the extraction or purification of a specific solute species, it can be useful to consider the breakthrough curve of the system. These are used to show the concentration of species exiting a column against a useful measure of throughput (time, volume)[98]. A typical breakthrough curve is shown in Figure 9. The time at which the solute begins to pass through the column without being adsorbed by the saturated stationary phase (typically estimated at 1-5% of the original solute concentration) is named the breakthrough time (t_b) [T], while the time when the bed is considered completely ineffective (95-99% of initial solute concentration) is given by t_d [T].

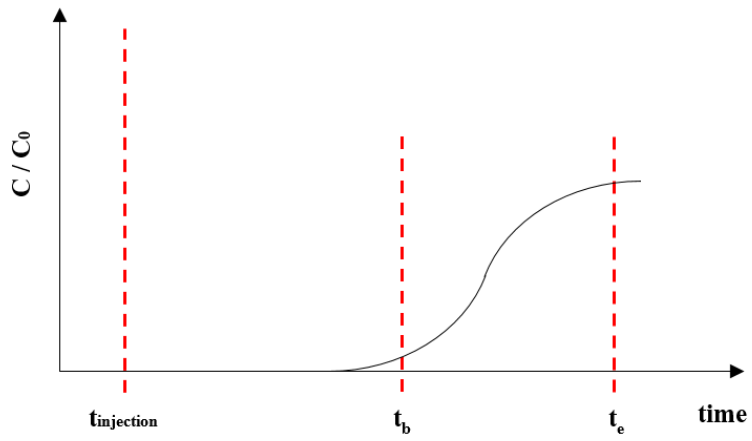

Figure 9, Example of a breakthrough curve where the solute is eluted from its breakthrough (t_b) to the time at which a bed is considered completely ineffective (t_d).

In some cases, the independent variable used in breakthrough analysis will be volume, or a multiple of the dimensionless quantity known as the hydraulic residence time (HRT) [T]. The HRT is equivalent to the time required for an inert specie to pass through the column with no interaction with the bed material, and is calculated from the column volume (V_{col}) [L^3] and the flowrate (Equation [28]). The dependent variable is usually given as a dimensionless fraction of some characteristic concentration (C/C_0), which in most cases is the maximum concentration of the feed.

$$HRT = \frac{V_{col}}{Q} = \frac{V_{col}}{A_{CS}u} \quad [28]$$

Whilst operating chromatography columns, it is desired to have as steep a breakthrough curve as possible, as this can result in the highest concentration of the target solute being eluted. This corresponds to the flow front of the initial solvent and solute passing through the column saturating the stationary phase as it moves, and then the eluent phase unbinding the solute with a non-dispersive flow front during the elution step[117]. The steeper the curve, the better the separation is from a practical point of view. Columns that are able to last longer or 'treat' a larger number of HRT before breakthrough occurs are more effective at performing the separation.

2.7 Computational Fluid Dynamics (CFD)

The term Computational Fluid Dynamics refers to any set of equations that computers can use to determine the dynamic properties of fluids. These equations can describe both steady state and transient systems with reasonable accuracy, restricted only by the computational resources used. All CFD models require a fluid domain to be mapped onto a 'mesh' where calculations are performed on small elements representing the fluid space, and each neighbouring element (cells or nodes) have interactions. The meshing process must be performed prior to any calculations of the fluid properties and can be computationally expensive and time consuming, especially when dealing with geometries that have fine features and require a higher resolution.

The traditional approach to fluid dynamics problems is to use the Navier-Stokes equations, which describe the fluid as a continuous medium[10] with a macroscopic approach. However, more recent CFD equations have attempted to describe fluids with a microscopic approach, in a way more similar to kinetic theory[131] (where the fluid is modelled as particles on a molecular level). The Lattice-Boltzmann equations describe a fluid on a mesoscopic or pseudo-particle level by modelling clusters of particles and using statistical models to describe their interactions, with the macroscopic properties of the fluid emerging from these calculations.

2.7.1 Navier-Stokes Equations

The Navier-Stokes (NS) equations were developed as fundamental equations to describe fluid flow[118]. The equations resolve to describe the flow velocity field over a given domain by taking into account convection, diffusion, viscous effect, and external and internal source terms. The NS equations are complex and are yet to be solved analytically for a general case, but solutions have been found for simplified cases. For an incompressible fluid, the Navier-Stokes equations may be represented by Equations [29] and [30]. Equation [29] is used to maintain the conservation of mass principal, where $\boldsymbol{u}$ [L T^{-1}] is the velocity vector, and Equation [30] is used to describe the conservation of momentum in the system, where P_s [M L^{-1} T^{-2}] is the system pressure, F [M L T^{-2}] is a body force term, ν [L^2 T^{-1}] the fluid viscosity, and ρ is the fluid density.

$$\nabla \cdot \boldsymbol{u} = 0 \qquad [29]$$

$$\frac{\partial \boldsymbol{u}}{\partial t} + (\boldsymbol{u} \cdot \nabla)\boldsymbol{u} - \nu \nabla^2 \boldsymbol{u} = -\frac{1}{\rho}\nabla P_s + \frac{F}{\rho} \qquad [30]$$

Most common CFD packages use the Navier-Stokes equations as the basis for making numerical approximations of a fluid. To obtain accurate simulation results, a high resolution mesh must be produced, a process that is often non-trivial and time-consuming[132]. When dealing with highly porous domains, alternative CFD methods with inherently faster meshing processes and the ability to parallelise the simulation calculations become more attractive than Navier-Stokes methods. The Lattice-Boltzmann Method is an example of an alternative CFD approach that is better suited to porous or complex geometry simulations, as it utilises a regular lattice based domain, which requires less pre-processing, and the calculations required are readily available for distribution in parallel computing.

2.7.2 The Lattice-Boltzmann Method (LBM)

The Lattice-Boltzmann Method can be referred to as a *pseudo-kinetic* CFD model as it describes clusters of particles that interact similar to kinetic theory, but operates on a scale between kinetic theory and traditional CFD models such as the Navier-Stokes[9]. This is possible because it is found that equations to describe the macroscopic properties of fluids are insensitive to the physical interactions of particles within the gas or liquid, and different approaches to describing a fluid on a particle level can result in the same macroscopic representations.

2.7.2.1 History of the LBM

The Boltzmann Equation is a statistical description of the kinetic theory of gases[133], and a discretised version is adapted for use in the Lattice Boltzmann equations. The Boltzmann equation describes a system of rarefied particles, such as a gas, which experience elastic collisions with each other and with the domain boundaries. For a system in three dimensional space, any particle can be described by its position in the domain, $\boldsymbol{x}(x, y, z)$, velocity, $\boldsymbol{\xi}(\xi_x, \xi_y, \xi_z)$, and a moment in time, t. The actual Boltzmann equation uses a probability density function (f) that describes the probability of finding a particle at any given location, with any given velocity, at any specific time (Equation [31]). A collision term ($C(f)$) is used to describe the particle collisions. The probability density function can be used to convert information from the discrete particle system to the macroscopic quantities of a continuous fluid (Equation [32])[134].

$$f = f(\boldsymbol{x}, \boldsymbol{\xi}, t) \quad [31]$$

$$\frac{\delta f}{\delta t} + \boldsymbol{\xi}\frac{\delta f}{\delta \boldsymbol{x}} = C(f) \quad [32]$$

The history and development of the LBM is examined in a thesis by Asinari, and describes how the LBM was adapted from the Lattice Gas Cell Automata by replacing Boolean occupation numbers with ensemble-averaged populations[9]. As the origins of the LBM are used to describe gaseous species, it is necessary to apply a correction to render the equations useful to describe liquids as well. For incompressible fluids, this is achieved by implementing an artificial speed of sound to converge to the compressibility limit[135]. The equations that result are still too complex to solve analytically and thus must be discretised for approximations to be calculated[136].

2.7.2.2 Lattice notation

In order to discretise the Lattice Boltzmann equations, it is necessary to define the lattices that the simulation will be performed on. Any domain has to be discretised onto a series of nodes that make up a continuous space, with each node being capable of representing a quadrature point. In Lattice Boltzmann simulations the lattice domains are given the notation *DXQY*, which describe a domain in 'X' spatial dimensions (*D*) with 'Y' quadrature points arranged around a lattice node (*Q*)[137]. A depiction of the of typical lattice arrangements *D3Q15* and *D3Q19* are shown in Figure 10, with each quadrature point being given the notation c_i, beginning with c_0 at the centre representing a specific node in the discrete lattice space. The other c_i (up to c_Q) represent the nearest neighbouring lattice cells.

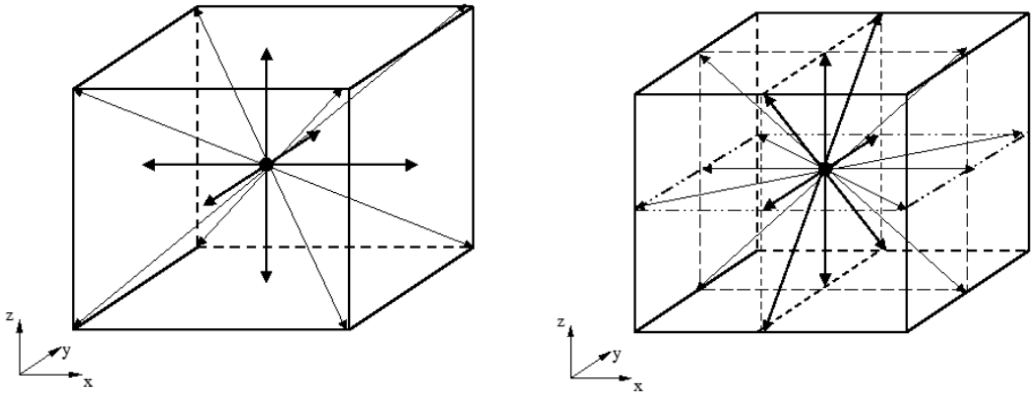

Figure 10, Example depictions of a D3Q15 (left) and D3Q19 (right) lattice with quadrature points. Reproduced from[138].

A higher number of quadrature points can be used to obtain more accuracy from the model, but comes at the cost of requiring more computational resources. Increasing *Q* can also result in the model being able to describe more phenomena, such as compressibility or non-isothermal flow[139].

2.7.2.3 Discretising the Lattice Boltzmann Equations (LBE)

To discretise the LBM equation for use in CFD it is necessary to convert the Boltzmann equation to a series of Hermite Polynomials then eliminate the velocity component through the use of Gauss-Hermite quadrature rules[140]. The resultant 'velocity-discrete' Boltzmann equation is capable of being evaluated at any quadrature point (c_i) (Equation [33]). It is important to note that whichever collision term model is used also needs to be discretised.

$$\frac{\delta f(t,x,c_i)}{\delta t} + c_i \frac{\delta f(t,x,c_i)}{\delta t} = C(f) \qquad [33]$$

To complete the discretisation both the left and right hand sides of Equation [33] need to be integrated, which requires the partial derivative terms on the left-hand side to be approximated using a numerical technique such as the trapezoidal rule. The result of this is the familiar Lattice Boltzmann equation (Equation [34]), where $C(f_i)$ represents the collision term that has been discretised.

$$f(x + c_i, t + 1, c_i) - f(x, t, c_i) = C(f_i) \qquad [34]$$

2.7.2.4 Collision models

When using the LBM, it is possible to use different models in place of the collision term. The simplest collision models are single relaxation time (SRT) models, with the most common being the Bhatnagar-Gross-Krook (BGK) collision model[141]. The BGK collision model is considered sufficient for solving problems with laminar velocity fields[142] and is second order accurate in space and time. In Equation [35], $F_i[f]$ is the value of the probability density function in a state of equilibrium as defined by the Maxwell-Boltzmann equilibrium distribution (Equation [36])[143], and ω is the collision operator given by Equation [37]. The collision operator equation includes the lattice viscosity (ν_l) and artificial speed of sound (c_s) to maintain lattice isotropy[144].

$$C_i(f) = -\omega(f(t,x,c_i) - F_i[f]) \quad [35]$$

$$F[f] = F(x,\xi,t) = \left[\frac{n(x,t)}{\left(2\pi RT(x,t)\right)^{\frac{3}{2}}}\right] \cdot e^{\left(\frac{\left(\xi - u(x,t)\right)^2}{2RT(x,t)}\right)} \quad [36]$$

$$\omega^{-1} = \frac{\nu_l}{c_s^2} + \frac{1}{2} \quad [37]$$

While the BGK collision model is often sufficient, there are also several other collision models which can be used for handling simulations with multiple lattices. When dealing with numerous physical phenomena such as momentum diffusivity, mass transfer, and heat transfer, it can be useful to generate a new lattice for each and then use a Multiple Relaxation Time (MRT) collision model in place of the BGK model[145,146]. Logically, the simplest MRT model is a Two Relaxation Time (TRT) method[147,148]. In TRT methods, one relaxation parameter is applied to either half of the populations to decrease the isotropy of collisions and increase the model's resilience.

MRT models can also exhibit enhanced stability and accuracy over SRT models, but may introduce an unnecessary level of complexity[149], and the choice of relaxation parameters can seem arbitrary[150]. With all collision models, the mathematics and derivations are considerably more complex than the content summarised in this section; full explanations and derivations can be found in references given.

2.7.2.5 Retrieving macroscopic variables

Thus far, the equations examined culminate in the discretised Lattice Boltzmann equation that is able to predict the properties of a fluid using the probability density function (Equation [33]). However, these solutions do not yet produce the macroscopic variables of the fluid that are often the target of CFD

simulations. To obtain macroscopic variables it is possible to simply calculate moments of the probability distribution function. In the case of steady state operation, the pressure and velocity of a Lattice Boltzmann domain can be calculated using Equations [38] and [39] respectively.

$$P(x) = \int f(x,\xi)\, d^3\xi \qquad [38]$$

$$u(x) = \frac{1}{u}\int \xi f(x,\xi)\, d^3\xi \qquad [39]$$

2.7.3 Using the LBM in computation

When conducting fluid simulations using the LBM the computational instructions can be divided into two categories; pre-processing, and calculation. The pre-processing step determines the geometry of the simulation, assigns lattice nodes and the phase state, and can determine the degree of code parallelisation. Parallelisation is the extent to which the calculations can be distributed across several cores to enhance computation efficiency and speed[151]. The pre-processing usually accounts for an insignificant amount of computation time, with the calculation step requiring the most computation power. The calculation instructions occur via multiple iterative steps also; collision, and streaming.

2.7.3.1 Pre-processing

Pre-processing refers to the initialisation and setup of a simulation, before any of the physical calculations and iterations are performed. It is critical to perform the pre-processing tasks appropriately to obtain accurate results. The first commands in the pre-processing stage determine the degree of parallelisation depending on how many cores are to be used in the simulation. The system geometry can then be uniquely defined and discretised onto a homogeneous grid of lattice nodes, either by using CAD input files or with explicit equations to define surfaces[9]. Lattice parameters are then calculated and if the code is to be executed on a parallel system, the domain is partitioned amongst the cores. The final step of the pre-processing stage is to define nodes as either fluid, solid, or a boundary between the two phases[8]. In doing this, it is possible to reduce the amount of computing resources as the nodes that are 'tagged' as solid can be treated as inert, and therefore only the location and nature of these nodes needs to be stored in memory.

2.7.3.2 Calculation

Following the pre-processing step all of the necessary system parameters are known and it is possible to progress the simulation, starting with some known initial conditions. The calculations performed by an LBM typically occur by iterating through a collision step and a streaming step[11,134,136,152]. The collision step involves the computation of the probability distribution function at every node and quadrature point, thus solving the Lattice Boltzmann Equations. The collision step records the incoming and outgoing populations for each quadrature point, while the streaming step that follows progresses the simulation by updating the information at each site[9].

These two steps are repeated several times until a convergence is met, and then performed for each desired time iteration until a simulation is considered complete. The properties of the fluid can be observed and recorded at any point during the simulation, but may require an extensive amount of computing resources to do so. The macroscopic properties of the fluid over any sub-domain may also be accessed by calculating the moments of the distribution function at any point of the simulation mesh.

2.7.3.3 Benefits of using the LBM

The benefits to using a Lattice Boltzmann Method solver for handling CFD problems include the simplification in pre-processing, high degree of parallelisation, and the ability to handle complex geometries. Complex geometries may be defined by relatively simple Cartesian equations, or even passed to an LBM solver such as the Palabos C++ library in the form of a stereo lithography (STL) file. While this is no different to many Navier-Stokes CFD solvers, the benefit with an LBM solver is the ability to model the geometry on a homogeneous grid of nodes, where with many Navier-Stokes CFD packages a custom mesh must be resolved before progressing the simulation. This can be both time consuming and prone to generating instabilities. The ability to parallelise the code provides more computational efficiency, with a higher number of cores reducing the time required for the calculation simulation step[9].

2.8 Additive manufacturing

The term additive manufacturing refers to the process of creating structures by combining a great number of smaller particles or wafer thin layers of material. Additive manufacturing technology has existed since at least 1988 when the first design of a 3D printer was patented by Charles Hull and called stereo lithography apparatus (SLA), a process in which ultraviolet (UV) light was used to selectively harden a polymer bath[153]. These early technologies were mostly used as proof of concepts and for novel applications, but over the past three decades additive manufacturing technologies have been developed

to afford far greater capabilities. These include the ability to print more refined and complex geometry, a wider range of printable materials, and various new techniques that can be used for different applications.

Additive manufacturing is also known by many other names, often corresponding to a specific technology or application, but all adhere to the concept of layer-wise construction. The designs of these structures are often produced from CAD files. Perhaps the most common term for additive manufacturing is 3D-printing, but this is not a perfect synonym; 3D printing technically infers that a print-head or nozzle is used in the manufacturing, while additive manufacturing typically refers to the creation of any 3D structure through layer by layer construction[154] (with exceptions including freeforming[155]). Another common name for an additive manufacturing process is rapid prototyping, which simply refers to the ease and speed with which designs can modified and printed. The various additive manufacturing techniques are suited to different applications[154]. The American Society for Testing and Materials standard ASTM F2792 categorises additive manufacturing techniques in seven distinct families as below[156]. It is worth noting that the standard has since been withdrawn due to the development of new additive manufacturing processes, but this standard still provides a useful overview of additive manufacturing technologies:

- Vat polymerisation – Is equivalent to SLA, and uses a pool of polymer selectively hardened by UV light exposure.
- Powder bed fusion – A bed of powder material (metal, plastics, or ceramics) is fused together by a high precision heat source (laser, electron beam).
- Binder jetting – Thin layers of powdered material are bonded together with the addition of a bonding agent, and may be performed with many materials.
- Material jetting – Structures are made by depositing layers of droplets that are then hardened to form the product. The hardening techniques can include printing molten polymers that will harden in ambient conditions, or hardening the droplets using curing techniques (e.g., UV light).
- Sheet lamination – Sheets of material are laminated together (glued, welding, etc.) layer by layer with unnecessary regions removed as the structure is built up.
- Material extrusion – Material (often thermoplastics) are extruded through a nozzle and deposited as tracks or beads to construct complex geometries layer by layer. This process can be coupled with the printing of support material, and is sometimes known as Fused Deposition Modelling (FDM).
- Directed energy deposition – A powder or wire feedstock (typically ceramic or metals respectively) is selectively melted at the surface of the existing layers to fuse to it and build up the component.

2.8.1 Advancements and advantages

The advancement of additive manufacturing techniques in the past few decades has introduced the capability to print materials in a range of materials and suitable for a variety of applications. It is possible to print polymers, plastics, metals, and composites with the current array of techniques available. The technology has proven useful in educational settings, medical practices, and even aeronautic manufacturing[157]. The rapidly improving technology surrounding additive manufacturing is also enabling the creation of smaller components and finer resolutions, with many 3D printers capable of printing features as small as 50 μm or finer. While additive manufacturing proves extremely advantageous in many situations, it is not without trade-offs. Some of the drawbacks of using additive manufacturing include rougher surface finishes, and in the case of metal sintering techniques it is possible to have induce fatigue and stresses in the final structure[4].

The benefits of additive manufacturing techniques include the ability to rapidly and easily create and modify structures, the ability to create functionalised materials with the use of specific print materials, and the ability to control geometry beyond the capabilities of traditional manufacturing techniques. Of particular interest in this work is the ability to print a functionalised structure simply by the choice of print material, and the ability to control geometry.

2.9 Work direction

The combination of additive manufacturing technology with MIP resins incorporated into the print material allows an adsorbent structure to be created in one step, without the need for separate generation of a support matrix and functionalisation. The other benefit is the ability to control internal pore structures in such a way that would not otherwise be achievable, thus opening up the field of column technology to new morphologies with potentially better performance than traditional column configurations. This is a result of the universal nature of additive manufacturing, which simply requires a layer-by-layer set of instructions to build any solid, hollow, or self-intersecting structure[157]. There has also been previous work conducted at the University of Canterbury to print and test TPMS structures, such as the PGD TPMS family, and analyse their performance in various applications. Therefore, it is appropriate to utilise additive manufacturing techniques to explore the optimization of filter with optimal dispersion and chromatographic performance. In particular, the TPMS family was explored to identify correlations between the structure of the porous media and performance in chromatographic and adsorption applications, as assessed through the use of computational fluid dynamics simulations.

Chapter 3 – Computational Fluid Dynamics Simulation Setup

In order to assess the performance of different porous structures in a packed column application, the use of advanced modelling techniques was implemented. The Lattice Boltzmann Equations were used to simulate fluid flow and passive-scalar transport of a metal contaminant through a network of pore channels representing the proposed filter. This chapter outlines the details of setting up these simulations, and justifies the models and methods used to represent these processes. To apply the Lattice Boltzmann Method, the open source C++ code library "Palabos" published by Flowkit[152] was used. The simulations required:

1. The generation of TPMS geometries using the level set equations mentioned in Chapter 2 (including modified equations).
2. Converging the velocity field within the Stokes regime.
3. Emulating dispersion and adsorption behaviour with advection diffusion equations.

The results of the simulations were finally used to select an enhanced packed bed geometry and assist with the development of more efficient packed beds, such as the proposed adsorption filter.

3.1 The capabilities of the LBM

When performing CFD simulations there are various sets of equations to choose from, and it is therefore important to consider the nature of the system being investigated to determine the best model to use. This research centres around flow in porous media, and observing the interactions at the solid-fluid interface of complex geometries; diffusion, dispersion, and surface adsorption. Therefore, a model capable of accurately representing the solid phase distribution, fluid flow through channels, and solute concentration was required. The LBM was found to be a suitable discretized set of equations, due to its ability to handle boundary conditions with simple algorithms derived from statistical mechanics[158]. LBM solvers differ from many CFD packages by deriving the continuum behaviour of fluids from kinetic theory, and recovering the macroscopic quantities such as pressure and density from the moments of statistical models. These algorithms track large numbers of pseudo-particles that comprise the fluid, and a probability density function determines the local density and interaction of these particles between time iterations.

The open source code library Palabos developed by Flowkit[152] allows users to implement the LBM with in-built parallelisation capabilities. One of the benefits of using parallel computing is that simulations run faster, as the calculations are not limited to serial execution. It is well documented that using *n* cores in parallel computing has the potential to achieve a decrease in calculation time[152] by a factor close to *n*.

The divergence from an exact factor of *n* is attributed to the computational overheads associated with communication between Central Processing Units (CPU's) in parallelised problems.

The Palabos software package was the preferred tool to conduct these simulations because of the ease with which it can handle complex geometries. The mesh used by Palabos is a regular cube lattice, which enables any geometry to be mapped onto a regular grid of points and avoids the cumbersome 'meshing' processes that other CFD packages require. In practice, the mapping of fluid-surface interface for complex TPMS over reasonably significant domain sizes (approximately 250,000 nodes) required only seconds to complete.

3.2 Implementing the LBM

In order to conduct the desired simulations, a script was written in C++ to describe the physical system and call functions from the Palabos code library to implement the LBM method. The script was developed from previous research carried out at the University of Canterbury to investigate dispersion within porous media[8,16]. Model developments included the ability to select whether there is intra-porosity (internal diffusion) in the solid material, and the monitoring of solute concentration in the fluid phase as well as the adsorbed solid phase.

The range of porous media structures investigated were all regular geometries, and therefore they could be defined by geometric equations (randomly packed spheres were not considered within this study). This was achieved by locating the surfaces of the fluid-solid interface and declaring the phases either side of the boundary to be fluid or solid. The surfaces of ordered sphere packing arrangements could be described using Cartesian equations, and TPMS structure surfaces were defined using level-set equations as provided by Wohglemuth[15] and Von Schnering[159] et al. Once the surfaces had been mapped onto the regular lattice, the surface functions were used to define inequalities that separated the lattice domain into fluid and solid nodes.

The inlet and outlet conditions, fluid dynamics, boundary conditions, and transport phenomena were specified in the pre-processing of the simulation. Each simulation then progressed through:

1. Resolving the velocity field.
2. Simulating an inert tracer species to determine dispersion behaviour,
3. Introducing a step increase of inert contaminant to observe column breakthrough
4. Simulating breakthrough with an adsorptive species.

Each of these aspects of the simulation are described in more detail below, including the post-processing and interpretation of simulation results.

3.3 Simulation setup

Prior to each simulation, a configuration file was created to define the geometry, flow properties, and solute behaviour. This included specifying the size and morphology of simulation domain, the flow velocity, boundary conditions, and the diffusion and adsorption parameters (all in physical units). These physical properties were used to generate analogous properties that possess discretized 'lattice units', a requirement for carrying out calculations with the LBM due to the spatial and temporal discretization of the fundamental equations used in the LBM. For most properties, the conversion to lattice units could be achieved by using arbitrary reference properties to produce dimensionless analogues of the physical quantity, or by the use of a dimensionless quantity to scale between the systems of units.

3.3.1 Spatial discretization

The spatial dimensions of the simulation were converted to lattice units by dividing them by a reference length characteristic to the system to make them dimensionless, then multiplying them by a reference length in lattice units. The reference length in both cases was the distance between two nodes (Δx), which is the related to the resolution of the simulation (R_x). The reference length of the physical system (Δx_p) [L] was determined using Equation [40] by considering the number of 'nodes' in the simulation grid that exist over a known characteristic length (Z_c) [L]. The reference length in the lattice was, for simplicity, chosen to have a length of unity. The effect of spatial discretization in 2D and 3D domains is exemplified in Figures 11 and 12, where higher spatial resolution recreates a more accurate representation of the original shape.

$$\Delta x_p = \frac{Z_c}{n_{nodes\ in\ Z_c}} = \frac{Z_c}{R_x - 1} \qquad [40]$$

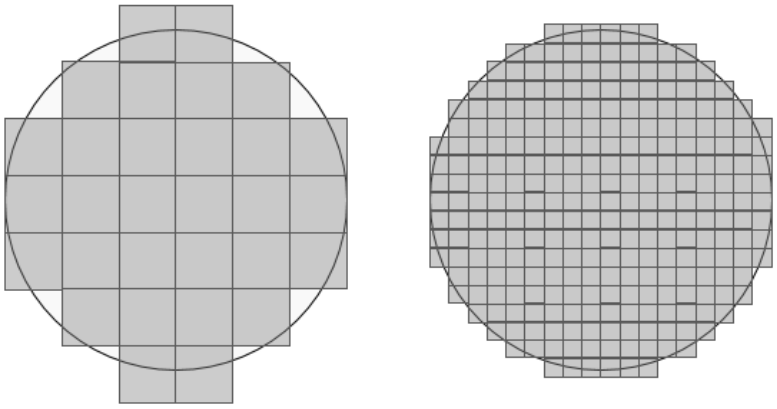

Figure 11. Representation of the effect of low (left) and high (right) resolution and voxelization in a 2D domain.

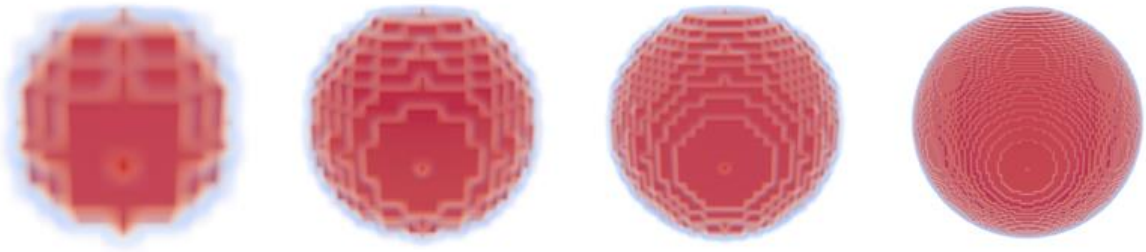

Figure 12. Voxel resolution of a sphere approximated using Palabos with resolution of (left to right) 11, 21, 31, and 91 nodes per unit cell. The resolution used for simulations was 31 nodes.

This method of converting length parameters (L) in lattice units is shown by Equations [41] and [42], where the subscripts 'p', 'D' and 'l' correspond to 'physical', 'dimensionless', and 'lattice' units respectively. Equation [43] shows the conversion in a single step, and how because the reference lattice unit was defined to have a value of unity, the conversion simplified to remove the dependence on Δx_l.

$$L_D = \frac{L_p}{\Delta x_p} \quad [41]$$

$$L_l = L_D \times \Delta x_l \quad [42]$$

$$L_l = \frac{L_p}{\Delta x_p} \times \Delta x_l = \frac{L_p}{\Delta x_p} \quad [43]$$

A higher spatial resolution will yield more accuracy, but with the trade-off of requiring more computational resources such as memory and simulation time. Previous work has shown that utilising a spatial resolution of 31 nodes in each direction for a periodic unit cell can produce accurate results without requiring excessive simulation time[8]. The study conducted by Dolamore[8] proved the Palabos code to have mesh independence when calculating the values of permeability and reduced plate height, confirming accurate convergence of the velocity and concentration lattices. For this study, a mesh independence test was carried out on the breakthrough adsorption performance measures. These were the dimensionless void volumes (V_D) that were eluted through the simulation domain prior to breakthrough (5% of the inlet concentration reaching the observed slice), and the dimensionless fraction of capacity (C_D) occupied by solute at breakthrough.

Each of these is discussed further Section 3.4.4, but the measure V_D is a variation of the hydraulic retention time (HRT) and C_D is equivalent to a saturation fraction. A systematic study into the accuracy was performed by increasing the resolution, and is shown in Figure 13, where it can be seen that the values of V_D and C_D obtained using 31 nodes differed by less than 5% when compared to the benchmark

61 node simulations. This was considered to be sufficiently converged to the benchmark solution to justify the improved efficiency[8] from operating at 31 nodes instead of 61. The void volumes calculated from adsorption breakthrough simulations were the slowest to converge and therefore showed the largest sensitivity to the mesh resolution.

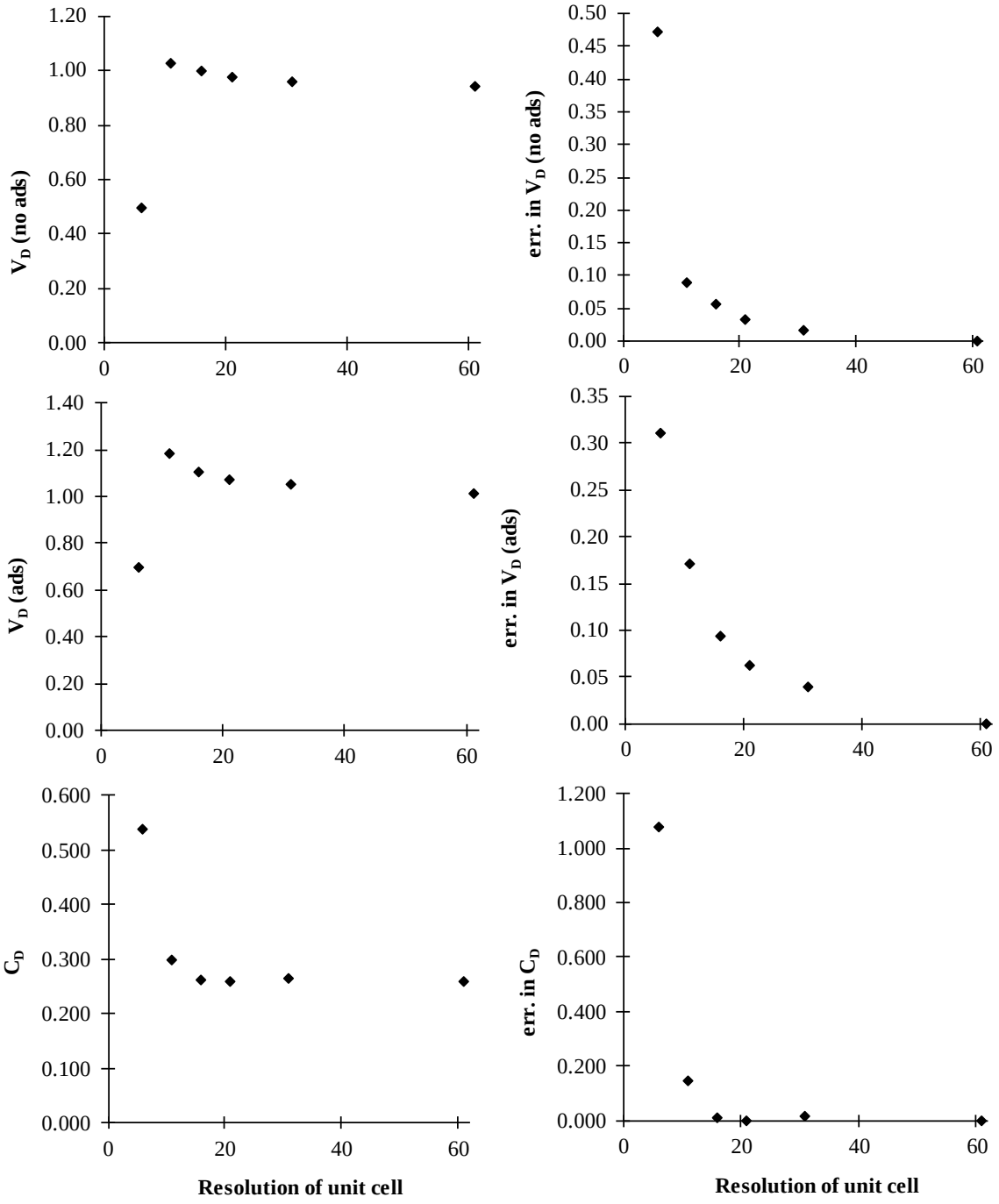

Figure 13. Mesh independence verification for the values of V_D and C_D from breakthrough simulations. The resolution of 61 nodes (the highest observed) was used as the basis for calculating errors.

3.3.2 Temporal discretization

The equations used in the LBM require time to be discretized, and therefore a suitable time step must be used between simulation steps[152]. This time step is used as the reference time for converting physical properties to lattice units similar to how it was performed for spatial dimensions; a reference time in lattice units (Δt_l) is used, which for simplicity is chosen to have a value of unity. The reference time in physical units (Δt_p) [T] was determined by the relationship between the kinematic viscosity of fluid and the kinematic viscosity in physical and lattice units, which is dependent on properties inherent to the LBM lattice. The lattice kinematic viscosity (ν_l) is related to the relaxation parameter (τ) used in the simulation, and for numerical stability ν_l was set to a value of $\nu_l = 1/6$ for use with the BGK collision operator[160,144]. This value for ν_l was calculated using Equation [44], where the relaxation parameter (τ) is required to equal one, and c_s is an artificial speed of sound set to $c_s = 1/\sqrt{3}$ to maintain lattice isotropy[144] for the D3Q19 lattice used in this work.

$$\nu_l = \frac{\tau - 0.5}{1/c_s^2} \qquad [44]$$

Using the newly calculated lattice viscosity, the dimensionless viscosity (ν_D) was obtained by dividing ν_l by the reference lattice time ($\Delta t_l = 1$) and length ($\Delta x_l = 1$) squared (Equation [45]). The real kinematic viscosity of the fluid (ν_p) is related to ν_D by the reference length (Δx_p) and the reference time (Δt_p), as shown in Equation [46]. This equation is rearranged to obtain the reference time of the physical system (Equation [47]).

$$\nu_D = \nu_l \times \frac{\Delta t_l}{\Delta x_l^2} = \nu_l \times \frac{1}{1} = \nu_l \qquad [45]$$

$$\nu_p = \nu_D \times \frac{\Delta x_p^2}{\Delta t_p} \qquad [46]$$

$$\Delta t_p = \frac{\nu_D}{\nu_p} \times \Delta x_p^2 = \frac{\nu_l}{\nu_p} \times \frac{\Delta t_l}{\Delta x_l^2} \times \Delta x_p^2 = \frac{\nu_l}{\nu_p} \times \Delta x_p^2 \qquad [47]$$

3.3.3 Converting other properties to lattice units

Determining properties such as the pressure within the lattice system required the conversion of mass between real, dimensionless, and physical units. This was achieved through relating the fluid density in physical (ρ_p) [M L^{-3}] and lattice (ρ_l) units using reference quantities. The lattice reference mass is also

set to $\Delta m_l = 1$ for simplicity, so $\rho_l = 1$ also as seen in Equation [48]. The dimensionless density is assigned the value of unity, and can be related to the physical density through Equation [49] using the physical reference parameters. It is a rearrangement of this (Equation [50]) that defines the physical reference mass (Δm_p) [M].

$$\rho_D = \rho_l \times \frac{\Delta x_l^3}{\Delta m_l} = \rho_l = 1 \quad [48]$$

$$\rho_p = \rho_D \times \frac{\Delta x_p^3}{\Delta m_p} = \rho_l \times \frac{\Delta x_p^3}{\Delta m_p} = 1 \times \frac{\Delta x_p^3}{\Delta m_p} = \frac{\Delta x_p^3}{\Delta m_p} \quad [49]$$

$$\Delta m_p = \frac{\rho_l}{\rho_p} \times \Delta x_p^3 = \frac{1}{\rho_p} \times \Delta x_p^3 \quad [50]$$

The majority of the remaining system properties have dimensions that are a combination of mass, length, and time. The process for converting these to lattice units requires calculation of their dimensionless analogues (using the reference properties as determined above), and then multiplying them by the corresponding lattice unit reference quantities (all set to unity). The process for finding the lattice velocity (u_l) is shown in Equation [51] below as an example. By defining lattice properties in this way there is consistency between dimensionless numbers in both sets of units, such as the Peclet number and Reynolds number. In addition to the properties already defined, the molecular weight (M_w) of the solute was used to determine a reference molar quantity.

$$u_l = u_D \times \left(\frac{\Delta x_l}{\Delta t_l}\right) = u_p \times \left(\frac{\Delta t_p}{\Delta x_p}\right) \times \left(\frac{\Delta x_l}{\Delta t_l}\right) = u_p \times \left(\frac{\Delta t_p}{\Delta x_p}\right) \quad [51]$$

3.3.4 Defining simulation geometry

The structure of the solid material used in each simulation was defined by using equations to locate the solid surface over a periodically repeating unit cell, and then extrapolating the results over the full simulation domain. For ordered sphere packing orientations, the surfaces of the particles were located by identifying the coordinates of particle centres within the unit cell and defining a spherical shell at a distance of one radius. The fluid nodes were then distinguished from the solid nodes by implementing an inequality to denote nodes that fell within the spherical shell. Equation [52] shows how each value of each node (lattice coordinates; x, y, z) was evaluated relative to the particle's centre (coordinates; x_0, y_0, z_0), where r_p is the radius of the particle in lattice units. For TPMS structures the surface was

identified using level-set equations to approximate the surface location, and an inequality was used to determine the distribution of solid and fluid nodes within the unit cell. Equations to describe the TPMS structures are catalogued in Appendix B, and an example case for the Schwarz Primitive structure is shown in Equation [53]. It is important to note that when defining the TPMS structures, the direction of the inequality and value of the right hand side of the equation determined the phase fractions of the unit cell, and therefore influenced the resultant porosity of the packing media.

$$if \begin{cases} (x-x_0)^2+(y-y_0)^2+(z-z_0)^2 \leq r_p^2 & ,solid\ node\ [1] \\ (x-x_0)^2+(y-y_0)^2+(z-z_0)^2 > r_p^2 & ,fluid\ node\ [0] \end{cases} \quad [52]$$

$$if \begin{cases} cos(x)+cos(y)+cos(z) \leq 0 & ,solid\ node\ [1] \\ cos(x)+cos(y)+cos(z) > 0 & ,fluid\ node\ [0] \end{cases} \quad [53]$$

Once the geometry of a periodic unit cell was defined by this methodology, the resultant solid was patterned over the entire simulation domain. This process resulted in the generation of scalar fields containing a one or a zero for each node in the simulation, relating to a solid or fluid node respectively. The surface nodes were located by iterating through each solid node in the scalar fields and inspecting the nearest neighbouring nodes for fluid nodes. Nodes that existed at the surface of the solid were identified to allow the user to decide whether to model alternative dynamics for diffusion into the solid, or to model surface phenomena such as adsorption.

3.3.5 Parallelisation

After defining the geometric boundaries of the simulation, if the simulation was to be computed in parallel, the domain was distributed amongst the multiple cores using open MPI software[161]. Two lattice structures were generated for colliding and streaming the fluid and concentration populations. The Palabos library and MPI software was capable of automatically partitioning the simulation domain between several cores and managing the communication between them. The simulations conducted in this work were performed using a Linux Operating System (OS), and the model was confirmed to produce the same results in serial and parallel computation following any model development.

3.3.6 Boundary conditions

The radial boundaries of the system were defined to be periodic to emulate a column of infinite width. These boundary conditions ensured that the conservation laws were maintained between opposing radial boundaries, and greatly reduced the computational resources required to simulate periodic behaviour. In practical columns, an infinitely wide column and periodic behaviour can never be achieved and

instead disruptions to periodic behaviour is observed as 'wall effects', which are the result of boundary layer formation[11,12]. Literature also supports that, in the case of packed columns of spherical particles, a column diameter to particle diameter ratio of 60 is large enough to negate wall effects in chromatographic analysis, although other studies[162] suggest values as high as 100 is required to approximate periodic behaviour.

Along the axial direction, a uniform velocity profile was applied to the inlet as a Dirichlet inlet condition and a Neumann condition was applied at the outlet. A zero pressure boundary condition was also applied at the outlet, in keeping with common CFD simulation configurations[163]. Entrance and exit lengths were also utilised in the periodic domain to alleviate entrance and exit effects, and achieve a fully developed flow profile across the 'periodic unit cell' in the middle of the simulation domain (Figure 14).

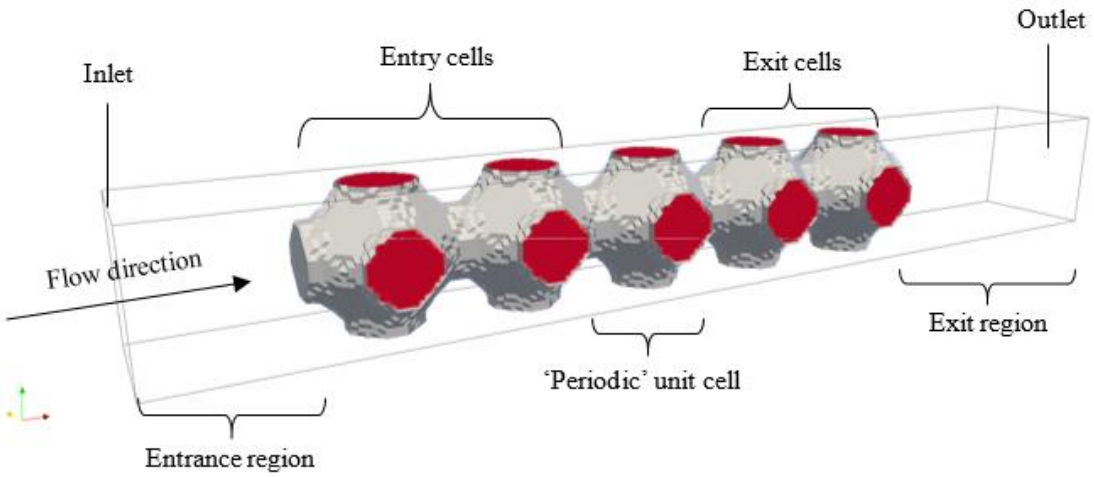

Figure 14. Annotation of the periodic simulation domain for Schwarz Primitive structure. Solid represented by red, and surface represented by grey.

The presence of an entrance region (1 unit cell in size) was to allow for changes in the concentration at the inlet to reach a stable condition before entering the simulation domain, because otherwise numerical 'jumps' could be observed when defining a step increase at the inlet concentration. The exit region was to allow for a smooth velocity profile to develop before reaching the Neumann boundary condition. The choice for how many entry and exit cells were required to have fully developed flow around the periodic cell was dependent on the simulation velocity (Pe). The number of cells was selected from observing the value of the reduced plate height calculated at different positions along a large simulation domain and determining when the value was stable. To calculate the values over a periodic unit cell, 'slices' of data were used from the inlet and outlet to the periodic cell (as seen in Figure 15).

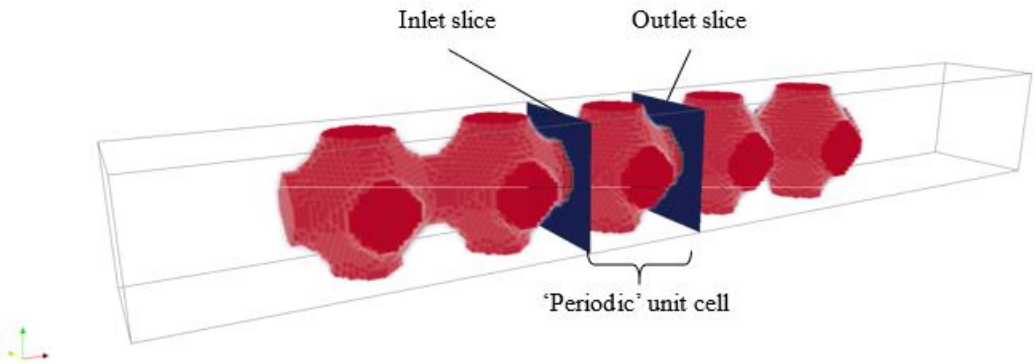

Figure 15. Location of inlet and outlet slices used to observe changes across a periodic unit cell.

It was found that geometries that experienced a higher amount of channelling (such as simple cubic spheres, or the Schwarz Primitive TPMS) typically required longer columns to reach fully developed flow profiles. For all geometries, it was found that at low system velocities (superficial $Pe \leq 50$) that two entry and exit cells were sufficient to produce a developed flow profile over the periodic cell. With increased system velocity higher numbers of cells were required, as can be seen for the case of the Schwarz Diamond geometry in Figure 16, which required approximately four entry and exit cells, and for a simple cubic (SC) sphere arrangement in Figure 17, which required close to seven unit cells. The longer domain required by the spheres can be attributed to its lower tortuosity and therefore the occurrence of channelling, requiring a longer domain for the flow to fully develop.

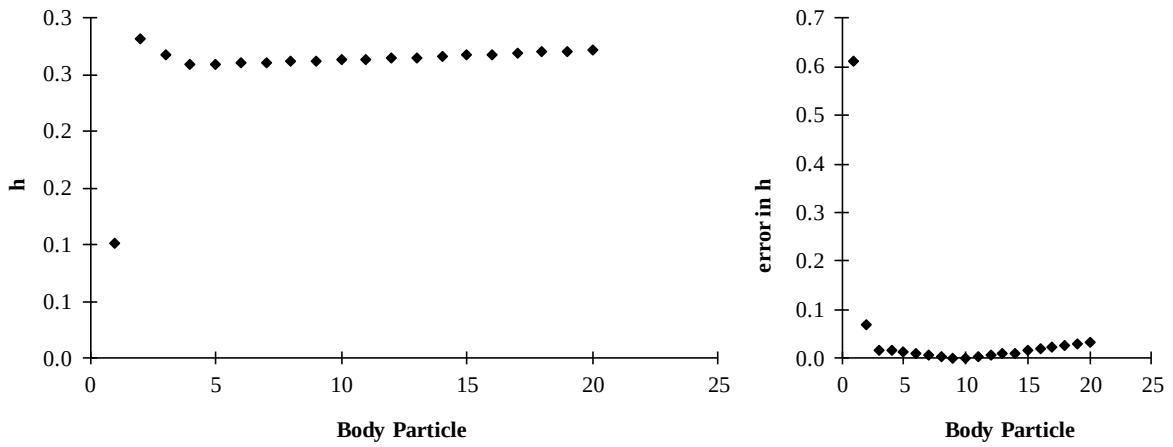

Figure 16. Convergence of the reduced plate height for the Schwarz Diamond TPMS packing arrangement over a 20 unit cell domain for superficial Pe=100.

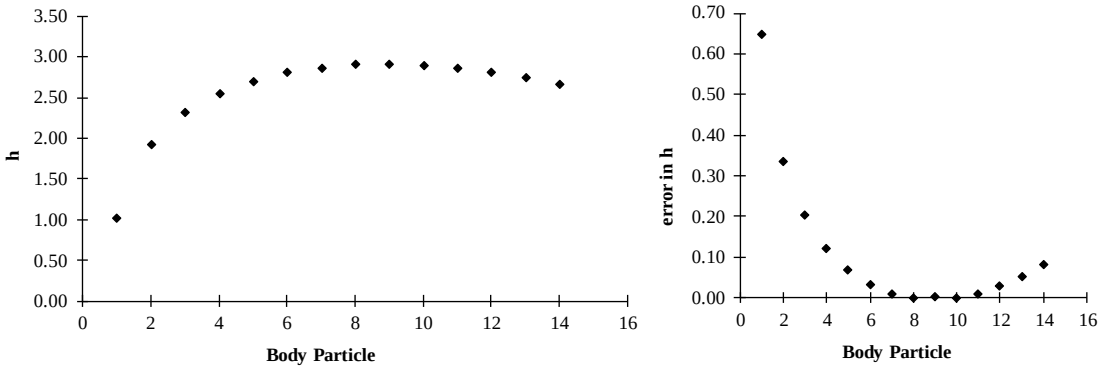

Figure 17. Convergence of the Simple Cubic (SC) sphere packing arrangement over a 15 unit cell domain (Pe=100).

For the velocity lattice, "bounce-back" conditions were defined at the fluid-solid surface to simulate a no-slip condition. The no-slip condition is used to describe the interaction between a viscous fluid and solid boundary[164], whereby at the surface the fluid velocity is assumed to be zero. As the distance from the wall increases through a boundary layer, the fluid velocity increases to reach a maximum channel velocity. Bounce-back conditions may be used to model the no-slip condition in LBM simulations[165,166], although it is acknowledged that using bounce-back conditions limits the accuracy and speed of simulations to some degree[167]. The simple implementation, handling of complex geometries, and computational efficiency achieved with bounce-back conditions were deemed to outweigh any potential drawbacks. The mathematical logic underpinning bounce-back boundary conditions involve interpolating the solid-fluid interface to exist halfway between solid and fluid nodes, and reflecting any incoming particles (f_{in}) which attempt to cross the interface back (f_{out}) to the node from which it originated[168]. At the pseudo-particle scale, the populations approaching the wall do not move over an iteration, which macroscopically reproduces a no-slip effect (Figure 18). It is the ability for the bounce-back condition to be implemented on the regular grid of solid and fluid nodes that allows the LBM to easily and accurately handle complex geometries, assuming the mesh has a sufficiently high resolution.

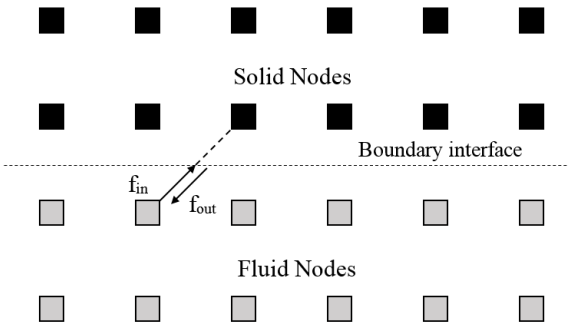

Figure 18. Visual representation of the bounce-back boundary condition implemented between fluid and solid nodes.

3.3.7 Defining the concentration lattice

Within the scope of this research the water contaminant concentration was estimated to be in the order of 100 ppm Cu at the inlet. Therefore, the assumption was made that the concentration of solute would not influence the velocity field or pressure within the fluid, and could be modelled as a scalar with passive transport[169]. The velocity lattice's resolved velocity at steady-state was coupled one-directionally to a secondary concentration lattice prior to dynamic modelling of the solute concentration in the column.

3.3.7.1 Concentration lattice dynamics

The concentration lattice was constructed with an equivalent D3Q19 lattice, and a domain size equal to the velocity lattice, to track the solute as a scalar between successive time steps. However, the use of two lattices is known to cause numerical instability in the Advection Diffusion Equation (ADE) when using a Single Relaxation Time (SRT), due to differences between relaxation parameters in each lattice model. Instead of implementing the BGK dynamics on the concentration lattice, a modified SRT method for advection-diffusion modelling developed by Perko and Patel was used[170]. This required the diffusion term to be represented by the combination of a reference diffusion parameter (D_{ref}) [$L^2\ T^{-1}$] and a deviated diffusion parameter ($\widetilde{D}$) [$L^2\ T^{-1}$] to amend numerical instability in the Single Relaxation Time model (SRT). The new value for the diffusion parameter is given by Equation [54].

$$D_m = D_{ref} + \widetilde{D} \qquad [54]$$

The effect this has on the Advection Diffusion Equation (ADE, Equation [55]) can be seen in Equation [56] below (ignoring source/sink terms, Q_s). In the ADE, the partial derivative of a solute's concentration (C) with respect to time is related to three terms; diffusion ($\nabla \cdot (D_m \nabla C)$), advection ($\nabla \cdot (uC)$), and an external term (Q_s). If there is no external cause for a change in concentration the source/sink term (Q_s) is ignored and the ADE is only dependent on the molecular diffusivity (D_m), concentration, and velocity of the system. The diffusion term is modelled in accordance with Fick's Law[94], while the advection term ensures that the solute behaves according to momentum of the bulk fluid flow and velocity field[5].

$$\frac{\partial C}{\partial t} = \nabla \cdot (D_m \nabla C) - \nabla \cdot (uC) + Q_s \qquad [55]$$

$$\frac{\partial C}{\partial t} = \nabla \cdot \left(D_{ref} \nabla C - \widetilde{D} \nabla C\right) - \nabla \cdot (uC) \qquad [56]$$

If the flux of the deviation term is converted to an advection term (Equation [57]), then it may be incorporated into the advective part of the equation (Equation [58]). The new parameter u_d [L T^{-1}] is a diffusive velocity term determined by using a first-order Chapman-Enskog expansion of the deviation term, and the advective velocity (u_a) [L T^{-1}] is simply the true advective velocity of the system (u). For a full derivation and explanation of the model, see the work of Perko and Patel[170].

$$\widetilde{D}\nabla C = u_d C, \qquad u_d = \frac{\widetilde{D}\nabla C}{C} \tag{57}$$

$$\frac{\partial C}{\partial t} = \nabla \cdot \left(D_{ref}\nabla C\right) - \nabla \cdot \left((u_a - u_d)C\right) \tag{58}$$

Despite the Perko model being less computationally efficient than the BGK model, it has still been found to be more efficient than Multiple Relaxation Time (MRT) models or Random Walking Particle Tracking methods (RWPT). The Perko dynamics model also provided a framework for the development of solute-solid interactions (such as the adsorption phenomena in this work) as a result of how the bulk motion of the solute[171] is modelled.

Investigations have shown that inaccuracies can occur when the value chosen for D_{ref} is smaller than the molecular diffusion (D_m) of the solute[170], or that instabilities occur[8] when D_{ref} is less than five orders of magnitude greater than D_m. Therefore to effectively use the Perko dynamics model, it was implemented on the concentration lattice, as it had the lower molecular diffusivity value (D_m as opposed to ν), and the reference diffusion parameter was set to equal the kinematic viscosity of water. This decision ensured that the relaxation parameters of both lattices were equal to one (meeting the stability criteria), and that the diffusion parameters were within stable bounds as determined by previous work.

3.3.7.2 Concentration boundary conditions

The boundary conditions applied to the concentration lattice were similar to those applied to the velocity lattice. In the radial direction, periodic boundaries were used to uphold the 'infinite column width' simplification, while in the axial direction Dirichlet and Neumann boundary conditions were used. For the case of the concentration lattice, the Dirichlet inlet condition was defined as a constant inlet concentration of 100 ppm (1.573 mol m^{-3}) of copper ions.

The boundary condition between the solid and fluid nodes was selected to suit the type of simulation being performed. When simulating an inert tracer passing through the column, as with dispersion RTD tests, a bounce-back type boundary condition was applied – equivalent to a no-slip boundary condition, or, for energy transport an adiabatic boundary condition[172]. Alternatively, for the cases where it was

desired to model internal porosity of the solid or reactive transport phenomena (adsorption), the bounce-back condition was modified to a solid-diffusion condition. It is important to note that the bounce-back condition for the velocity lattice remains, and this change only takes effect on the concentration lattice. A pore diffusion coefficient (D_{pore}) [L^2 T^{-1}] was selected to be an order of magnitude lower than the diffusivity of the solute in the fluid media (Equation [59]) based on empirical studies[173] that observed diffusion within solids with porosities[174,175] ranging from 0.2-0.4. The distinction between the channel pores (porous media network) and the internal pores represented by D_{pore} is shown in Figure 19.

$$D_{pore} = 0.1 \times D_m \qquad [59]$$

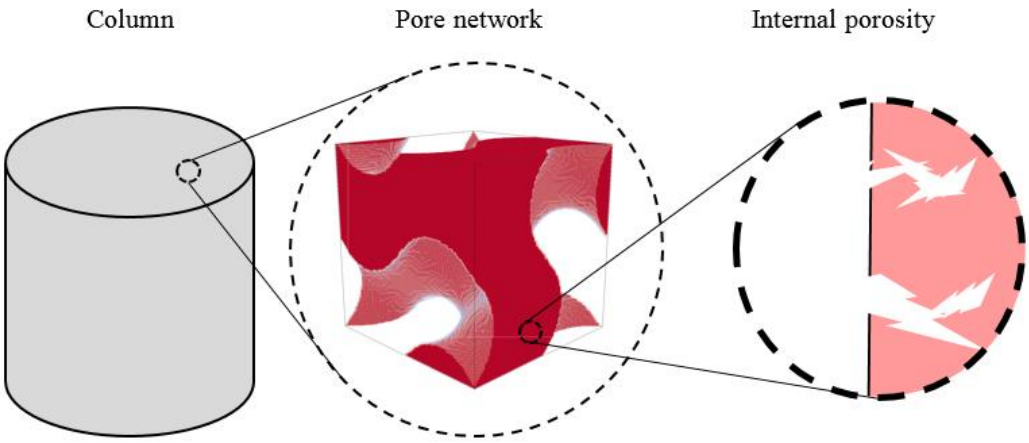

Figure 19. Depiction of relative scales for column porosity, and packing media internal porosity.

The pore diffusion coefficient was used to estimate the transport properties of the solute within the solid phase. Once a solute particle moved from the fluid nodes onto a solid node, it was assumed that the velocity within the solid phase was zero and transport only occurred via molecular diffusion (as determined by the estimated pore diffusivity, D_{pore}). One of the main reasons for modelling internal porosity of the solid phase in this way was to reduce the computational requirements for modelling this phenomenon; if the geometry of internal pores were modelled exactly, a much higher mesh resolution would be required and therefore greater memory and simulation time. The memory requirements and simulation times of the Palabos LBM library are known to increase with resolution (R_x) at the orders of at least $O(R_x^3)$ and $O(R_x^5)$ respectively[8]. Additionally, modelling of the morphology of the internal pore networks was outside of the scope of this work (and 3D printing capabilities).

Following the declaration of the concentration lattice, and the coupling of the velocity field from the BGK lattice, collision and streaming operations could be performed. The macroscopic density of the

concentration lattice corresponded to the solute concentration and could be recovered using the moments of the population density function for this secondary lattice[176].

3.3.7.3 Solid phase interaction

As mentioned in the previous section, the interactions between the solute and the solid phase could be modified to model different phenomena. In this work, three main cases were observed; an inert solute pulse passing through the column, a step change increase of inert solute at the column inlet, and a reactive solute step change. For the inert solute, the solid-solute interactions were handled by the bounce-back boundary conditions. However, for the adsorption scenario a combination of solid diffusion and bounce-back boundary conditions were used to model the solid-solute interactions.

While the model had been developed to accommodate diffusion deep into the solid material, the context of this research (3D printed MIPs) only required surface phenomena to be modelled. To represent surface interactions without depth diffusion occurring, the surface nodes were defined to accommodate solid diffusion with the pore diffusion boundary conditions while the 'buried' solid nodes were defined with bounce-back dynamics. A representation of this is shown in the Figure 20.

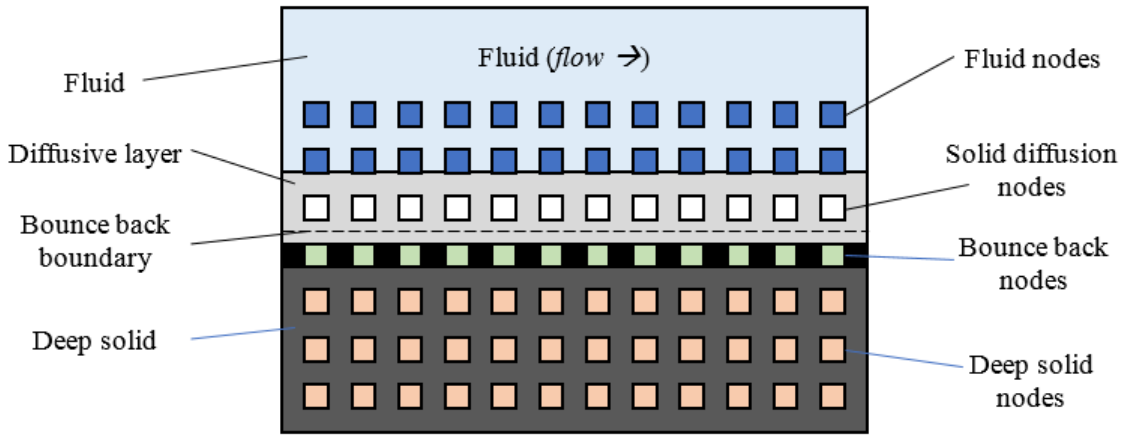

Figure 20. Graduation of fluid to solid nodes with different dynamics and boundary conditions identified.

Following the declaration of all the required boundary conditions, the solute was able to diffuse into, through, and back out of the solid surface. To simulate the surface reaction, an adsorption model was implemented to provide a source/sink term at locations where there would be active sites for adsorption (as discussed below).

3.3.7.4 Adsorption modelling

The adsorption model used in this work was a form of the Langmuir isotherm. This was chosen because of its simplicity[36] and suitability to model surface adsorption (equivalent to monolayer formation)[38,177]. Many other models exist, such as the Brunauer–Emmett–Teller (BET) isotherm[39], but the Langmuir isotherm was selected as it was expected to sufficiently recreate the MIPs chemistry. The Langmuir isotherm was implemented using the modified rate equation as given below (Equation [60])[178].

$$r_{rxn} = -\frac{dC}{dt} = k_{ads} C_{bulk} \left(1 - \frac{C_{ads}}{C_{cap}}\right) - k_{des} \left(\frac{C_{ads}}{C_{cap}}\right) \quad [60]$$

In this equation, the rate of reaction (r_{rxn}) [N L^{-3} T^{-1}] was calculated based on the driving force between the concentration in the bulk fluid (C_{bulk}) [N L^{-3}] and the concentration of solute adsorbed to the surface of the solid (C_{ads}) [N L^{-3}]. To fully define the rate of surface binding, the adsorption rate constant (k_{ads}) [T^{-1}], desorption rate constant (k_{des}) [N L^{-3} T^{-1}], and specific capacity of the solid (C_{cap}) [N L^{-3}] were required. However, because the LBM utilizes a discretized system it was also necessary to discretize the Langmuir rate equation. This was achieved by modifying the value of the physical parameters to maintain their meaning at the scale of a surface node in the simulation. The main requirement for achieving this was to ensure that the surface capacity of the solid phase was converted correctly to a 'node capacity'. The concentration in the bulk would already be discretized, and the reaction rate constants could easily be converted into lattice units.

The node capacity ($\hat{C}_{cap}$) [N] was determined using the surface area of the solid material (SA_{ads}) [L^2] and the known maximum depth of surface diffusion and binding (d_{ads}) [L]. Using these parameters, it was possible to calculate (Equation [61]) the volume at the surface of the solid (V_{ads}) [L^3] where binding sites would exist. Then the total capacity of a specific geometry ($C_{tot-cap}$) [N] could be found (Equation [62]), and divided by the number of surface nodes in the simulation (n_{surf}, determined within Palabos) to define the value of $\hat{C}_{cap}$ (Equation [63]).

$$V_{ads} = SA_{ads} \times d_{ads} \quad [61]$$

$$C_{tot-cap} = V_{ads} \times C_{cap} \quad [62]$$

$$\hat{C}_{cap} = \frac{C_{tot-cap}}{n_{surf}} \quad [63]$$

The adsorption rate at each solid node could then be calculated at any point in time to determine the rate of solute adsorption. This amount was then used as a source/sink term in the lattice colliding and streaming operation. Any material removed from the simulation domain was stored in a scalar field mapped onto the simulation geometry to keep track of the concentration of solute adsorbed at each solid node. The amount of adsorbed solute ($\hat{C}_{ads}$) [N] was retrieved from this scalar field when calculating the local adsorption rate of the next time step. The final discretized form of the adsorption model is given in Equation [64], where the bulk concentration was the concentration of solute diffusing through the solid node ($\hat{C}_{bulk}$) [N]. In practice, a time scaling factor of ten was applied to all of the adsorption rate in each iteration to reduce the computation time without compromising the simulation accuracy[179].

$$r_{rxn} = -\frac{dC}{dt} = k_{ads}\hat{C}_{bulk}\left(1 - \frac{\hat{C}_{ads}}{\hat{C}_{cap}}\right) - k_{des}\left(\frac{\hat{C}_{ads}}{\hat{C}_{cap}}\right) \quad [64]$$

The specific capacity of a MIP is largely dependent on the specific chemistry and preparation methods[180,181], thus a considerable range of capacity values are reported in the literature. Additionally, the literature indicates that the saturation concentration of the solid depends on the concentration of Cu in the bulk fluid. By assuming that the reaction rate would not be the limiting step in the adsorption process but that it would be diffusion or mass transfer limited, the adsorption rate constant (k_{ads}) was selected to be 1x10^{-4} mol m^{-3} s^{-1} (to approximate the values found in literature), and the desorption rate constant (k_{des}) was approximated to be four orders of magnitude lower than k_{ads}. This was justified as MIPs form non-covalent bonds, and it was expected without an eluent species present there would be a minimal degree of desorption and the solute could be assumed to be fixed at the adsorption site.

The specific capacity (C_{ads}) used for simulations was 10 mol m^{-3}. This is an order of magnitude lower than the values presented in literature, but allowed for faster simulations and thus enabled more geometries to be compared. The lower capacity was not expected to influence the relative performance of each geometry because only the initial stages of the adsorption (until breakthrough) were being observed, and changes in process chemistry were considered in Chapter 7. The adsorption parameters were held constant across all simulations to allow for the relative performance between each geometry to be fair and independent of the lower capacity. Chapter 7 examined the effects of altering the adsorption model parameters.

3.3.7.5 Multi-scale lattice model

The mass transport system being modelling in this work included phenomena that were solved on two different time scales; the dispersion of the solute, and the time required to achieve a lattice relaxation parameter of unity for resolving the velocity field. The fact that these occurred at different time scales

are what allow the simulation to be set up as a multi-scale model[179]. The multi-scale model was implemented to reduce the computation time of the advection-diffusion simulations by applying a scaling factor to all mass transport parameters. This would enable the ADE to be evaluated less frequently, but with an approximately equivalent degree of solute transport occurring on the global simulation time scale. This was necessary as it was not possible to decouple the global time scale from the velocity and concentration lattices.

To achieve this scaling, once the advection velocity (u_a) had been passively copied to the concentration lattice it could be increased by an integer value, and a corresponding number of global iterations would thus not be evaluated for this lattice. To maintain the Pe number the diffusivity was scaled by the same integer. This reduced the number of computations required to implement the ADE behaviour, while still approximating the unscaled transport. However, while it is known that the error associated with the model increases with the scale factor, Dolamore[8] determined that a scaling factor of 10 would reduce the computation time by 10 while also keeping errors produced by this scaling to less than 1%. Therefore, the scaling was deemed acceptable.

3.4 Simulation data

The simulations conducted were performed to identify an enhanced geometry for use in packed column applications. The performances of different structures were evaluated through the use of various parameters that describe; geometric properties, the velocity fields within the fluid channels, solute dispersion, breakthrough capacity, and adsorption capacity. The possibility of relating any of these performance measures to the structure of the solid media through correlation was also investigated, to better guide further studies into enhanced geometries.

3.4.1 Geometric parameters

3.4.1.1 Characteristic length

To calculate the geometric properties for all of the candidate geometries, a single high resolution unit cell (91 nodes) was generated with the Palabos code and used to determine each of the relevant properties. When starting to conduct simulations these simulations with new geometries, difficulties arose from trying to compare the different media. This was largely due to the conventions used in previous work prescribing different definitions of the characteristic length for each class of geometry. The characteristic length (L_c) [L] of a packed bed is used to calculate the reduced plate height (h) as the measure of dispersion, as well as the dimensionless permeability (k'). A review of the possible

definitions for a characteristic length was conducted to determine a robust definition that was applicable to all of the geometries considered.

A more in depth review of these definitions can be found in Appendix A.4. For particle packed columns, the particle diameter is commonly used for L_c (for non-spherical particles this can be derived from the circumdiameter). However, this measurement possesses no direct relationship to the fluid channels through which dispersion actually occurs, and for continuous media the 'particle diameter' remains undefined. Without a precedent for selecting L_c for a monolithic TPMS packing, prior research at the University of Canterbury[8] used the periodic axial length of a unit cell. Following this review, it was found that this definition also did not possess a strong enough relationship to the fluid space of the packed media and therefore this definition was not used.

Other works have used a hydraulic diameter for ducts with a constant cross section[182], with some adaptations to attempt to apply a hydraulic diameter definition to non-uniform flow channels. These definitions are related to the fluid space, but are complex and/or cumbersome to calculate for TPMS structures, and must be found using numerical approximations. It is also possible to calculate a diameter for a cylindrical pipe with an equivalent hydrodynamic resistance (R_H) to the simulated media[183], but this requires a solution to the flow fields to be calculated, whereas a purely geometric definition would be more robust. Ultimately, the definition selected was an alternative hydraulic diameter, originally used to describe porous systems.

The porous hydraulic diameter ($d_{h,pore}$) [L] is calculated purely from the geometric properties of a periodic unit cell (Equation [65]), which for unordered packed beds can be estimated from a large sample size. It is calculated from the specific surface area (a) [L^2 L^{-3}] as given by Equation [66], and the porosity[2] (ε). The specific surface area is the ratio of wetted surface area (A_w) [L^2] to the bulk volume (V_{cell}) [L^3], and is also a useful parameter for estimating the capacity available for surface adsorption phenomena. This definition for L_c can be applied to all of the various geometries considered, and was related directly to the properties of the fluid channels of the system.

$$d_{h,pore} = 4 \times \frac{\varepsilon}{a} \quad [65]$$

$$a = \frac{A_w}{V_{cell}} \quad [66]$$

When initializing the simulations, it was decided for two reasons that the geometries would be compared on the basis of equivalent unit cell sizes rather than a basis of having equivalent $d_{h,pore}$ values. First, the unit cell dimensions are easy to define as a system input, whereas $d_{h,pore}$ requires calculation after the unit cell size is specified. To calculate structures with equivalent $d_{h,pore}$ would require some

iteration, and is unnecessary when the characteristic length is used to normalize the results to remove the dimensional dependency for comparison. The second reason was because in practical settings, the column dimensions impose a physical limitation on space, and thus using unit cells of equivalent size allows for direct comparisons. Also, in additive manufacturing, printers with different resolutions would not be necessary to produce different sized unit cells. For the sphere packing orientations, the diameter of the sphere was set to the periodic length of the TPMS unit cell. This resulted in the periodic unit cells for the body-centred cubic (BCC) and face-centred cubic (FCC) structures being larger than for simple cubic (SC), but the same printer resolution could be used because the spheres were the same size.

3.4.1.2 Surface area and volume

The available surface area is an important consideration in the field of packed bed technology as it relates to the interface for many reactive processes. Additionally, the volume of a unit cell was of importance to allow for the calculation of the specific surface area. The volume of the unit cell was obtained by multiplying the edge lengths of the unit cell domain, and the surface area was calculated using the in-built Palabos commands for estimating surface area from STL files. The specific surface area is a measure of how effectively the solid phase is distributed within the unit cell, with a higher specific surface area providing more area for adsorption to occur. Therefore geometries with a higher specific surface area are preferable for packed beds, but the associated pressure drop and fluid shear associated with higher surface area must also be taken into account.

3.4.1.3 Porosity and sphericity

In the same way that a higher specific surface area can relate to better adsorption capacity, porosity (ε) can relate to the pressure drop and have practical implications about packed bed construction. A lower porosity usually corresponds to more restricted flow paths, and thus a higher pressure gradient is required to induce flow through a less porous packed column. The porosity of each structure was determined by taking the ratio of fluid nodes to solid nodes in the high resolution unit cell. The solid (V_{solid}) [L^3] and fluid volumes (V_{fluid}) [L^3] were then estimated by multiplying the porosity by the total unit cell volume. The sphericity[184] of the unit cell could then be calculated according to Equation [67], and was also calculated for each geometry.

$$\Psi = \frac{\pi^{\frac{1}{3}}(6V_{solid})^{\frac{2}{3}}}{A_w} \qquad [67]$$

3.4.2 Velocity field observation

The pressure and velocity field could be recovered by taking the appropriate moments of the probability density function at any time step of the simulation. The raw velocity field data consisted of the axial components of velocity and the pressure at each node within the system, which for solid nodes was defined to be zero for both velocity and pressure. It was possible to export this data at selected time intervals within VTI files (Visual Tool Kit Image data), which contain Visualization Tool Kit (VTK) Image data written using the VTK C++ library, and could be examined using Kitware's Paraview[185] data visualization software. Using the velocity field data, it was possible to calculate the tortuosity (T), the specific and dimensionless permeabilities (k, k'), normalized mean velocity deviation ($\bar{u}_{dev}$), and the Bejan number (Be, a dimensionless measure of the pressure drop, as defined in Section 3.4.2.3).

3.4.2.1 Tortuosity and permeability

Upon convergence of the velocity field, the pressure and velocity components at each node (subscript *i*) within the periodic unit cell were written to a VTK file. A Python script was then used to calculate the tortuosity (according to Equation [68]) of a periodic unit cell from its axial components (x, y, z). The permeability was calculated from the porosity and pressure at the inlet and outlet slices of the unit cell.

$$T = \frac{\sum_{i=1}^{n}(u_i)}{\sum_{i=1}^{n}(u_{z,i})} = \frac{\sum_{i=1}^{n}\left(\sqrt{u_{x,i}^2 + u_{y,i}^2 + u_{z,i}^2}\right)}{\sum_{i=1}^{n}(u_{z,i})} \quad [68]$$

Permeability is a measure of how difficult it is for a fluid or gas to flow through a porous medium, for the case of laminar flows it may be used to estimate the pressure drop associated with transmitting a fluid by using Darcy's law[78]. A higher permeability (k) [L^2] is favourable for achieving lower pressure drops. Within the Stokes flow regime the permeability of the solid phase is constant and a property determined by the fluid channel geometry. To be able to compare systems on varying scales, the permeability is divided by the square of a characteristic length used to describe the porous medium, resulting in the dimensionless permeability (k'), as seen in Equation [69]. Figure 21 shows validation that the tortuosity and permeability of the columns are calculable independent of the system flow rate within the Stokes regime.

$$k' = \frac{k}{L_c^2} \quad [69]$$

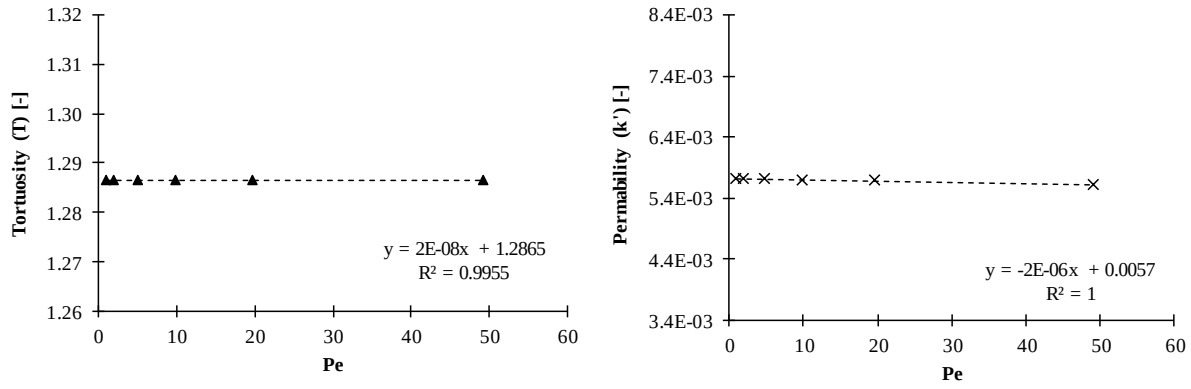

Figure 21. Plot to show that tortuosity and permeability are independent of the Peclet number within the Stokes regime. Data produced from simulations using the SD geometry.

It is important to note that the permeability values calculated in this work were made dimensionless using the porous media hydraulic diameter ($d_{h,pore}$) as the characteristic length, which differs from other literature and are therefore not directly comparable. However, a simple conversion factor using the two definitions of characteristic lengths allowed the dimensionless permeability to be compared. To validate the values of k' found from these simulations, the dimensionless permeability was recalculated using the diameter of the spheres as L_c and k' were compared to literature values for SC, BCC, and FCC packing orientations (Table 2).

Table 2. Comparison of permeabilities calculated for different packed sphere arrangements.

Previous Work	**SC [x10^{-3}]**	**BCC [x10^{-4}]**	**FCC [x10^{-4}]**
Schure et al.[7]	2.46	4.96	1.70
Khirevich[142]	-	4.92	-
Zick et al.[186]	2.52	5.01	1.72
Sangani et al.[187]	2.52	5.04	1.71
Dolamore[16]	2.51	4.93	1.71
This work (31 node resolution)	2.42	5.11	1.59

The permeability values calculated by other studies used higher spatial resolutions than this work (91 nodes for a unit cell compared to 31, a necessary sacrifice for computational efficiency), and therefore some differences in the permeability values can be seen. It is worth noting that the study performed by Dolamore[8] used the same Palabos library as a precursor to this research, and the permeabilities were calculated using the higher resolution thus show a much closer agreement with other literature. While acknowledging the reduced accuracy caused by the lower spatial resolution used in this study, it was determined that the model successfully modelled flow fields within the laminar flow regime.

The permeability of TPMS structures was also compared with literature values found through other numerical studies in Table 3. The results show reasonable agreement, with the difference likely to be a result of the different resolutions used in each simulation. It is again important to point out that the permeability values shown here were made dimensionless using the periodic cell length as opposed to the hydraulic diameter as the characteristic length.

Table 3. Comparison of permeabilities calculated the basic TPMS configurations.

Previous Work	**SP [x10^{-3}]**	**SG [x10^{-3}]**	**SD [x10^{-3}]**
Jung et al.[116] (151 nodes)	3.48	2.29	1.44
Guest et al.[115] (30 nodes)	3.19	-	-
This work (31 node resolution)	3.22	2.19	1.38

3.4.2.2 Normalized mean velocity deviation

The normalized mean deviation of the velocity field ($\bar{u}_{dev}$) was used to describe non-homogeneity in the velocity field within the channel. It was calculated according to Equation [70], where u_i [L T^{-1}] is the velocity magnitude at a fluid node within the system, n is the number of fluid nodes, and $\bar{u}$ [L T^{-1}] is the average velocity magnitude of all fluids nodes considered. This differs from the tortuosity of the system by considering velocity as a scalar quantity, rather than decomposing it into its directional components. It is proposed that $\bar{u}_{dev}$ may relate directly to the mass transport of a solute within the fluid, as a uniform flow field would have a lower mass transfer resistance[17]. A value of zero for $\bar{u}_{dev}$ would equate to the ideal case where all fluid nodes share the same velocity magnitude. The reasoning for the channel structure being able to influence this phenomena is found from the Van Deemter equation, revisited from Equation [24].

$$\bar{u}_{dev} = \frac{\sum_{i=1}^{n} |u_i - \bar{u}|}{n \times \bar{u}} \quad [70]$$

$$HETP = A + \frac{B}{u_s} + Cu_s \quad [24]$$

The A term in the Van Deemter equation is attributed to random eddy flows, which are minimized by the use of periodic ordered structures such as TPMS. The B term is related to diffusion, therefore when operating at or above the optimal flowrates the effects of diffusion were less important. Additionally, when only considering one species, the diffusion coefficient will be constant in each system. The C term however, is related to mass transfer resistance between the mobile and stationary phases[96], a

phenomena that would worsen with large boundary layer formation near the solid surface. If the boundary layer could be reduced by manipulating the stationary phase geometry without compromising the superficial flow velocity, it is reasonable to expect that lower height equivalent to theoretical plates could be achieved. Therefore, the value of $\bar{u}_{dev}$ was calculated for each structure where values closer to zero were indicative of homogeneity.

3.4.2.3 Dimensionless pressure drop, Bejan number

The pressure drop over a periodic unit cell (ΔP) [M $L^{-1}T^{-2}$] was calculated by finding the difference between the pressures at the inlet and outlet to the central periodic unit cell ($P_{in},\ P_{out}$) [M L^{-1} T^{-2}]. For constant geometry and fluid properties, the ΔP varied with both the physical scale and flowrate. To remove the scale dependency, a dimensionless form of pressure drop known as the Bejan number (Be) was calculated according to Equation [71]. In this equation ΔP is made dimensionless by multiplying the channel length between pressure observations (L_x) [L] and dividing it by the fluid's density (ρ) [M L^{-3}] and kinematic viscosity (ν) [L^2 T^{-1}]. The Bejan number was first proposed as a dimensionless pressure drop number by Bhattacharjee and Grosshandler[188], and has since been generalized for use in a range of diffusive systems[189,190,191].

$$Be = \frac{\Delta P L_x^2}{\rho \nu^2} \qquad [71]$$

The Bejan number, while independent of the system scale, is still dependent on the flowrate through the system. To condense the different Be number corresponding to each system velocity into a single parameter, a rate of change for the dimensionless pressure drop was introduced. The rate of change of the Bejan number ($\dot{Be}$) is able to provide information about the pressure differentials associated with increasing the flowrate (Pe) through any geometry. As only Stokes regime flowrates were observed, the value of $\dot{Be}$ was expected to be constant and could therefore be calculated from any two known Pe and Be (Equation [72]). This was a result of the pressure drop being directly related to the superficial velocity within this regime, as shown by Darcy's law. To validate this claim, the pressure drop and Be were observed for a range of Pe through the Schwarz Diamond structure (Figure 22), where there is a prominent linear trend and the $\dot{Be}$ was calculated from the line of best fit gradient to be 0.9024.

$$\dot{Be} = \frac{Be_2 - Be_1}{Pe_2 - Pe_1} \qquad [72]$$

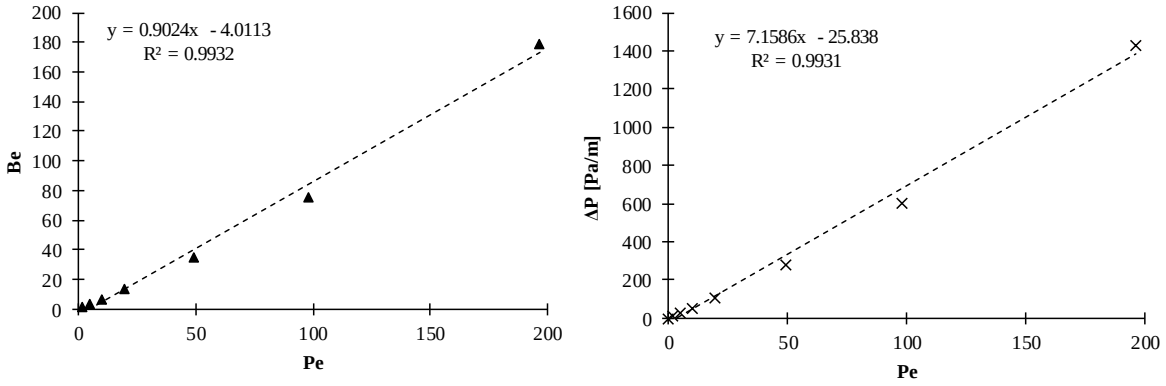

Figure 22. Verifying the linearity of the Bejan number against system flowrate (channel Peclet number) for the SD geometry.

3.4.3 Dispersion characteristics

3.4.3.1 Reduced plate height

As discussed in Chapter 2, the chromatographic performance of a packed column can be evaluated using the height equivalent to a theoretical plate ($HETP$) [L] to quantify axial dispersion. The use of the porous hydraulic diameter ($d_{h,pore}$) as the characteristic length used to calculate the dimensionless reduced plate height (h) was thought to allow a fair comparison between different geometries. To calculate the $HETP$ the method of moments was used[125]. This required a pulse of solute to be injected at the inlet to the simulation domain, then for the average concentration at the inlet and outlet of the periodic cell to be monitored until the pulse had passed through the column.

The inlet pulse for measuring the plate height could not be modelled as the ideal case (the Dirac delta function) due to numerical instabilities caused by the steep gradient. Instead, the pulse concentration change was modelled as a function of time ($C(t)$) [N L^{-3}] using the hyperbolic tangent function as shown in Equation [73]. In this model C_{max} [N L^{-3}] is the peak concentration at the inlet, t [T] is the time step of the simulation, and the constants $a_{pulse}, b_{pulse}, c_{pulse}$ amd d_{pulse} are constants that modify the steepness and duration of the pulse. An example of how the inlet pulse is modelled and observed relative to the simulation iterations is shown in Figure 23. The concentrations profiles were determined by recording the concentration at equal time intervals until the concentration in the outlet slice fell below a specified tolerance, and the data was processed in MATLAB[192]. A lower value for the reduced plate height would indicate a lesser degree of axial band broadening throughout the column, which is beneficial for improving the chromatographic separation and efficiency. The calculation of the reduced plate height was validated against correlations for Taylor[193] and Taylor-Aris[194] dispersion in a cylindrical capillary by Dolamore[8] in precursory work done using the Palabos library.

$$C(t) = C_{max}\left(tanh\left(\frac{t}{a_{pulse}} + b_{pulse}\right) + tanh\left(\frac{-t}{c_{pulse}} + d_{pulse}\right)\right) \quad [73]$$

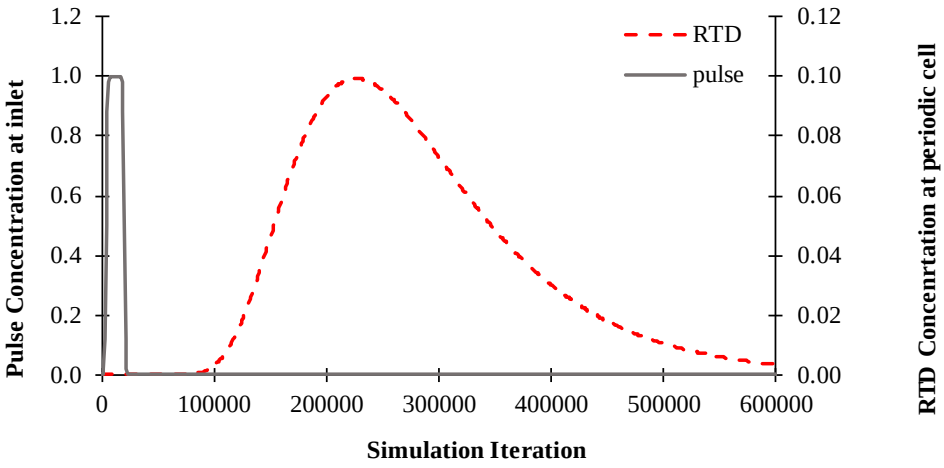

Figure 23. Depiction of how the inlet pulse is modelled and measured in the simulation time domain.

For each geometry the reduced plate height was calculated for several Pe, and the lowest value of h found was nominated as the minimum reduced plate height (h_{min}) for that structure. A more accurate estimate of h_{min} could be found by parameter fitting a Van Deemter curve to the data and interpolating the minimum, but for simplicity the lowest observed value was used. To illustrate the selection of h_{min} Figure 24 below shows the Van Deemter curve produced when observing the Schwarz Diamond structure over superficial Pe ranging from 1 to 100. The minimum h was determined to occur when the superficial Peclet number was 20 and thus the h_{min} for the SD geometry was 0.137.

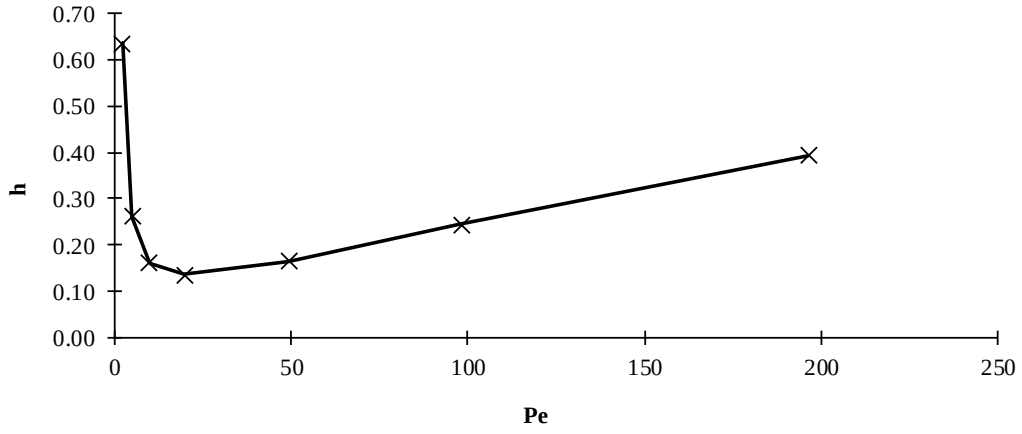

Figure 24. Van Deemter curve the SD geometry with a minimum h value at Pe = 20.

3.4.3.2 Separation impedance

In addition to using the reduced plate height to assess dispersion, the separation impedance (E) is commonly used. This is because the separation impedance encompasses the degree of difficulty associated with passing fluid through the column and can indicate pressure gradient requirements. For these simulations E was calculated according to Equation [74], using the dimensionless permeability and minimum reduced plate heights of each geometry (Equation [74]).

$$E = h^2\phi = h_{min}^2\left(\frac{1}{k'}\right) \quad [74]$$

3.4.4 Column breakthrough

In addition to assessing the chromatographic separation efficiency, this work builds upon previous research by attempting to directly assess the performance of each geometry when used in an adsorptive filter application. Simulations were conducted whereby the concentration of a contaminant at the inlet was increased with a step change and the concentration profile throughout the column was observed over time. The breakthrough for the simulations was defined as when the concentration at the outlet of the periodic cell reached a specified tolerance, which in this study was set to 5% of the inlet concentration (indicating the start of breakthrough and bed exhaustion). The onset of breakthrough was chosen as the condition to terminate the simulation to match the practical application of the water filter; when heavy metals are present in the eluted fluid the filter would be considered ineffective, and ready for regeneration.

Breakthrough simulations were conducted using a step increase of solute concentration at the inlet for cases with and without the adsorption model activated. To then assess breakthrough performance of different geometries dimensionless parameters for the volume of fluid treated and the fraction of column capacity utilized were defined.

3.4.4.1 Dimensionless volume of fluid treated

The dimensionless volume of fluid treated was defined to allow comparisons between domains of varying scale, and to take into account the porosity of different packing structures. In effect, the dimensionless volume (V_D) is a measure of how many multiples of the fluid space upstream of the periodic unit cell (V_{void}) [L^3] could be passed through the column (V_{elute}) [L^3] prior to breakthrough occurring, and is defined by Equation [75]. The quantity of fluid treated when breakthrough occurs was determined by multiplying the breakthrough time (t_{bt}) [T] by the flowrate (Q) [$L^3\ T^{-1}$], which was in

turn found from the superficial column velocity (u_s) [L T^{-1}] and the cross sectional area of the domain (A_{CS}) [L^2]. The denominator quantity, equivalent to the fluid space upstream of the fluid cell, was defined to be a sum of the entrance region, or lead volume (V_{lead}) [L^3], and the void space (εV_{cell}) [L^3] of the entrance cells (n_{ent}).

$$V_D = \frac{V_{elute}}{V_{void}} = \frac{t_{bt} \times Q}{n_{ent}\varepsilon V_{cell} + V_{lead}} = \frac{t_{bt} \times u_s \times A_{CS}}{n_{ent}\varepsilon V_{cell} + V_{lead}} \quad [75]$$

Defining V_D this way enabled a fair comparison of columns that had different numbers of entry cells. The actual quantity of volume treated did not allow for such comparisons, nor did the number of unit cell volumes treated, despite being a close analogy of the hydraulic residence time often used in breakthrough performance assessment. To verify that the dimensionless volume was independent of the number of unit cells used as entry used, V_D was calculated for every cell along a 20 unit cell domain using the SD geometry (superficial Pe = 100) and is shown in Figure 25. It can be seen that the dimensionless volume remains relatively constant irrespective of the position along the column (within the periodic region) as the additional entrance cells were accounted for with this formula. The values of V_D calculated within the periodic region varied by less than 2%.

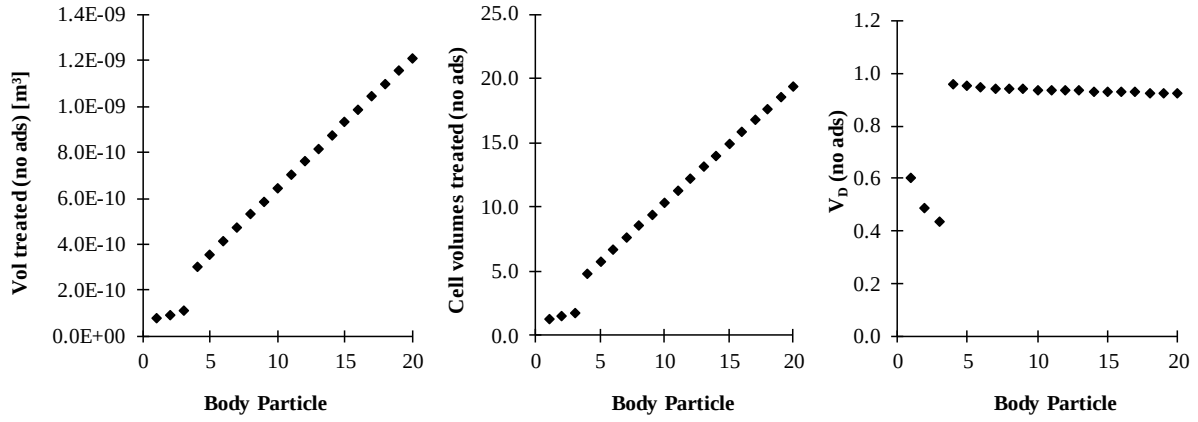

Figure 25. Comparison of (left to right); The volume treated by a column of 500 µm SD unit cells when observing breakthrough at each cell along the column, the number of unit cell void quantities treated, the dimensionless volume parameter as calculated at each body particle.

3.4.4.2 Fraction of capacity

In addition to comparing the quantity of contaminated fluid that each geometry is able to treat, it is useful to compare the effective uptake of solute and how close the solid is to saturation when breakthrough occurs. The benefits of conducting these CFD simulations over experimental observations

is that it was trivial to calculate the concentration of solute adsorbed by the solid phase using the Palabos code library. To then report this molar quantity as a dimensionless parameter, the occupied fraction of capacity (C_D) was defined. This was found by dividing the amount of solute adsorbed at the breakthrough (C_{uptake}) [N] by the available molar capacity of the solid (C_{CAP}) [N]. The form of the equation used was similar to that of the dimensionless volume, and is given in Equation [76]. For the case of modelling solids with full internal porosity, V_{ads} would be equivalent to the volume of the solid phase, while for surface adsorption, V_{ads} is the wetted surface multiplied by a known limiting depth of adsorption (d_{ads}) [L].

$$C_D = \frac{C_{uptake}}{C_{CAP}} = \frac{C_{uptake}}{\hat{C}_{cap} \times V_{ads}} = \frac{C_{uptake}}{\hat{C}_{cap} \times (A_w \times d_{ads})} \quad [76]$$

3.5 Simulation procedure

3.5.1 Simulation run-through

To maximise the autonomous runtime for simulations and minimising the setup time, the script was written to allow for the three solute transport simulations (dispersion with a pulse injection, breakthrough with a step increase, and breakthrough with adsorption behaviour enabled) to run consecutively from a checkpoint taken when the velocity field had converged (prior to solute being introduced to the column). When each of the solute transport simulations reached their end condition (concentration tolerance at the outlet of the periodic unit cell) the relevant data was exported for processing, and the simulation either returned to the checkpoint or concluded.

3.5.2 Simulations conducted

The first set of simulations summarized in Chapter 4 observes the performance of the three basic TPMS structures (SP, SG, SD) against the performance of regular sphere packing arrangements (SC, BCC, FCC). This was to confirm there are potential performance benefits in using TPMS structures for adsorption applications, before refining the structures of TPMS to search for further performance enhancement. The results in Chapter 5 summarize the performance of several other TPMS structures and then identify geometric or velocity field dependent properties that correlate with improved performance. The effects of varying the porosity of the TPMS structures, and rotating each structure relative to the axis of flow were also investigated, and are summarized in Chapter 6. To explore the potential to extend the results from this study, Chapter 7 describes the effects of changing the system scale and adsorption parameters.

3.5.3 Simulation parameters

For the results summarized in Chapters 4 to 6 the spherical particle diameters were held constant at 500 µm, and unit cell edge length was fixed at 500 µm prior to rotations. The diffusivity of copper in water and within the solid media were estimated as 9.5×10^{-10} m^2 s^{-1} and 9.5×10^{-11} m^2 s^{-1}, respectively, and the adsorption and desorption constants used in the Langmuir adsorption model were held constant at 1×10^{-4} s^{-1} and 1×10^{-8} mol m^{-3} s^{-1}, respectively. The specific capacity used in simulations was 10 mol m^{-3}, although the values of these constants were varied for the investigation in Chapter 7. All of the baseline physical parameters used in this study are summarized in Table 4.

Table 4. Summary of physical parameters used in baseline modelling.

Constant physical property being modelled	Symbol	Value	Units
Diameter of unit cell in sphere packing	d_p	500	µm
Edge length of base line unit cell (TMPS)	L_x	500	µm
Fluid density	ρ	998	kg m^{-3}
Fluid kinematic viscosity	ν	1×10^{-6}	m^2 s^{-1}
Solute diffusivity in fluid	D_m	9.5×10^{-10}	m^2 s^{-1}
Solute diffusivity in solid	D_{pore}	9.5×10^{-11}	m^2 s^{-1}
Reference solute diffusivity	D_{ref}	1×10^{-6}	m^2 s^{-1}
Inlet solute concentration	C_{in}	1.5783	mol m^{-3}
Initial system concentration	C_0	0	mol m^{-3}
Baseline adsorption rate constant	k_{ads}	1×10^{-4}	s^{-1}
Baseline desorption rate constant	k_{des}	1×10^{-8}	mol m^{-3} s^{-1}
Solid phase specific capacity	$\hat{C}_{cap}$	10	mol m^{-3}
Maximum depth of surface adsorption	d_{ads}	40	Å
Molecular weight of solute	M_w	63.546	g mol^{-1}
Breakthrough tolerance	-	5%	-

3.5.4 Setup summary

Using the capabilities of the Lattice Boltzmann Method, the properties of various packed bed morphologies were tested using CFD simulations. The LBM and the Palabos code library were found to be suitable for representing the complex geometries encountered in packed beds such as tortuous pore networks, and enabled the inclusion of surface adsorption within the model. The accuracy of these methods was assessed in this chapter by comparing the simulated results with literature values, and deemed acceptable for the purposes of comparative tests. The results of these simulations were used to indicate the best performing media for reducing axial dispersion, and for implementation in breakthrough applications. The recommended configurations will be able to provide benefits over a range of packed bed technologies, including the design of a novel heavy metal water filter. Additionally,

the results provide insights into how distribution of the solid phase can alter the performance of a packed column without changing the process chemistry. Possible solutions are almost infinite, and thus only the select field of TPMS structures were examined in detail to find enhanced media. Chapter 4 first proves the advantages of monolithic structures such as TPMS over traditional packed sphere configurations.

Chapter 4 – Comparison of TPMS with Ordered Sphere Properties

Before exploring the full potential of TPMS and monolithic structures the performance of these structures was compared to ordered arrangements of spherical particles, which are commonly used for industrial and analytical column packing configurations. By characterizing and comparing the dispersion and adsorption properties, the potential benefits of monolithic solid phase media was shown.

4.1 Geometries compared

There is a longstanding consensus in the field of packed bed technologies that packed spheres produce the best performance in chromatographic applications, due to reportedly minimal axial dispersion[7,102]. This belief is reflected in literature and in practice, with most practical columns over the last half-century being constructed with particles as the packing media; spheres being the simplest and most efficient particles to manufacture. Only with recent developments in CFD technology and manufacturing capabilities has it been possible to investigate other, more complex structures. A family of complex geometries derived from TPMS were investigated in this work to identify geometries with the potential to outperform ordered arrangements of spherical particles. The three main ordered sphere arrangements are the simple cubic, body-centred cubic, and face-centred cubic. These were compared with their TPMS analogues; the Schwarz Primitive, Schoen Gyroid, and Schwarz Diamond structures (Figure 26).

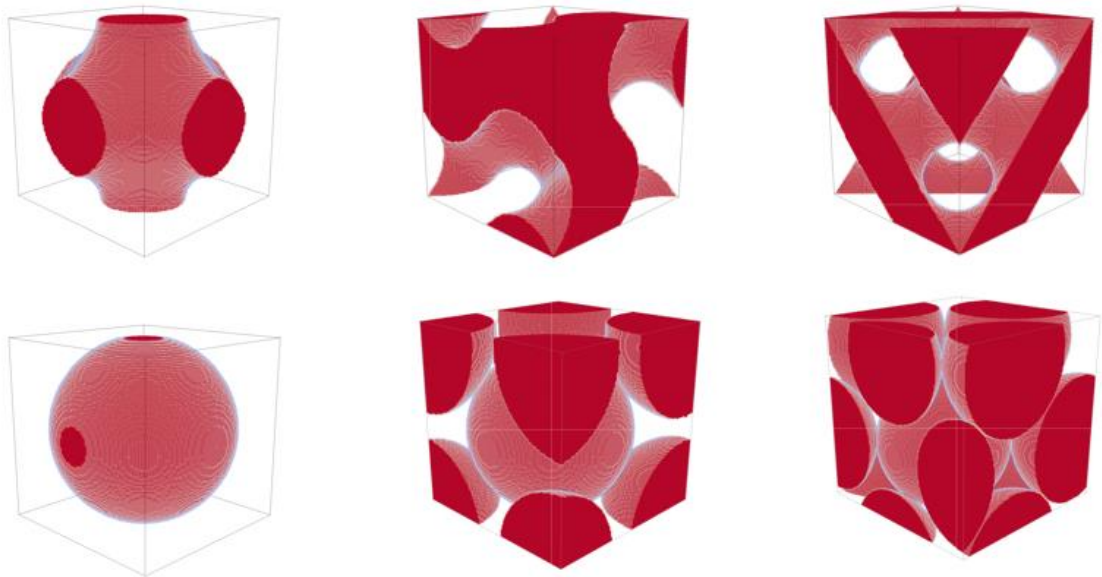

Figure 26. Comparison of (clockwise from top left) Schwarz Primitive, Schoen Gyroid, Schwarz Diamond, Face-Centred Cubic, Body-Centred Cubic, and Simple Cubic unit cells.

4.2 Geometric properties

For the ordered sphere orientations, it was possible to calculate the geometric properties of a unit cell analytically. However, for the TPMS structures the analytical solutions are more difficult to obtain and thus a numerical approximation for the geometric properties was used. The numerical estimates of the geometric parameters from the stereo-lithography files generated to describe the unit cells in each simulation. To validate the numerical estimates were correct the analytical and numerical values for the sphere packing orientations were compared. The geometric properties of the unit cells for the arranged spheres and TPMS geometries (Figure 26) are summarized in Table 5.

Table 5. Comparison of geometric properties of SC, BCC and FCC sphere packing (d = 500 µm) with the SP, SG, and SD TPMS structures (unit cell size 500 µm). All geometries constructed with a resolution of 31 nodes in each direction.

Shape	**Method**	**Cell Volume** [mm^3]	**Surface Area** [mm^2]	**Cell Porosity** [-]	**Sphericity** [-]	**Specific SA** [mm^{-1}]
SC	Analytical	0.125	0.785	0.476	1.00	6.28
	Estimate	0.125	0.797	0.480	0.98	6.37
BCC	Analytical	0.193	1.571	0.321	0.79	8.14
	Estimate	0.182	1.568	0.313	0.77	8.62
FCC	Analytical	0.351	3.142	0.255	0.63	8.94
	Estimate	0.327	3.007	0.255	0.63	9.20
SP	Estimate	0.125	0.632	0.504	1.20	5.05
SG	Estimate	0.125	0.819	0.500	0.93	6.55
SD	Estimate	0.125	1.018	0.500	0.75	8.14

When comparing the analytical and numerically determined properties of the arranged spheres it was found that the estimates (calculated from the voxelized representations of each media) were mostly in agreement with the analytical values. The biggest deviation was seen to occur in the BCC and FCC orientations, where for the FCC arrangement the cell volume was estimated at just under 7% of the true value. These differences were determined to be a result of making the simulation domain periodic in the radial directions and discretizing the representation of geometry, forcing the radial dimensions to be adjusted so that they were equal to an integer number of voxels with allowances for the periodicity. The error in the volume estimation influenced the specific surface area estimate. It was found that the remaining properties could be estimated with less than 3% of error. Given the moderate resolution of the simulation (31 nodes), it was decided that the estimation of the geometric properties was acceptable for use in further calculations.

It can be seen that the surface area increased for each sphere arrangement, which provided a larger number of active sites for adsorption. However, the cell volume also increased as a result of positioning more particles within the unit cell (each with a 500 μm diameter), making the specific surface area a better measure of available reactive surface. Even when comparing the specific surface areas the FCC packing had the highest value (8.94 mm^{-1}), but this came with a much lower porosity, which was expected to negatively affect the pressure drop requirements. When looking at the TPMS geometric parameters it was noted that the surface area and specific surface area also increased through SP, SG, and SD respectively. This supports the analogy between the SC, BCC and FCC orientations and the PGD family of TPMS structures. The highest TPMS specific surface area was calculated for the SD structure with a value of 8.14 mm^{-1}, which suggested a lower adsorption capacity than the FCC packing. The benefits that the SD and other TPMS have over arranged spheres is that they maintain a porosity of 50% while providing a high specific surface area, therefore were likely to provide a higher column fluid capacity and reduce pressure gradient requirements.

It was predicted that the sphericity of each unit cell would be directly related to the specific surface area, as sphericity is effectively a dimensionless measure of the volume distribution within a unit cell. This was confirmed in Figure 27, where a strong linear trend is seen. Both the sphericity (Ψ) and specific surface area (a) relay useful information to describes the adsorption reaction interface and would be used in identifying relationships with the performance measures outlined in Chapter 3. From the relationship found in Figure 27, it was determined that a geometry which possessed a low Ψ and a high a would be best for maximising the capacity of a packed bed.

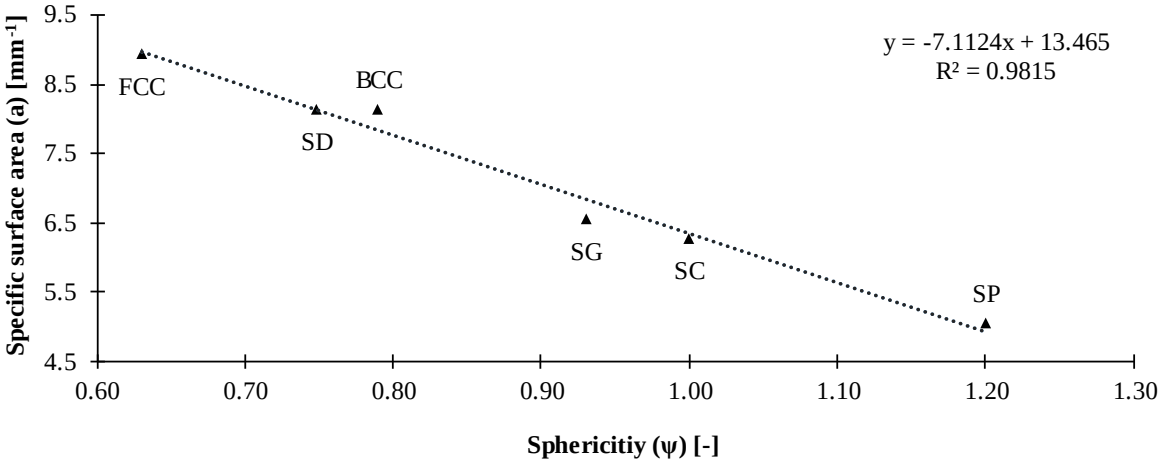

Figure 27. Relationship between sphericity and specific surface area for basic TPMS and sphere packing.

4.3 Flow properties

The velocity field was evaluated using the two parameters that were predicted to influence the mass transfer of the solute within the channels; the tortuosity (T), and the normalized mean deviation of the velocity field ($\bar{u}_{dev}$). The tortuosity describes the deviation from flow parallel to the main axis and $\bar{u}_{dev}$ provides information about the non-homogeneity of the scalar channel velocity, and both were hypothesised to be related the mass transfer resistance in the radial direction of a channel. From a practical perspective, the pressure requirement to pass fluids through porous media is of equal importance as the flow field characteristics. Therefore, the dimensionless permeability (k') and the rate of dimensionless pressure drop increase with respect to flow ($\dot{Be}$**)** were calculated from the converged periodic velocity field, and are shown in Table 6 along with T and $\bar{u}_{dev}$.

Table 6. Comparison of pressure and velocity performance measures for sphere packing and basic TPMS structures.

Shape	**Characteristic Length** L_c $[mm^{-1}]$	**Flow tortuosity** T **[-]**	**Normalized mean** u **deviation** $\bar{u}_{dev}$ **[-]**	**Dimensionless permeability** k' **[-] x10^{-3}**	**Bejan number gradient** $\dot{Be}$ **[-]**
SC	0.303	1.031	0.853	6.57	0.324
BCC	0.158	1.101	0.762	5.43	4.027
FCC	0.114	1.327	0.498	3.82	17.154
SP	0.399	1.031	0.786	5.06	0.204
SG	0.305	1.240	0.498	5.88	0.362
SD	0.246	1.287	0.416	5.70	0.897

The first observation that could be made was that the tortuosity increased for the sphere and TPMS structures with solid phase distribution that possessed greater surface area. By definition, a higher tortuosity related to higher radial and lower axial velocity components, Conversely, a low tortuosity would result from large axial components and could be the result of flow channelling[95,5]. Figure 28 shows a two dimensional view of each unit cell from the perspective of the flow axis. For the less tortuous candidates (SC, SP) it was possible to see 'through' the structure and thus some degree of channelling occur. The normalized mean velocity deviation could also be related to channelling and tortuosity, with higher T indicating a lower $\bar{u}_{dev}$ value as shown in Figure 29. The TPMS structures proved to have lower $\bar{u}_{dev}$ values than their sphere packing counterparts, which supported the conjecture that TPMS are able to more effectively homogenize the velocity field defined by their fluid channel networks. The SG and SD structures are likely to have lower $\bar{u}_{dev}$ values than their analogous BCC and FCC structures in part due to their higher porosity; the lower porosities of the sphere arrangements would result in larger maximum channel velocities and thus larger velocity gradients to form between the walls and the centre of the channel[195].

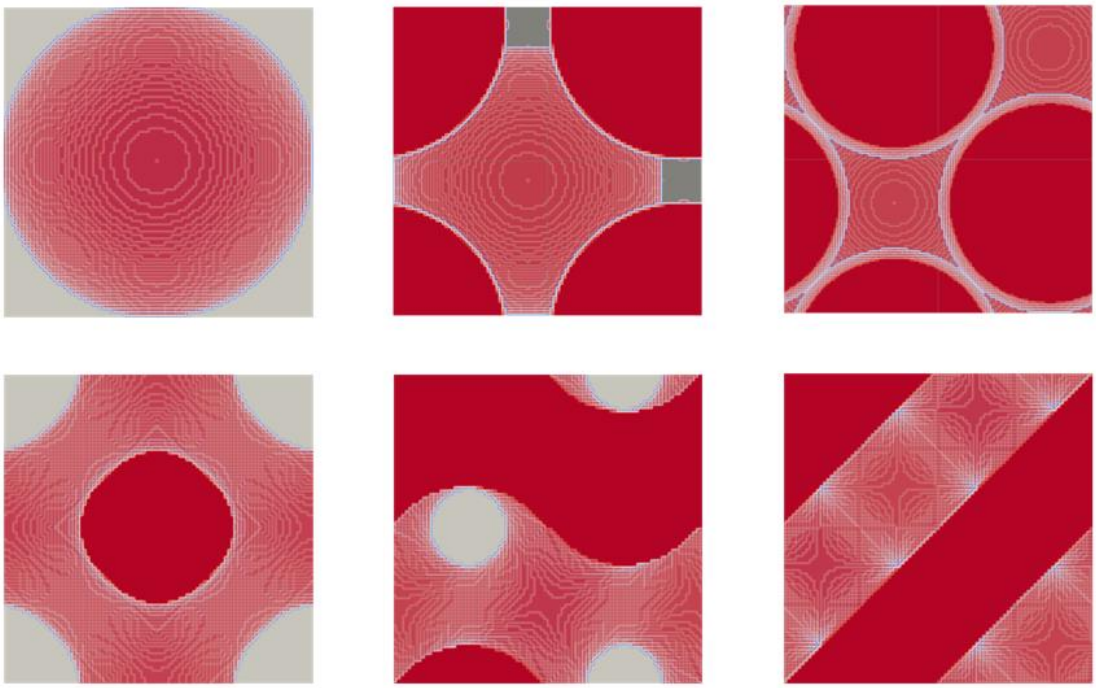

Figure 28. Axial view of basic column packing structures with grey representing the end surface of the unit cell. Clockwise from top left: SC, BCC, FCC, SD, SG, and SP.

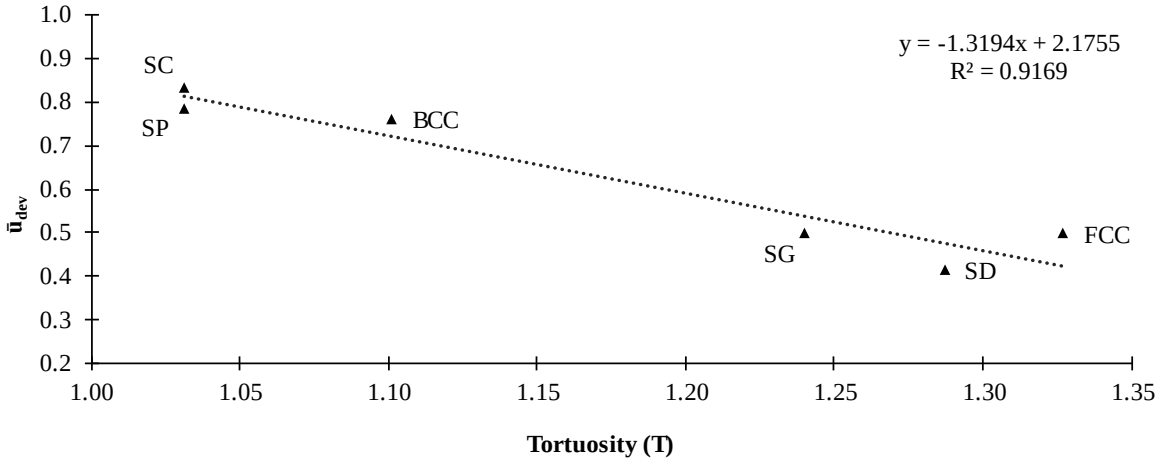

Figure 29. Correlation between the normalized mean velocity deviation and the tortuosity for the periodic flow fields.

The dimensionless permeability and pressure drop gradient were revealed to be most strongly to the geometric properties (such as the porosity) of each structure, and this was explored more in Chapters 5, 5, and 6 with larger data sets. However, it was noted that while improvements in T and $\bar{u}_{dev}$ were identified through the SP, SG, and SD TPMS, there were significantly less dramatic changes in k' and $\dot{B}e$ when contrasted with the arranged spheres, as all were compared at 50% porosity. The PGD family were shown to have favourably lower $\dot{B}e$, and FCC proved to have the least desirable properties.

4.4 Dispersion and separation impedance

The results displayed in this section aimed to resolve the limitations of previous studies that faced difficulties in comparing the reduced plate height (h) for different classes of packing media. This was achieved by using a more robust definition of characteristic length (L_c) when calculating the dimensionless h from the height equivalent to a theoretical plate ($HETP$) determined through simulation. A previous study performed by Dolamore[8] on arranged spheres and TPMS structures found that the minimum reduced plate heights (h_{min}) within the Stokes flow regime increased in the order; SD < FCC < SG < BCC < SP < SC. However, this analysis was performed using the particle diameter as the L_c for spheres and with the unit cell edge length as L_c for the TPMS structures. These results were recreated for validation purposes, and then recalculated using the new definition of L_c (Section 3.4.1.1), and the reduced plate height for a range of Pe (Figure 30).

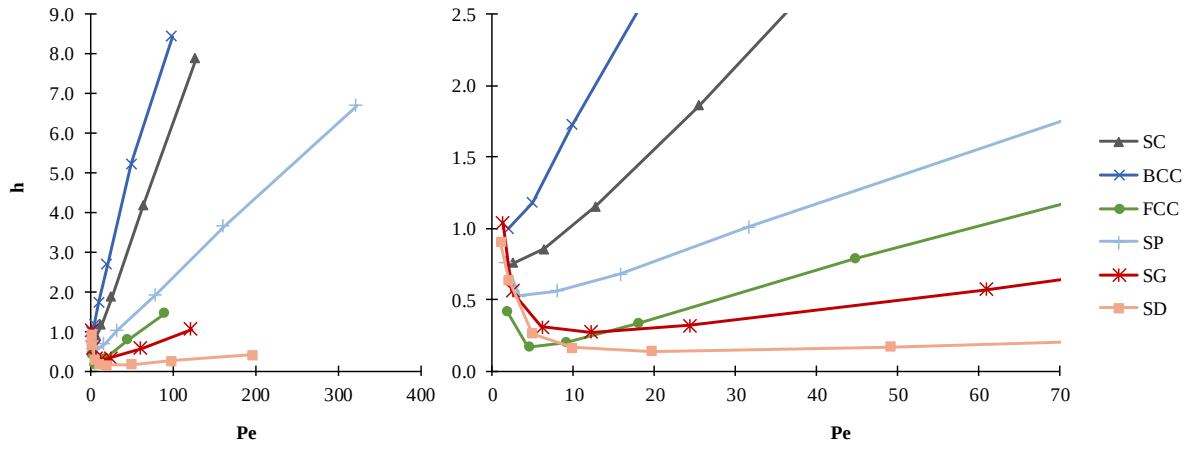

Figure 30. Comparison of Van Deemter curves for different solid phase geometry. Observing reduced plate height over large range of channel Pe (right), investigating the optimum Pe (left) for each structure.

The Peclet number used as the independent variable was the average channel Peclet number (Pe) within the channel. It was calculated according to Equation [77] by dividing the inlet Peclet number by the porosity of the system, effectively using the superficial velocity of the channel. It is also worth noting that each geometry was modelled for the same set of inlet superficial velocities, but when the average channel Peclet number was calculated the division by the characteristic length ($d_{h,pore}$ unique to that geometry) caused the channel Pe to differ (as can be seen in Figure 30).

$$Pe = \frac{u_s L_c}{\varepsilon D_m} = \frac{Pe_{inlet}}{\varepsilon} \qquad [77]$$

A clear Van Deemter curve was obtained for each geometry, and an optimum operating condition for reducing axial dispersion was identified by the local minima (h_{min}). The minimum reduced plate heights were taken as the lowest data point recorded, but could be found more accurately by examining more flowrates near the optimum or through extrapolation. It can also be seen that each of the curves display different gradients above their optimum, with the SD structure having the shallowest.

Above the optimum column Pe the axial dispersion occurs mostly due to the 'C' term in the Van Deemter equation, which is related to the mass transfer resistance[196]. A less steep ascension of the Van Deemter curve relates to a lower 'C' term and less degradation in the separation quality when increasing the Pe above the optimum. This effectively indicated that the SD and SG geometries were able to perform at higher system flowrates without significant reductions in performance, while the BCC and SC configurations quickly deviated from optimum performance. In addition to determining the reduced plate height and optimum flowrates for each geometry, the separation impedance was calculated, with all parameters shown in Table 7.

Table 7. Optimum channel Peclet number, minimum reduced plate height, and corresponding separation impedance for SC, BCC, FCC, SP, SG and SD geometries.

Shape	Pe	h_{min}	E
SC	2.5	0.75	41.2
BCC	2.0	1.00	58.9
FCC	4.5	0.17	1.9
SP	3.2	0.52	27.1
SG	12.2	0.27	6.3
SD	19.7	0.14	1.6

From the analysis of the dispersion measures it was evident that the PGD structures were recommended to outperform their sphere packing analogues in chromatographic applications. The structure with the lowest separation impedance and plate height was the Schwarz Diamond TPMS, which was also found to have the highest optimum flowrate with an average channel Peclet number of 19.7. These results show that TPMS are desirable choices for separation media as they have the potential to perform at higher flowrates with equal if not better efficiency when compared to basic sphere packing orientation. In particular it was determined that the SD geometry should be investigated further.

4.5 Breakthrough results

To extend the results beyond dispersion modelling with an inert RTD pulse test, the results from breakthrough simulations were collated to observe their performance as an adsorptive medium. This involved modelling a concentration step change at inlet and monitoring which arrangement could elute the largest dimensionless void volume (V_D) before the breakthrough condition was observed. The fraction of the solid phase capacity occupied (C_D) at the breakthrough was also used to measure the effective utilisation of the sorbent and uptake of solute. The breakthrough condition was defined to be when 5% of the inlet concentration was present in the fluid of the periodic unit cell's outlet. Breakthrough simulations were carried out twice; once with an inert solute to obtain a baseline value for the dimensionless volume that could elute through the column purely as a result of advection and diffusion, and once with the adsorption model implemented as described in Section 3.3.7. To illustrate the typical improvement that could be achieved between both cases, the results for the SD geometry at different Peclet are shown in Figure 31.

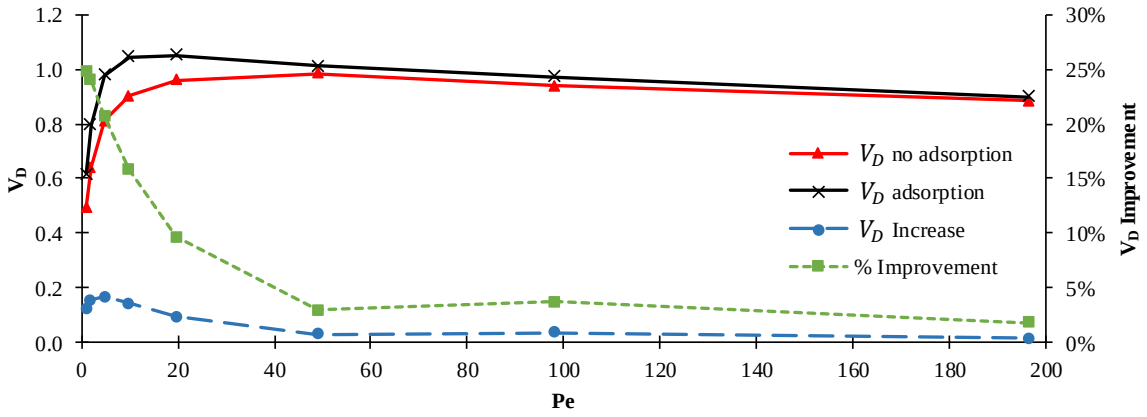

Figure 31. Comparison of the dimensionless void volumes treated by the SD arrangement with and without adsorption, including quantitative and percentage improvement in V_D treated.

The value of V_D was shown to increase when simulating adsorption, with the most dramatic improvements occurring at lower flowrates, thus confirming that the adsorption phenomena was mass transfer limited and not reaction rate limited, fitting the context of MIP surface reactions[180,197]. Similarly, it was found that at high system flowrates the V_D for the adsorption and inert breakthrough cases approach the same values, indicating that solute was being carried through the domain faster than it could reach the active sites at the surface. The plots of V_D and C_D against Peclet for each packing geometry is shown are Figures 32, 33, and 34 below.

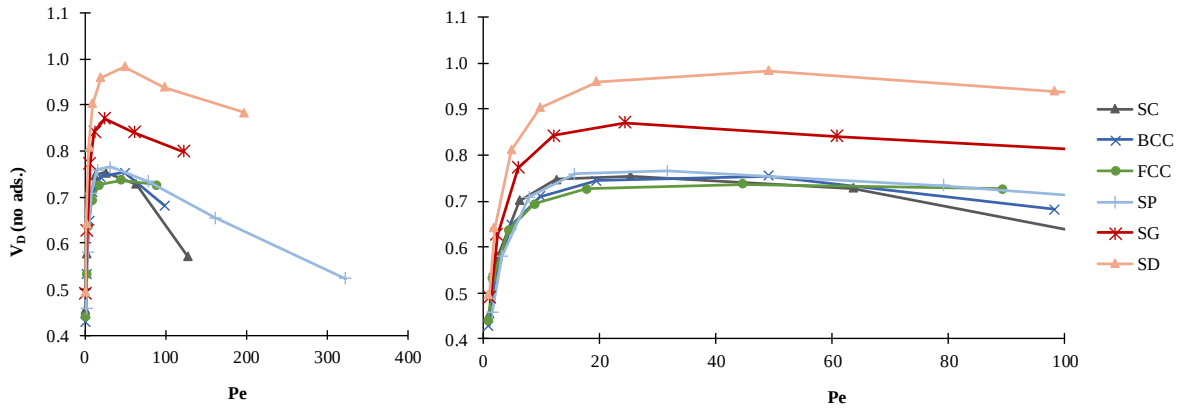

Figure 32. Dimensionless void volumes required to pass through the column until breakthrough occurs for basic sphere and TPMS structures. Observing the total investigated data range (left), and focused on the local maxima (right).

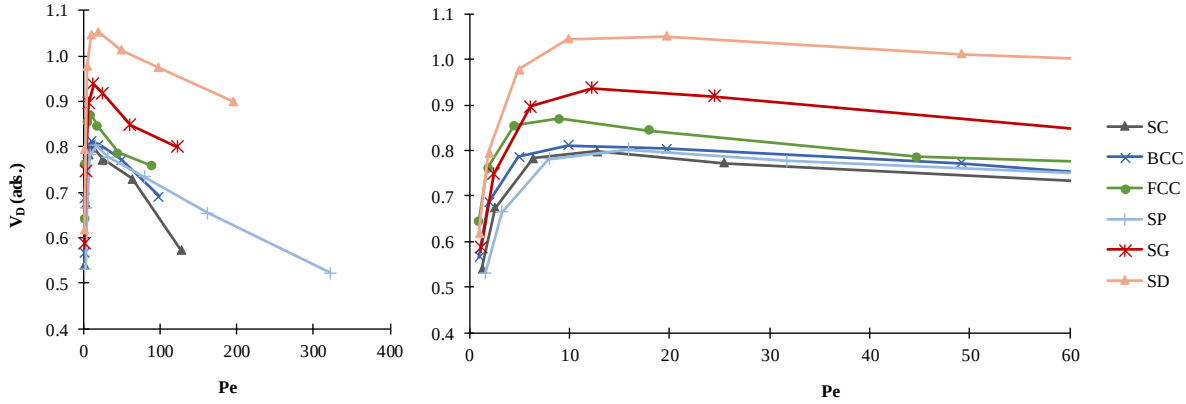

Figure 33. Dimensionless void volumes treated by the column until breakthrough occurs for basic sphere and TPMS structures. Observing the total investigated data range (left), and focused on the local maxima (right).

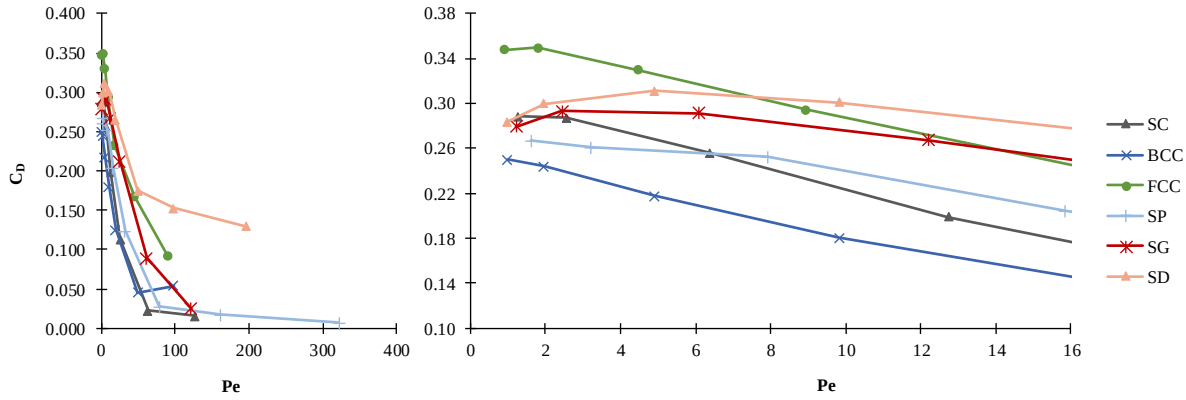

Figure 34. Dimensionless fraction of solid phase capacity occupied when breakthrough occurred for ordered spheres and basic TPMS. Observing the total investigated data range (left), and focused on the local maxima (right).

It is evident that the basic TPMS structures were able to treat larger quantities of fluid before the 5% breakthrough was observed, with the SD once again showed the best performance. When compared with the dispersion results, there was much less distinction between the three arranged sphere configurations, while notable changes in performance were still seen for the TPMS. The maximum C_D for each structure was very near the lowest flowrates examined in this study, with the local maxima for the BCC and SP geometries not being observed within the range of Pe studied. It was found that the fraction of capacity occupied was highest for the FCC ordered sphere arrangement, which was likely a product of the lower porosity. The SD was still a favourable geometry with the second highest C_D, which was achieved at a higher flowrate than the FCC orientation. Most of the simulations were able to fill 20-30% of solid phase capacity before breakthrough at low system flowrates, while at higher flowrates the adsorbed solute tended toward 0% quickly, except in the case of the SD. The geometries with high tortuosity and lower $\bar{u}_{dev}$ were seen to reach higher C_D, which is likely due to the association between a homogenised velocity field and lower mass transfer resistances. To compare the optimal conditions for the breakthrough simulations, the best performance from each simulation is summarized in Table 8 below.

Table 8. Summary of optimum operating conditions for dimensionless volume and capacity fraction occupied when 5% breakthrough is observed (using k_{ads}=1x10^{-4} s^{-1}, k_{des}=1x10^{-8} mol m^{-3} s^{-1}, specific capacity = 10 mol m^{-3}) for SC, BCC, FCC, SP, SG and SD geometries.

Shape	Pe	V_D	Pe	$V_D(ads.)$	Pe	C_D
SC	25.5	0.754	12.7	0.798	1.3	0.288
BCC	49.1	0.754	9.8	0.812	1.0	0.250
FCC	44.7	0.736	8.9	0.871	1.8	0.349
SP	31.7	0.765	15.8	0.803	1.6	0.267
SG	24.4	0.870	12.2	0.937	2.4	0.293
SD	49.1	0.984	19.7	1.052	4.9	0.311

The adsorption simulation results maintained the established trends of FCC outperforming BCC, in turn outperforming SC, as well confirming the TPMS analogue. The only exception to this found within Table 8 is that BCC had a lower maximum C_D than SC. Another observation that can be made is that the TPMS structures achieved their best performance at higher system velocities than the packed spheres, which from a practical perspective would be beneficial for carrying out filtration and adsorption processes faster and more efficiently. For this reason, the Schwarz Diamond geometry is still the primary candidate for use in the adsorption filter packed bed. The findings all indicated that monolithic structures such as TPMS would have improved performance over an ordered arrangement of spherical particles, and therefore further investigation was justified.

4.6 Performance relationships

One of the goals of this work was to identify any correlations between the properties of the various packing structures and their performance as an adsorptive media. In the ideal case, a strong relationship between the geometric properties of the unit cell would correlate to performance in the mass transport simulations, as this would allow preliminary 'screening' of geometries in future investigations. The sphericity (Ψ) specific surface area (a) and void fraction (ε) were of particular interest as these were proposed to be able to influence the adsorptive capacity, flow pathways, and pressure drop within the system. When attempting to discern a correlation between the permeability, separation impedance, and pressure drop gradient with the geometric properties, no relationship was found that fit both the sphere and TPMS data. However, several relationships between the geometry and the flow parameters were identified when analysing a larger data set of TPMS simulations and this is elaborated upon in Chapters 5, 6, and 7.

Similarly, no relationship between the geometry and the reduced plate height could be identified with the limited data set. When only considering the three TPMS structures there did appear to be a correlation between specific surface area and the breakthrough performance. The maximum V_D and C_D found from the breakthrough simulations is shown in Figure 35. As would be expected, with a higher specific surface area there was greater capacity for adsorption and thus higher void volume and fraction of capacity was achieved. To confirm this intuitive relationship more TPMS structures were investigated, as described in Chapter 5.

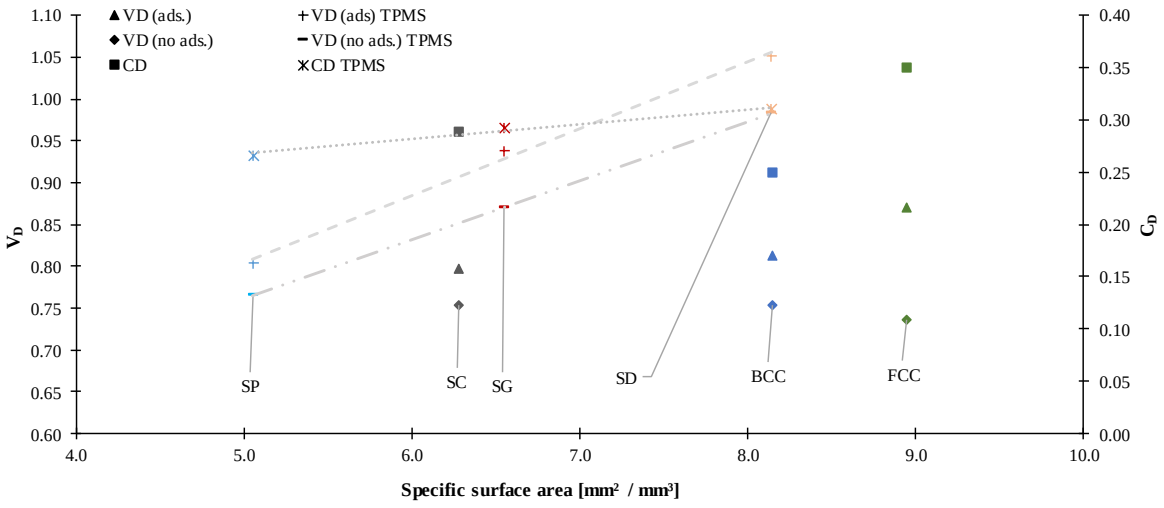

Figure 35. Relating the values of V_D and C_D to the specific surface area of a unit cell.

In the absence of additional strong relationships between geometric properties and dispersion or adsorption parameters, the flow properties were also investigated. To determine the flow field properties would still require a simulation to resolve the velocity field, but if correlations existed between the flow metrics and adsorption performance then these results could still assist future studies. The strongest trend was found between the normalized mean velocity deviation and the minimum reduced plate heights (Figure 36), but once again this was only notable for the TPMS and not the sphere arrangements. Each correlation was only based on the PGD family of TPMS, and thus were revisited with the addition of more data from each chapter.

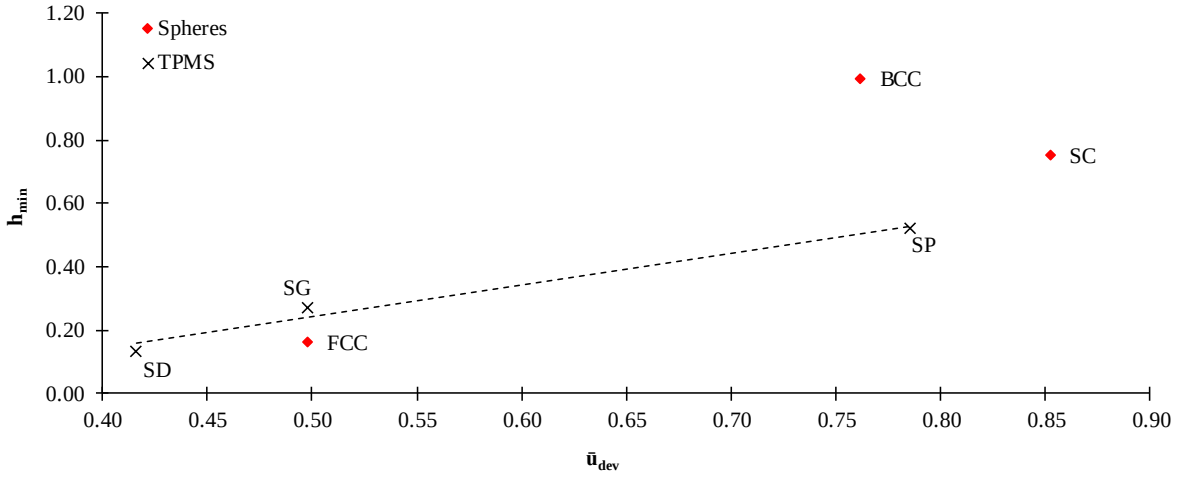

Figure 36. Relationship between the normalized mean velocity deviation and the reduced plate height.

4.7 Discussion and conclusions

This chapter examined the dispersion properties and breakthrough of ordered packed spheres (SC, BCC, FCC) with the basic TPMS structures (SP, SG, SD) to confirm the potential of ordered monolithic structures to have better performance in packed bed applications. In continuing the work done by Dolamore[8], the simulations were periodic in the radial direction to simulate an infinitely wide column thus removing the consideration of wall effects[198]. The TPMS structures were found to generally have higher specific surface areas than the packed sphere counterparts, indicating they would accommodate higher degrees of adsorption. This was confirmed by observing quantity of dimensionless void volumes that were required to flow through the column before breakthrough occurred, without compromising the fraction of total solid phase capacity that was occupied at the 5% breakthrough.

In general, the Schwarz Diamond TPMS was found to be able to operate at higher system velocities while achieving the highest value of V_D observed and also achieve one of the highest C_D. To further promote the use of SD for packed beds, it showed the slowest degradation of performance when operating at higher system velocities, making it attractive from a practical and economical perspective. The pressure drop requirements were also lower with the TPMS structures, and the permeability and dimensionless pressure drop gradient were found to relate directly to the porosity of each packing. After investigating the performance of each of the basic packed sphere and TPMS structures and determining that the SD was the most viable geometry to outperform traditional packed beds, the justification for why these structures perform better were considered.

It has already been noted that solid phase media that are able to reduce random eddy effects experience less axial dispersion and band broadening within chromatography columns, and have the potential for improved performance in packed beds used for filtration purposes. However, as all of the structures observed were ordered and periodic in nature all would experience reduced eddy effects, and the difference in performance must be attributed to other factors. Each simulation was carried out using the same solute (copper ions), meaning the difference in performance cannot be attributed to different diffusivities, and must be a result of mass transfer resistance differences[17]. Lower values of $\bar{u}_{dev}$ had been proposed to relate to lower mass transfer resistance within the fluid channel, and the findings from the initial simulations appeared to support this claim for TPMS but not for ordered spheres. Therefore $\bar{u}_{dev}$ was identified as a potential screening parameter to guide enhancement of packed bed media.

It is important to acknowledge that the comparisons made between ordered packed spheres and monolithic TPMS structures has only been done with ordered particles subject to point contacts, and without rotations relative to the axis of flow. The work performed by Dolamore[8] also investigated the effect of particle overlap (a necessary consideration for designing a column that will not reorient itself during operation), and rotating the packing relative to the axis of flow. The findings include that introduction of particle overlap can reduce the performance, but the effect is less pronounced in the more tortuous media (such as FCC). Applying a rotation relative to the axis of flow however, was found to produce smaller plate heights and separation impedance for most cases. A rotated arrangement of the SC packing was found to be one of the overall best performing structures, with a h_{min} value of 0.26 when converted to use the new L_c. While this was a significant improvement, it can be seen that this still did not outperform the Schwarz Diamond structure (h_{min} of 0.137). In addition to the ordered sphere arrangements, the dispersion properties of randomly packed spheres was observed by both Dolamore and Schure et al.[7], however the ordered spheres were found to have lower minimum plate heights and thus were not included in this study.

The breakthrough results suggested that mass transfer is enhanced in the TPMS structures with regular flow channels, a finding which is supported by much of the literature that examines the use of TPMS

over a wide range of applications. Studies by Torquato et al.[114] have indicated that the Schwarz Primitive and Schwarz Diamond structures are the preferred choices for composites with multi-functionality (each phase defined by the TPMS level-set equation favours different functionality). In particular these structures were found to be favourable for the combined transport of electricity and heat[113], however mass transport capability is often directly relatable to heat transfer. Other work has also suggested that TPMS are favourable for their mechanical properties such as the bulk modulus for use in scaffolding[199], and topological optimisation algorithms are capable of approximating TPMS structures[200].

The breakthrough results did not take into account the mass transfer resistance imposed by the specific adsorption model used, which would include phenomena such as pore diffusion and concentration gradients. However, MIPs are regarded for having fast reaction rates[181] and systems involving metal ion targeting MIPs are generally regarded as being diffusion or transport limited[201]. The use of the Langmuir isotherm to model adsorption was deemed to be accurate enough and a reasonable assumption of MIP adsorption[202]. If a different adsorption model were to be used it is reasonable to expect that the same relative performance by each geometry would be observed, and only the specific results would change.

Irrespective of the specific model being used to represent the MIP surface reaction, all simulations were conducted using the same parameters and therefore the models' impact on the adsorption process was constant across all cases and any difference in performance would be a result of the specific geometry used. Therefore the results from this study are able to provide a comparative look at each packed bed geometry, where changing the model or experimental parameters would not be expected to significantly affect the ranked performance of each structure (this concept was tested in Chapter 7).

Chapter 5 – Performance of Additional TPMS Geometries

Once it was established that ordered monolithic structures had the potential to outperform traditional packing media, additional TPMS were considered. Each TPMS structure was again evaluated based on its geometric properties, velocity field, and performance in mass transport simulations. The geometries that were considered included several surfaces with level-set equations[203,159] defined by Wohlgemuth[15] and included the; Schoen IWP, F-RD, P2-GD, L, and D' surfaces. The solid phase defined by these surfaces are shown in Figure 37, and the equations used to define them are shown in Appendix B.

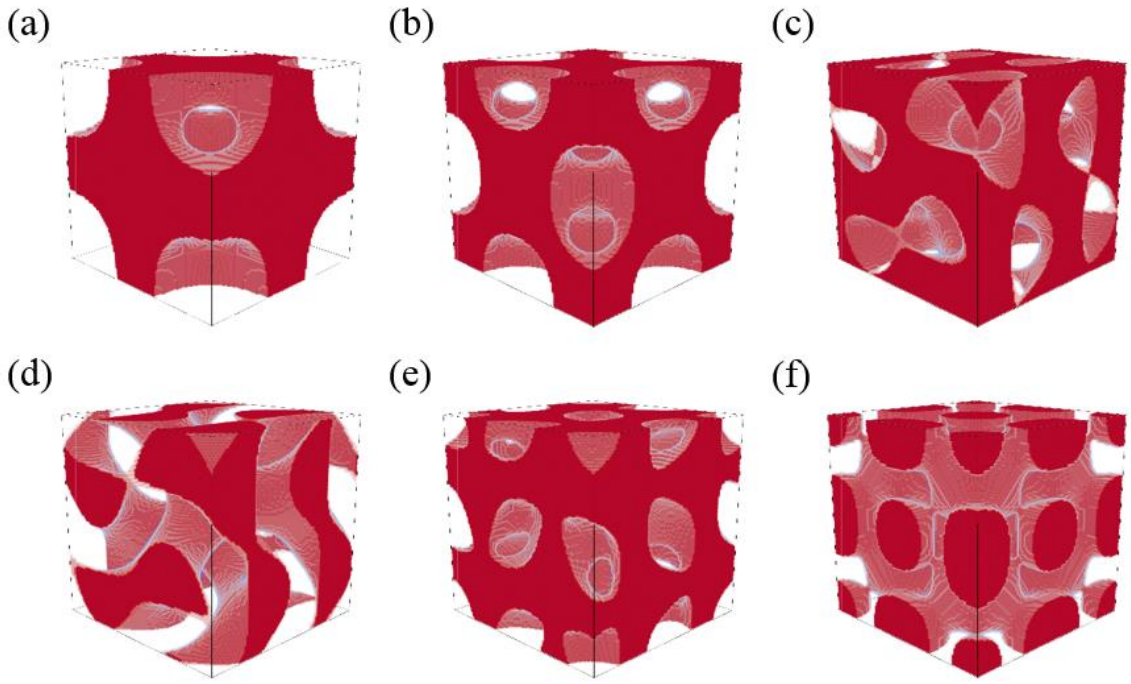

Figure 37. Image of the; (a) Schoen IWP <-0.25, (b) F-RD > 0, (c) P2-GD > 0, (d) DSG > 0, (e) L >-0.15, (f) D' < 0.20.

When defining these new geometries, some of the level-set equations required the equation be set to a value other than zero. For example, the Schoen IWP and FRD surfaces defined by Equations [78] and [79] each separate two discrete phases (to be defined as either fluid or solid). The direction of the inequality determined which phases were declared as fluid or solid, with each having a different geometry, permeability, and performance from the other (Figure 38). For the IWP and FRD surfaces, the constant used for right hand side of equations were required to be -0.25 and 0 respectively. Deviations from these values made the surface equations no longer approximate 'minimal' surfaces.

$$\cos(x)\cos(y) + \cos(z)\cos(x) + \cos(y)\cos(z) = -0.25 \qquad [78]$$

$$0.8\cos(x)\cos(y)\cos(z) + 0.1\cos(2x)\cos(2y)\cos(2z) - 0.1(\cos(2x)\cos(2y) + \cos(2y)\cos(2z) + \cos(2z)\cos(2x)) = 0 \quad [79]$$

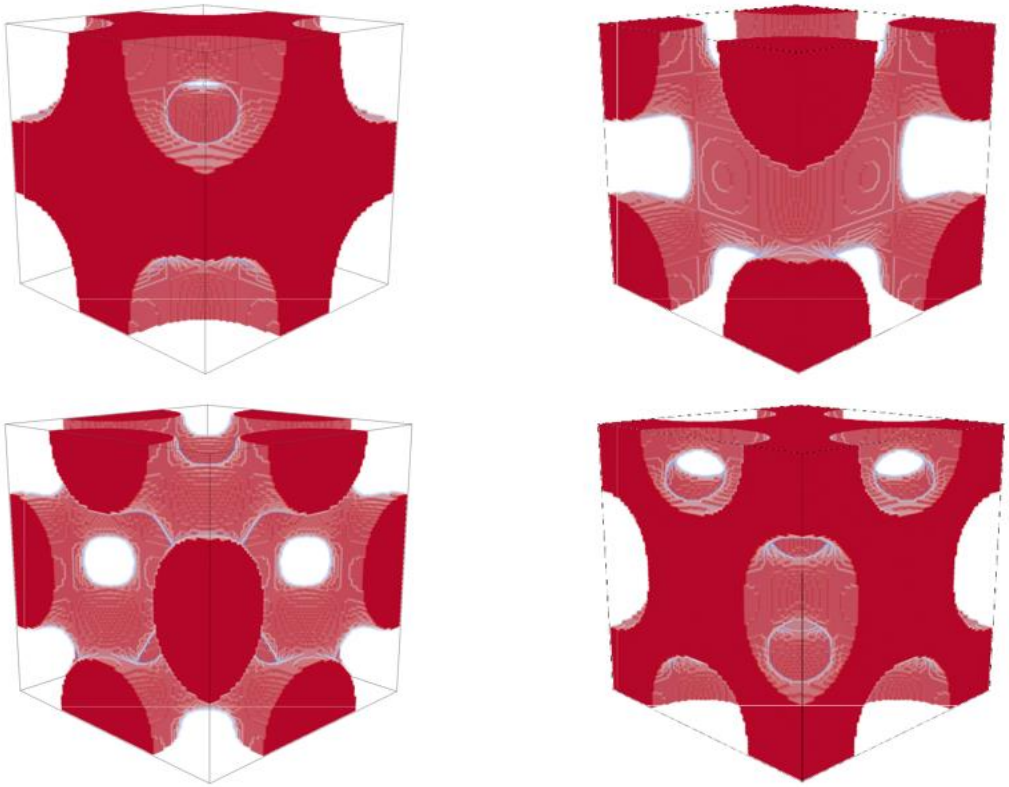

Figure 38. Comparison of the solid phased defined by using the level set equation with (clockwise from top left) IWP < -0.25, IWP < -0.25, FRD > 0, and FRD < 0.

The work conducted by Dolamore[8] indicated that when the solid phase was declared using the 'IWP < -0.25' and the 'FRD > 0' inequalities, the dispersion performance was better than for phase defined by reversing the direction of the inequality (the conjugate phase declaration). Dolamore's results were recreated in this work by investigating both fluid phases of the IWP and FRD surfaces, and confirming lower reduced plate heights were calculated (with the new L_c definition) using the nominally preferred inequality. When observing the breakthrough results from the two IWP and FRD data sets, it was seen that the better performing 'IWP < -0.25' solid phase also produced higher V_D and C_D than its counterpart, but that the 'FRD > 0' solid phase had higher V_D and C_D values (shown in the sections below). This highlighted the importance of needing to investigate both phases for non-symmetric TPMS to develop a full understanding of how each geometry would perform in a packed column. Of the TPMS structures in the entirety of this work, only the SP, SG, and SD surfaces were known to separate two identical phases (at 50% porosity) and thus did not require specific declarations of the fluid and solid phases. Due to a limitation of computational resources, only one of the possible phases for each of the remaining TPMS were investigated (as they were defined in Figure 1).

5.1 Geometric properties

The geometric properties of the eight new TPMS geometries are shown in Table 5. It was found that for all of the new unit cells investigated that the porosity was no longer equal to 50% (due to the asymmetry of the two discrete phases), which was found to affect the permeability and pressure drop across the unit cells. All of the unit cells were by definition the same size, and so the greater surface areas calculated for the FRD, P2GD, DSG, L and D structures also afforded each a greater specific surface area than the PGD family of TPMS. As was expected, for the phases defined by the IWP and FRD surfaces, each had the same specific surface area, and only differed in their porosity and sphericity. The L and D structures in particular were found to have significantly higher specific surface areas than the other structures, nearly twice that of SD, and would therefore would have a higher adsorptive capacity. However, these two structures also proved to have the lowest porosities of all the TPMS considered, and therefore would be subject to larger pressure drop.

Table 9. Comparison of geometric properties for various TPMS structures with unit cell size 500 µm. All geometries constructed with a resolution of 31 nodes.

Property	**Cell Volume** [mm³]	**Surface Area** [mm²]	**Cell Porosity** [-]	**Sphericity** [-]	**Specific SA.** [mm^{-1}]
SP	0.125	0.632	0.504	1.20	5.05
SG	0.125	0.819	0.500	0.93	6.55
SD	0.125	1.018	0.500	0.75	8.14
IWP <-0.25	0.125	0.941	0.509	0.80	7.53
IWP >-0.25	0.125	0.941	0.491	0.82	7.53
FRD <0	0.125	1.293	0.534	0.56	10.34
FRD >0	0.125	1.293	0.466	0.62	10.34
P2GD	0.125	1.366	0.476	0.57	10.93
DSG	0.125	1.368	0.567	0.51	10.95
L	0.125	1.684	0.385	0.52	13.47
D	0.125	1.836	0.434	0.45	14.69

5.2 Flow properties

The parameters obtained from resolving the Stokes flow velocity profiles through each structure are summarized in Table 6. The tortuosity values ranged from 1.03 to 1.35, suggesting that in the least suitable columns the bulk flow is almost entirely along the main axis ($T = 1$) with little to no radial advection occurring. Conversely, the highly tortuous structures such as the SD and L geometries were experiencing radial flow components amounting for on average 25% of the velocity magnitude, thus undeniably illustrating a reduction in linear channelling. The permeability values were all found to be

within the same order of magnitude, whereas the pressure drop gradient ($\dot{B}e$) varied over two orders of magnitude. A relationship between the TPMS unit cells geometry and permeability or dimensionless pressure drop was conjectured to exist, and by considering previous studies into permeability correlations, such as the Carman-Kozeny[83] and Ergun[86] equations, it was known the exact relationship may be complex. The types of equations have been discussed at length to determine relationships for different class of packed beds, with the most widely accepted describing beds of spherical particles.

Table 10. Comparison of pressure and velocity performance measures for additional TPMS.

Shape	Characteristic Length L_c $[mm^{-1}]$	Flow tortuosity T [-]	Normalized mean u deviation $\bar{u}_{dev}$ [-]	Dimensionless permeability k' [-] x10^{-3}	Bejan number gradient $\dot{B}e$ [-]
SP	0.399	1.031	0.786	5.06	0.204
SG	0.305	1.240	0.498	5.88	0.362
SD	0.246	1.287	0.416	5.70	0.897
IWP <-0.25	0.271	1.290	0.432	2.82	1.156
IWP >-0.25	0.261	1.054	0.751	5.89	0.580
FRD <0	0.206	1.172	0.514	4.09	1.914
FRD >0	0.180	1.273	0.463	4.12	2.561
P2GD	0.174	1.213	0.601	5.28	2.215
DSG	0.207	1.142	0.408	6.83	1.165
L	0.114	1.351	0.432	3.54	12.377
D	0.118	1.088	0.666	4.68	8.486

The relationship between geometry and permeability for TPMS structures was not well known, but it was found that a modified form of the Carman-Kozeny equation could be used to relate system parameters to the numerically determined permeability (Equation [6]). In Equation [81], a rearrangement of the modified equation is shown, where the inverse of the dimensionless permeability (k') derived from Darcy's law[6] was equated this to the porosity, sphericity and a constant (c_{CK}). It is important to note that when using this correlation the characteristic length (L_c) that was used to reduce the dimensions of the specific permeability (k) was the edge length of the unit cell (L_x) [L]. This was because when using the hydraulic diameter was used, no trend could be observed. The relationship given by Equation [81] is shown in Figure 39, where it can be seen that the traditional constants of 150 or 180 did not provide as good a fit as using the value of 215 (R^2 = 0.973). Thus agreeing with the results of Dolamore[8], which suggested a value for c_{CK} of 230 provided a good fit for the SP, SG, and SD geometries.

$$-\frac{dP}{dz} = u_s \frac{c_{CK} \nu \rho}{\Psi^2 L_c^2} \frac{(1-\varepsilon)^2}{\varepsilon^3} \quad [80]$$

$$\frac{1}{k'} = \frac{L_c^2}{k} \approx \frac{\left(-\frac{dP}{dz}\right)}{u_s \nu \rho} = \frac{c_{CK}}{\Psi^2} \frac{(1-\varepsilon)^2}{\varepsilon^3} \quad [81]$$

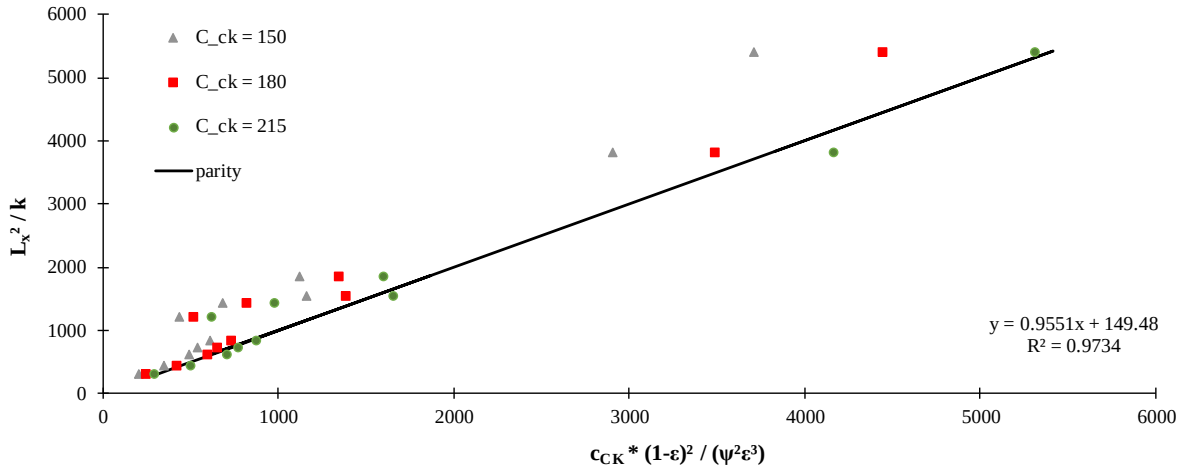

Figure 39. Correlation to determine the permeability of TPMS structures, based on the Carman-Kozeny equation (using the axial distance of a unit cell as characteristic length).

To further investigate the relationship between $\bar{u}_{dev}$ and T made in Chapter 4, the tortuosity of the additional TPMS studied were plotted against the normalized mean deviated velocity (Figure 40). A negative trend was still evident but considerably weaker, with the DSG showing as an outlier. Therefore, it could not be claimed that pore geometries that influence a higher degree of tortuosity and radial flow were necessarily able to better homogenize the velocity gradients present in the fluid flow.

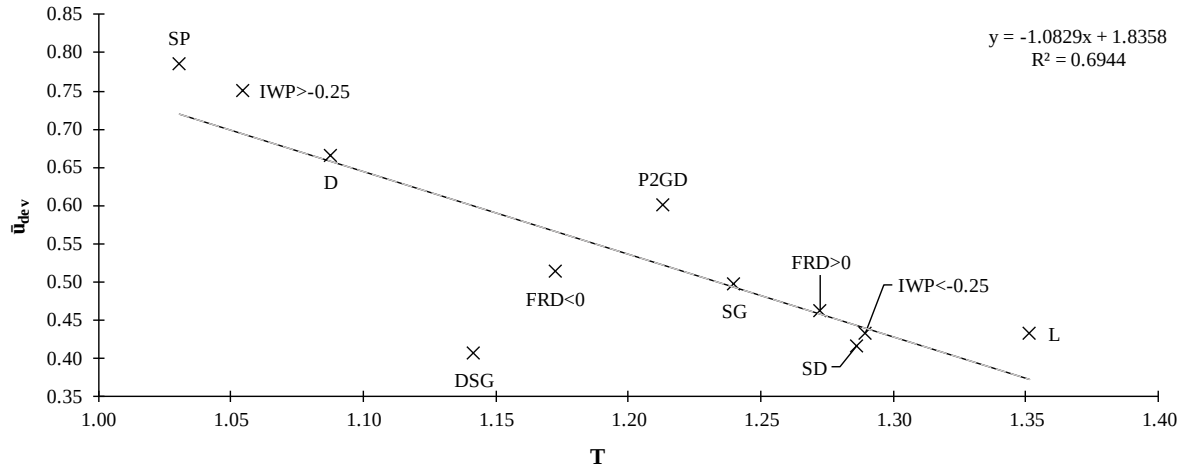

Figure 40. Relating the channel tortuosity with the mean deviated velocity for TPMS.

In addition to fitting the permeability data to a Carman-Kozeny type equation, the dimensionless pressure drop could be related directly to the inverse of the characteristic length (Figure 41). The characteristic length ($L_c = d_{h,pore}$) encompassed the effects of flow resistance from its dependency on the porosity (account for increased velocity gradients) and the specific surface area (incorporating shear rate from surfaces), thus providing a strong justification for why it related to the pressure drop requirement. The characteristic length was normalized by the axial length of the periodic unit cell (L_x) [L] to remove dimensional dependency, and a constant of 0.2 was used to fit the data. The constant of 0.2 was used to translate the data to the origin, and was related to the lowest ratio of L_x to L_c observed (for the case of the L surface).

This relation proved to be very strong, and would allow predictions of the pressure drop requirements to be made based on the geometry of TPMS packed bed unit cell.

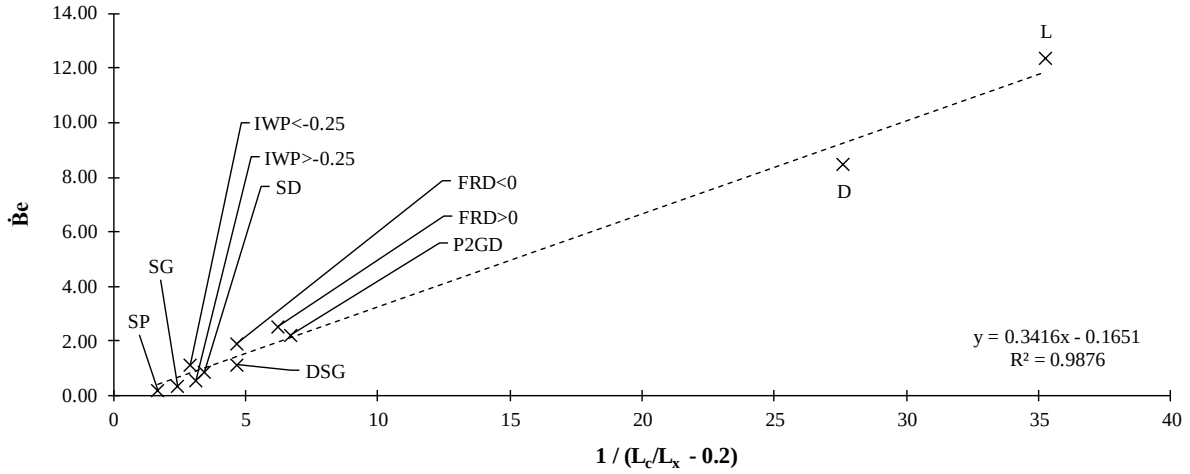

Figure 41. Correlation between geometry and the dimensionless pressure drop gradient (Bejan number) for TPMS.

5.3 Dispersion and separation impedance

Van Deemter plots were generated for all of the additional TPMS and are shown in Figure 41. It was found that the Schwarz Diamond structure still presented the lowest reduced plate height, although the Double Schoen Gyroid (DSG) structure had very similar performance. One benefit of the DSG was that it had the highest flowrate at which h_{min} was observed. Despite DSG having a higher optimal Peclet number, the SD geometry still had a lower plate height at the equivalent flow rate despite not being the h_{min} for SD. The worst performing geometries had both the highest h values as well as the steepest Van Deemter curves above h_{min} were the SP, IWP > -0.25, and D structures.

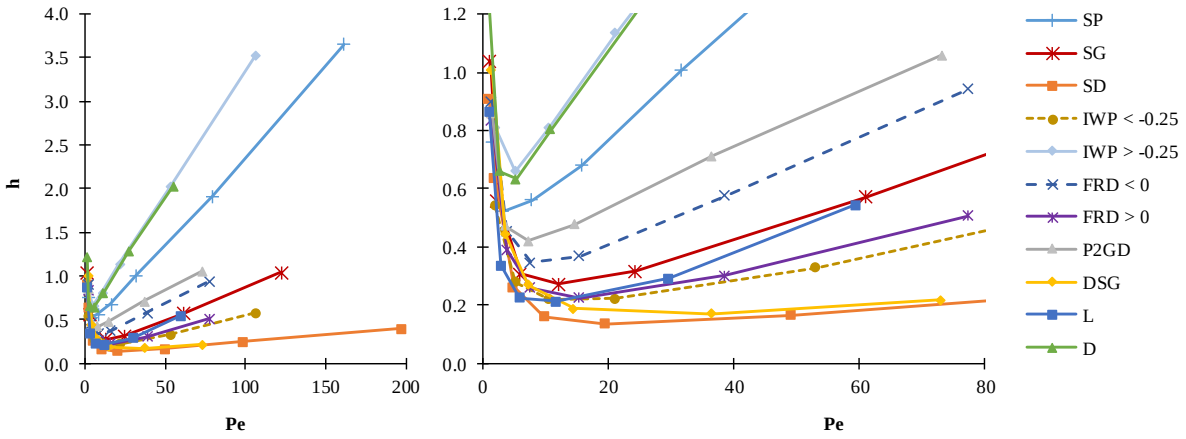

Figure 42. Reduced plate height Van Deemter curves for more TPMS structures.

The optimum channel Peclet number, minimum reduced plate height, and the corresponding separation impedance values for each TPMS are compared in Table 7. When comparing the IWP and FRD data sets it is seen that fluid phases with a lower h_{min} also had a more favourable separation impedance (E). It was also noted that a lower minimum reduced plate height generally corresponded with a higher optimal flow rate in the dispersion tests. In general, structures that experienced less axial dispersion would be expected to operate at higher Pe as well. Of all the geometries, only the DSG appears to have a plate height and separation impedance that could be considered competitive with the SD geometry. The optimum operating conditions of the DSG were marginally higher than the SD, and the rates at which h_{min} and E increased were low, similar to those of the SD orientation.

Table 11. Optimum channel Peclet number, minimum reduced plate height, and corresponding separation impedance for TPMS geometries.

Shape	Pe	h_{min}	E
SP	3.2	0.52	27.1
SG	12.2	0.27	6.3
SD	19.7	0.14	1.6
IWP <-0.25	10.6	0.22	8.7
IWP >-0.25	5.3	0.66	36.5
FRD <0	7.7	0.35	15.8
FRD >0	15.5	0.23	5.8
P2GD	7.3	0.42	16.0
DSG	36.5	0.17	2.4
L	11.9	0.21	5.0
D	5.4	0.63	37.3

5.4 Breakthrough results

The dimensionless void volumes able to be passed through each structure before breakthrough occurred with and without adsorption modelled are displayed in Figure 43, and the total fraction of capacity occupied at breakthrough (for the adsorption case) is shown in Figure 44. Interestingly, the relative performance of each structure from the dispersion modelling did not correspond exactly with the breakthrough results as it did for the SP, SG, and SD geometries. In the absence of adsorption, breakthrough performance largely corresponded to the dispersion modelling, with the SD, DSG, and L achieving some of the highest V_D values. When reviewing the adsorption results, it was seen that many of the new TPMS geometries considered were competitive with the PGD family. Structures such as the L and D surfaces (with notably higher specific surface areas) had high V_D and C_D, and also showed the greatest improvement between the inert and adsorption simulations.

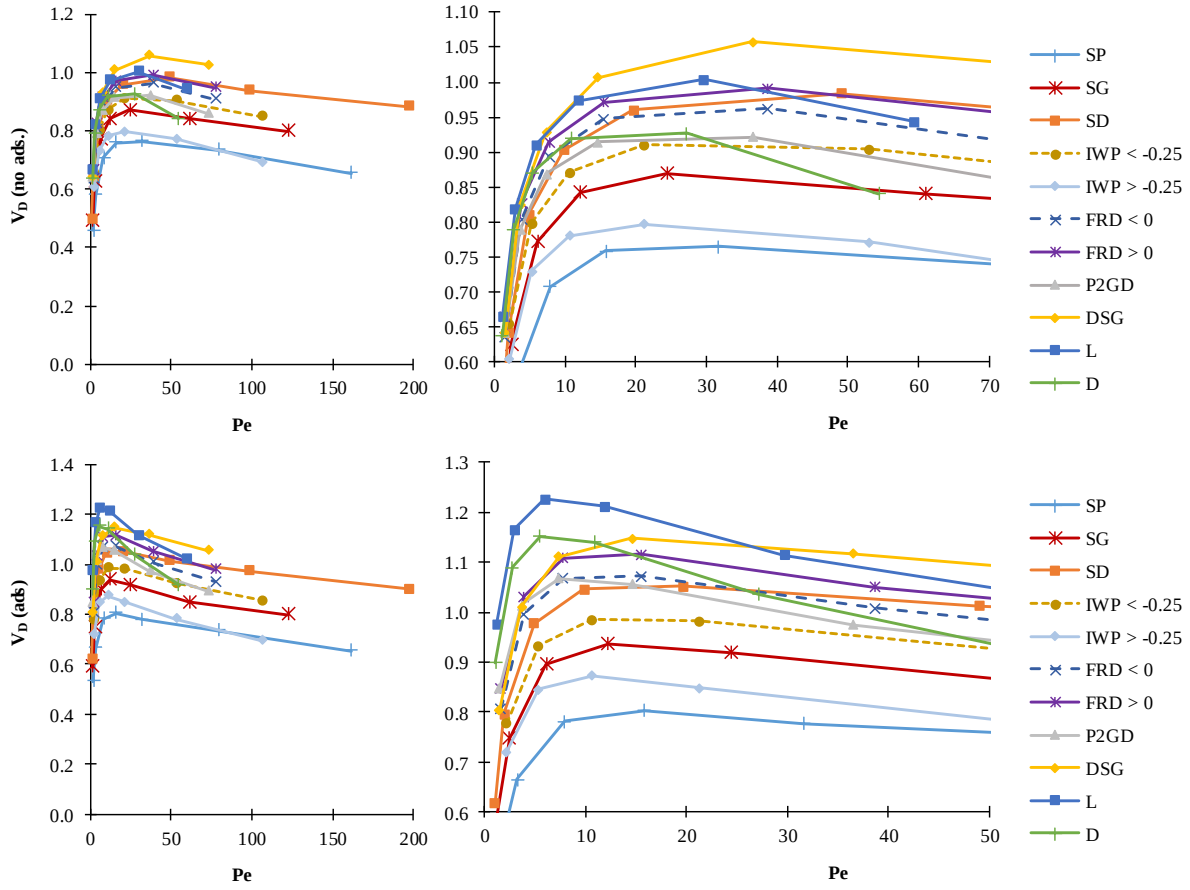

Figure 43. Dimensionless void volumes required to pass through the column until breakthrough occurs for TPMS structures with (bottom) and without (top) adsorption modelling.

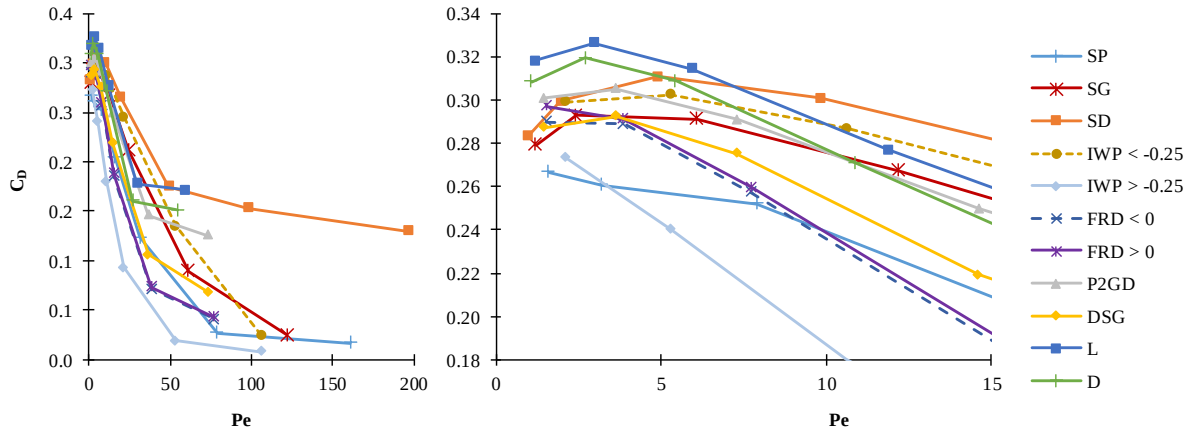

Figure 44. Dimensionless fraction of solid phase capacity occupied when breakthrough occurred for more TPMS. Full range of Peclet observed (left) and closer examination of maxima (right).

The optimum operating conditions for a column to obtain maximum V_D and C_D values with each geometry are shown in Table 12. For the instances where a local maximum was not observed, such as can be seen for the C_D of the SP and IWP > -0.25 unit cells, the highest value was used in its place. Across all surfaces it was shown that higher fractions of the solid capacity would be occupied at lower Pe. The overall adsorption process was confirmed to be mass transfer limited in this case, as the reaction at the wall was assumed to be fast relative to the transport from the fluid channel to the surface. It also appeared that the minimum loading achieved at low Pe was likely to be over 20% for any media, whereas at high Pe it was very likely that loading would tend to zero. The different rates at which this loading decreased could be used to identify structures that are better suited to applications with faster flowrate requirements.

Table 12. Summary of optimum operating conditions for dimensionless volume and capacity fraction occupied when 5% breakthrough is observed (using k_{ads}=1x10^{-4} s^{-1}, k_{des}=1x10^{-8} mol m^{-3} s^{-1}, specific capacity = 10 mol m^{-3}) for TPMS.

Shape	Pe	V_D	Pe	$V_D(ads.)$	Pe	C_D
SP	31.7	0.765	15.8	0.803	1.6	0.267
SG	24.4	0.870	12.2	0.937	2.4	0.293
SD	49.1	0.984	19.7	1.052	4.9	0.311
IWP <-0.25	21.3	0.910	10.6	0.985	5.3	0.302
IWP >-0.25	21.3	0.797	10.6	0.874	2.1	0.273
FRD <0	38.7	0.962	15.5	1.072	1.5	0.290
FRD >0	38.7	0.991	15.5	1.116	1.5	0.297
P2GD	36.6	0.921	7.3	1.068	3.7	0.305
DSG	36.5	1.057	14.6	1.147	3.7	0.293
L	29.7	1.003	5.9	1.227	3.0	0.327
D	27.2	0.927	5.4	1.153	2.7	0.320

5.5 Correlations

The additional TPMS data obtained in this chapter were used to identify or strengthen correlations between the geometric and flow parameters of the system, and the chromatographic or adsorption performance measures. One such trend identified in Chapter 4 that was supported by the findings in this chapter was that with higher specific surface area a higher V_D and optimum loading capacity could be achieved. Figure 45 shows that there is a strong positive correlation between the specific surface area and higher V_D and C_D. It was also found that the sphericity could be used in place of the specific surface area, and yielded an equally strong correlation. It is worth noting that in the case with the IWP and FRD structures, one of each of the solid phase designations fits the general trend better. This may suggest that for all non-symmetric TPMS, there is a single phase better suited to comprise the solid media (diffusion transport) and one that is better suited to comprise the fluid channels (advection diffusion transport), which may explain why the P2GD structure did not have as high a V_D and C_D as the DSG, despite possessing a very similar specific surface area.

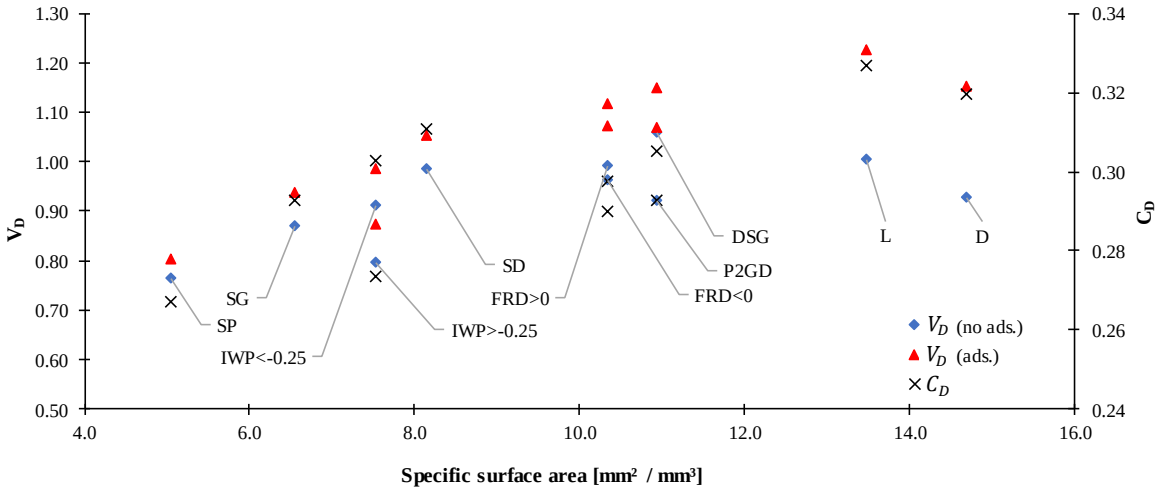

Figure 45. Adsorptive capacity (V_D, C_D) against specific surface area for TPMS.

An important consideration from Figure 45 was that the maximum capacity fraction and void volumes treated do not necessarily correspond to the same operating flowrate. As was seen in Table 12, the flowrate at which the maximum C_D occurred was likely to be at a lower flowrate than that at which the maximum V_D was calculated. However, the L surface was able to treat a large volume of fluid and reach a high fraction of capacity. Plotting the value of C_D obtained from each structure's $V_{D,max}$ simulation did not reveal an exact relationship between the two parameters (Figure 46), suggesting bed media could not be intentionally designed to achieve high V_D and C_D concurrently. However, from a practical perspective, the trend observed in Figure 45 could be used to guide manufacturing decisions, and select structures better suited to either high elution capacities, or high utilisation of the bed capacity.

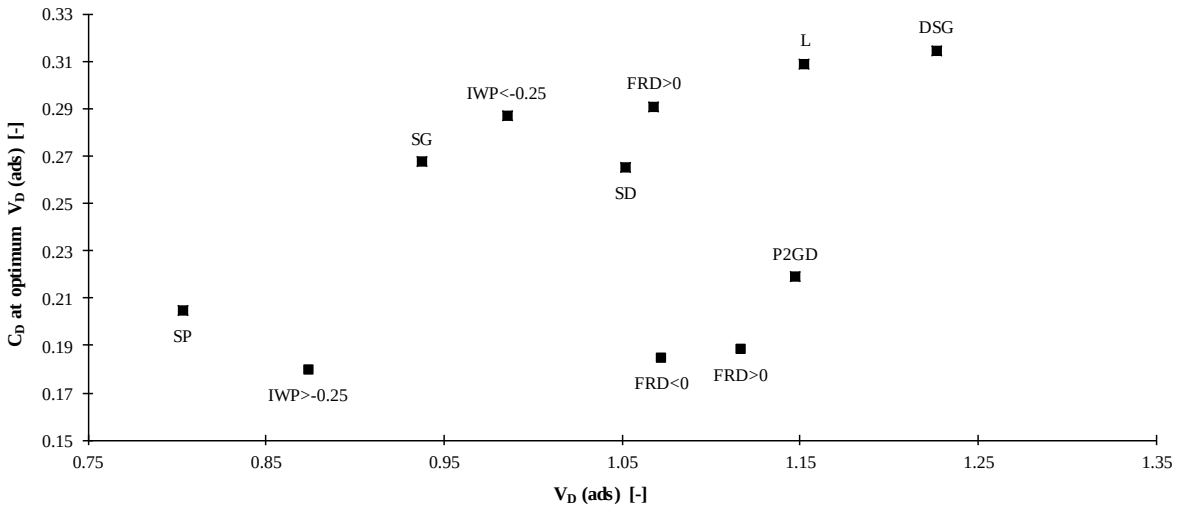

Figure 46. Plot of the maximum V_D treated with adsorption modelling, and the corresponding C_D.

Another correlation that was identified from Chapter 4 and confirmed for the additional TPMS was the linear relationship between $\bar{u}_{dev}$ and h_{min}. Figure 47 shows the strong relationship, with only the SP and D structures showing a significant deviation from the trend. This provides an opportunity to assess the dispersion performance of a structure from a resolved velocity field, without needing to conduct an RTD simulation or other method for determining the plate height. This correlation could potentially be used to predict chromatographic performance using the resolved velocity field, which would be much less time consuming than conducting a full RTD simulation.

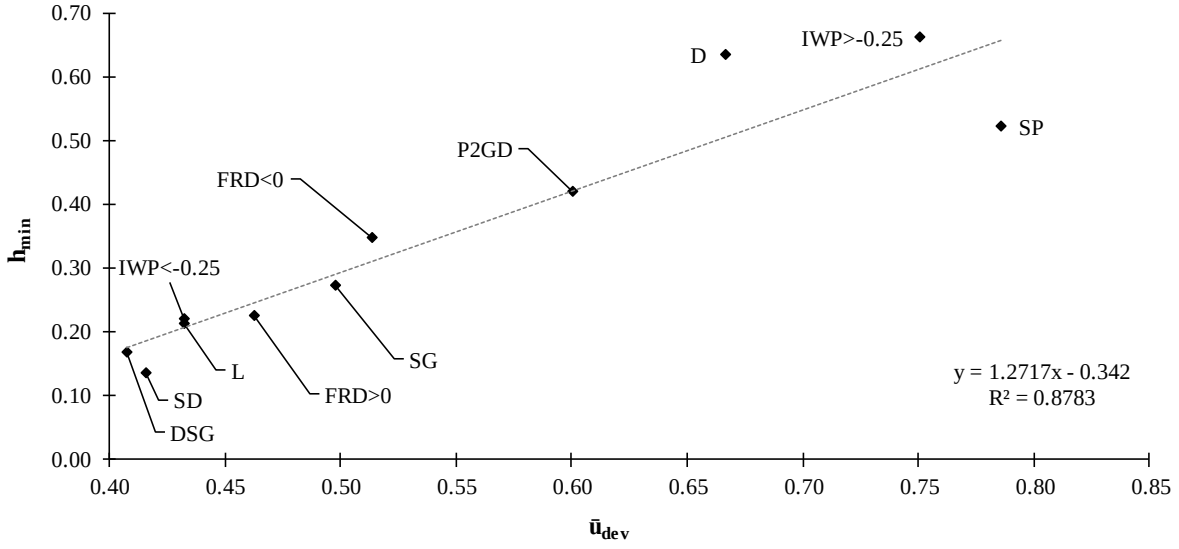

Figure 47. Correlation between minimum reduced plate height and the normalized mean velocity deviation for TPMS.

5.6 Discussion

In this chapter, several more TPMS structures were simulated for use in packed bed applications and compared to the three basic TPMS structures; SP, SG, and SD. The performance of monolithic TPMS had already been shown to challenge the performance of traditionally used particulate packing when operated within the Stokes flow regime, by having the potential to reduce axial dispersion and increase column dynamic capacity. Therefore any additional improvements upon the performance of the SD structure identified in Chapter 4 would have the potential to yield even better column performance. For the new TPMS structures introduced in this chapter (Schoen IWP, FRD, P2GD, DSG, L, and D surfaces), each level set equation describes the TPMS surface between two non-symmetric discrete phases and therefore possessed different properties when designated as fluid and solid phases.

The IWP and FRD surfaces were investigated with fluid represented as both possible phases, and it was confirmed that one phase designation did have enhanced performance over the other, thereby making it a requirement to investigate both phases in future work. However, due to computational resource limitations, only one fluid phase designation for each of the remaining TPMS geometries was investigated. The pressure drop requirements were shown to be directly related to the characteristic length of a TPMS structure, whereby a unit cell with a smaller characteristic length (hydraulic diameter) would incur higher pressure drop. The two factors that influence this are a lower porosity and a high specific surface area (which relates to shear stresses). This relationship could be used to predict the feasibility of packed bed geometries for applications with a known target flowrate or limiting pressure differential, as media with large pressure requirements could be excluded. The geometry with the highest permeability and lowest pressure drop was found to be the Schwarz Primitive, which was in keeping with findings from Jung[116] and Torquato. After assessing several TPMS and sphere arrangements, they elected the Schwarz Primitive to have the lowest permeability and indicated a relationship between minimizing specific surface area higher permeability.

The dispersion results indicated that SD was still the highest performing monolithic structure, closely followed by the DSG, which had the highest Pe at which the minimum reduced plate height was observed. It was then found that the ranking of performance from the RTD modelling did not necessarily correspond with the performance ranking of the breakthrough simulations. While the SD geometry was able to perform well in both simulations, the DSG had a higher V_D but did not achieve a loading higher than the SD despite possessing a greater specific surface area. The L and D surfaces on the other hand were able to reach much higher V_D and C_D despite having had relatively large h_{min}. These benefits were accompanied with the tradeoff of requiring a higher pressure gradient to induce flow through the L and D structures. For this reason, separation impedance (E) is an attractive measure of column effectiveness, as it characterizes both dispersion and flow resistance. The structures with the lowest separation impedances were still found to be the Schwarz Diamond and Double Schoen Gyroid.

The DSG structures physically differed from SD and the rest of the TPMS considered in this chapter by possessing two discrete solid phases that make up the monolithic network, as well as the fluid phase. This is partly what provides the DSG with a high specific surface area, thus making it an ideal candidate for adsorption processes. From a practical point of view, if each of the solid phases could be printed with differently functionalized media, then it becomes possible to use the DSG in adsorption processes to target more than one solute at a time.

Using the adsorption model parameters in this study, it was found that slow flowrates would favour a higher uptake of contaminant to the packed bed material, because the overall adsorption process was mass transfer limited. To enhance the rate of mass transfer from the fluid channel to the surface of the packed bed, structures that reduce variations in the velocity profile are favourable. Because is a correlation between the homogenization of the velocity field and the performance measures (h_{min}, V_D, C_D), any property that can relate the geometry of a periodic unit cell to the regularity of the velocity field (T, $\bar{u}_{dev}$) would be beneficial in selecting optimal media. However, simply increasing tortuosity or reducing the velocity field gradient alone was not sufficient to guarantee a high performing porous bed. A combination of geometric and flow field influences culminate in better performance, and this provided the motivation to further explore monolithic packed beds through modifying TPMS in Chapter 6.

Chapter 6 – Performance of Manipulated TPMS Geometries

To further build upon the understanding of how the fluid channels in porous media were able to influence packed column performance, several manipulations to the basic TPMS structures were investigated. In Chapters 4 and 5 it was shown that the specific surface area (and sphericity) of TPMS was weakly correlated with the maximum adsorption measures (V_D, C_D) each morphology achieved at optimal Pe. These correlations were found by generalizing largely different geometries, as each TPMS was shown to have greatly different distributions of fluid and solid within the unit cell. Some TPMS such as the PGD family possessed relatively thick flow channels and solid networks (up to half a unit cell in diameter), whereas the L and D surfaces were comprised of much smaller conduits. In this chapter, more nuanced changes in geometry were examined to see if more reliable trends could be found and exploited for use in designing enhanced packed bed media. The influence of unit cell orientation relative to the flow axis, and channel width (examined by varying the porosity) PGD family of TPMS geometries was explored.

6.1 Geometry manipulations

6.1.1 Unit cell rotations

The effect of orientation of an ordered packing relative to the flow axis is known to affect the chromatographic performance[8], therefore the effect of rotating these monolithic porous media was also investigated. Any reorientations capable of enhancing the tortuosity or decreasing the mean deviated velocity were expected to increase chromatographic and breakthrough performance, therefore it was expected the SP structure would benefit the most from rotation. The SP, SG and SD unit cells underwent single and double rotations (abbreviated to 1R and 2R respectively) to result in the new unit cells as shown in Figure 48. As the inlet boundary conditions were required to be implemented on an inlet surface, rather than reorienting the unit cell boundaries the geometry within the unit cell was rotated in accordance with common Miller indices notation[204]. To implement this manipulation, rotation matrices were applied to the level set equations. For the natural unit cell [100] no rotation matrix was applied, but for the single rotation orientation [110] a singular rotation 2D matrix (Equation [73]) was applied, and for the double rotation [111] Equation [73] was implemented twice with an appropriate angle (θ) in each 2D plane[205]. To show the effect of applying Equation [73], a set pair of coordinates (x, y) rotated by angle θ would result in the new coordinates (x', y') as shown in Equation [83]. The 1R orientation underwent a $\pi/4$ rotation in the YZ plane (where Y and Z were radial relative to the flow), while the 2R orientation was subject to a $\pi/4$ rotation in the YZ plane and subsequent $tan^{-1}(1/\sqrt{2})$ rotation in the XZ plane, both about the origin (with the origin defined as the corner of the bounding box of a non-

rotated unit cell). These rotations required the unit cell dimensions to be redefined to accommodate the rotation of the surfaces, also causing changes to the geometric properties.

$$rot = \begin{bmatrix} cos(\theta) & -sin(\theta) \\ sin(\theta) & cos(\theta) \end{bmatrix} \quad [82]$$

$$\begin{cases} x' = xcos(\theta) - ysin(\theta) \\ y' = xsin(\theta) + ycos(\theta) \end{cases} \quad [83]$$

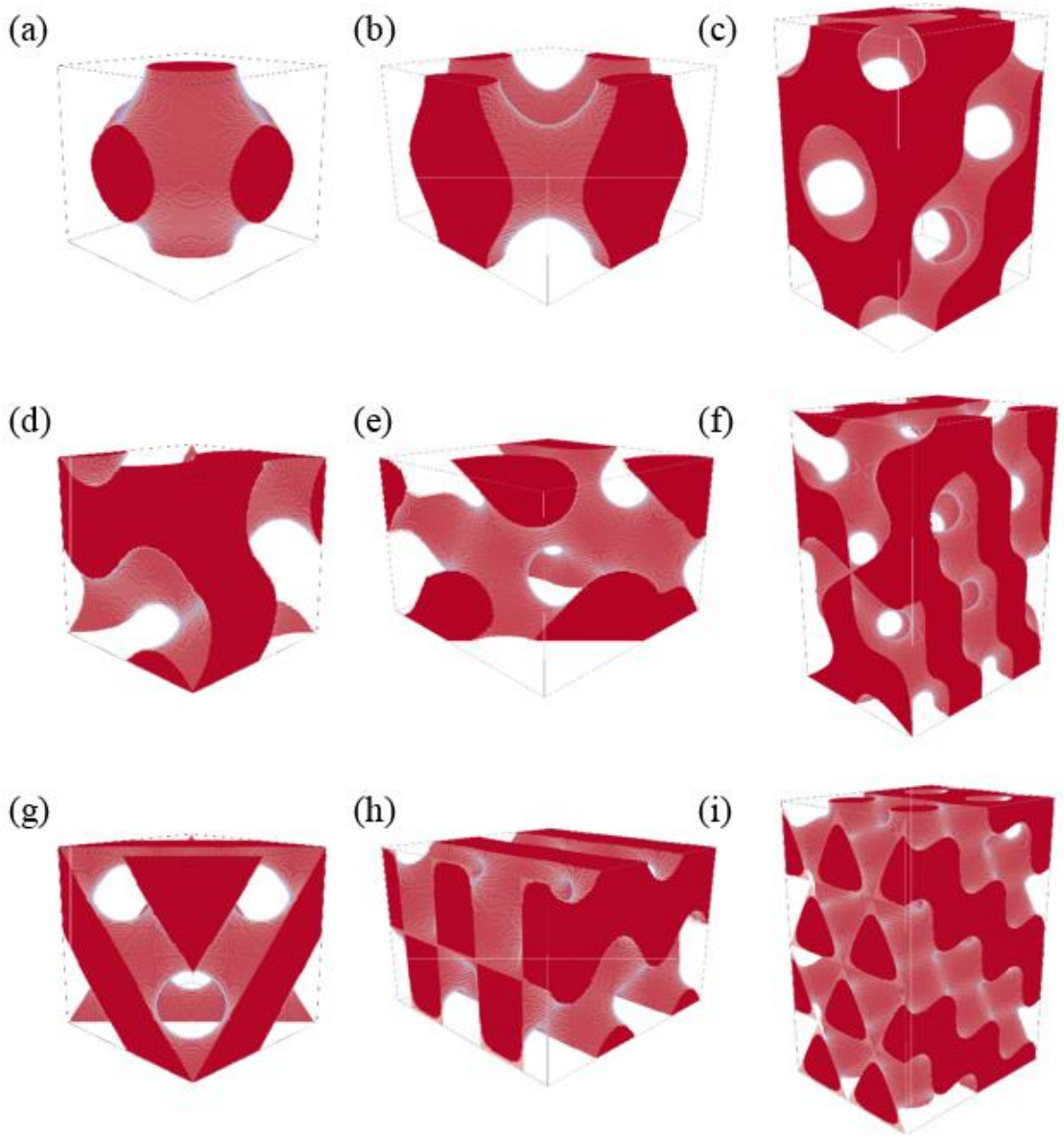

Figure 48.(a) The Schwarz Primitive (SP) unit cell [100] and the unit cells defined by (b) single [110] and (c) double rotations [111] (d). Schoen Gyroid (SG) unit cell [100] and the unit cells defined by (e) single [110] and (f) double rotations [111]. (g) Schwarz Diamond (SD) unit cell [100] and the unit cells defined by (h) single [110] and (i) double rotations [111].

6.1.2 Channel width and porosity

In addition to manipulating the orientation of the unit cells relative to the flow axis, the porosity of each structure was changed by varying the constant value used in the TPMS level set inequalities. To restrict and widen the flow channels the constant was varied from; -0.6, -0.3, 0, 0.3, 0.6. The resultant unit cells, which were no longer truly 'minimal', are shown in Figure 49.

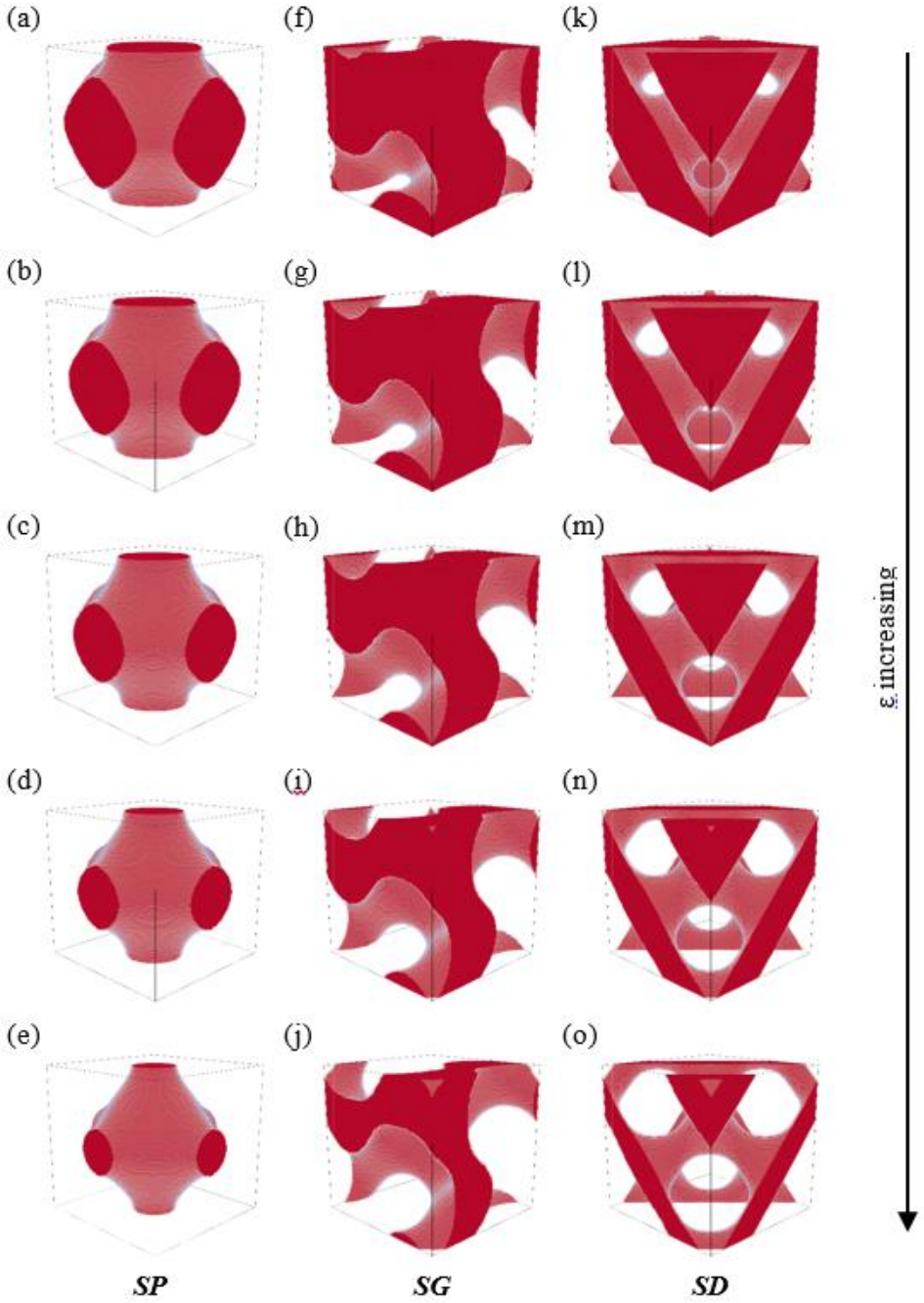

Figure 49. Basic TPMS structures with varying porosity; (a) SP ε = 0.33, (b) SP ε = 0.42, (c) SP ε = 0.50, (d) SP ε = 0.59, (e) SP ε = 0.67, (f) SG ε = 0.31, (g) SG ε = 0.40, (h) SG ε = 0.50, (i) SG ε = 0.60, (j) SG ε = 69, (k) SD ε = 0.25, (l) SD ε = 0.38, (m) SD ε = 0.50, (n) SD ε = 0.62, (o) SD ε = 0.75.

6.2 Geometric properties

The geometric properties for each of the rotated TPMS are shown in Table 13. The first measure that can be noted is that the porosity is unchanging for all cases (within voxelization errors), confirming that the rotation was successful in reorienting the solid phase without changing the actual structure itself. The volume and surface area increased with each rotation, which was a result of the increasing unit cell size. The relative edge lengths of the new unit cell representations in the 1R, and 2R state were elongated in the (x, y, z) directions by factors of $(1,\sqrt{2},\sqrt{2})$, and $(2\sqrt{3}/\sqrt{2},\sqrt{2},\sqrt{2})$ respectively. This was because the rotation was applied about the origin at the corner of a bounding box, requiring the edge lengths to be changed by Pythagorean factors to maintain periodicity. If the rotation had been applied about the centre of the unit cell, the unit cell would have been able to remain the same size. Despite the edge length elongation, the specific surface area was expected to remain constant irrespective of the rotation applied, which was proven by the data in Table 13 (although small variations were seen due to the aforementioned numerical errors). The sphericity on the other hand was seen to decrease in all cases when the rotations were applied. This was because sphericity depends on both the surface area and volume of a unit cell, which increase at different rates. As the specific surface area remained constant through the rotations, it would be expected that any differences in performance could be attributed to the changes in the velocity field and flow properties. However, as the sphericity was seen to change with rotation, it was used in the search for trends.

Table 13. Comparison of geometric properties for rotated TPMS structures with unit cell size 500 μm (before rotation).

Shape	**Cell Volume** [mm³]	**Surface Area** [mm²]	**Cell Porosity** [-]	**Sphericity** [-]	**Specific SA.** [mm^{-1}]
SP	0.125	0.632	0.504	1.20	5.05
SP 1R	0.249	1.253	0.500	0.96	5.03
SP 2R	0.747	3.771	0.499	0.67	5.05
SG	0.125	0.819	0.500	0.93	6.55
SG 1R	0.249	1.638	0.500	0.74	6.58
SG 2R	0.747	4.975	0.500	0.50	6.66
SD	0.125	1.018	0.500	0.75	8.14
SD 1R	0.249	2.039	0.500	0.59	8.19
SD 2R	0.747	6.210	0.500	0.40	8.31

When performing the next set of manipulations the porosity was varied as a direct result of altering the level set equations for the PGD structures. The geometric properties of the resultant structures with varying porosities and channel widths are shown in Table 5. For each base TPMS (SP, SG, SD), the highest specific surface area was observed when porosity was unmodified at 50%. As the porosity diverged from 50%, dimensions of the unit cell remained unchanged, but the specific surface area

decreased as a result of translating the interfacial surface. The PGD TPMS equations divide the unit cell into two identical phases at 50% porosity; deviating from this porosity resulted in one smaller phase with a lesser surface area separating the two phases. All other geometric measures were also changed as a result of the manipulation. The different porosities obtained for each structure resulted from using the same inequality constants [-0.6, -0.3, 0.0, 0.3, 0.6] in the level set equations, instead of determining which values provided set porosities for each base TPMS.

Table 14. Comparison of geometric properties for basic TPMS structures with modified porosity, unit cell size 500 µm.

Shape	**Cell Volume** [mm³]	**Surface Area** [mm²]	**Cell Porosity** [-]	**Sphericity** [-]	**Specific SA.** [mm^{-1}]
SP (ε=0.33)	0.125	0.572	0.332	1.61	4.58
SP (ε=0.42)	0.125	0.609	0.418	1.38	4.87
SP (ε=0.50)	0.125	0.632	0.504	1.20	5.05
SP (ε=0.59)	0.125	0.612	0.589	1.09	4.90
SP (ε=0.67)	0.125	0.579	0.674	0.99	4.63
SG (ε=0.31)	0.125	0.759	0.306	1.25	6.07
SG (ε=0.40)	0.125	0.803	0.404	1.07	6.42
SG (ε=0.50)	0.125	0.819	0.500	0.93	6.55
SG (ε=0.60)	0.125	0.803	0.596	0.82	6.42
SG (ε=0.69)	0.125	0.759	0.694	0.72	6.07
SD (ε=0.25)	0.125	0.891	0.252	1.12	7.13
SD (ε=0.38)	0.125	0.986	0.377	0.89	7.89
SD (ε=0.50)	0.125	1.018	0.500	0.75	8.14
SD (ε=0.62)	0.125	0.986	0.623	0.64	7.89
SD (ε=0.75)	0.125	0.891	0.748	0.54	7.13

6.3 Flow properties

When rotations were applied to the TPMS structures, significant changes were observed in the velocity field and the induced pressure drops (shown in Table 15). The one parameter which did not appear to change as a result of the rotations (except due to numerical errors) was the dimensionless permeability, which by definition is a constant property[6] of the porous media (within the Stokes flow regime). The characteristic length was also unaffected by rotation. The tortuosity, normalized mean velocity deviation, and dimensionless pressure drop gradient all showed changes as a direct result of reorientation. For the Schwarz Primitive structure higher T and lower $\bar{u}_{dev}$ were achieved with both rotations (Figure 48) as a result of reducing the ability for fluid to channel through the domain. However, for both the SG and SD rotations T decreased and $\bar{u}_{dev}$ increased when changed from their natural

orientation. This suggests that the performance of the rotated SG and SD would degrade when compared to their natural orientations by increasing the degree of preferential flow through the media.

Table 15. Comparison of flow properties for various rotated TPMS structures with unit cell size 500 µm (before rotation).

Shape	Characteristic Length L_c $[mm^{-1}]$	Flow tortuosity T [-]	Normalized mean u deviation $\bar{u}_{dev}$ [-]	Dimensionless permeability k' [-] x10^{-3}	Bejan number gradient $\dot{Be}$ [-]
SP	0.399	1.031	0.786	5.06	0.204
SP 1R	0.397	1.178	0.599	5.05	0.544
SP 2R	0.396	1.274	0.450	5.07	1.018
SG	0.305	1.240	0.498	5.88	0.362
SG 1R	0.304	1.197	0.535	5.85	1.049
SG 2R	0.300	1.120	0.688	6.00	1.997
SD	0.246	1.287	0.416	5.70	0.897
SD 1R	0.244	1.125	0.671	5.88	2.106
SD 2R	0.241	1.154	0.566	5.84	4.137

In all cases, the $\dot{Be}$ increased when rotations were applied. This should not be misinterpreted as the pressure drop requirements increasing between the rotated geometries of the TPMS, as within the Stokes flow regime the pressure drop through the medium is independent of orientation. It was found that rate of change for the pressure drop per unit length in real units ($\Delta P/L$) [M L^{-1} T^{-2}] for each structure was in fact constant (Figure 50), and that the changes in $\dot{Be}$ were caused by the change in unit cell dimensions. When converting the results from the dimensionless analysis back to physical units the equivalent pressure drops were recovered.

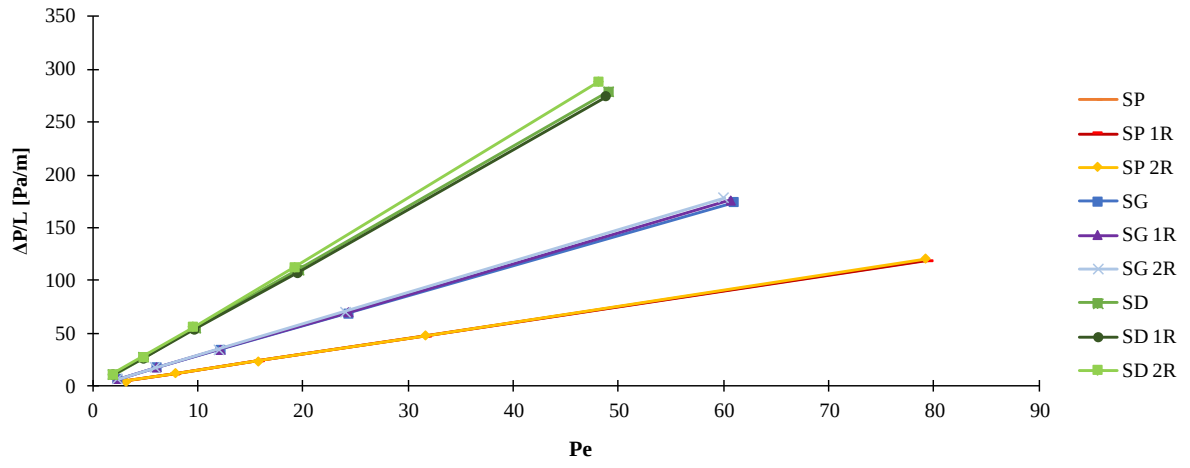

Figure 50. Pressure drop per unit length shown to be constant for the rotated SP, SG, and SD structures.

As differing unit cell sizes were found to influence the rate of change of the Bejan number, it was determined that the dimensional rate of pressure drop change ($\Delta P/(L.Pe)$) [M L^{-2} T^{-1}] would need to be observed for each of the structures observe thus far to confirm the relative performance would be upheld. For equivalent unit cells it was expected the relative order of $\dot{B}e$ would be the same as for the dimensional rate of pressure drop change, but that ranking of the BCC and FCC packing structures may differ. By directly comparing the pressure drop gradients in Figure 51 it was confirmed that the relative pressure drop requirement ranking is maintained for unit cells of equivalent size, and that for elongated unit cells (BCC, FCC, and rotated TPMS) $\dot{B}e$ and $\Delta P/(L.Pe)$ were not equivalent measures. From the dimensional pressure drop rates shown in Figure 51, it can be concluded that the L and D structures are subject to significantly higher pressure drops than originally perceived, and conversely that the BCC and FCC orientations have lower pressure drop requirements.

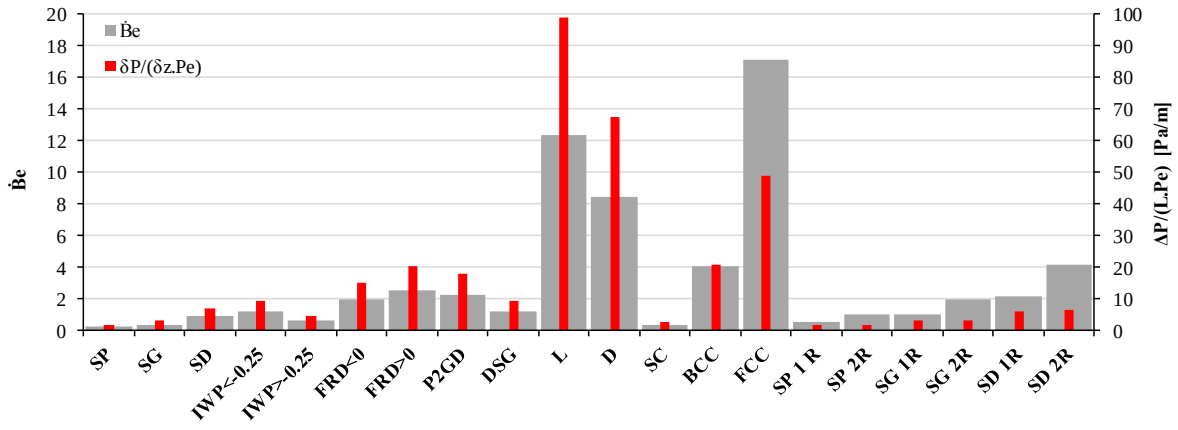

Figure 51. Observing the dimensionless (Ḃe) and dimensional (dP/(dz.Pe)) rates of pressure drop for previously observed geometries.

Table 16 shows the flow properties of the SP, SG, and SD geometries with varied porosity and channel widths. It was found that all of the flow properties shared monotonically increasing or decreasing relationships with porosity. Increasing the channel width (higher ε) resulted in less tortuous velocity profiles as there was less solid media obstructing axial flow. The mean deviated velocity term decreased with porosity. In previous chapters, the dispersion and breakthrough performance were found to be related to these parameters, as the relationship between T and $\bar{u}_{dev}$ was shown to be approximately linear. By visually inspecting the tortuosity and deviated velocity (Figure 52) it was found that varying the porosity caused deviations from an otherwise strong relationship between the two variables when only considering the packed media with 50% porosity (shown with linear regression). It was also found that when varying the porosity for a single TPMS equation, the changes in tortuosity and $\bar{u}_{dev}$ were highly regular.

Table 16. Comparison of flow properties for basic TPMS structures with modified porosity, unit cell size 500 µm.

Shape	Characteristic Length L_c $[mm^{-1}]$	Flow tortuosity T [-]	Normalized mean u deviation $\bar{u}_{dev}$ [-]	Dimensionless permeability k' [-] x10^{-3}	Bejan number gradient $\dot{Be}$ [-]
SP (ε=0.33)	0.290	1.038	0.882	1.93	0.861
SP (ε=0.42)	0.343	1.033	0.837	3.62	0.343
SP (ε=0.50)	0.399	1.031	0.786	5.06	0.204
SP (ε=0.59)	0.481	1.029	0.733	5.83	0.108
SP (ε=0.67)	0.582	1.026	0.664	6.53	0.062
SG (ε=0.31)	0.202	1.307	0.577	3.74	1.225
SG (ε=0.40)	0.251	1.275	0.535	4.86	0.630
SG (ε=0.50)	0.305	1.240	0.498	5.88	0.362
SG (ε=0.60)	0.371	1.202	0.464	6.64	0.209
SG (ε=0.69)	0.457	1.162	0.432	7.14	0.121
SD (ε=0.25)	0.141	1.433	0.472	2.45	6.010
SD (ε=0.38)	0.191	1.356	0.438	4.24	1.665
SD (ε=0.50)	0.246	1.287	0.416	5.70	0.897
SD (ε=0.62)	0.316	1.223	0.389	6.81	0.354
SD (ε=0.75)	0.420	1.160	0.360	7.44	0.167

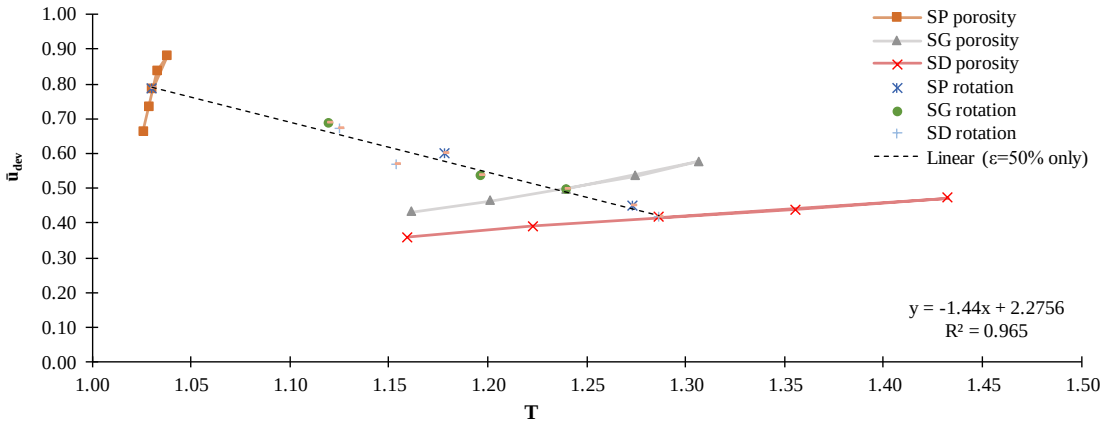

Figure 52. Relating the tortuosity of the flow channel to the normalized mean deviated velocity for rotated and varied porosity SP, SG, and SD structures. Trend line fitted to geometry with 50% porosity only.

Through regression and the rejection of several models, it was determined that T shared a strong correlation to $\bar{u}_{dev}$ when ε with an exponent of 0.25 (Figure 53). Referring back to Table 16 it can be seen that the dimensionless permeability increases and Bejan gradient decreases with higher porosity. This was a direct result of there being wider channels and thus it is becoming easier for the structure to transmit fluid. The same hyperbolic correlation between the characteristic length and $\dot{Be}$ from Chapter 5 was relevant for the manipulated TPMS data (Figure 54). Similarly, the permeability could be related to geometry through the Carman-Kozeny relationship (Equation [80]) and is shown for all TPMS data in Figure 55 (using the axial edge length as L_C).

$$-\frac{dP}{dz} = u_s \frac{c_{CK} \nu \rho}{\Phi^2 L_c^2} \frac{(1-\varepsilon)^2}{\varepsilon^3} \quad [80]$$

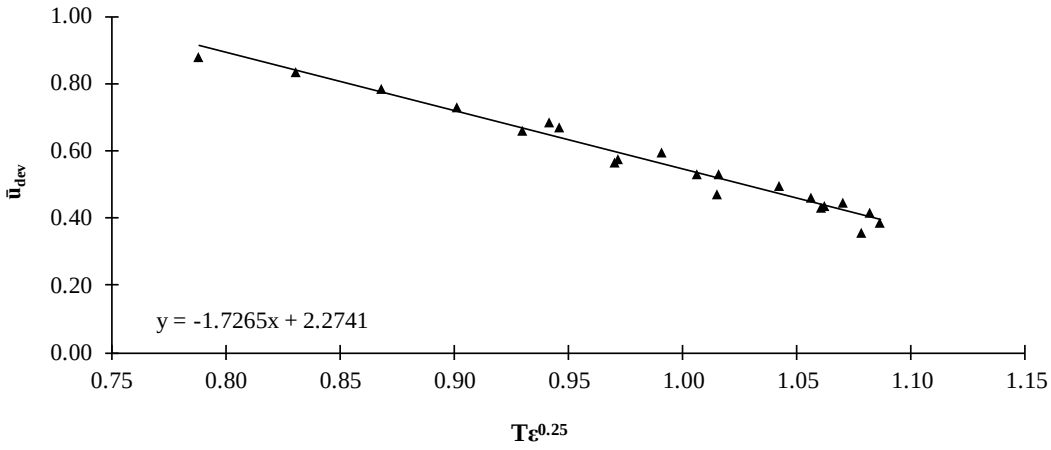

Figure 53. Relating tortuosity and geometry to the normalized mean velocity deviation for manipulated TPMS geometries.

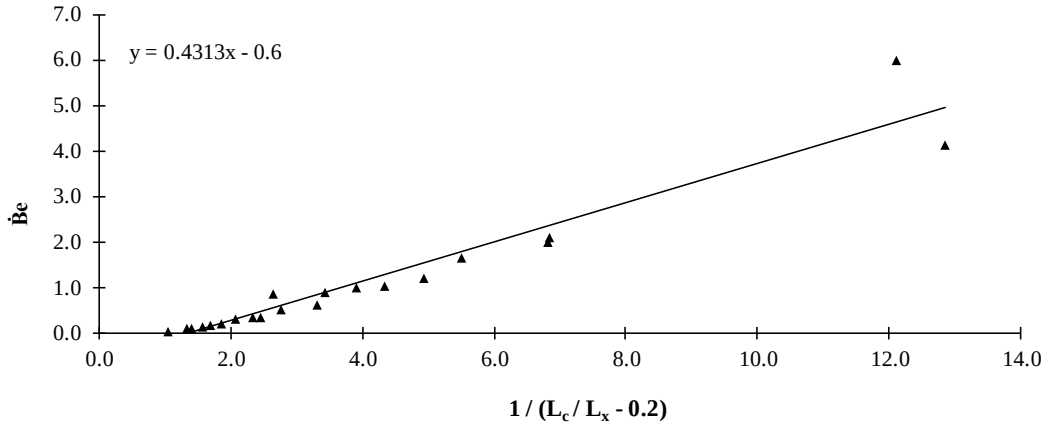

Figure 54. Dimensionless pressure drop related to the characteristic length of the geometry for manipulated TPMS.

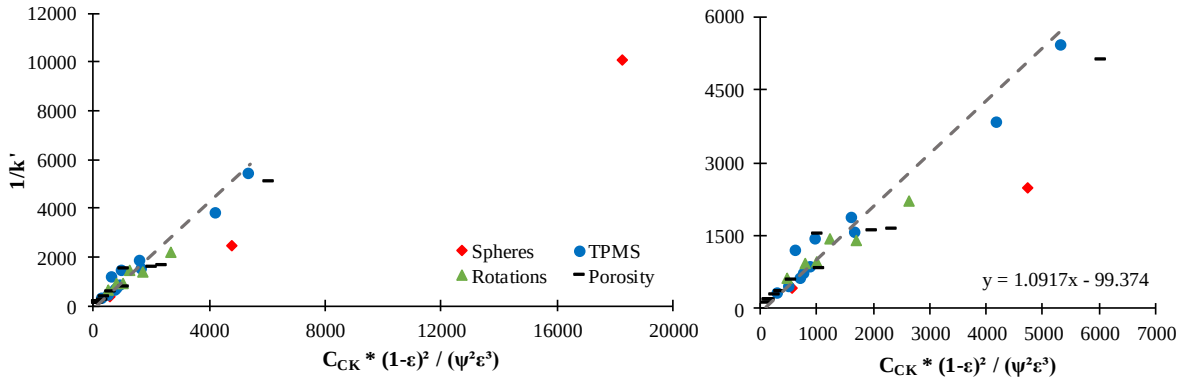

Figure 55. Modified Carman-Kozeny relationship (c_{CK} = 215) between TPMS permeability and geometric factors.

6.4 Dispersion results

The results from conducting the mass transport simulations at different Pe for the rotated geometries are summarized in Figure 56 through Figure 59 for the reduced plate height, inert breakthrough V_D, and adsorption breakthrough V_D and C_D respectively. For the reduced plate height results it was found that the SP geometry underwent a significant improvement through the rotations. In fact, the twice rotated SP geometry was shown to be competitive with the Schwarz Diamond structure in both having a high optimum Pe and achieving a low h_{min}. This was not wholly unexpected, as there was a large reduction in the $\bar{u}_{dev}$ achieved with each rotation. When observing the Schoen Gyroid it was found that applying a single rotation achieved an improvement in h, but applying the two rotations resulted in worse performance. Similarly for the Schwarz Diamond structure, two rotations provided a slight improvement, but a single rotation resulted in worse performance than the original Schwarz Diamond.

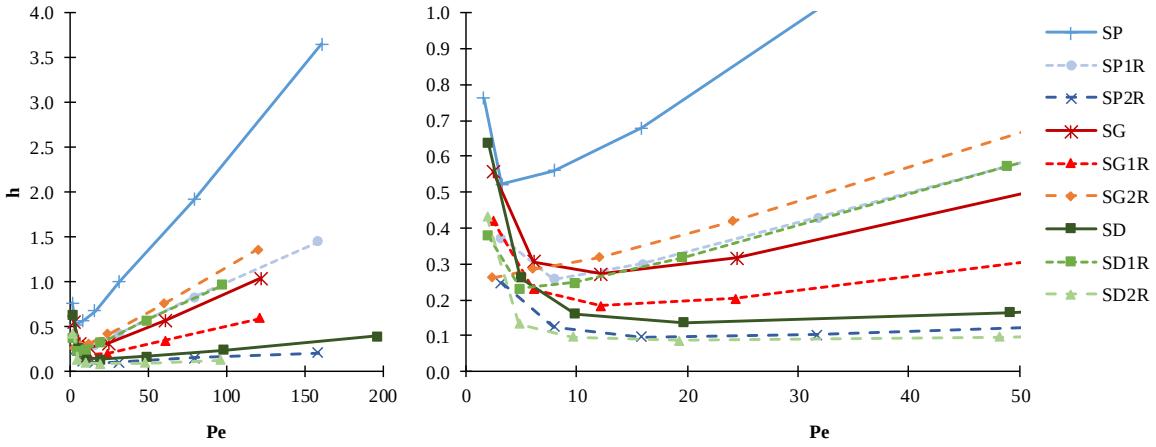

Figure 56. Reduced plate height Van Deemter plots for the rotated SP, SG, and SD geometries.

The minimum plate heights of the SP 2R and SD 2R orientations were found to have the lowest plate heights, and actually were improvements from the SD in its natural orientation. Additionally, the separation impedance for each of these structures was lower suggestion better chromatographic performance, and the SD 2R orientation was able to achieve the same flowrate as the SD with this desirable level of axial dispersion. These findings suggest that determining the best orientation of the unit cell relative to the flow axis can greatly influence the degree of axial dispersion. The natural orientations as they were used in the work are defined arbitrarily by their level set equations, and by no means guarantee an optimal configuration orthogonal to the inlet. While only three orientations were observed for each structure, any combination of rotations could be investigated to determine the optimum orientation of each geometry, but this was outside of the scope of this work and may be the basis of further research. The optimum flow conditions for each structure are summarized in Table 17.

Table 17. Optimum channel Peclet number, minimum reduced plate height, and corresponding separation impedance for rotated TPMS geometries.

Shape	Pe	h_{min}	E
SP	3.2	0.52	27.1
SP 1R	7.9	0.26	6.6
SP 2R	15.9	0.10	0.9
SG	12.2	0.27	6.3
SG 1R	12.2	0.18	2.9
SG 2R	2.4	0.26	5.7
SD	19.7	0.14	1.6
SD 1R	4.9	0.23	4.6
SD 2R	19.3	0.09	0.6

It was concluded that out of the three main orientations observed, the SP and SG structures may show a significant reduction in band broadening when rotated, while the SD structure in its natural and 2R orientations performed well. To further evaluate the rotations, the adsorption characteristics are shown in the next section. The Van Deemter plots from varying the porosity are shown in Figure 57 for each of the SP, SG and SD structures.

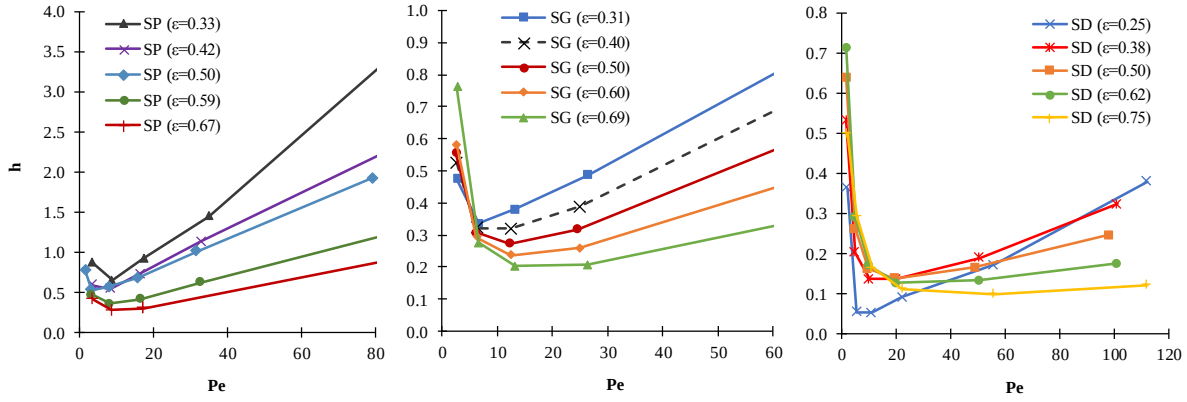

Figure 57. Van Deemter plots for SP, SG, and SD TPMS with varying porosity.

For the case of the SP and SG structures it was clear that increasing the porosity caused a direct reduction of the reduced plate height. This indicated that slight widening of the fluid channels caused less axial dispersion and thus an improvement in chromatographic performance. For all cases, the minimum reduced plate height was also found to occur at a higher Pe when the porosity increased, suggesting that more porous structures would be advantageous both for higher throughputs and for less axial dispersion. This was contradicted only by the case of the SD with a porosity of 25%, which did show a steeper Van Deemter plot and thus poorer performance at high flow rates, but at low flowrates

attained the lowest h value from the data set (0.052). Apart from this one case (which was beyond the porosities examined for the other structures), the SD results followed the same identified trends. It is thought that this result was due to fluid channels being so narrow in the 25% porous SD structure that the tortuous pathways were accentuated and resulted in much less opportunity for channelling to occur. Thus, the solute would have been carried with the curvature of the channels and not had much opportunity to diffuse axially. The optimum dispersion results for the varying porosity geometries are shown in Table 18.

Table 18. Optimum channel Peclet number, minimum reduced plate height, and corresponding separation impedance for basic TPMS structures with modified porosity.

Shape	Pe	h_{min}	E
SP (ε=0.33)	8.7	0.64	6.9
SP (ε=0.42)	8.2	0.54	8.4
SP (ε=0.50)	3.2	0.52	27.1
SP (ε=0.59)	8.2	0.35	11.9
SP (ε=0.67)	8.6	0.28	14.2
SG (ε=0.31)	6.6	0.33	8.8
SG (ε=0.40)	12.5	0.32	10.8
SG (ε=0.50)	12.2	0.27	6.3
SG (ε=0.60)	12.5	0.24	15.9
SG (ε=0.69)	13.2	0.20	19.8
SD (ε=0.25)	11.2	0.05	9.5
SD (ε=0.38)	20.3	0.14	12.7
SD (ε=0.50)	19.7	0.14	1.6
SD (ε=0.62)	20.3	0.13	20.9
SD (ε=0.75)	56.1	0.10	28.3

One other aspect of the dispersion results that was not pursued within this study is the degree to which radial dispersion is influenced by geometry. It may have equal relevance to the design of a laminar adsorption column to understand how the pore network can increase radial dispersion and increase the rate of mass transfer throughout a packed bed without increasing axial dispersion.

6.5 Breakthrough results

The values for the V_D achieved with the rotated TPMS is shown in Figure 58 and was found to mostly display the same relative performance ranking as the dispersion results. The increase in performance afforded by the SP rotations is evident in both the inert and adsorption breakthrough simulations, however neither could outperform the SD in its natural orientation. The improvements in V_D were less pronounced than with h due to the value of V_D being weighted by lead volume of the simulation domain, which is similar to the hydraulic retention time of a practical column. The Peclet number for optimal V_D decreased when simulating adsorption, as was the case with all prior simulations. However, even at the higher flowrates there were noticeable improvements. For example, in the case of the top performing geometry (SD) at an average channel Peclet number of 49.1 the value of V_D for the inert and adsorption simulations were 0.984 and 1.013.

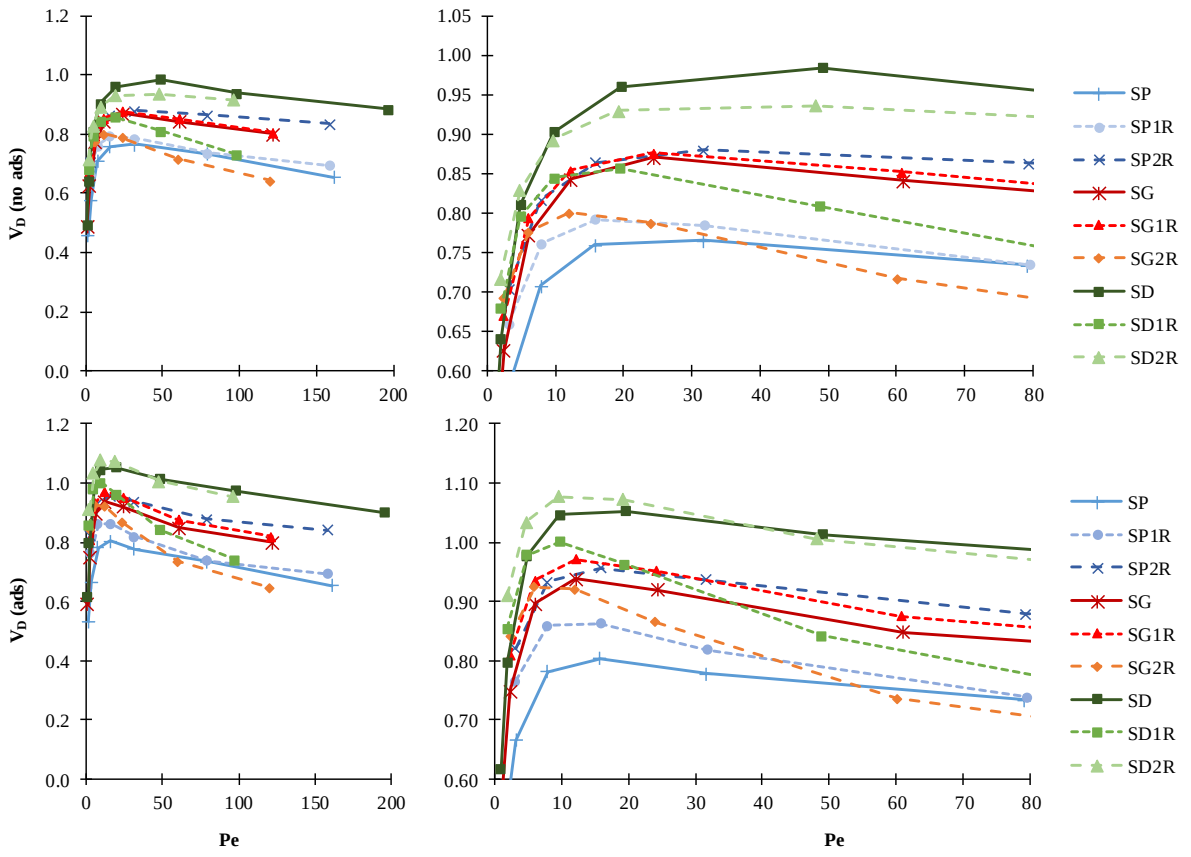

Figure 58. Breakthrough void volumes treated by rotated SP, SG, and SD geometries

The fraction of capacities that were occupied for each of the manipulations showed the SD, SD 2R, and SP 2R media to achieve the most efficient use of adsorptive material prior to the 5% breakthrough observation (Figure 59). The same uptake efficiencies that were observed at high flow rates were mostly

consistent over the full range of Pe observed, and for channel Pe < 20 all geometries achieved at least 20% of capacity occupied, with a fast decline as Pe increased beyond 20. The highest observed V_D and C_D are shown for the rotated TPMS in Table 19.

Table 19. Summary of optimum operating conditions for dimensionless volume and capacity fraction occupied when 5% breakthrough is observed (using k_{ads}=1x10^{-4} s^{-1}, k_{des}=1x10^{-8} mol m^{-3} s^{-1}, specific capacity = 10 mol m^{-3}) for rotated basic TPMS.

Shape	Pe	V_D	Pe	$V_D(ads.)$	Pe	C_D
SP	31.7	0.765	15.8	0.803	1.6	0.267
SP 1R	15.9	0.792	15.9	0.862	3.2	0.298
SP 2R	31.7	0.879	15.9	0.956	3.2	0.316
SG	24.4	0.870	12.2	0.937	2.4	0.293
SG 1R	24.3	0.876	12.2	0.971	6.1	0.276
SG 2R	12.0	0.800	6.0	0.924	2.4	0.308
SD	49.1	0.984	19.7	1.052	4.9	0.311
SD 1R	19.5	0.857	9.8	1.001	2.0	0.304
SD 2R	48.1	0.936	9.6	1.078	9.6	0.333

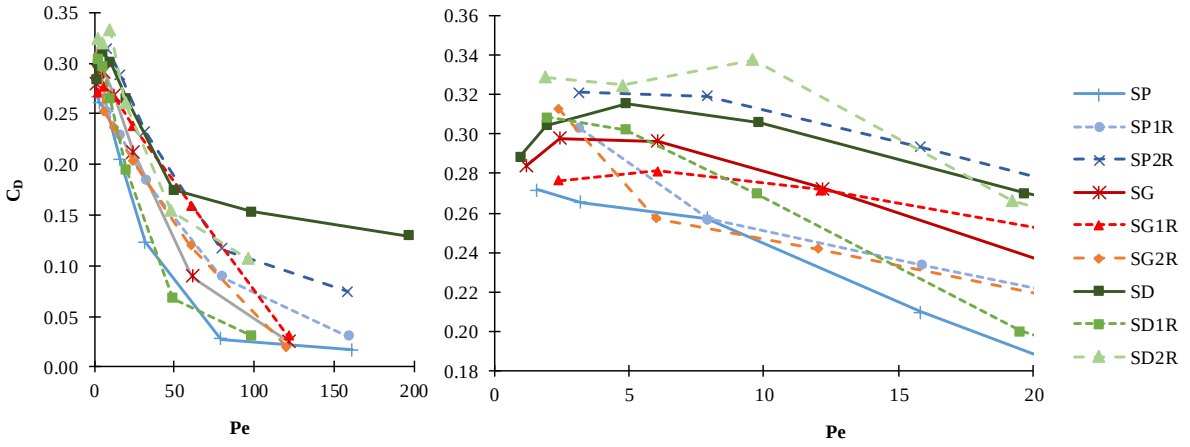

Figure 59. Fraction of capacity occupied by rotated SP, SG, and SD TPMS geometries.

The breakthrough findings for porosity changes were also in keeping with the results from the dispersion tests with SD outperforming SG and SP. Figure 60 shows that the dimensionless void volume that could be eluted consistently increased with higher porosity in both the inert and adsorption simulations. For Peclet above the maximum C_D observed, the fraction of the adsorption capacity occupied was shown to also increase with higher porosities (Figure 61). It was shown that lower porosity structures achieved higher loading as the Pe tends to zero, although operating at such low flowrates would not always be practical for real applications.

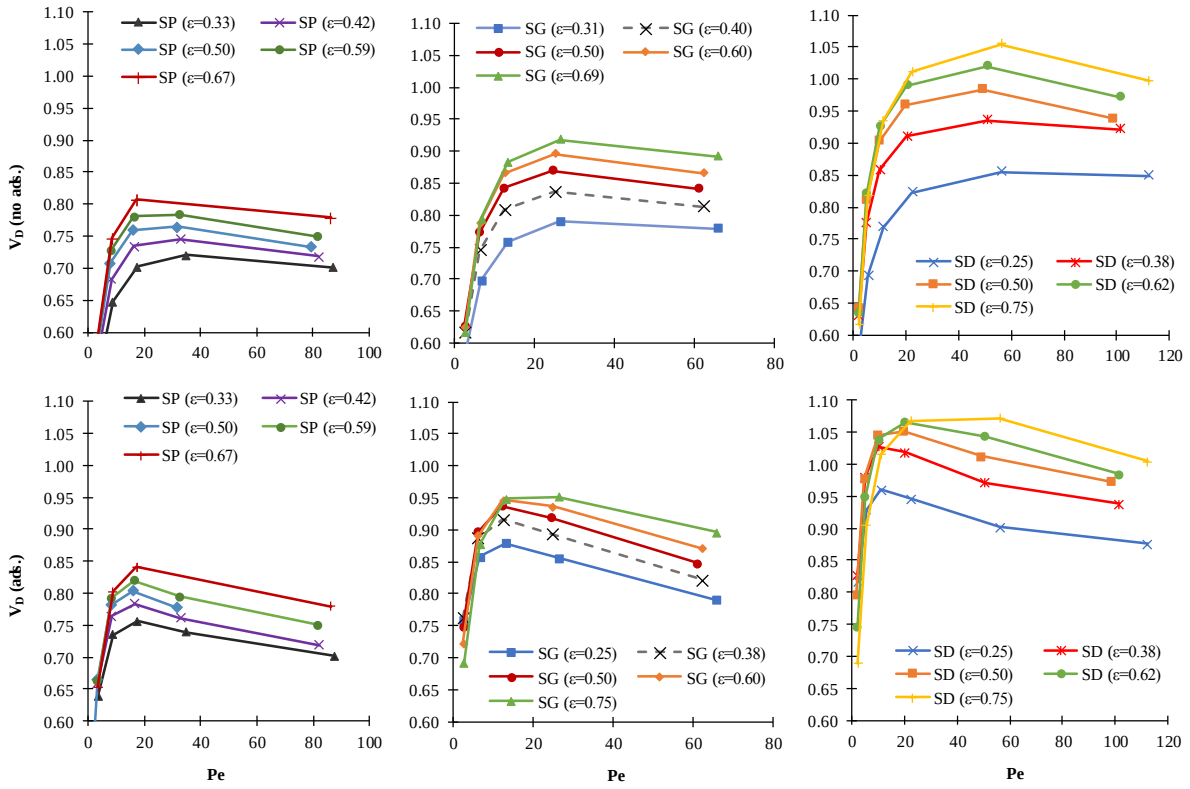

Figure 60. Dimensionless void volumes eluted through columns before breakthrough was observed for the SP, SG, and SD geometries with varying porosity.

It was noted that for ε greater than 50% the profile of the C_D maintained a concave down shape until larger Pe; a property that could be exploited in the design of the adsorption filter. At the lowest porosities the maximum C_D could not be observed within the range of Pe that were investigated, but from the trend in the 25% porous SD data it was conjectured that the maximum would occur at much lower Pe for structures with porosity much lower than those observed in this study ($\varepsilon < 0.25$). It is possible that this would occur at lower flowrates because when the diffusive transport is a more dominant transport force (low Pe), a reduced channel diameter increases the probability of solute coming in contact with the walls through diffusive transport and adsorbing. It was hypothesised that the relationship between the maximum C_D may take the form of a modified hyperbolic curve (depicted in Figure 62), similar to a Van Deemter curve, although without further data this cannot be confirmed. The optimal flowrates to achieve the highest values of V_D and C_D for the different porosity structures is summarized in Table 20. From observing best performance in each category it can be concluded that the base structure (i.e. which TPMS) has a greater effect on the maximum volume and adsorbent utilisation than changing porosity and channel width, as in each case the SD was the highest and SP the lowest.

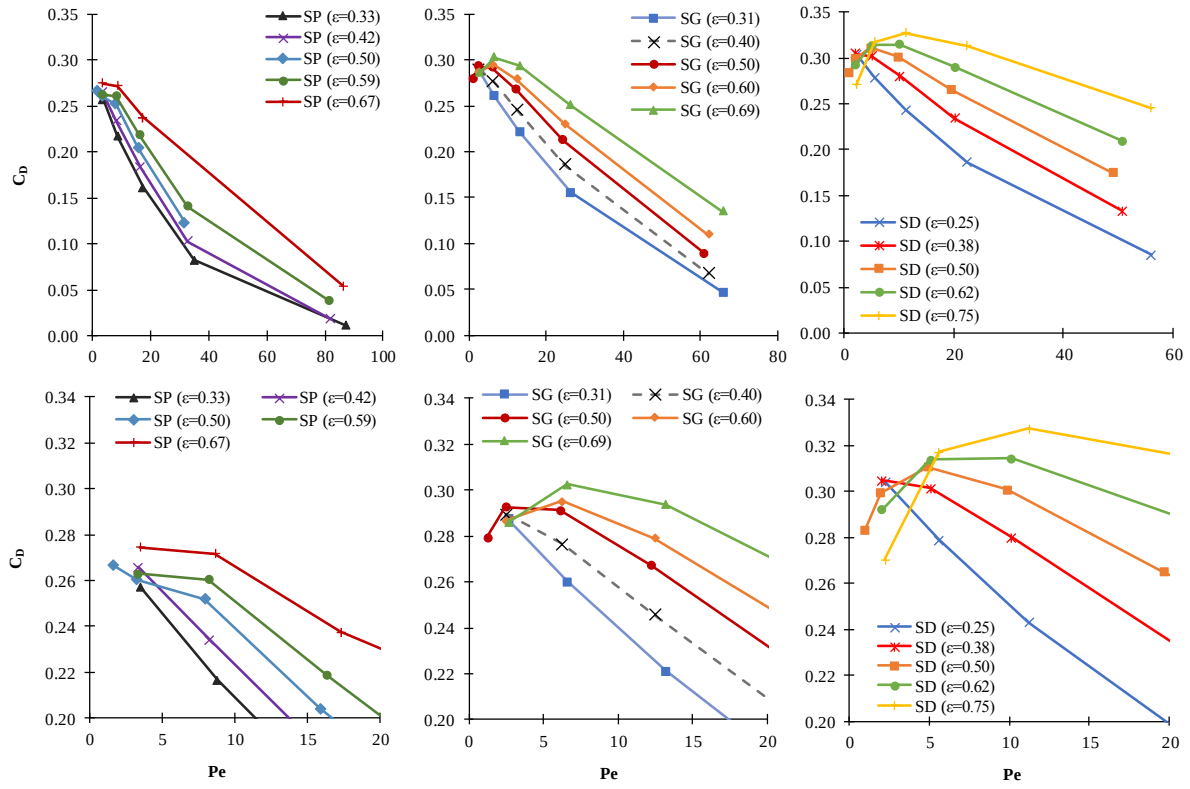

Figure 61. Fraction of capacity filled for the adsorption simulation with porosity varying with the SP, SG, and SD TPMS geometries.

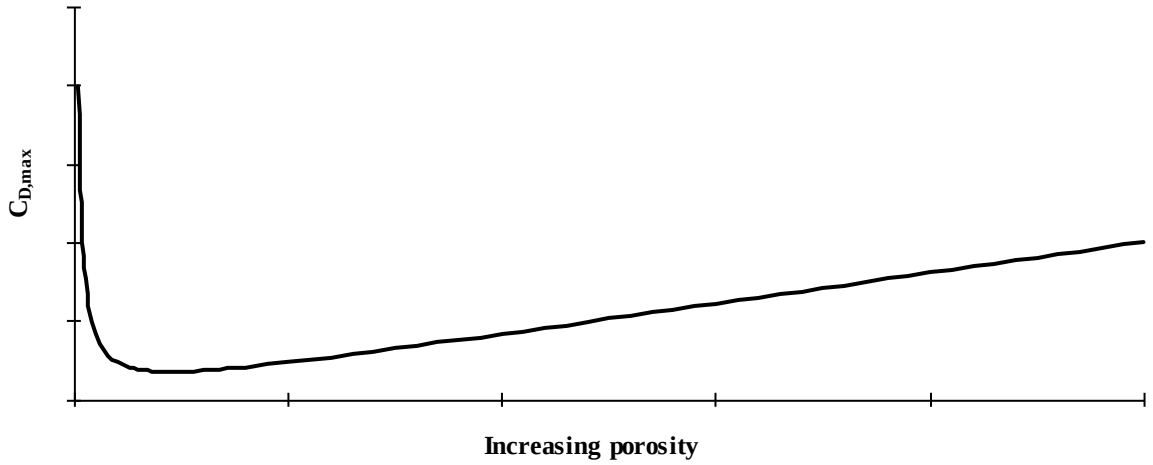

Figure 62. Hypothesised relationship between the maximum capacities that a structure could achieve relative to its porosity, when operated at the optimal Peclet number for each structure and unique porosity.

Table 20. Summary of optimum operating conditions for dimensionless volume and capacity fraction occupied when 5% breakthrough is observed (using k_{ads}=1x10^{-4} s^{-1}, k_{des}=1x10^{-8} mol m^{-3} s^{-1}, specific capacity = 10 mol m^{-3}) for basic TPMS with varying porosity.

Shape	Pe	V_D	Pe	$V_D(ads.)$	Pe	C_D
SP (ε=0.33)	34.9	0.721	17.5	0.756	3.5	0.257
SP (ε=0.42)	32.8	0.745	16.4	0.784	3.3	0.266
SP (ε=0.50)	31.7	0.765	15.8	0.803	1.6	0.267
SP (ε=0.59)	32.7	0.784	16.3	0.819	3.3	0.263
SP (ε=0.67)	17.3	0.807	17.3	0.841	3.5	0.275
SG (ε=0.31)	26.3	0.790	13.2	0.879	2.6	0.288
SG (ε=0.40)	24.9	0.836	12.5	0.916	2.5	0.289
SG (ε=0.50)	24.4	0.870	12.2	0.937	2.4	0.293
SG (ε=0.60)	24.9	0.896	12.5	0.946	6.2	0.295
SG (ε=0.69)	26.3	0.919	26.3	0.952	6.6	0.303
SD (ε=0.25)	56.1	0.855	11.2	0.960	2.2	0.304
SD (ε=0.38)	50.7	0.935	10.1	1.028	2.0	0.305
SD (ε=0.50)	49.1	0.984	19.7	1.052	4.9	0.311
SD (ε=0.62)	50.7	1.020	20.3	1.066	10.1	0.315
SD (ε=0.75)	56.1	1.055	56.1	1.072	11.2	0.327

6.6 Correlations

The rotated TPMS and modified porosity results were plotted against the previously determined correlation between specific surface area and the maximum V_D and C_D values (Figure 63). The results show the new data mostly conformed to the existing trend, although due to a large amount of scattering this trend was more qualitative than quantitative. It is clear from the results of the rotated geometries that the specific surface area alone was not a strong enough predictor of V_D and C_D, as each of the rotations possessed the same specific surface area yet achieved significantly different maximums. The faint correlation between the value of C_D achieved at the maximum V_D was identified for the manipulated TPMS (Figure 64). By plotting these two variables, it is evident that varying the porosity has a much more systematic effect on divergence from the fitted trend, whereas rotations has less predictable influences.

The minimum reduced plate heights for the manipulated TPMS were plotted against the normalized mean deviated velocity terms, and a scattered increasing trend was found (Figure 65). These results also display how rotations and reorientation of the unit cells exhibit a lack of predictable behaviour, while the changes in porosity cause systematic changes in the h_{min} and $\bar{u}_{dev}$ relationship. The direct relationship between the two parameters was determined to be too weak to predict any reduced plate heights with accuracy, and that other characteristics of the unit cells are required to explain and predict the chromatographic performance of each media.

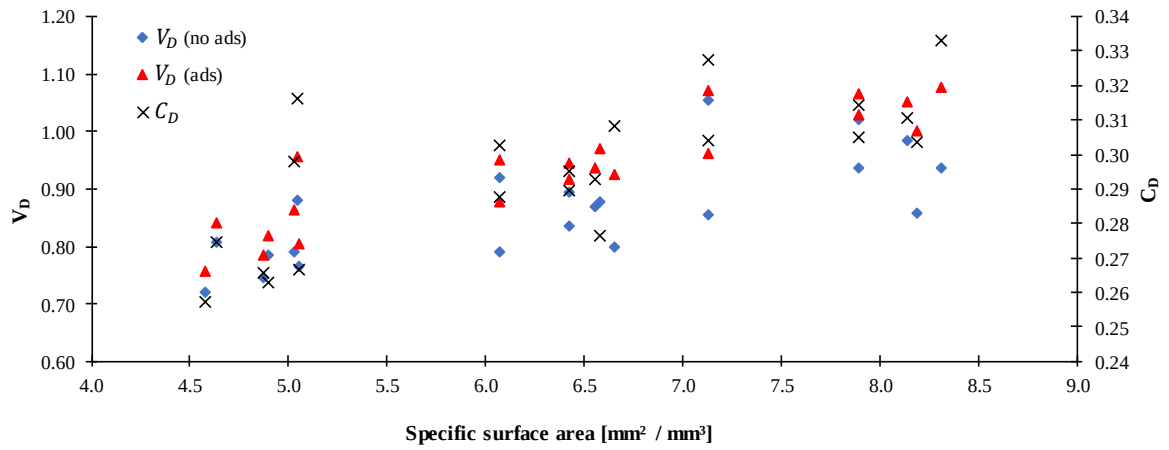

Figure 63. Relationship between adsorptive capacity and the specific surface area for manipulated TPMS.

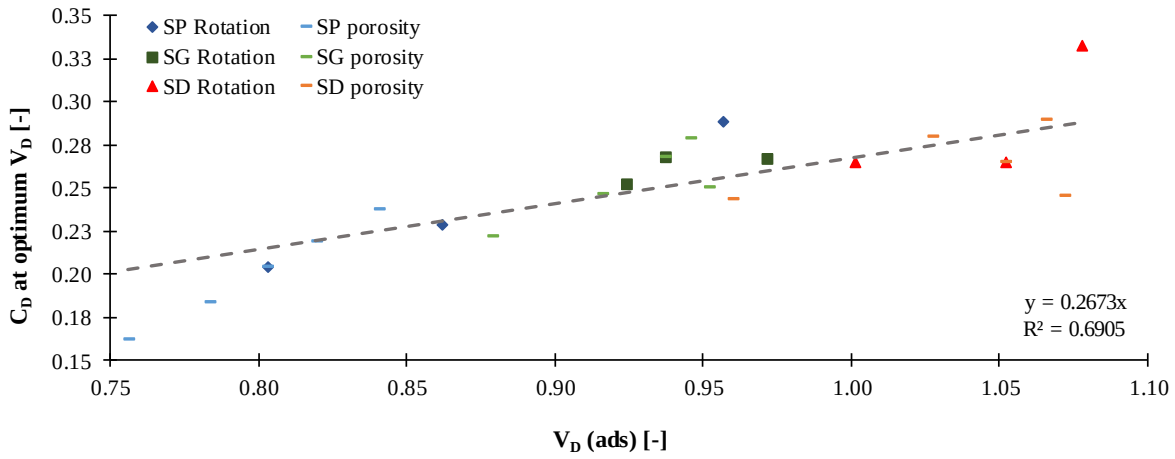

Figure 64. Relating the solute uptake to the optimum V_D flowrate.

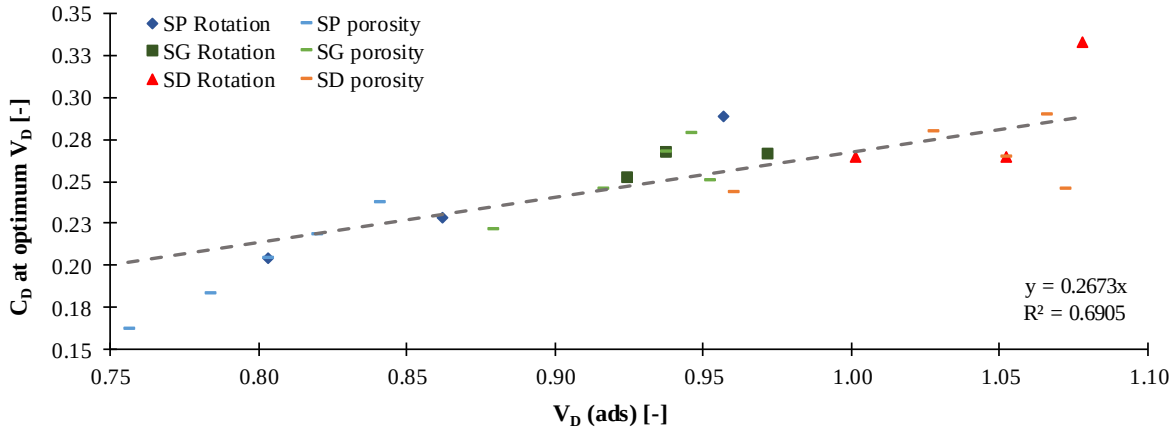

Figure 65. Relating the mean standardized velocity deviation to the minimum reduced plate height.

6.7 Discussion

In addition to exploring the many varied TPMS structures that can be used to define porous networks, a systematic study was performed on how manipulating the solid phase geometry of TPMS influenced mass transport within the fluid phase. The specific manipulations of the geometries explored included rotating the orientation of the material relative to the axis of flow, and varying the porosity of the fluid phase either side of 50%. Rotations were unable to change properties inherent to the solid, such as permeability and specific surface area, but were able to greatly influence the velocity field, as was witnessed when applying two rotations to the Schwarz Primitive structure. In contrast, varying the porosity did change the geometric measures of the unit cell, while also influencing flow properties such as the tortuosity. For the adsorption and breakthrough performance, high specific surface area was desired, and higher radial velocity components were proposed to encourage mass transfer.

Ultimately, it was found that rotations could be used to prevent channelling occurring through a column to reduce axial dispersion and provide better performance in a packed bed adsorption or breakthrough application. It was determined that orientation had a large influence on performance for all three of the SP, SG, and SD structures examined, but it could not quantitatively be determined prior to simulation which orientation was most favourable. Some predictions could be based on visual inspection of the unit cell along the main flow axis by assessing the probability of channelling occurring prior to simulation. Small trial and error simulations such as those conducted in this chapter may offer insight as to which orientations are favourable for specific geometries. For robustness, a numerical technique for relating the orientation to performance is needed to fully exploit orientation as a packed bed design parameter. The ability to determine the best orientation for any periodic geometry was identified as an area of research that could provide significant returns in performance without compromising any other system properties. Techniques such as Random Walking Particle Methods[171], or other simulation techniques which depend on calculating the average surface normal vector visible along the flow axis, could be used in such a study.

From the simulations conducted with varying porosity it was determined that axial dispersion and reduced plate height could be predictably altered with slight changes in TPMS porosity. Higher and lower porosities could be used to achieve lower axial dispersion if applied correctly. The majority of the data indicated that a higher porosity resulted in better chromatographic performance, but in the case of the SD geometry the 25% porous structure had the lowest plate height observed in the data set, although this was achieved at a much lower Pe. To test whether very low porosities were also capable of delivering reduced plate heights, simulations were conducted using SP and SG geometries with porosities of 27% and 24%, respectively (Figure 66). The simulations were carried out with an inlet Peclet number of 5 and the results are summarized in Table 21 (comparing optimum conditions) and Table 22 (all simulations conducted with an inlet Peclet of 5).

*Table 21. Comparison of low porosity and 50% porosity with high porosity SP and SG geometries. *For the SP and SG geometries with low porosities, only an inlet Peclet of 5 was examined, therefore the h may not be the minimum attainable.*

Shape	Pe	h_{min}	$V_{D,max}$	$C_{D,max}$
SP ε=0.27	9.4	0.70	0.714	0.168
SP ε=0.50	3.2	0.52	0.803	0.267
SP ε=0.67	8.6	0.28	0.841	0.275
SG ε=0.24	7.1	0.22	0.810	0.209
SG ε=0.50	12.2	0.27	0.937	0.293
SG ε=0.69	13.2	0.20	0.952	0.303
SD ε=0.25	11.2	0.05	0.960	0.304
SD ε=0.50	19.7	0.14	1.052	0.311
SD ε=0.75	56.1	0.10	1.072	0.327

Table 22. Comparison of low porosity and 50% porosity with high porosity SP and SG geometries. All geometries assessed at an inlet Peclet number of 5.

Shape	Pe	h_{min}	$V_{D,max}$	$C_{D,max}$
SP ε=0.27	9.4	0.70	0.714	0.168
SP ε=0.50	8.0	0.56	0.782	0.252
SP ε=0.67	8.6	0.28	0.803	0.272
SG ε=0.24	7.1	0.22	0.810	0.209
SG ε=0.50	6.1	0.31	0.897	0.291
SG ε=0.69	6.6	0.28	0.877	0.303
SD ε=0.25	5.6	0.05	0.929	0.279
SD ε=0.50	4.9	0.26	0.978	0.311
SD ε=0.75	5.6	0.29	0.905	0.317

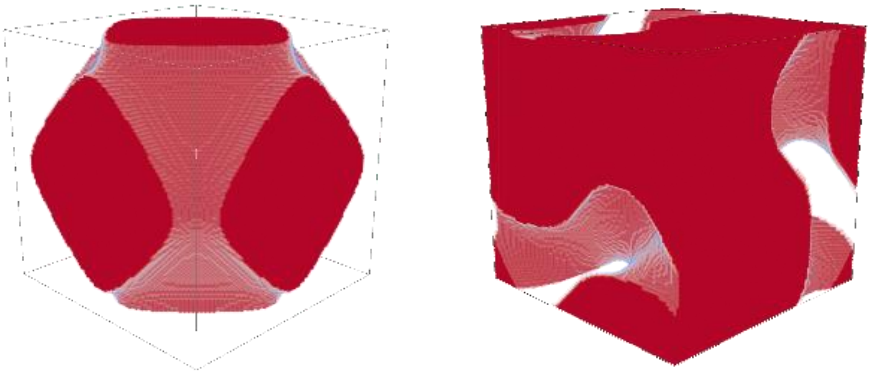

Figure 66. Images of the low porosity SP (left) and SG (right) geometries, with 27% and 24% porosities, respectively.

The results of the additional low porosity simulations showed performance degradation across most metrics, leading to the conclusion that porosity on its own cannot be used to greatly influence results. Even if the low porosity SP and SG were not simulated at their optimal flowrates, when compared against the other porosities at equivalent Peclet they still display less desirable performance. The distribution of solid and fluid space within the unit cell (i.e., the selection of the TPMS) has been proven in each set of tests to be the most important factor in attaining desirable performance, but porosity has been illustrated to have some influence. However, one of the main benefits proposed for using monolithic TPMS in these applications is due to the ability to deliver low plate heights with higher porosity and thus a higher column capacity. As such, it is still recommended that when designing an efficient packed media the porosity be chosen near or above the 50% porosity of the natural structure.

Other possible TPMS manipulations that were not tested within this work include: changing the periodicity of the structure in the radial direction to try increase radial mixing (Figure 67a), bloating specific limbs of the solid phase (Figure 67b), and combining surfaces. Combining TPMS geometries was shown to be possible for similar space groups by Wohlgemuth[15] and was performed in a study of dispersion modelling by Dolamore[8]. Each of these further manipulations are easily achievable by adding numerical constants to the level set equations that define each TPMS, and could be studied to gain further insight into porous bed design. Although, as it has already been alluded to, the packed bed performance relies largely on the TPMS structure itself (distribution of solid phase), and the orientation relative to the flow axis, which makes generalizing findings difficult.

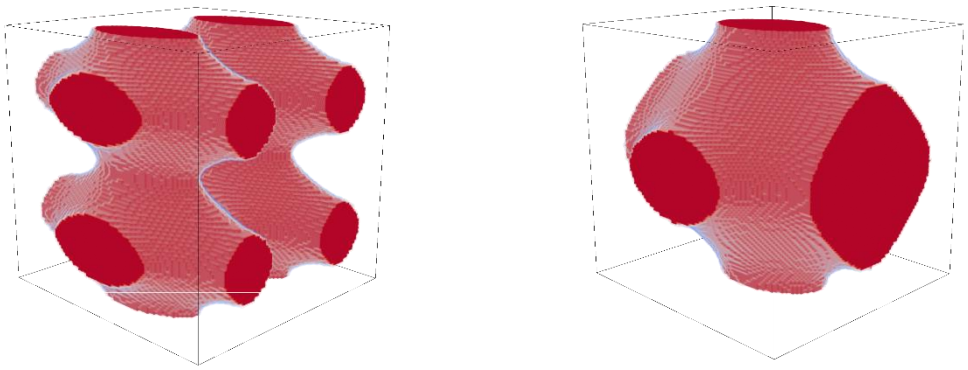

Figure 67. (a) Depiction of modifying unit radial periodicity for the SP structure (left), and (b) bloating a solid limb of the solid structure (right).

Chapter 7 – Practical Considerations for Implementing Results

In addition to comparing the relative performance of each geometry in Chapters 4 to 6, further considerations were made to relate the findings to practical applications. This chapter investigates the accuracy of the heuristics and correlations determined from the previous chapters, the impact of column walls, the effects of changing the adsorption model parameters, and the shape of the solute profile as it moves through a column.

7.1 Heuristics and predictions

Based on the results and heuristics found throughout this work, a final geometry was designed to illustrate the exploitability of each relationship. The learnings from each chapter were used to guide the selection of a new modified geometry, intended to show minimal axial dispersion and possess enhanced adsorption characteristics. The new geometry was based on one of the TPMS examined in Chapter 5 and was manipulated with modifications derived from Chapter 6. In addition to designing an enhanced geometry, the geometric and flow properties ($a, \Psi, L_c, T, \bar{u}_{dev}$) were then used to predict the mass transport measures (h_{min}, V_D, C_D) from the identified correlations. The predictions were then compared with simulation results.

7.1.1 Summary of correlations

Throughout each chapter, attempts to generalize relationships between the geometry, flow field, and column performance were made. Some correlations were strong, such as the relationship between tortuosity and the normalized mean velocity deviation, but many showed significant scatter or were only applicable to subsets of data. Before selecting a new geometry and making predictions about its performance, these correlations were reformulated using the data collected from all simulations (including the naturally oriented TPMS, rotated TPMS, and TPMS with varying porosity). The strongest relationships between the geometry, flow field, pressure drop, dispersion, and breakthrough performance are summarized in Figures 68 – 72, and additional relationships can be found in Appendix C. Many of the correlations were determined through parameter fitting processes. Additionally, the sphere arrangements were excluded from the generalizations as they did not fit the same trends as the TPMS structures, and are seen in the plots as outliers.

Figure 68 shows a prominent relationship between the tortuosity, geometry, and the normalized mean standard deviation for a periodic unit cell. In searching through the data, it was determined that no strong correlations existed between solely the geometric parameters or flow properties and the

performance of each structure, confirming that neither measure could be used to fully describe or predict improvements. A combination of the geometry and flow measures offered a more complete description of the system, and thus provided stronger correlations. Figure 69 displays a correlation between the geometry, flow properties, and minimum reduced plate height. However, this relationship was too weak to make accurate predictions of h_{min}. It was also found that the rotated structures were the least conforming. In Figure 70 the relationship between the flow and geometry of a unit cell was related to the breakthrough performance measures, although a significant spread could be observed in the data. The characteristic length (L_c) of each unit cell was normalized by the axial edge length of the unit cell (L_x) to remove the dimensional dependency.

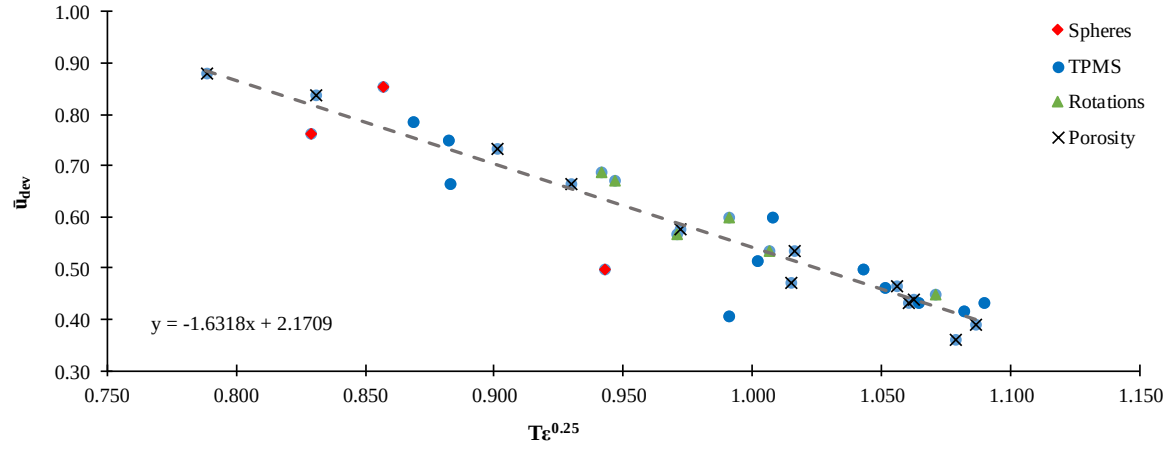

Figure 68. Correlation between the tortuosity and geometric properties of the media and the normalized mean deviated velocity.

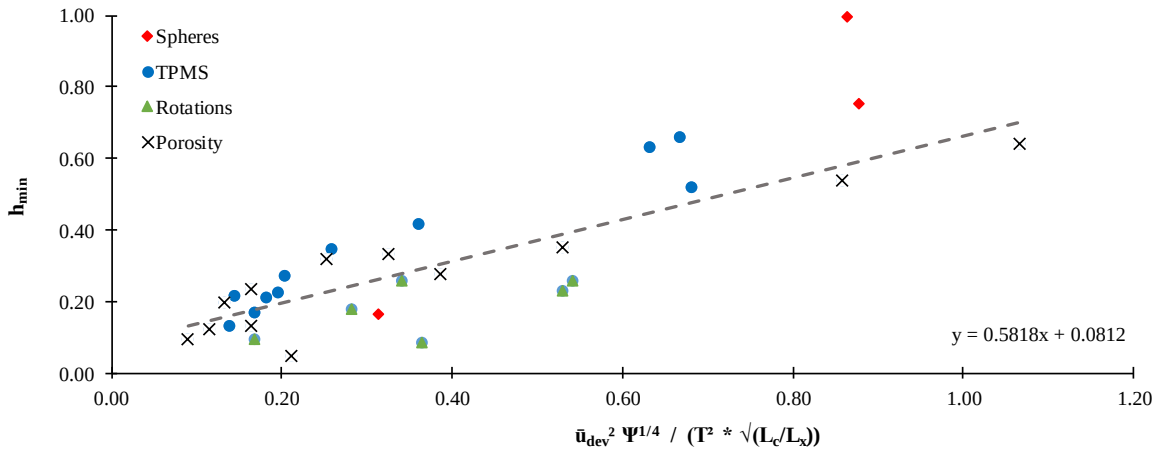

Figure 69. Relating the geometry and flow field parameters to the minimum reduced plate height.

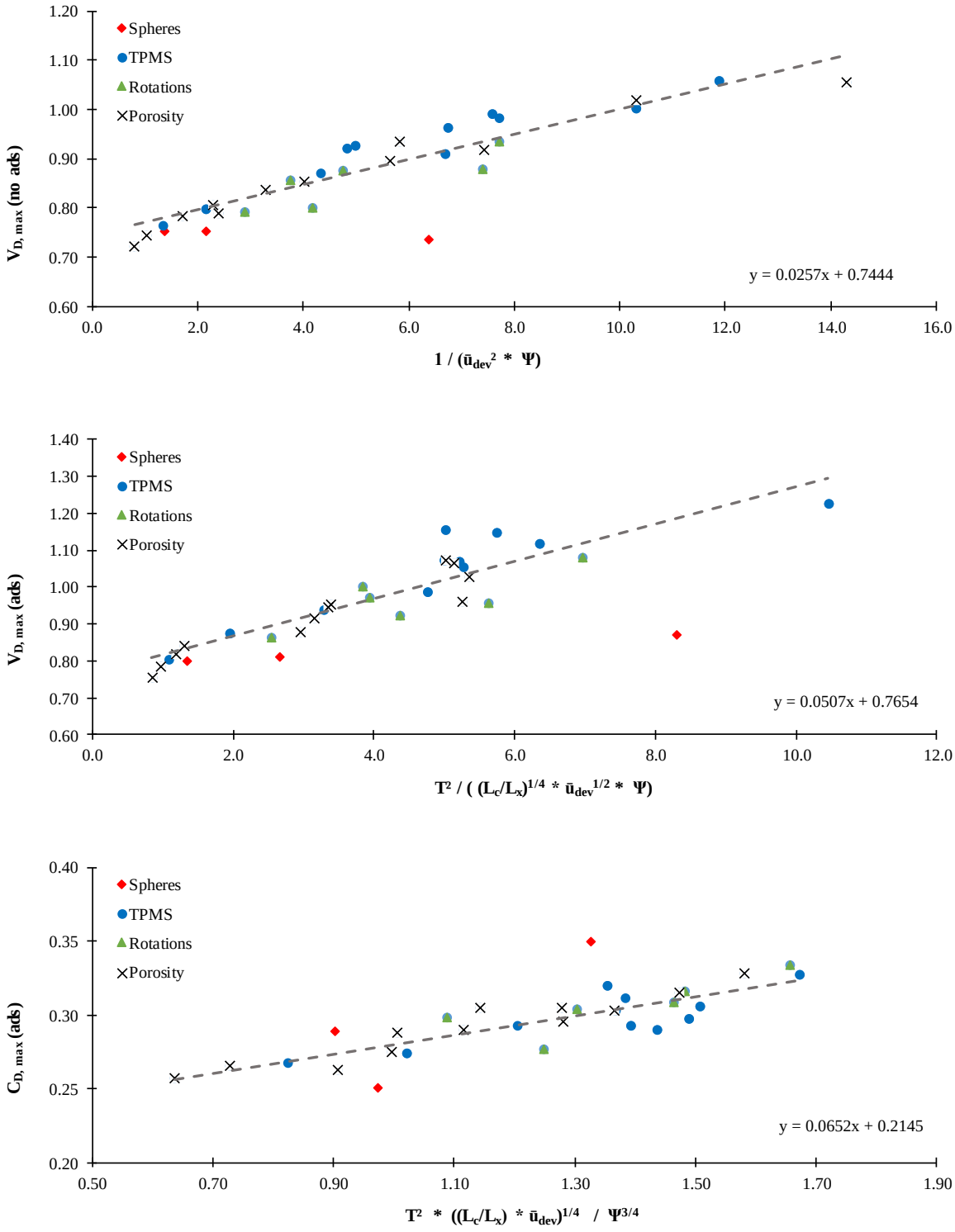

Figure 70. Correlations between the geometric and flow properties of TPMS unit cells, and the maximum breakthrough performance measures V_D and C_D. (Top to bottom) Inert breakthrough V_D, adsorption V_D, adsorption C_D.

The dimensionless pressure drop gradient and permeability were related to geometry of a unit cell in Figures 71 and 72 respectively, and in both cases strong correlations were found. These relationships verified that the range of *Pe* observed were highly laminar and within the Stokes regime, as permeability

and pressure drop increased with Pe. Figure 71 relates the normalized characteristic length of a unit cell to $\dot{B}e$ through an adjusted hyperbolic function, where the translation of 0.2 related to the minimum L_c/L_x observed from the TPMS data set. In Figure 72 the dimensionless permeability was calculated using the axial unit cell length to reduce the dimensions of k, thus allowing a good fit when using the modified Carman-Kozeny[82] equation from Chapter 5.

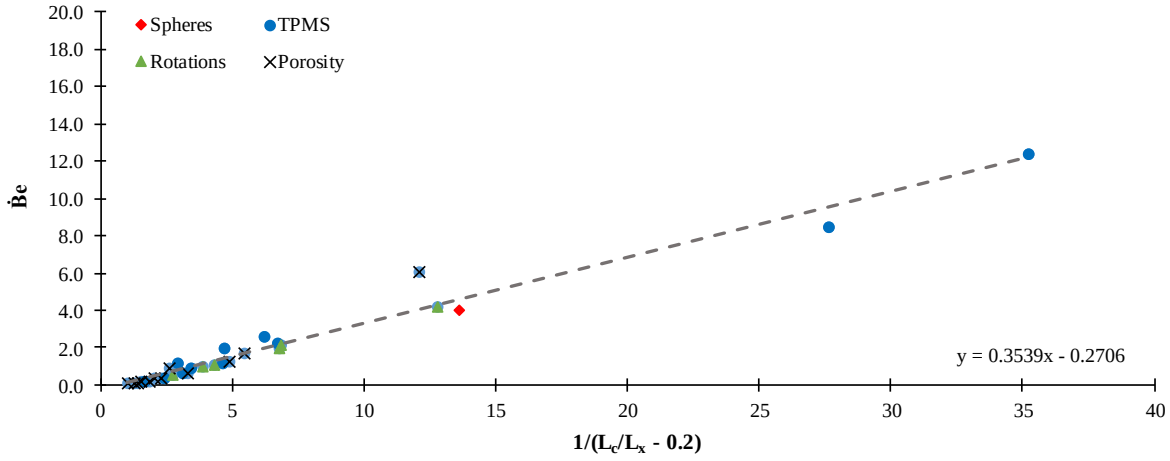

Figure 71. Pressure drop gradient (Ḃe) related to the normalized characteristic length. Sphere packing excluded from the fitted trend.

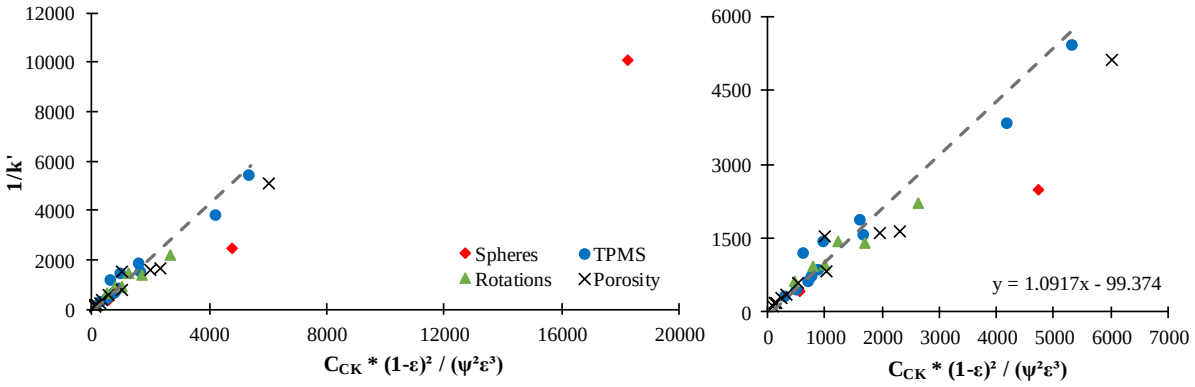

Figure 72. Fitting TPMS data to the Carman-Kozeny equation using a constant c_{CK} of 215, using the dimensionless permeability reduced by using the axial length of the unit cell. Sphere packing excluded from the fitted trend.

Many of the alternative relationships shown in Appendix C relate the performance metrics solely to the geometric parameters, as this would be the most useful type of correlation to use in selecting potential enhanced packing structures. Unfortunately, none of the generalized relationships were deemed strong enough for use in designing porous media. However, they did reveal that a geometry with a higher specific surface area was likely to provide higher values of V_D and C_D.

7.1.2 Predicting improved performance

An effective bed geometry was developed by exploiting the bed characteristics known to relate to higher performance. As it had been identified that a higher specific surface area increased the adsorption capacity, the scope was therefore limited to geometries with moderate or high specific surface area, excluding the SP, SG, and IWP surfaces from contention. Secondly, it was decided that the L and D surfaces had high pressure drop requirements and thus they were eliminated due to the practical implications (despite possessing the highest specific surface areas of the TPMS examined). For the remaining geometries (SD, FRD, P2GD, DSG) the separation impedance, dispersion, and breakthrough characteristics were considered. The SD and DSG geometries were determined to be the base structures that had the most potential to provide improved performance.

For both the SD and DSG geometries, it was expected that there would be less axial dispersion at higher porosities (a claim that was proven for the SD case in Chapter 6). The ability to use high packed bed porosities is an exploitable trait of using monoliths, whereas in particle packed columns typical bed porosities[206] range from 30-60%. A high target porosity was decided to be ~80% as this produced thin 'sheets' of solid phase. Exceeding this would approach printable resolution limitations, or may affect the structural integrity in real systems. After setting the target porosity, the best orientation to use (natural, 1R, 2R) was considered. The best performance was expected to be obtained from either the SD in its natural or 2R orientation, or from the DSG surface in any of the three possible orientations. Without knowing the effect rotations would have on the channelling through the DSG structure, it was difficult to predict whether they would improve performance. By considering that without rotation the DSG possessed T and $\bar{u}_{dev}$ values of 1.14 and 0.408 respectively, there was scope to improve the tortuosity (which ranged from 1.0 – 1.4), but the velocity field was already largely homogenized (typically ranging from 0.36 – 0.9). Before conducting mass transfer simulations, the geometric and flow properties for the DSG 1R and DSG 2R (Figure 73) were calculated and are summarized in Table 23.

Table 23. Geometric properties for the selected top geometries with a unit cell edge length of 500 µm.

Shape	**Porosity** ε [-]	**Sphericity** Ψ [-]	**Specific surface area** a [mm^{-1}]	**Characteristic length** L_c [mm]	**Tortuosity** T [-]	**Normalized mean** u **deviation** $\dot{u}_{dev}$ [-]
SD	0.500	0.748	8.14	0.246	1.287	0.416
SD 2R	0.500	0.404	8.31	0.241	1.154	0.566
DSG	0.567	0.506	10.95	0.207	1.142	0.408
DSG 1R	0.568	0.397	11.07	0.205	1.132	0.429
DSG 2R	0.567	0.272	11.22	0.202	1.113	0.463

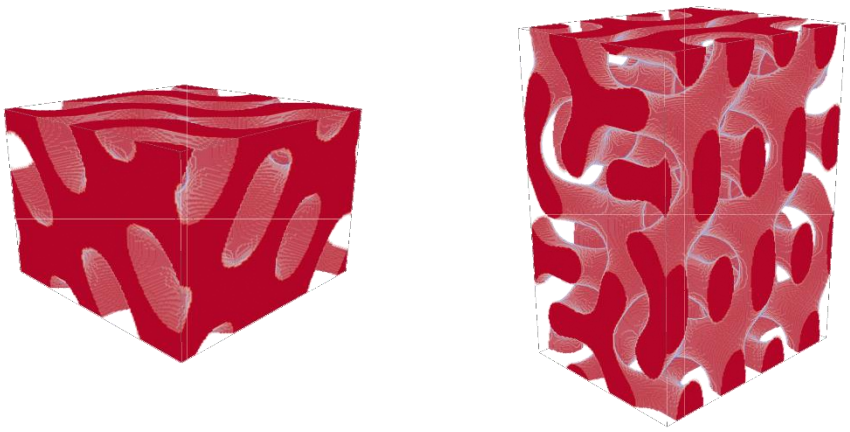

Figure 73. Depiction of the rotated DSG 1R (left) and DSG 2R (right) geometries.

The pressure drop ($\dot{B}e,\ k'$), dispersion (h_{min}), and adsorption metrics (V_D, C_D) were then compared according to Table 24. The properties for the DSG 1R and DSG 2R structures were estimated from the correlations outlined in Section 7.1.1. The DSG geometries were expected to be attain higher adsorption parameters while the SD geometries showed lower axial dispersion.

Table 24. Geometric properties for the selected top geometries. Quantities denoted with were determined used the correlations found in Section 7.1.1.*

Shape	Bejan slope $\dot{B}e$	Permeability k' x10^{-3}	Reduced plate height h_{min}	Void volume (inert) $V_{D,max}\ (no\ ads)$	Void volume (adsorption) $V_{D,max}\ (ads)$	Capacity fraction $C_{D,max}$
SD	0.90	5.70	0.137	0.984	1.052	0.311
SD 2R	4.14	5.84	0.086	0.936	1.078	0.333
DSG	1.17	5.28	0.170	1.057	1.147	0.293
DSG 1R*	1.41	8.36	0.204	1.096	1.106	0.314
DSG 2R*	1.46	5.78	0.232	1.185	1.254	0.338

Despite the predicted values for the rotated DSG orientations suggesting better performance, in Chapter 6 the effects of orientation were shown to be unpredictable only considering the large rotations of the Miller indices orientations. Given that the rotated DSG structures had less favourable tortuosity and normalized mean deviated velocity terms than the natural DSG, the DSG 1R and DSG 2R configurations were eliminated from consideration. Ultimately it was decided that the DSG orientation would be tested with a higher porosity, as the SD structure had already been largely explored (although the SD 2R with high porosity was also expected to improve upon the structures already explored). However, when assessing the DSG geometry at ~80% porosity it became apparent that the specific distribution of solid material would allow a significant amount of channelling, and an alternative porosity of approximately 64% was nominated. Both modifications are shown in Figure 74.

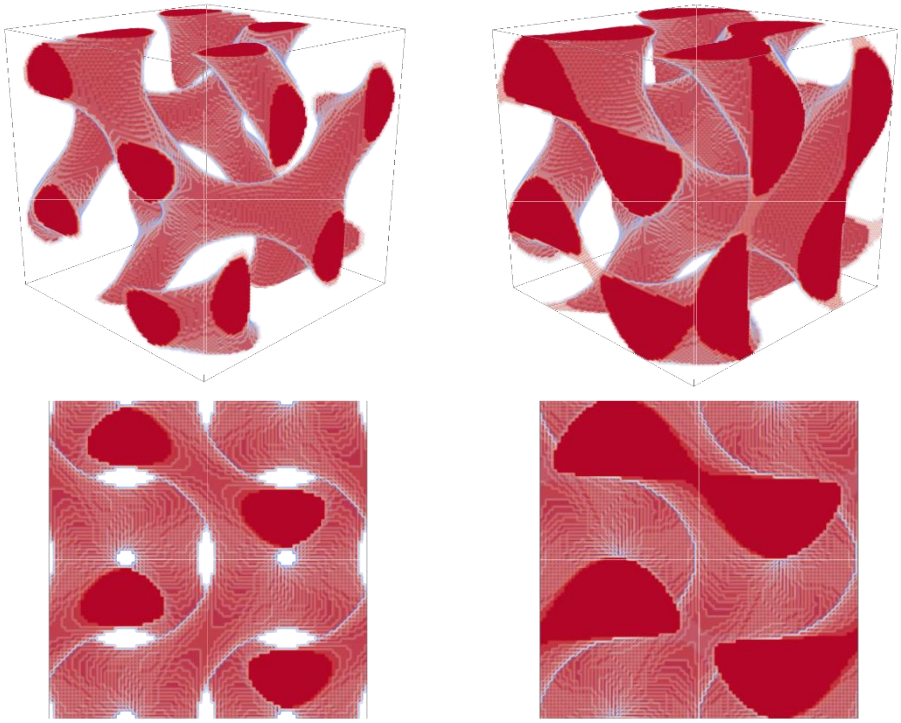

Figure 74. Depiction of the DSG unit cell with (left) ~80% porosity and (right) ~64% porosity. Top row images are the projected 3D views, and the bottom row displays the views along the axial direction.

Each of the performance measures from the enhanced geometry simulation (DSG, ε = 0.64) were compared to all other structures, with the performance of the modified and unmodified DSG highlighted (Figure 75). The modified DSG structure was shown to have one of the most desirable Van Deemter curves, and achieved the highest V_D values for the inert breakthrough simulation. In the adsorption simulations the designed geometry was also seen to have the highest V_D at higher flowrates. The maximum capacity fractions occupied by the new DSG manipulation did not excel when compared to rest of the geometries, but an improvement upon the natural DSG was achieved. The results were also compared with the predictions obtained using the correlations from Section 7.1.1 (Table 25), but revealed significant discrepancies. These were attributed to the scatter of the data, therefore confirming that the relationships could not be used as accurate prediction tools, and only for qualitative guidance.

Table 25. Predictions and simulation results for the DSG (ε = 0.64) geometry.

Method	**Bejan slope** $\dot{Be}$	**Permeability** k' **x10^{-3}**	**Reduced plate height** h_{min}	**Void volume (inert)** $V_{D,max}\ (no\ a.)$	**Void volume (adsorption)** $V_{D,max}\ (ads)$	**Capacity fraction** $C_{D,max}$
Prediction	0.917	9.64	0.165	1.086	1.020	0.310
Result	0.685	7.38	0.121	1.073	1.139	0.292

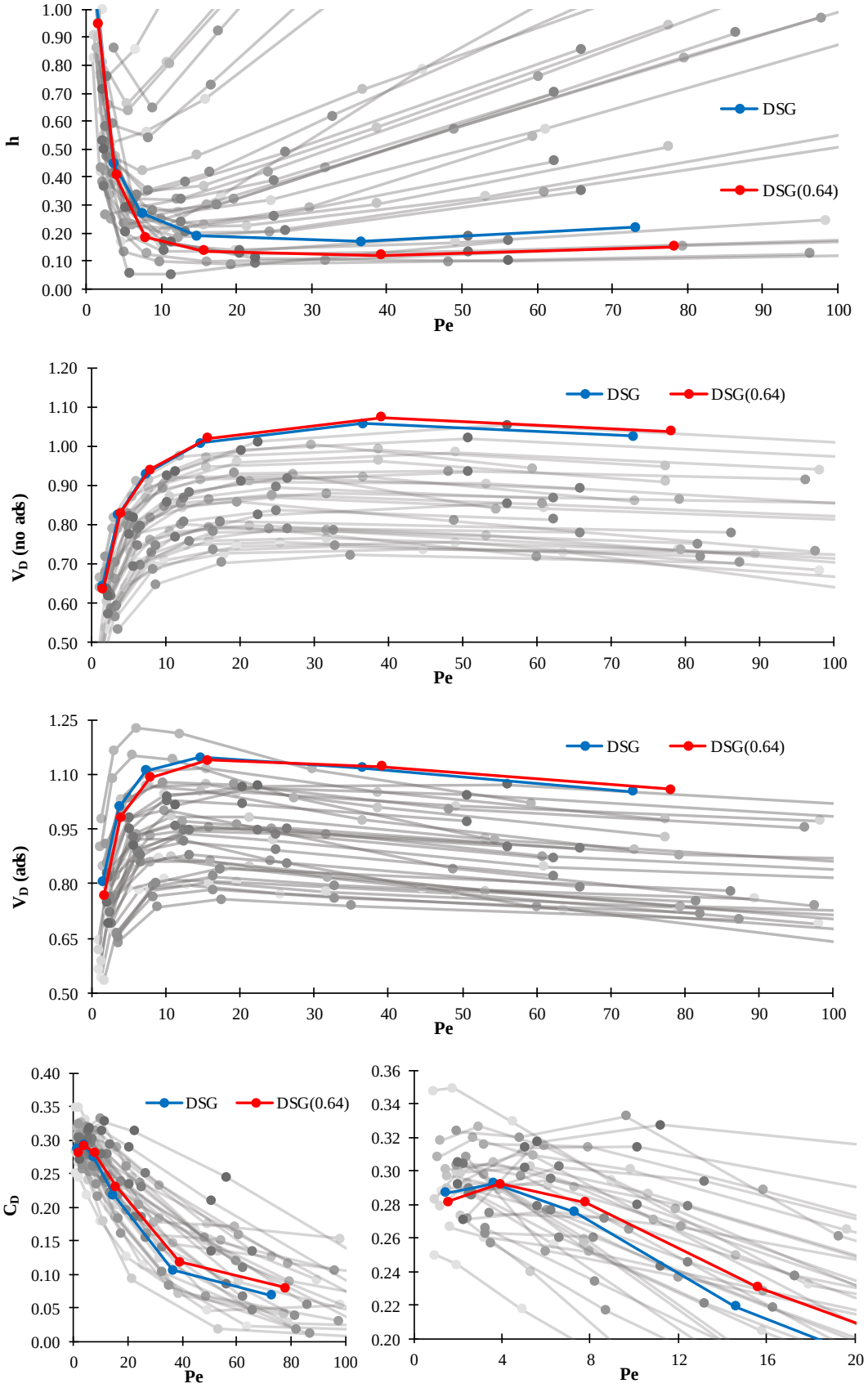

Figure 75. Comparison of modified DSG (ε=0.64) geometry with natural DSG and all other geometries. Top to bottom; Reduced plate height, dimensionless void volumes, and fraction of capacity at various Peclet numbers

7.1.3 Evaluation

Ultimately, the knowledge of how packed bed geometry influences column flow and adsorption phenomena was successfully used to develop an enhanced packed bed media. The solid distribution and channel structures were harnessed to provide performance that, while not optimal, was enhanced from the original structures. The ability to predict specific performance measures was severely limited by the scatter of the data used to formulate general trends, although qualitative predictions were possible. The general heuristics that were developed throughout this study include the following guidelines;

- A higher specific surface area will allow for greater dimensionless volumes to be treated, and a higher C_D to be achieved at the breakthrough.
- Within the Stokes flow regime the geometry of the structure (such as lower porosity) can be directly related to the pressure gradient requirements according to the correlations identified (with reasonable accuracy).
- Reductions in column channelling will reduce axial dispersion and increase the breakthrough performance. This may be partially assessed through high tortuosity and low normalized mean deviated velocities, where major changes toward favourable T and $\bar{u}_{dev}$ were likely to show improved performance.
- Each geometry will have an optimal orientation relative to the main axis of flow that will reduce channelling and axial dispersion, and increase mass transfer phenomena. A visual assessment paired with inspection of the T and $\bar{u}_{dev}$ values may be used as a screening method to differentiate between possible orientations.

Part of the difficulty in creating the generalized trends is because each TPMS is vastly different in structure from any other. The fluid space and flow properties pertaining to any one structure may vary greatly from others despite having similar geometric measures (a, Ψ, L_c). Relationships that are more accurate were obtained when considering reduced geometry sets, and limiting the scope of each relationship. For example, within the families of the SP, SG, and SD geometries, it was observed that changing the porosity altered each measure of performance in a very systematic manner. These relationships could be used to form much stronger predictions for a given structure, and used to enhance that structure to meet operating requirements (pressure drop, throughput, capacity, etc.).

7.2 Effects of column walls

To investigate the minimum column size that could approximate an 'infinitely wide' column, a series of simulations were conducted where cylindrical bounding walls were included, thus causing 'wall effects' to be captured within the simulations. It has been reported by Knox et al. that when using ordered sphere particles, a particle to column diameter ratio of approximately 60 is required to negate wall effects and recover 'periodic' behaviour within the packed column[12]. For randomly oriented spheres Maier et al. suggests this ratio is closer to 100[207]. For TPMS (or equivalent monolithic structures) no equivalent ratio exists, therefore these figures were used as guidelines within these investigations. The simulations were conducted using the Schwarz Diamond TPMS at 50% porosity with an inlet Peclet number of 20. The geometries consisted of a cylindrical domain with a diameter equivalent to an integer number of unit cells, and an axial length that consisted of; a single entrance length, two entry cells, a periodic unit cell, two exit cells, and two exit lengths. The geometry for a four unit cell diameter column with wall is shown in Figure 76 below.

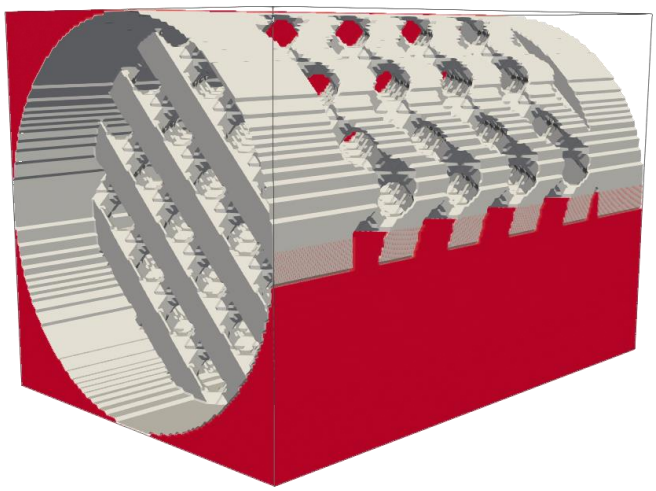

Figure 76. Depiction of a column domain, surfaces shown by grey and solid (with cutaway quadrant) represented in red.

Due to the large increases in the computational resources required to model these domain sizes, simulations could only be conducted for diameters equivalent to 4, 6, 8 and 10 unit cells. It was decided that the results from the periodic simulation for SD with a Peclet number of 20 could represent a column with 30 unit cells diameter (based on the findings for a column of 60 spheres by Knox et al.) as the TPMS structure possessed twice as many fluid channels per unit cell. The results are shown in Figure 77, where the reduced plate heights, dimensionless void volumes and capacity fractions for different width columns were compared to the periodic unit cell.

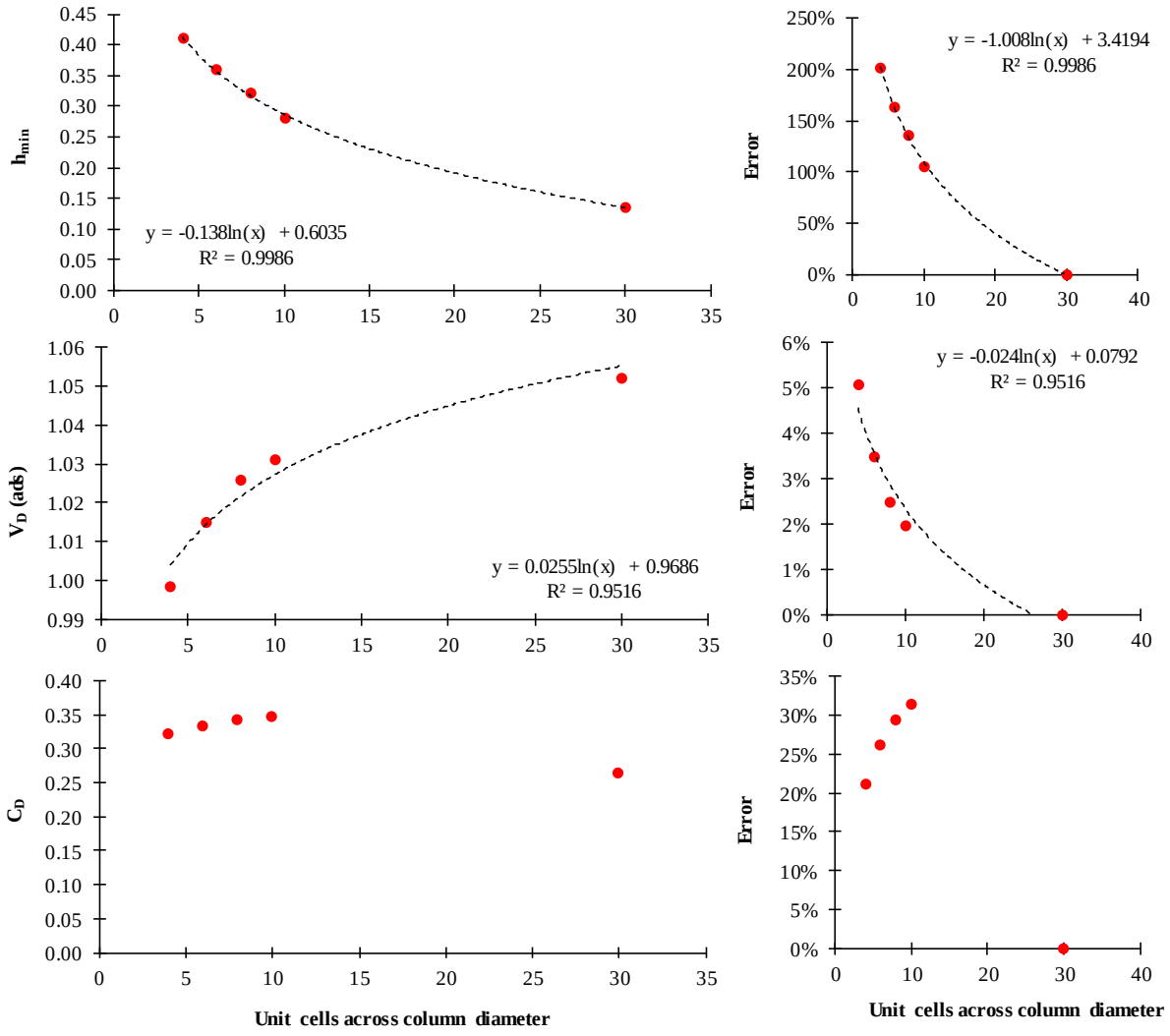

Figure 77. Plots of the error in h_{min}, V_D, and C_D caused by wall effects when comparing with the periodic unit cell data. Generated using the SD geometry with a Peclet number of 20 at the inlet.

The reduced plate height and capacity fraction were greatly affected by the presence of wall effects, whereas the dimensionless void volume only varied by a small amount. It was initially thought that the plate height was affected by channelling at the walls, as has been the case in other CFD dispersion studies[162]. However, these studies were carried out using columns packed with sphere particles that are more prone to channelling than TPMS. The monolithic structures were embedded into the column walls, which would lessen the extent of (but not entirely negate) channelling effects[8]. The large difference in h_{min} was attributed to the interruption of a fully developed velocity field due to extra shears caused by the walls, resulting in a larger degree of axial dispersion. It was also likely that eddy effects would be introduced near the walls. The convergence to the infinite column approximation of h_{min} and the error was approximated with a logarithmic line of best fit. Observation of the errors suggests that wall effects would be significant in columns even a few cells smaller than the limiting case of a 30 unit cell diameter column.

The convergence of V_D values was also modelled logarithmically, but the maximum variation between the 4 unit cell diameter column and the infinite medium was only slight at just over 5%. This could be explained by the walls disrupting the velocity field and introducing a small degree of channelling or influencing eddy currents that allowed preferential flow through the column. The smaller errors compared to h_{min} were attributed to the V_D calculation being largely dependent on the weighting of the hydraulic residence time required for the solute front to reach the periodic cell.

The fraction of capacity occupied at breakthrough was actually seen to increase for the small column to unit cell diameter ratios, resulting in large errors with the value of C_D for the periodic unit cell. It was thought that when wall effects were significant (at low unit cell to column diameter ratios), the additional drag at the walls could act to 'hold up' solute within the column and allow more of it to be adsorbed than would be if the velocity profile was developed and fully periodic. If this were the case, it would be expected that a plot of C_D against the particle to column diameter ratio would show an optimum where solute uptake would be at its greatest, before reducing as the ratio approached an approximation to an infinitely wide column (when wall effects would be considered negligible again). Irrespective of this claim, it was determined that the periodic unit cell results were only valid in the case of large column diameter to unit cell ratios (approximately 30 or greater), and that when extrapolating the results for smaller columns the values of h_{min} and C_D would be subject to considerable error.

One consideration that was not made in this investigation was whether the presence of wall effects would have the ability to change the relative performance of different packed bed geometries. It is likely that some packed bed configurations would be subject to significantly more channelling that others, but without conducting simulations to investigate the effects of this it is unclear if the relative performance would be maintained for small unit cell to column diameter ratios.

7.3 Changing adsorption parameters

Industrially, packed beds are used in numerous applications, each with unique chemistry and reactivity. Therefore it was deemed important to consider alternative adsorption parameters as part of this study. Thus far, comparisons had only been made between different TPMS structures for different flow rates, while all other parameters were held constant. In an attempt to generalize the claims pertaining to the relative performance of each TPMS, the PGD family of structures were simulated using an alternative set of adsorption parameters to observe their ranking and verify if the same relative performance would be obtained. This was achieved by increasing the capacity and adsorption rate constants to better represent practical MIP chemistry. The new adsorption parameters maintained the maximum sorption depth of 40 Å, emulating surface adsorption, and utilised adsorption (k_{ads}) and desorption (k_{des})

constants of 21.95 s^{-1} and 21.95x10^{-4} mol m^{-3} s^{-1} respectively. The specific capacity of the MIP was estimated to be 316,000 mol m^{-3} of active surface material (or 1.26x10^{-3} mol m^{-2} as a function of surface area). No other system parameters were modified, but it was noted that these changes still only pertained to modelling a surface reaction with first order Langmuir kinetics, and modelling other reaction schemes is a potential area to extend this research.

7.3.1 Kinetics comparison

Using these new parameters, simulations were again carried out for the SP, SG, and SD geometries to confirm the relative trends in performance. The geometric properties, flow measures, and dispersion results remained unchanged as the parameter modifications only affected the adsorption model and breakthrough simulations.

The resultant plots for the dimensionless volume and capacity fraction are shown in Figure 78 and Figure 79. It was evident that increasing the reaction rate and capacity resulted in a longer breakthrough time and as such more fluid to be eluted at lower Peclet (when the system was more diffusion limited). At higher Peclet, advection dominated the mass transport within the system and so improvements upon the slower reaction kinetics and lower capacity were far less significant. Figure 80 displays how the dimensionless void volumes that were eluted through the SD column prior to breakthrough increased significantly with faster adsorption kinetics, particularly at lower Pe.

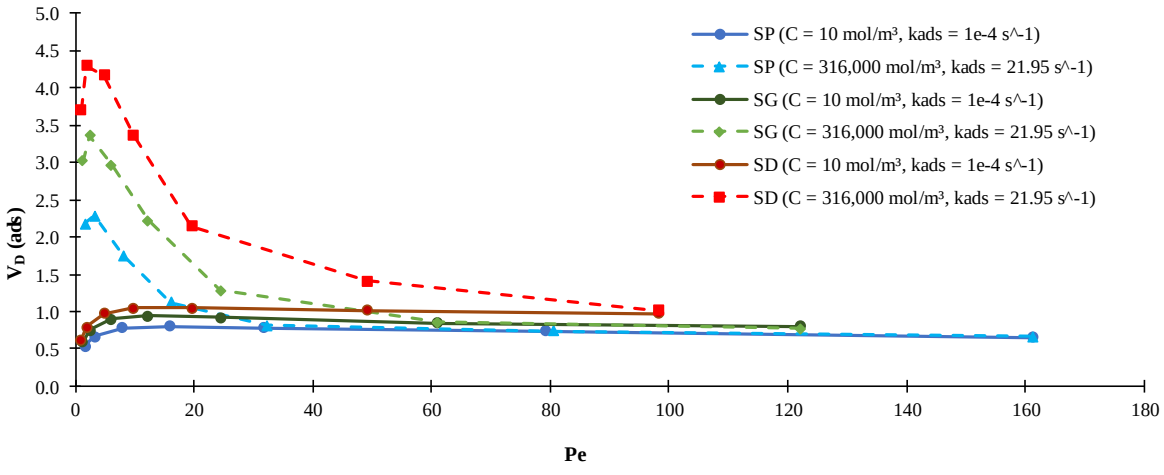

Figure 78. Comparison of the dimensionless void volumes required to observe breakthrough for SP, SG, and SD geometries using increased solid capacity and adsorption rate constant.

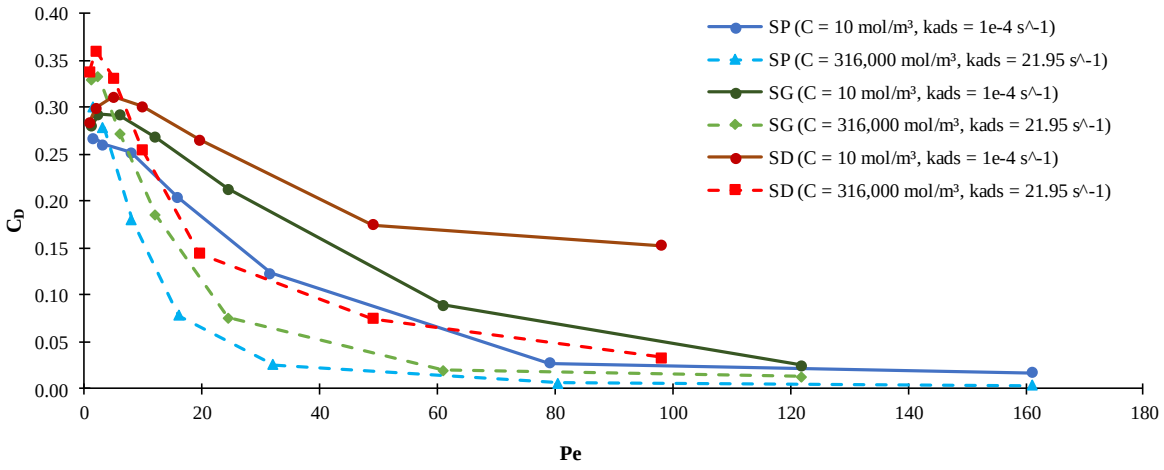

Figure 79. Comparison of capacity fraction occupied when breakthrough occurs for the SP, SG, and SD geometries with different adsorption solid capacity and adsorption rate constant.

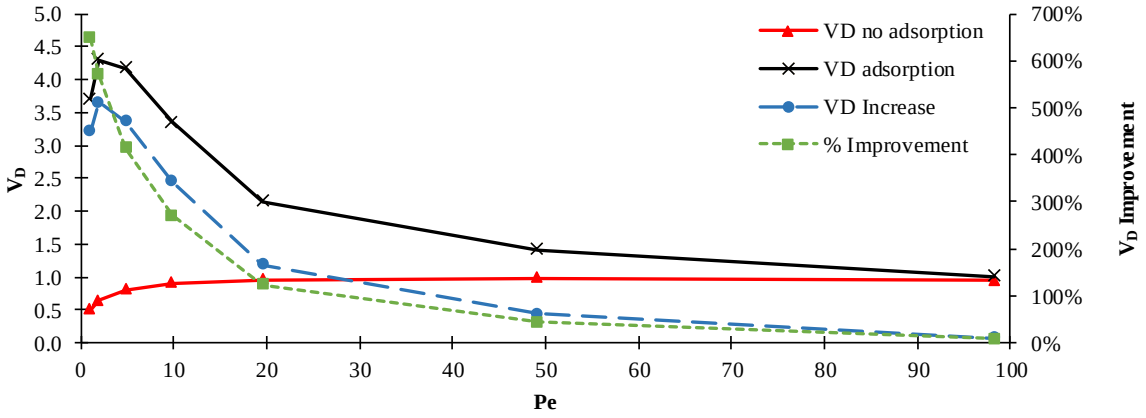

Figure 80. Improvement of the V_D observed for the SD geometry at a Peclet of 20 for the case of no adsorption, and fast adsorption kinetics with increased solid phase capacity.

It was also evident that the combination of parameters used in the high capacity simulations allowed for more solute to be removed from the bulk fluid, but at higher flowrates actually caused lower loading to be achieved at the breakthrough condition. This is seen in Figure 79 where for flowrates with Pe of 10 or higher reveals the C_D of the high capacity were lower than their C_D of the low counterparts (while preserving the descending order from SD, SG to SP). As the capacity and reaction rate were both increased, the concentration gradient and driving force for adsorption near the wall would have increased too. Therefore, the lower C_D was in the second round of simulations was determined to be a result of the higher capacity solid phase requiring longer to reach the same degree of loading. This enabled the advection of solute through the column to have a greater influence, as material could be carried through the structure to cause breakthrough to be observed before equivalent loading was

achieved. This was a direct result of the time required for solute to diffusive from the centre of the channel to the walls being larger than the advection time for the solute to reach the periodic breakthrough slice. As it was proven in previous chapters, this could be overcome by modifying the porosity and channel width of the structure.

The results from using alternative adsorption parameters reaffirmed the relative order of performance for the SP, SG and SD geometries. The Schwarz Diamond was still found to outperform the Schoen Gyroid, and the Schwarz Primitive structure (subject to the most channelling) was still found to have the worst performance (Figure 81). The comparison between the simulations with slow and fast adsorption modelling was performed solely on a qualitative basis, as the exact relationship between the advection, diffusion rate, reaction rate, and system scale is complex in transient systems. However, by showcasing the same trend in each case it is reasonable to expect that the same relative performance would be obtained over a wide range of adsorption parameters. Systematic changes that may be able to change the relative performance could include: modelling other reaction schemes, or increasing the flowrate beyond the Stokes regime, as the onset of turbulence could introduce unforeseen mass transfer effects.

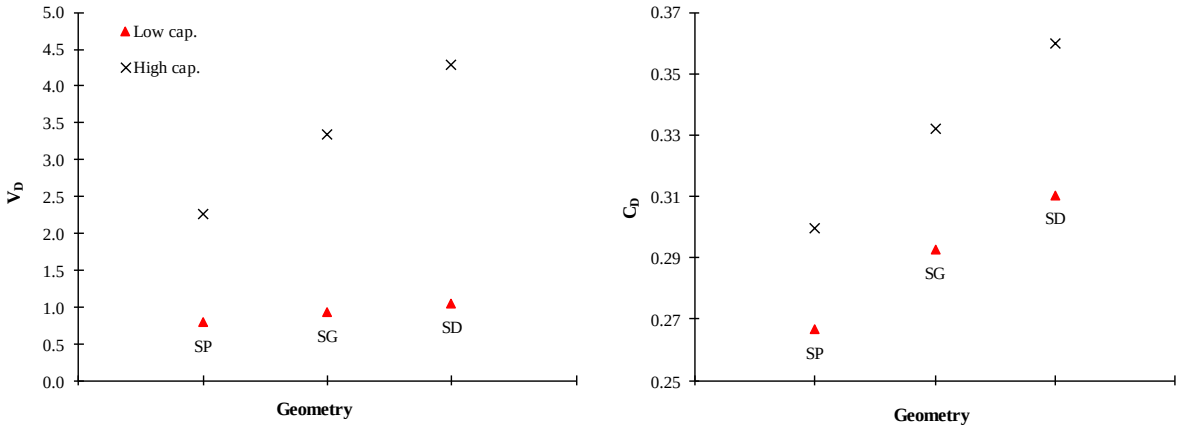

Figure 81. Comparison of best V_D and C_D obtained with different adsorption parameters.

One additional conclusion that could be made from observing the comparison in Figure 81 was that with faster kinetics and a higher saturation capacity, the improvements in V_D which resulted from geometry selection were emphasised. The improvement seen in V_D between the SP and SD in the high and low capacity simulations increased from 30.1% to 88.5%. The changes in the fraction of capacity were less pronounced, suggesting that the loading capacity had a greater dependence on the length of the column and linear fluid velocity.

7.3.2 Damköhler number

When observing systems with mass transport and reactions occurring on different time scales, the Damköhler number is sometimes used to infer the limiting time scale. The Damköhler number (Da) is a dimensionless quantity used to observe the ratio of mass transport in a bulk fluid to a reaction rate[208]. There are many definitions that have been derived to suit various systems, but at its base it is a ratio of reaction timescale to the time required for mass transport phenomena (Equation [23]). The Damköhler number differs from the Thiele modulus, which specifically refers to diffusion within pores[209], or the Biot number, which is a ratio of the bulk and pore diffusion rates[210]. Typically the Damköhler number is used to determine the conversion that can be achieved within a system at a steady state of operation[211], where values below 0.1 and greater than 10 are expected to describe a system with conversion less than 10% and greater than 90% respectively. The second Damköhler number (Da_{II}) as given in Equation [85][212] is used in cases where there is an interfacial reaction such as absorption (the exact formulation is dependent on the order of the reaction).

$$Da = \frac{Reaction\ rate}{Transport\ rate} = \frac{Convection\ or\ diffusion\ time}{Reaction\ time} \quad [84]$$

$$Da_{II} = \frac{Reaction\ rate}{Transport\ rate} = \frac{k_{ads} C_{cap} L_c}{C_0 D_m} \quad [85]$$

Given that the use of Da is typically reserved for steady state operations, the validity of applying it to make comparisons for the 5% breakthrough data required extending the use of Da beyond its intended purpose. An alternative custom ratio of the diffusive transport time to the reaction time was developed to allow some comparison between the two systems. The initial conditions were used in the calculations, and the reaction time was obtained from the first order Langmuir adsorption constant, whereas the diffusive time was related to the solute diffusing through a unit cell (thus assuming the mass transport was diffusion dependent). The ratio of these time scales is given by Equation [86], and the resultant Da for the slow and fast kinetics simulations ranged between 0.006 – 0.017 and 1390 – 3810 respectively. Due to the custom definition used to define Da, it is important to acknowledge that these numbers do not adhere to the typical correlations for Da. While this was a crude method for comparing system time scales it did exhibit that, with the faster adsorption parameters and higher capacity, the effects of diffusion become more significant. In general terms, this calculation suggests that higher k_{ads} and C_{cap} results in a higher C_D at breakthrough (for a diffusion dominated system, as seen in Figure 79). At higher flowrates an advection transport time would be needed in calculation of this ratio.

$$\frac{Reaction\ rate}{Transport\ rate} = \frac{Diffusion\ time}{Reaction\ time} = \frac{k_{ads} L_c^2 C_0}{C_0 D_m} \quad [86]$$

7.4 Other Considerations

In addition to wall effects and the adsorption parameters, several other factors were identified as important considerations when trying to apply the findings from this study. These included the development of the concentration profile as it progressed through the column, the size of the mass transfer zone within a column, and the ineffective bed length that would not be utilized when breakthrough occurred (length of unused bed).

7.4.1 Concentration profile

In practice, when performing a fixed bed reaction the entirety of the packing material is not utilized concurrently. Instead, the concentration profile or solute front advances from the column inlet to the outlet, and in the case of an adsorption column the bed material reacts as this front advances. At any axial coordinate along the column, the average concentration will increase from the initial column concentrating (often zero mol m^{-3}), through the breakthrough condition (5% of C_0), until it reaches the inlet concentration and the bed is saturated at capacity[213] (illustrated in Figure 82). In the ideal case, the loading of the solid phase material occurs with perfect radial mixing and no axial dispersion. Real systems do not share these properties and so a 'mass transfer zone' where the majority of the reaction occurs is defined as the length of bed between the solute front and saturated bed material. When the solute profile is fully developed, the mass transfer zone may also be used to approximate an unused length of bed material that would not reach saturation (if operating the column to the 5% outlet breakthrough condition). This can be a useful consideration in the practical design and construction of a column[214].

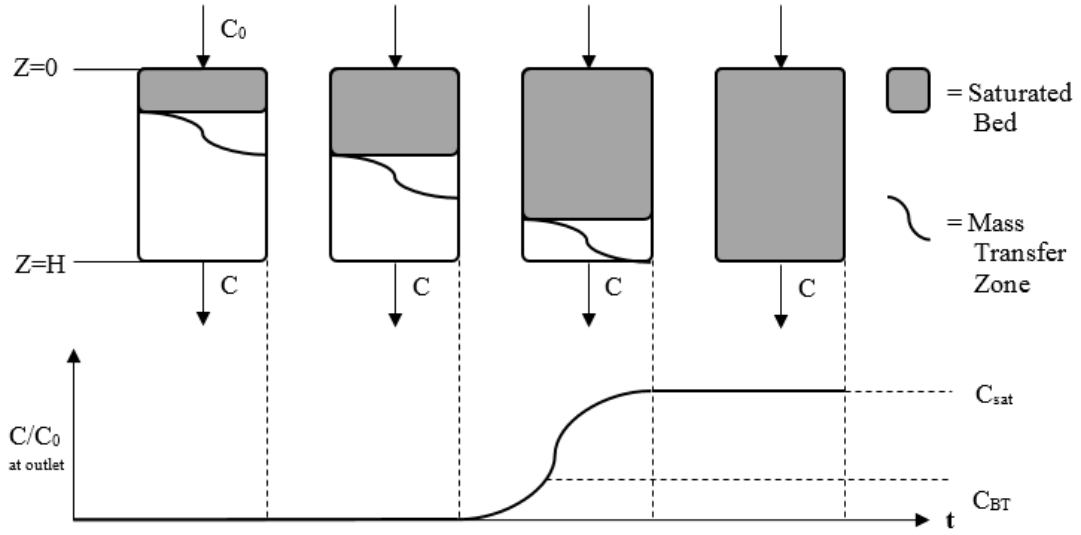

Figure 82. Depiction of breakthrough within a column and the 'mass transfer zone'.

Estimating each of these parameters required simulations to be conducted over progressively longer column domains until the bulk concentration achieved a steady state achieved concentration profile. Both generating a larger simulation domain and operating until steady state resulted in increased computation time, therefore only a test case was modelled. The dynamic concentration profiles over several periodic unit cells is shown in Figure 83, where the concentration profile shows only minor development between the entry slice observed and the 8th body cell. Observationally, it could be determined that the 5% breakthrough condition would occur approximately four unit cells downstream of where solute front reached >95% of the inlet concentration, indicating a large presence of solute to assist the solid phase in reaching saturation. To help determine the length of the mass transfer zone, the solute loading for each unit cell was calculated and is shown in Figure 84. It was found that the value of C_D decreased from saturation to approximately 60% over a length of eight unit cells. Combining the information from both graphs lead to the conclusion that despite the concentration profile propagating through the column with a width of approximately four unit cells, the mass transfer zone would need to be longer than the eight unit cells shown, as each cell was still approaching saturation.

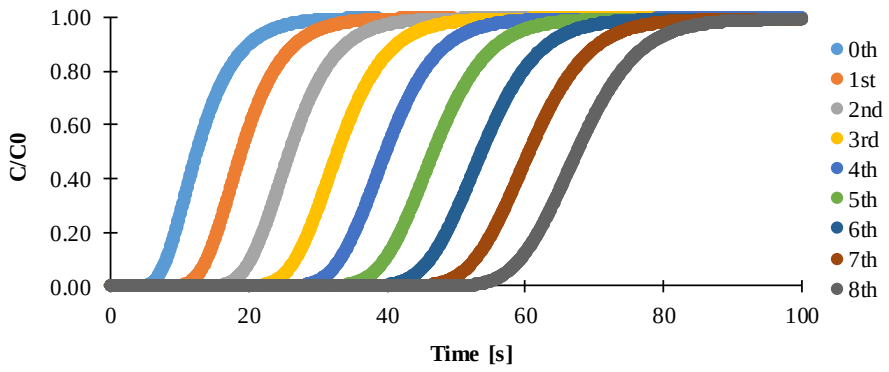

Figure 83. Breakthrough profiles along the axial direction. Using the SD geometry with an inlet Peclet number of 20.

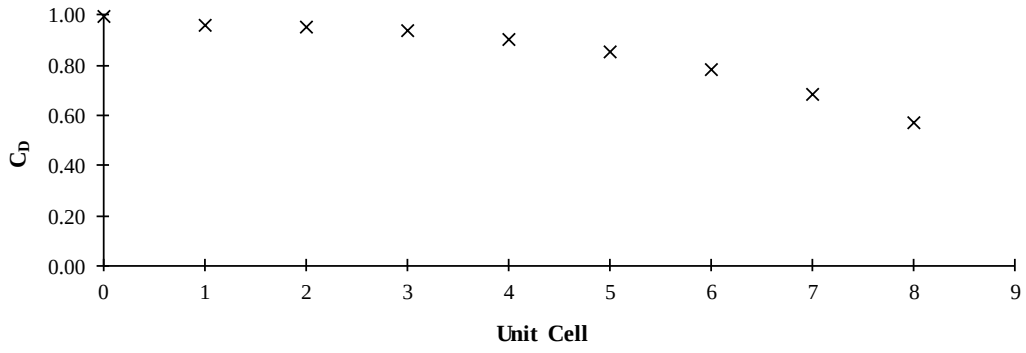

Figure 84. Fraction of capacity occupied at each unit cell along the axial direction.

These results suggest that for the SD geometry with an inlet Peclet of 20 that the length of unused bed was greater than eight cells in length, but was unlikely to be greater than thirty (by means of extrapolating the data from Figure 84). It must also be acknowledged that the length of unused bed would vary with both the flow rate used and the TPMS structure used. Therefore, a figure of 100 or fewer unit cells is recommended to provide an order-of-magnitude estimate when designing a practical column with these parameters. A typical adsorption column[215,216] might utilize particles with a diameter of 0.5 mm (equivalent to the 500 µm unit cells in this study), which would correspond to an estimated length of unused bed of 0.05 m. If the minimum column diameter to unit cell ratio of 30 were used, a column would need to be designed with a 0.015 m diameter. Typical columns have lengths up to several meters, or have bed length to diameter ratios of approximately 100. Using this ratio infers a bed length of 1.5 m for the 500 µm particle column discussed above, which is within the typical range. This would correspond to a length of unused bed occupying 0.05 m (3.33%) of the total bed.

7.4.2 Other model capabilities

The model implemented with the LBM was used to observe breakthrough in the context of an adsorption filter, but could be used to simulate various alternative systems. It has already been illustrated that changes can be made between the geometry, flowrate, and scale of the system being observed, but other possible extensions include: modelling different interphase phenomena, observing bed exhaustive processes instead of breakthrough, and simulating consecutive process steps (such as unbinding or elution steps for the adsorption filter).

Alternative process chemistry, such as adsorption on a solid phase with internal porosity, could be explored. By redefining the dynamics of the solid phase, the solid diffusivity parameter could be adjusted to match the diffusion rate within the internal pores to physical systems. Additionally, the specific adsorption model and respective parameters used could be determined through parameter fitting exercises to align with experimental results. This would require the experiments and simulations to be carried out in conjunction to ensure they complement one another and remain within the capabilities of each process.

The model is also capable of simulating transient processes until a steady state is achieved, as opposed to concluding at an enforced breakthrough condition. Modelling steady state (saturated bed) operations would better represent the recovery processes of valuable solutes, as achieving a high degree of solid phase loading is more important than the concentration in the permeate fluid. It would then also be useful to simulate an elution step following the binding operation, by introducing a third species that un-binds the adsorbed solute. All of these capabilities are readily available within the code and Palabos library, therefore providing a large scope for the continuation of this work.

Chapter 8 – Conclusions and Recommendations

8.1 Conclusions

With the advances in additive manufacturing technologies such as 3D printing, the precise control of packed bed morphology and internal pore networks are possible, allowing structures to be designed for enhanced heat and mass transfer. This provided the motivation to ascertain properties that were correlated with reduced mass transfer resistance, and identify a packed bed geometry with improved chromatographic and adsorption performance. Throughout this work, numerical modelling was used to investigate the effect that packed bed geometry has on the operating efficiency of packed columns. The objectives of this work were to confirm the findings of previous work (that ordered monolithic packing structures provide better performance over arranged particles), and determine what properties of TPMS relate to enhanced performance. Both of these objectives were achieved, and enhanced geometries were identified using dispersion and breakthrough simulations. Knowledge acquired from these simulations was used to improve the design of a highly selective adsorption filter intended to remove trace heavy metal contaminants from water. The generalized heuristics that have been developed hold the potential to influence all packed bed technologies, by illustrating how the solid phase morphology can be exploited for gains in performance.

The Lattice Boltzmann Method for fluid dynamic modelling was implemented using the open-source code library "Palabos". Simulations of Stokes flow through a periodic domain allowed comparisons to be made in the context of an infinitely wide column. A trace contaminant species (in the ppm range) was introduced to the column as a pulse or step increase at the inlet using passive scalar transport principals. This allowed the axial dispersion and breakthrough performance of each geometry to be assessed. The flow properties and solute transport measures were verified against literature cases, and a Langmuir isotherm was used to model a surface adsorption reaction in the breakthrough simulations (as representative of the adsorption characteristics of MIPs). The parameters of particular interest to this study were the specific capacity of each morphology, the chromatographic reduced plate height, and dimensionless measures of the throughput volume and solute-loading achieved when a 5% breakthrough condition was observed. In carrying out this analysis, the characteristic length of a periodic unit cell was redefined to be the porous hydraulic diameter, so to be applicable to all morphologies and allow a fair comparison between particle and monolithic packing structures.

In Chapter 4 the performance of ordered sphere arrangements was compared to the performance of the monolithic structures defined by the Schwarz Primitive (SP), Schoen Gyroid (SG), and Schwarz Diamond (SD) TPMS. The results confirmed that the monolithic structures generally possessed higher specific surface areas and porosities, preferable for the operation of chromatography and adsorption columns. The TPMS structures were also subject to lower pressure drop requirements and experienced

lower axial dispersion than the sphere packing structures, even at higher flowrates. All of these findings supported the use of ordered monolithic packing morphologies as an efficient media, with the SD structure displaying the best performance in all measures. When considering the results of the breakthrough simulations it was also evident that the TPMS were more effective at reducing the mass transfer resistances relating to the adsorption process. It was suggested that this is because of reduced channelling and an increased tortuosity and velocity field homogenization. The monolithic structures were not contrasted with randomly packed spheres as prior studies confirmed improved performance when using ordered arrangements of particles in these contexts. Additionally, it was noted that any arrangement of spheres would be subject to point contacts between particles and thus highly unstable for practical operation. A 'particle overlap' was used by Dolamore[8] to create more stable continuous solid phase structures from various particle arrangements, which reduced the column capacity and increased the pressure drop requirement. Therefore, TPMS were determined to be more practical candidates for a practical packed bed morphology.

After establishing that ordered monolithic structures were superior to ordered arrangements of spheres, additional TPMS structures and modified SP, SG, and SD geometries were examined. In Chapter 5 it was determined that the SD and Double Schoen Gyroid (DSG) structures were the most viable candidates for a highly efficient media as they were able to perform well at higher flowrate while maintaining reasonable pressure drop gradients. The introduction of TPMS modifications (orientation relative to flow axis, porosity) in Chapter 6 then provided insight as to how the morphology of each structure influenced axial dispersion and breakthrough performance. Rotating the monolithic structure to reduce channelling through the column could achieve significant improvements in column performance without compromising permeability, but without being able to predetermine orientations that reduced channelling (prior to simulation) this manipulation was deemed difficult to exploit. It is possible that physical imaging technologies could be used to investigate the optimal orientation angle for each structure by identifying an orientation with the least channelling. Porosity shared a much more intuitive relationship with performance; increased porosity lead to reduced axial dispersion and improved breakthrough performance. Many attempts to relate the geometric properties and velocity field measures to performance proved that generalizing all monolithic media with high accuracy was not feasible. When examining smaller subsets of structures, such as varying the porosity of one TPMS structure, significantly stronger trends between geometry, flow, and performance were identified. However, qualitative trends between morphology and enhanced performance were illustrated. The properties of a periodic unit cell that generally produced enhanced results and lower mass transfer resistances included; higher specific surface area, a lower degree of channelling, homogenization of the velocity field, and increased tortuosity.

Using the findings from Chapters 4 through 6 a new TPMS structure was 'designed' with the intent of displaying low axial dispersion and good breakthrough performance measures. In Chapter 7 a modified

Double Schoen Gyroid structure with increased porosity was selected, and was confirmed to have low axial dispersion and a high dimensionless volume throughput prior to the breakthrough condition. While the generalized correlations were not able to accurately predict the exact performance, the result did confirm that the qualitative trends between geometry and performance could be exploited to achieve more efficient packed beds. However, two of the most important factors when designing improved packed beds were found to be the base TPMS structure used, and the orientation relative to the flow axis, indicating that simulation techniques would still be required to determine enhanced media.

Ultimately, it was determined that out of all the geometries observed, the SD or DSG were the best base structures from which to develop enhanced packed beds. With reference to the design of an adsorption filter, it is recommended that either of these structures be pursued for use in a practical column, while ensuring it would adhere to the limitations imposed by the 3D printing and manufacturing techniques. These structures showcased the lowest pressure drops, a capability to handle the highest flowrates without degraded performance, and a reasonable solid phase capacity. It is also noted that these structures would also be likely to have enhanced performance in heat transfer applications as well (such as heat exchangers), due to the commonalities between heat and mass transfer processes. Therefore this work on the design of enhanced packed bed media may contribute to the growing interest in packed bed design, and be of significance to a large range of processes.

8.2 Limitations

Chapter 7 examined many of the limitations of this study, and assessed the applicability of results. This included considering the assumptions surrounding unit cell periodicity, the adsorption model, and the lengths of unused bed and mass transfer zone within a physical column. By including bounding walls in the radial direction, column ‘wall effects’ were captured and used to determine that the results from this study only related to columns with a diameter equal to or greater than approximately 30 unit cells. Smaller columns showed significant deviations from the periodic results obtained throughout this work. The choice of the adsorption model and adsorption model parameters were addressed as factors that could limit the breadth of applications for these findings. A first order rate law representing the Langmuir isotherm was used for modelling, and therefore applying these finding to systems with alternative reactions and chemistry may not be straightforward. A small investigation into the impact of changing the adsorption parameters revealed that the relative performance of each structure was maintained irrespective of the parameters used. It was also shown that, for systems with faster kinetics and higher solid phase capacity, the potential gain from using enhanced geometries was greater. The results from the adsorption modelling were also used to determine the length of unused bed that may be required near the outlet of a practical breakthrough column. While it is acknowledged that this length

would vary with the choice of TPMS and flowrate, the unsaturated section of bed material was estimated to likely be near thirty unit cells, but would be in the order of 100 or fewer unit cells.

Other limitations of this study that were less thoroughly addressed included the range of operating flowrates that were examined, and assessing performance at steady state saturation. Only highly laminar flow rates pertaining to the Stokes flow regime were observed in this study. It is acknowledged that many industrial packed bed technologies operate in turbulent regimes[214] and thus one of the shortcomings of this study may be in the limited applicability of results at high flowrates. It is unknown whether the relative performance of each structure would be maintained over the turbulent flow regime, as it is likely that changes in the velocity field would develop under turbulent conditions. In some cases, turbulent flow has been shown to induce desirable dispersion profiles within packed columns[217]. Additionally, as the context spurring this investigation sought enhanced breakthrough performance, the steady state adsorption profiles were not examined. This reduced the computational resources required significantly, but prevented analysis of the results in the context of achieving saturation of a packed bed (such as solute recovery). It is unknown whether the relative performance of each structure would be equivalent when assessing steady state adsorption profiles, although it would not be unreasonable to expect as much given these results would just be an elongation of the time observed. Both the extension of the flow regime and operating the columns until reaching steady state could be investigated using the techniques and model as described in this work.

The objective of this work was to manipulate the morphology of a packed bed to obtain enhanced mass transfer characteristics. This objective of topology optimization is one with limitless possible solutions, therefore to reduce the initial scope the study was limited to TPMS structures. This decision was based upon previous studies that suggested that ordered packing structures possess favourable properties, and that TPMS geometries in particular displayed desirable performance in chromatographic applications. Making this decision allowed the family of TPMS structures to be thoroughly explored, but left many geometries unexamined. It is possible that structures not derived from TPMS may have superior characteristics. For example, a periodic structure with a pore network that reduces the channel diameter in proportion to the distance along the flow axis (tapering channel widths) may benefit from reductions in the required diffusive distance, thus countering axial diffusion effects. Discovering a universally ‘optimal’ packed bed morphology is unlikely given the breadth of possible solutions, and the reduced scope of TPMS geometries further limited the possibility of optimal structures being discovered. However, the study was able to yield enhanced performance through a systematic approach to packed bed design and provided useful insights to assist in further studies.

8.3 Recommendations

As outlined above, within the context of the enhanced sorption filter, it is recommended that the Schwarz Diamond (SD) or Double Schoen Gyroid (DSG) structures be used in the design of an ordered packed bed. Either TPMS if manipulated through reorientation or modifying the porosity would be expected to display some of the best performance of all morphologies considered. Each structure showcased desirable performance with a low degree of axial dispersion and desirable adsorption capacities. Both also possessed practical and economic incentives to be used, such as low pressure requirements and high throughput capabilities. When designing further enhanced media, it is recommended that the findings in Chapter 7 be considered, and used as qualitative guidelines to distribute solid phase material in an effective manner that reduces mass transfer resistance. Further modifications could also be investigated, such as the 'stretching' of structures in the radial and axial directions. A study conducted on elliptical particles found that when spheres were 'stretched' in the radial axes they were subject to less axial dispersion[110], providing a basis to investigate this type of manipulation with TPMS structures.

Several other areas for potential further research were identified throughout this study. These include the extension of results into higher flow velocities to observe the influence of turbulent flow, examining additional manipulations to TPMS structures, and testing alternative adsorption models or process chemistry. Further additions to the model capabilities could include competitive binding with multiple contaminant solutes, for which similar adsorption models are readily available in literature[37]. However, the most useful extension of this work would be to validate the model with direct comparisons to experimental data. This would provide insight into how the solid diffusivity parameter relates to the real system, and strengthen the use of the model as a predictive tool. One additional aspect of column operation that could be investigated is the effect a sinusoidal inlet velocity would have on the mass transfer properties. Existing research suggests that an oscillating velocity profile may enhance mass transfer within a porous system[218], although this would cause a significant increase in difficulty when modelling the system.

In applying the findings from this work to the design of the metal sorption filter, there are many practical aspects that must be considered. It is recommended that the manufacturing dimensions and operating parameters remain within the limitations of this study: maintaining a column diameter to unit cell ratio of at least 30, and factoring in an estimated length of unused bed material (100 unit cells) for efficient design. Additionally, the filter should be operated within an appropriate range of flow rates, and several filter units should be available to run in cycles to compensate for the regeneration time that would be required. With these limitations considered, the results of this investigation into the efficiency of packed bed geometries can be applied to a wide range of processes. Monolithic structures such as TPMS provide better column economy, and are a promising alternative to traditional packing media.

References

1. Ministry of Health. Annual Report on Drinking-water Quality 2016-2017. 2018: 149. Annual Report.

2. Kolev N. *Packed bed columns: for absorption, desorption, rectification and direct heat transfer*. 1st ed. Amsterdam;Boston;: Elsevier, 2006.

3. Wakao N and Kaguei S. *Heat and mass transfer in packed beds*. New York: Gordon and Breach Science Publishers, 1982.

4. Frazier WE. Metal Additive Manufacturing: A Review. *Journal of Materials Engineering and Performance* 2014; 23: 1917-1928. DOI: 10.1007/s11665-014-0958-z.

5. Bird RB, Stewart WE and Lightfoot EN. *Transport Phenomena*. John Wiley & Sons, 2007.

6. Darcy H. *Les fontaines publiques de la ville de Dijon: exposition et application*. Victor Dalmont, 1856.

7. Schure MR, Maier RS, Kroll DM, et al. Simulation of ordered packed beds in chromatography. *Journal of Chromatography A* 2004; 1031: 79-86. DOI: https://doi.org/10.1016/j.chroma.2003.12.030.

8. Dolamore F. In Silico analysis of flow and dispersion in ordered porous media. 2017.

9. Asinari P. Multi-scale analysis of heat and mass transfer in mini/micro-structures. *Itay: Politecnico di Torino* 2005: 243-262.

10. Doering CR and Gibbon JD. *Applied analysis of the Navier-Stokes equations*. Cambridge University Press, 1995.

11. De Klerk A. Voidage variation in packed beds at small column to particle diameter ratio. *AIChE journal* 2003; 49: 2022-2029.

12. Knox JH and Parcher JF. Effect of the column to particle diameter ratio on the dispersion of unsorbed solutes in chromatography. *Analytical Chemistry* 1969; 41: 1599-1606.

13. Heftmann E. *Chromatography: Fundamentals and applications of chromatography and related differential migration methods-Part B: Applications*. Elsevier, 2004.

14. Martin A and Synge RM. A new form of chromatogram employing two liquid phases: A theory of chromatography. 2. Application to the micro-determination of the higher monoamino-acids in proteins. *Biochemical Journal* 1941; 35: 1358.

15. Wohlgemuth M, Yufa N, Hoffman J, et al. Triply Periodic Bicontinuous Cubic Microdomain Morphologies by Symmetries. *Macromolecules* 2001; 34: 6083-6089. DOI: 10.1021/ma0019499.

16. Dolamore F, Fee C and Dimartino S. Modelling ordered packed beds of spheres: The importance of bed orientation and the influence of tortuosity on dispersion. *Journal of Chromatography A* 2018; 1532: 150-160. DOI: https://doi.org/10.1016/j.chroma.2017.12.004.

17. Siouffi A-M. About the C term in the van Deemter's equation of plate height in monoliths. *Journal of Chromatography A* 2006; 1126: 86-94.

18. Meybeck M. Global analysis of river systems: from Earth system controls to Anthropocene syndromes. *Philosophical Transactions of the Royal Society B: Biological Sciences* 2003; 358: 1935-1955. DOI: 10.1098/rstb.2003.1379.

19. Schulze RE. River Basin Responses to Global Change and Anthropogenic Impacts. In: Kabat P, Claussen M, Dirmeyer PA, et al. (eds) *Vegetation, Water, Humans and the Climate: A New Perspective on an Interactive System*. Berlin, Heidelberg: Springer Berlin Heidelberg, 2004, pp.339-374.

20. Becker A, Bonell M, Feddes RA, et al. Responses of Hydrological Processes to Environmental Change at Small Catchment Scales. In: Kabat P, Claussen M, Dirmeyer PA, et al. (eds) *Vegetation, Water, Humans and the Climate: A New Perspective on an Interactive System*. Berlin, Heidelberg: Springer Berlin Heidelberg, 2004, pp.301-338.

21. Holland HD and Petersen U. *Living Dangerously: The Earth, Its Resources, and the Environment*. Princeton University Press, 1995.

22. Mackenzie FT. *Our Changing Planet: An Introduction to Earth System Science and Global Environmental Change*. Prentice Hall, 2011.

23. BusinessWire. NanoStruck Announces 96% Recovery of 9.1 GMS/Ton Gold from Tailing Samples. 2014.

24. Sutherland K and Dickenson TC. *Filters and filtration handbook*. 5th ed. Oxford: Elsevier/Butterworth-Heinemann, 2008.

25. Baker MN. *The quest for pure water; the history of water purification from the earliest records to the twentieth century*. New York: American Water Works Assn., 1949, p.xiv, 527 p.

26. Lee KP, Arnot TC and Mattia D. A review of reverse osmosis membrane materials for desalination—Development to date and future potential. *Journal of Membrane Science* 2011; 370: 1-22. DOI: https://doi.org/10.1016/j.memsci.2010.12.036.

27. Tien C and Payatakes AC. Advances in deep bed filtration. *AIChE Journal* 1979; 25: 737-759.

28. Bailey MRAC, Mike M.; A Cox, Ron C.; A Cross-Rudkin, P. S. M.; A Hurst, B. Lawrance; A McWilliam, Robert C.; A Rennison, R. W.; A Ruddock, E. C.; A Sutherland, R. J. M.; A Swailes, Tom. *Biographical Dictionary of Civil Engineers in Great Britain and Ireland*.

29. Humphrey JL and Keller GE. *Separation process technology*. New York: McGraw-Hill, 1997.

30. Boyd CE and Tucker CS. Handbook for aquaculture water quality. *Handbook for Aquaculture Water Quality* 2014: 439.

31. Strickland JD and Parsons TR. A practical handbook of seawater analysis. Ottawa: Canada.Fisheries Research Board of Canada, 1972.

32. World Health Organization. *Guidelines for drinking-water quality: recommendations*. World Health Organization, 2004.

33. Sengupta P. Potential health impacts of hard water. *International journal of preventive medicine* 2013; 4: 866.

34. Rodríguez-Lado L, Sun G, Berg M, et al. Groundwater arsenic contamination throughout China. *Science* 2013; 341: 866-868.

35. Chakraborti D, Rahman MM, Mukherjee A, et al. Groundwater arsenic contamination in Bangladesh—21 Years of research. *Journal of Trace Elements in Medicine and Biology* 2015; 31: 237-248.

36. Ruthven DM. *Principles of adsorption and adsorption processes*. New York: Wiley, 1984.

37. Masel RI. *Principles of adsorption and reaction on solid surfaces*. New York: Wiley, 1996.

38. Langmuir I. The adsorption of gases on plane surfaces of glass, mica and platinum. *Journal of the American Chemical Society* 1918; 40: 1361-1403. DOI: 10.1021/ja02242a004.

39. Brunauer S. Adsorption of Gases in Multimolecular Layers. *Journal of the American Chemical Society* 1938; 60: 309-319. DOI: 10.1021/ja01269a023.

40. Skinner LM and Sambles JR. The Kelvin equation—a review. *Journal of Aerosol Science* 1972; 3: 199-210. DOI: https://doi.org/10.1016/0021-8502(72)90158-9.

41. Jaksland CA, Gani R and Lien KM. Separation process design and synthesis based on thermodynamic insights. *Chemical Engineering Science* 1995; 50: 511-530. DOI: https://doi.org/10.1016/0009-2509(94)00216-E.

42. Seader JD, Henley EJ and Roper DK. *Separation process principles*. New York: Wiley, 1998.

43. Coskun O. Separation techniques: Chromatography. *Northern Clinics of Istanbul* 2016; 3: 156-160. DOI: 10.14744/nci.2016.32757.

44. Barthomeuf D. Basic Zeolites: Characterization and Uses in Adsorption and Catalysis. *Catalysis Reviews* 1996; 38: 521-612. DOI: 10.1080/01614949608006465.

45. Adachi T and Isobe E. Fundamental characteristics of synthetic adsorbents intended for industrial chromatographic separations. *Journal of Chromatography A* 2004; 1036: 33-44. DOI: https://doi.org/10.1016/j.chroma.2003.09.018.

46. Bansal RC and Goyal M. *Activated carbon adsorption*. CRC press, 2005.

47. Fu F and Wang Q. Removal of heavy metal ions from wastewaters: A review. *Journal of Environmental Management* 2011; 92: 407-418. DOI: https://doi.org/10.1016/j.jenvman.2010.11.011.

48. Bailey SE, Olin TJ, Bricka RM, et al. A review of potentially low-cost sorbents for heavy metals. *Water Research* 1999; 33: 2469-2479. DOI: https://doi.org/10.1016/S0043-1354(98)00475-8.

49. De Gisi S, Lofrano G, Grassi M, et al. Characteristics and adsorption capacities of low-cost sorbents for wastewater treatment: A review. *Sustainable Materials and Technologies* 2016; 9: 10-40. DOI: https://doi.org/10.1016/j.susmat.2016.06.002.

50. Nguyen TAH, Ngo HH, Guo WS, et al. Applicability of agricultural waste and by-products for adsorptive removal of heavy metals from wastewater. *Bioresource Technology* 2013; 148: 574-585. DOI: https://doi.org/10.1016/j.biortech.2013.08.124.

51. Hegazi HA. Removal of heavy metals from wastewater using agricultural and industrial wastes as adsorbents. *HBRC Journal* 2013; 9: 276-282. DOI: https://doi.org/10.1016/j.hbrcj.2013.08.004.

52. Hutagalung SS, Muchlis I, Herlambang B, et al. Removal of chemical and biological contaminants on peat water by ozone-based advanced oxidation processes with reverse osmosis. In: *2014 2nd International Conference on Technology, Informatics, Management, Engineering & Environment* 19-21 Aug. 2014 2014, pp.288-291.

53. Barakat MA. New trends in removing heavy metals from industrial wastewater. *Arabian Journal of Chemistry* 2011; 4: 361-377. DOI: https://doi.org/10.1016/j.arabjc.2010.07.019.

54. Herrmann J-M. Heterogeneous photocatalysis: fundamentals and applications to the removal of various types of aqueous pollutants. *Catalysis Today* 1999; 53: 115-129. DOI: https://doi.org/10.1016/S0920-5861(99)00107-8.

55. ITRI. ITRI Introduces Three Environmental Technologies: Green Glass Adsorbent Technology for Industrial Wastewater Treatment; SoPoWake for Landslide Detection; URABat Aluminum Battery for Safety and One-Minute Charging. 2016.

56. Lee J, Farha OK, Roberts J, et al. Metal–organic framework materials as catalysts. *Chemical Society Reviews* 2009; 38: 1450-1459.

57. Sun DT, Peng L, Reeder WS, et al. Rapid, Selective Heavy Metal Removal from Water by a Metal–Organic Framework/Polydopamine Composite. *ACS Central Science* 2018; 4: 349-356. DOI: 10.1021/acscentsci.7b00605.

58. Andersson LI, Paprica A and Arvidsson T. A highly selective solid phase extraction sorbent for pre-concentration of sameridine made by molecular imprinting. *Chromatographia* 1997; 46: 57-62. DOI: 10.1007/BF02490930.

59. Rosi NL, Eckert J, Eddaoudi M, et al. Hydrogen storage in microporous metal-organic frameworks. *Science* 2003; 300: 1127-1129.

60. Boehle T. Large pore of MOF-5 with yellow ball. Wikimedia Commons: Boehle, Tony, 2010.

61. Haupt K, Linares AV, Bompart M, et al. Molecularly imprinted polymers. *Molecular imprinting*. Springer, 2011, pp.1-28.

62. Schirhagl R. Bioapplications for Molecularly Imprinted Polymers. *Analytical Chemistry* 2014; 86: 250-261. DOI: 10.1021/ac401251j.

63. Yoshimatsu K, Reimhult K, Krozer A, et al. Uniform molecularly imprinted microspheres and nanoparticles prepared by precipitation polymerization: The control of particle size suitable for different analytical applications. *Analytica Chimica Acta* 2007; 584: 112-121. DOI: https://doi.org/10.1016/j.aca.2006.11.004.

64. Holthoff EL and Bright FV. Molecularly templated materials in chemical sensing. *Analytica Chimica Acta* 2007; 594: 147-161. DOI: https://doi.org/10.1016/j.aca.2007.05.044.

65. Wackerlig J and Lieberzeit PA. Molecularly imprinted polymer nanoparticles in chemical sensing – Synthesis, characterisation and application. *Sensors and Actuators B: Chemical* 2015; 207: 144-157. DOI: https://doi.org/10.1016/j.snb.2014.09.094.

66. Liu J-q and Wulff G. Functional Mimicry of Carboxypeptidase A by a Combination of Transition State Stabilization and a Defined Orientation of Catalytic Moieties in Molecularly Imprinted Polymers. *Journal of the American Chemical Society* 2008; 130: 8044-8054. DOI: 10.1021/ja8012648.

67. Levi L, Raim V and Srebnik S. A brief review of coarse-grained and other computational studies of molecularly imprinted polymers. *Journal of molecular recognition* 2011; 24: 883-891. DOI: 10.1002/jmr.1135.

68. Maier NM and Lindner W. Chiral recognition applications of molecularly imprinted polymers: a critical review. *Analytical and Bioanalytical Chemistry* 2007; 389: 377-397. DOI: 10.1007/s00216-007-1427-4.

69. Wang GQ, Yuan XG and Yu KT. Review of Mass-Transfer Correlations for Packed Columns. *Industrial & Engineering Chemistry Research* 2005; 44: 8715-8729. DOI: 10.1021/ie050017w.

70. Whitaker S. Flow in porous media I: A theoretical derivation of Darcy's law. *Transport in porous media* 1986; 1: 3-25.

71. Vafai K. *Porous media: applications in biological systems and biotechnology*. CRC Press, 2010.

72. Tschernich RW. *Zeolites of the World*. Harbinger House, 1992.

73. Schotting RJ, van Duijn HC and Verruijt A. *Soil mechanics and transport in porous media: selected works of G. de Josselin de Jong*. Springer Science & Business Media, 2008.

74. Liu P and Chen G-F. *Porous materials: processing and applications*. Elsevier, 2014.

75. Narayan R, Colombo P, Halbig M, et al. *Advances in Bioceramics and Porous Ceramics V*. Wiley, 2012.

76. Eaves D. Handbook of polymer foams. *polimeri* 2004; 25: 1-2.

77. Oberacher H and Huber CG. Capillary monoliths for the analysis of nucleic acids by high-performance liquid chromatography–electrospray ionization mass spectrometry. *TrAC Trends in Analytical Chemistry* 2002; 21: 166-174. DOI: https://doi.org/10.1016/S0165-9936(02)00304-7.

78. Bear J. *Dynamics of fluids in porous media*. Courier Corporation, 2013.

79. Keener R, Maneval J, Östergren K, et al. Mechanical deformation of compressible chromatographic columns. *Biotechnology progress* 2002; 18: 587-596.

80. Lage J, De Lemos M and Nield D. Modeling turbulence in porous media. *Transport phenomena in porous media II*. Elsevier, 2002, pp.198-230.

81. Lage J and Antohe B. Darcy's experiments and the deviation to nonlinear flow regime. *Journal of fluids engineering* 2000; 122: 619-625.

82. Carman PC. *Flow of gases through porous media*. New York: Academic Press, 1956, p.182 p.

83. Carman PC. Fluid flow through granular beds. *Chemical Engineering Research and Design* 1997: S32-S48.

84. Kozeny J. Uber kapillare leitung der wasser in boden. *Royal Academy of Science, Vienna, Proc Class I* 1927; 136: 271-306.

85. Erdim E, Akgiray Ö and Demir İ. A revisit of pressure drop-flow rate correlations for packed beds of spheres. *Powder Technology* 2015; 283: 488-504. DOI: https://doi.org/10.1016/j.powtec.2015.06.017.

86. Ergun S and Orning AA. Fluid Flow through Randomly Packed Columns and Fluidized Beds. *Industrial & Engineering Chemistry* 1949; 41: 1179-1184. DOI: 10.1021/ie50474a011.

87. Ozahi E, Gundogdu MY and Carpinlioglu MÖ. A modification on Ergun's correlation for use in cylindrical packed beds with non-spherical particles. *Advanced Powder Technology* 2008; 19: 369-381.

88. Li L and Ma W. Experimental Study on the Effective Particle Diameter of a Packed Bed with Non-Spherical Particles. *Transport in Porous Media* 2011; 89: 35-48. journal article. DOI: 10.1007/s11242-011-9757-2.

89. Allen KG, von Backström TW and Kröger DG. Packed bed pressure drop dependence on particle shape, size distribution, packing arrangement and roughness. *Powder Technology* 2013; 246: 590-600. DOI: https://doi.org/10.1016/j.powtec.2013.06.022.

90. Barrande M, Bouchet R and Denoyel R. Tortuosity of Porous Particles. *Analytical Chemistry* 2007; 79: 9115-9121. DOI: 10.1021/ac071377r.

91. Ghanbarian B, Hunt AG, Ewing RP, et al. Tortuosity in porous media: a critical review. *Soil science society of America journal* 2013; 77: 1461-1477.

92. Matyka M and Koza Z. How to calculate tortuosity easily? In: *AIP Conference Proceedings 4* 2012, pp.17-22. AIP.

93. Stocker T. *Introduction to Climate Modelling*. Springer Berlin Heidelberg, 2011.

94. Hassanizadeh SM. Derivation of basic equations of mass transport in porous media, Part 2. Generalized Darcy's and Fick's laws. *Advances in water resources* 1986; 9: 207-222.

95. Bruderer-Weng C, Cowie P, Bernabé Y, et al. Relating flow channelling to tracer dispersion in heterogeneous networks. *Advances in Water Resources* 2004; 27: 843-855. DOI: https://doi.org/10.1016/j.advwatres.2004.05.001.

96. Van Deemter JJ, Zuiderweg F and Klinkenberg Av. Longitudinal diffusion and resistance to mass transfer as causes of nonideality in chromatography. *Chemical Engineering Science* 1956; 5: 271-289.

97. Poole CF. The essence of chromatography. *Journal of analytical chemistry (New York, NY)* 2005; 60: 193-193. DOI: 10.1007/s10809-005-0020-2.

98. Bidlingmeyer BA. *Preparative liquid chromatography*. Elsevier, 1987.

99. Nawada S, Dimartino S and Fee CJ. The Effects of bead overlap on chromatographic performance in 3D printed packed bed columns. *International Labmate* 2014. Article.

100. Davis ME. Ordered porous materials for emerging applications. *Nature* 2002; 417: 813. Review Article. DOI: 10.1038/nature00785.

101. Mees PA, Nandakumar K and Masliyah J. Instability and transitions of flow in a curved square duct: the development of two pairs of Dean vortices. *Journal of Fluid Mechanics* 1996; 314: 227-246.

102. Svec F, Tennikova TB and Deyl Z. *Monolithic materials: preparation, properties and applications*. Elsevier, 2003.

103. Mallik R and Hage DS. Affinity monolith chromatography. *Journal of separation science* 2006; 29: 1686-1704.

104. Meeks W and Pérez J. *A survey on classical minimal surface theory*. American Mathematical Soc., 2012.

105. Lidin S and Larsson S. Bonnet transformation of infinite periodic minimal surfaces with hexagonal symmetry. *Journal of the Chemical Society, Faraday Transactions* 1990; 86: 769-775.

106. Pérez J and Ros A. The space of properly embedded minimal surfaces with finite total curvature. *Indiana University Mathematics Journal* 1996: 177-204.

107. Ken Brakke. Triply Periodic Minimal Surfaces, http://facstaff.susqu.edu/brakke/evolver/examples/periodic/periodic.html#psurface (accessed 16.08.2018 2018).

108. Lottes F, Arlt W, Minceva M, et al. Hydrodynamic impact of particle shape in slurry packed liquid chromatography columns. *Journal of Chromatography a* 2009; 1216: 5687-5695.

109. Kirkland JJ and DeStefano JJ. The art and science of forming packed analytical high-performance liquid chromatography columns. *Journal of Chromatography A* 2006; 1126: 50-57. DOI: https://doi.org/10.1016/j.chroma.2006.04.027.

110. Li L, Yan X, Yang J, et al. Numerical investigation on band-broadening characteristics of an ordered packed bed with novel particles. *Applied Energy* 2017; 185: 2168-2180. DOI: https://doi.org/10.1016/j.apenergy.2016.03.045.

111. Nawada S, Dimartino S and Fee C. Dispersion behavior of 3D-printed columns with homogeneous microstructures comprising differing element shapes. *Chemical Engineering Science* 2017; 164: 90-98. DOI: https://doi.org/10.1016/j.ces.2017.02.012.

112. Ziman JM. *Principles of the Theory of Solids*. Cambridge university press, 1979.

113. Torquato S and Donev A. Minimal surfaces and multifunctionality. *Proceedings of the Royal Society of London Series A: Mathematical, Physical and Engineering Sciences* 2004; 460: 1849-1856. DOI: 10.1098/rspa.2003.1269.

114. Torquato S, Hyun S and Donev A. Optimal design of manufacturable three-dimensional composites with multifunctional characteristics. *Journal of Applied Physics* 2003; 94: 5748-5755.

115. Guest JK and Prévost JH. Design of maximum permeability material structures. *Computer Methods in Applied Mechanics and Engineering* 2007; 196: 1006-1017.

116. Jung Y and Torquato S. Fluid permeabilities of triply periodic minimal surfaces. *Physical Review E* 2005; 72: 056319. DOI: 10.1103/PhysRevE.72.056319.

117. Robards K, Robards K, Haddad PR, et al. *Principles and practice of modern chromatographic methods*. Academic Press, 1994.

118. Currie IG and Currie I. *Fundamental mechanics of fluids*. CRC Press, 2002.

119. Barnes J. *High performance liquid chromatography*. John Wiley & Sons, 1992.

120. Grushka E and Grinberg N. *Advances in Chromatography*. CRC Press, 2007.

121. Wu C-s. *Column handbook for size exclusion chromatography*. Academic Press, 1999.

122. Yamamoto S, Nakanishi K and Matsuno R. *Ion-exchange chromatography of proteins*. CRC Press, 1988.

123. Hage DS and Cazes J. Handbook of Affinity Chromatography, Second Edition, http://public.eblib.com/choice/publicfullrecord.aspx?p=256969 (2005).

124. Ganetsos G and Barker PE. *Preparative and production scale chromatography*. CRC Press, 1992.

125. Jonsson JA. *Chromatographic theory and basic principles*. CRC Press, 1987.

126. Kucera P. *Microcolumn high-performance liquid chromatography*. Elsevier, 2000.

127. Nic M, Hovorka L, Jirat J, et al. *IUPAC Compendium of Chemical Terminology-The Gold Book*. International Union of Pure and Applied Chemistry, 2005.

128. Knox JH. Band dispersion in chromatography–a new view of A-term dispersion. *Journal of Chromatography A* 1999; 831: 3-15.

129. Seki K and Bagchi B. Relationship between entropy and diffusion: A statistical mechanical derivation of Rosenfeld expression for a rugged energy landscape. *The Journal of chemical physics* 2015; 143: 194110.

130. Novotny MV and Ishii D. *Microcolumn Separations: Columns, Instrumentation and Ancillary Techniques*. Elsevier Science, 2011.

131. Asinari P. Viscous coupling based lattice Boltzmann model for binary mixtures. *Physics of Fluids* 2005; 17: 067102.

132. Sarrate J and Staten M. *Proceedings of the 22nd International Meshing Roundtable*. Springer International Publishing, 2013.

133. Cercignani C. The boltzmann equation. *The Boltzmann Equation and Its Applications*. Springer, 1988, pp.40-103.

134. Guo Z and Shu C. *Lattice Boltzmann method and its applications in engineering*. World Scientific, 2013.

135. Dellar PJ. Incompressible limits of lattice Boltzmann equations using multiple relaxation times. *Journal of Computational Physics* 2003; 190: 351-370. DOI: https://doi.org/10.1016/S0021-9991(03)00279-1.

136. Succi S and Succi S. *The lattice Boltzmann equation: for fluid dynamics and beyond*. Oxford university press, 2001.

137. Dellar PJ. Lattice Boltzmann algorithms without cubic defects in Galilean invariance on standard lattices. *Journal of Computational Physics* 2014; 259: 270-283. DOI: https://doi.org/10.1016/j.jcp.2013.11.021.

138. Premnath KN and Abraham J. Three-dimensional multi-relaxation time (MRT) lattice-Boltzmann models for multiphase flow. *Journal of Computational Physics* 2007; 224: 539-559.

139. Scagliarini A, Biferale L, Sbragaglia M, et al. Lattice Boltzmann methods for thermal flows: Continuum limit and applications to compressible Rayleigh–Taylor systems. *Physics of Fluids* 2010; 22: 055101.

140. Gogolin AO, Tsitsishvili EG and Komnik A. *Lectures on Complex Integration*. Springer International Publishing, 2013.

141. Reider MB and Sterling JD. Accuracy of discrete-velocity BGK models for the simulation of the incompressible Navier-Stokes equations. *arXiv preprint comp-gas/9307003* 1993.

142. Khirevich S. High-performance computing of flow, diffusion, and hydrodynamic dispersion in random sphere packings. 2011.

143. He X and Luo L-S. A priori derivation of the lattice Boltzmann equation. *Physical Review E* 1997; 55: R6333.

144. Flekkøy E. Lattice Bhatnagar-Gross-Krook models for miscible fluids. *Physical Review E* 1993; 47: 4247.

145. Yoshida H and Nagaoka M. Multiple-relaxation-time lattice Boltzmann model for the convection and anisotropic diffusion equation. *Journal of Computational Physics* 2010; 229: 7774-7795. DOI: https://doi.org/10.1016/j.jcp.2010.06.037.

146. Chai Z, Shi B, Guo Z, et al. Multiple-relaxation-time lattice Boltzmann model for generalized Newtonian fluid flows. *Journal of Non-Newtonian Fluid Mechanics* 2011; 166: 332-342. DOI: https://doi.org/10.1016/j.jnnfm.2011.01.002.

147. Kuzmin A, Ginzburg I and Mohamad AA. The role of the kinetic parameter in the stability of two-relaxation-time advection–diffusion lattice Boltzmann schemes. *Computers & Mathematics with Applications* 2011; 61: 3417-3442. DOI: https://doi.org/10.1016/j.camwa.2010.07.036.

148. Servan-Camas B and Tsai FTC. Lattice Boltzmann method with two relaxation times for advection–diffusion equation: Third order analysis and stability analysis. *Advances in Water Resources* 2008; 31: 1113-1126. DOI: https://doi.org/10.1016/j.advwatres.2008.05.001.

149. Servan-Camas B and Tsai FTC. Non-negativity and stability analyses of lattice Boltzmann method for advection–diffusion equation. *Journal of Computational Physics* 2009; 228: 236-256. DOI: https://doi.org/10.1016/j.jcp.2008.09.005.

150. Ginzburg I. Equilibrium-type and link-type lattice Boltzmann models for generic advection and anisotropic-dispersion equation. *Advances in Water Resources* 2005; 28: 1171-1195. DOI: https://doi.org/10.1016/j.advwatres.2005.03.004.

151. Chen S and Doolen GD. Lattice Boltzmann Method for fluid flows. *Annual Review of Fluid Mechanics* 1998; 30: 329-364. DOI: 10.1146/annurev.fluid.30.1.329.

152. Flowkit. Course Materials in Palabos Training Course. Laussane, Switzerland: Flowkit Ltd., 2014.

153. Hull CW. Apparatus for production of three-dimensional objects by stereolithography. Google Patents, 1986.

154. Bandyopadhyay A and Bose S. *Additive manufacturing*. Boca Raton, FL: CRC Press, 2016.

155. Vaezi M, Seitz H and Yang S. A review on 3D micro-additive manufacturing technologies. *The International Journal of Advanced Manufacturing Technology* 2013; 67: 1721-1754. journal article. DOI: 10.1007/s00170-012-4605-2.

156. Standard A. F2792-12a, 2012,"Standard Terminology for Additive Manufacturing Technologies" ASTM International. West Conshohocken, PA, 2012, DOI: 10.1520/F2792-12A. *Laser Enclosure Cooling Head Deposition Head Delivery Powder Ar Carrier Gas Cr*; 2.

157. Bandyopadhyay A and Bose S. *Additive manufacturing*. CRC Press, 2015.

158. Huber C, Shafei B and Parmigiani A. A new pore-scale model for linear and non-linear heterogeneous dissolution and precipitation. *Geochimica et Cosmochimica Acta* 2014; 124: 109-130. DOI: https://doi.org/10.1016/j.gca.2013.09.003.

159. Von Schnering H and Nesper R. Nodal surfaces of Fourier series: fundamental invariants of structured matter. *Zeitschrift für Physik B Condensed Matter* 1991; 83: 407-412.

160. Pan C, Luo L-S and Miller CT. An evaluation of lattice Boltzmann schemes for porous medium flow simulation. *Computers & Fluids* 2006; 35: 898-909. DOI: https://doi.org/10.1016/j.compfluid.2005.03.008.

161. Gabriel E, Fagg GE, Bosilca G, et al. Open MPI: Goals, concept, and design of a next generation MPI implementation. In: *European Parallel Virtual Machine/Message Passing Interface Users' Group Meeting* 2004, pp.97-104. Springer.

162. Tobis´ J and Vortmeyer D. Scale-up effects due to near-wall channelling in isothermal adsorption columns: on the limitations in the use of plug flow models. *Chemical Engineering and Processing: Process Intensification* 1991; 29: 147-153. DOI: https://doi.org/10.1016/0255-2701(91)85014-F.

163. Mueller J-D. *Essentials of Computational Fluid Dynamics*. CRC Press, 2015.

164. Day MA. The no-slip condition of fluid dynamics. *Erkenntnis* 1990; 33: 285-296.

165. Yin X and Zhang J. An improved bounce-back scheme for complex boundary conditions in lattice Boltzmann method. *Journal of Computational Physics* 2012; 231: 4295-4303. DOI: https://doi.org/10.1016/j.jcp.2012.02.014.

166. Zou Q and He X. On pressure and velocity boundary conditions for the lattice Boltzmann BGK model. *Physics of fluids* 1997; 9: 1591-1598.

167. Ginzbourg I and Adler P. Boundary flow condition analysis for the three-dimensional lattice Boltzmann model. *Journal de Physique II* 1994; 4: 191-214.

168. Rohde M, Kandhai D, Derksen J, et al. Improved bounce-back methods for no-slip walls in lattice-Boltzmann schemes: Theory and simulations. *Physical Review E* 2003; 67: 066703.

169. Kirby BJ. *Micro-and nanoscale fluid mechanics: transport in microfluidic devices*. Cambridge university press, 2010.

170. Perko J and Patel RA. Single-relaxation-time lattice Boltzmann scheme for advection-diffusion problems with large diffusion-coefficient heterogeneities and high-advection transport. *Physical Review E* 2014; 89: 053309.

171. Hassan AE and Mohamed MM. On using particle tracking methods to simulate transport in single-continuum and dual continua porous media. *Journal of Hydrology* 2003; 275: 242-260. DOI: https://doi.org/10.1016/S0022-1694(03)00046-5.

172. Dai Q and Yang L. LBM numerical study on oscillating flow and heat transfer in porous media. *Applied Thermal Engineering* 2013; 54: 16-25. DOI: https://doi.org/10.1016/j.applthermaleng.2013.01.020.

173. Grathwohl P. *Diffusion in natural porous media: contaminant transport, sorption/desorption and dissolution kinetics*. Springer Science & Business Media, 2012.

174. Jung S, Ehlert S, Pattky M, et al. Determination of the interparticle void volume in packed beds via intraparticle Donnan exclusion. *Journal of Chromatography A* 2010; 1217: 696-704. DOI: https://doi.org/10.1016/j.chroma.2009.12.010.

175. Gritti F and Guiochon G. Effect of the surface coverage of C18-bonded silica particles on the obstructive factor and intraparticle diffusion mechanism. *Chemical Engineering Science* 2006; 61: 7636-7650. DOI: https://doi.org/10.1016/j.ces.2006.08.070.

176. Wagner AJ. A practical introduction to the lattice Boltzmann method. *Adt notes for Statistical Mechanics* 2008; 463: 663.

177. Langmuir I. The constitution and fundamental properties of solids and liquids. Part I. Solids. *Journal of the American Chemical Society* 1916; 38: 2221-2295. DOI: 10.1021/ja02268a002.

178. Liu Y and Shen L. From Langmuir kinetics to first-and second-order rate equations for adsorption. *Langmuir* 2008; 24: 11625-11630.

179. Fish J. *Multiscale methods: bridging the scales in science and engineering*. Oxford University Press on Demand, 2010.

180. Birlik E, Ersöz A, Denizli A, et al. Preconcentration of copper using double-imprinted polymer via solid phase extraction. *Analytica Chimica Acta* 2006; 565: 145-151. DOI: https://doi.org/10.1016/j.aca.2006.02.051.

181. Wang S and Zhang R. Selective Solid-Phase Extraction of Trace Copper Ions in Aqueous Solution with a Cu(II)-Imprinted Interpenetrating Polymer Network Gel Prepared by Ionic Imprinted Polymer (IIP) Technique. *Microchimica Acta* 2006; 154: 73-80. journal article. DOI: 10.1007/s00604-006-0484-2.

182. Ahmed S and Brundrett E. Characteristic lengths for non-circular ducts. *International Journal of Heat and Mass Transfer* 1971; 14: 157-159. DOI: https://doi.org/10.1016/0017-9310(71)90147-5.

183. Pfitzner J. Poiseuille and his law. *Anaesthesia* 1976; 31: 273-275. DOI: 10.1111/j.1365-2044.1976.tb11804.x.

184. Wadell H. Volume, shape, and roundness of quartz particles. *The Journal of Geology* 1935; 43: 250-280.

185. Henderson A, Ahrens J and Law C. *The ParaView Guide*. Kitware Clifton Park, NY, 2004.

186. Zick A and Homsy G. Stokes flow through periodic arrays of spheres. *Journal of fluid mechanics* 1982; 115: 13-26.

187. Sangani AS and Acrivos A. Slow flow through a periodic array of spheres. *International Journal of Multiphase Flow* 1982; 8: 343-360.

188. Bhattacharjee S and Grosshandler W. The formation of a wall jet near a high temperature wall under microgravity environment. In: *ASME 1988 National Heat Transfer Conference, Volume 1* 1988, pp.711-716.

189. Awad MM. The science and the history of the two Bejan numbers. *International journal of heat and mass transfer* 2016; 94: 101-103. DOI: 10.1016/j.ijheatmasstransfer.2015.11.073.

190. Klein RJ, Klein RJ, Lorenzini G, et al. Dimensionless pressure drop number for non-newtonian fluids applied to Constructal Design of heat exchangers. *International journal of heat and mass transfer* 2017; 115: 910-914. DOI: 10.1016/j.ijheatmasstransfer.2017.07.122.

191. Mohamed M. A new definition of Bejan number. *Thermal Science* 2012; 16: 1251-1253.

192. MatLab M and Release ST. Natick. *Massachusetts, United States: The MathWorks Inc* 2012.

193. Frankel I and Brenner H. On the foundations of generalized Taylor dispersion theory. *Journal of Fluid Mechanics* 1989; 204: 97-119.

194. Giddings JC. *Dynamics of chromatography: principles and theory*. CRC Press, 2017.

195. Rosenhead L. *Laminar Boundary Layers: An Account of the Development, Structure, and Stability of Laminar Boundary Layers in Incompressible Fluids, Together with a Description of the Associated Experimental Techniques*. Clarendon Press, 1963.

196. Edge T. Chapter 4 - Turbulent flow chromatography in bioanalysis. In: Wilson ID (ed) *Handbook of Analytical Separations*. Elsevier Science B.V., 2003, pp.91-128.

197. Say R, Birlik E, Ersöz A, et al. Preconcentration of copper on ion-selective imprinted polymer microbeads. *Analytica Chimica Acta* 2003; 480: 251-258. DOI: https://doi.org/10.1016/S0003-2670(02)01656-2.

198. Broeckhoven K and Desmet G. Approximate transient and long time limit solutions for the band broadening induced by the thin sidewall-layer in liquid chromatography columns. *Journal of Chromatography A* 2007; 1172: 25-39.

199. Fee C. 3D-printed porous bed structures. *Current Opinion in Chemical Engineering* 2017; 18: 10-15. DOI: https://doi.org/10.1016/j.coche.2017.07.003.

200. Zhang S, Vijayavenkataraman S, Lu WF, et al. A review on the use of computational methods to characterize, design, and optimize tissue engineering scaffolds, with a potential in 3D printing fabrication. *Journal of Biomedical Materials Research Part B: Applied Biomaterials* 2019; 107: 1329-1351. DOI: 10.1002/jbm.b.34226.

201. Liu Y, Liu Z, Gao J, et al. Selective adsorption behavior of Pb(II) by mesoporous silica SBA-15-supported Pb(II)-imprinted polymer based on surface molecularly imprinting technique. *Journal of Hazardous Materials* 2011; 186: 197-205. DOI: https://doi.org/10.1016/j.jhazmat.2010.10.105.

202. Gu T. Scale-Up of Liquid Chromatography using General Rate Models. *Mathematical Modeling and Scale-up of Liquid Chromatography*. Berlin, Heidelberg: Springer Berlin Heidelberg, 1995, pp.111-120.

203. Gandy PJF, Bardhan S, Mackay AL, et al. Nodal surface approximations to the P,G,D and I-WP triply periodic minimal surfaces. *Chemical Physics Letters* 2001; 336: 187-195. DOI: https://doi.org/10.1016/S0009-2614(00)01418-4.

204. Tilley RJ and Tilley R. *Understanding solids: the science of materials*. Wiley Online Library, 2004.

205. Salomon D. *Computer graphics and geometric modeling*. Springer Science & Business Media, 2012.

206. Pushnov AS. Calculation of average bed porosity. *Chemical and Petroleum Engineering* 2006; 42: 14-17. journal article. DOI: 10.1007/s10556-006-0045-x.

207. Maier R, Kroll D and Davis H. Diameter-dependent dispersion in packed cylinders. *AIChE journal* 2007; 53: 527-530.

208. Fogler HS. *Elements of Chemical Reaction Engineering*. Prentice Hall PTR, 2006.

209. Levenspiel O. Chemical reaction engineering. *Industrial & engineering chemistry research* 1999; 38: 4140-4143.

210. Rousseau RW. *Handbook of Separation Process Technology*. Wiley, 1987.

211. Van Duijn CJ, Mikelić A, Pop IS, et al. Chapter 1 Effective Dispersion Equations for Reactive Flows with Dominant Péclet and Damkohler Numbers. In: Marin GB, West D and Yablonsky GS (eds) *Advances in Chemical Engineering*. Academic Press, 2008, pp.1-45.

212. Gervais T and Jensen KF. Mass transport and surface reactions in microfluidic systems. *Chemical engineering science* 2006; 61: 1102-1121.

213. Kopsidas O. *Scale up of adsorption in fixed-bed column systems*. University of Piraeus, 2016.

214. Benitez J. *Principles and Modern Applications of Mass Transfer Operations*. New York, UNITED STATES: John Wiley & Sons, Incorporated, 2016.

215. Knaebel KS. A" How-To" Guide for Adsorber Design. *Adsorption Research, Inc, Dublin, Ohio* 1990.

216. Army U. *Engineering and design: Adsorption design guide, Design Guide No*. 2001. DG 1110-1-2.

217. Guo B, Yu A, Wright B, et al. Simulation of Turbulent Flow in a Packed Bed. *Chemical Engineering & Technology* 2006; 29: 596-603. DOI: 10.1002/ceat.200500292.

218. Bell MJ. Wind pumping in a snow pack related to atmospheric turbulence. 1993.

219. Tufenkji N and Elimelech M. Correlation equation for predicting single-collector efficiency in physicochemical filtration in saturated porous media. *Environmental science & technology* 2004; 38: 529-536.

220. Iwasaki T, Slade JJ and Stanley WE. SOME NOTES ON SAND FILTRATION [with Discussion]. *Journal (American Water Works Association)* 1937; 29: 1591-1602.

221. Langmuir I. The constitution and fundamental properties of solids and liquids. Part I. Liquids. *Journal of the American Chemical Society* 1917; 39: 1848-1906. DOI: 10.1021/ja02254a006.

222. Ebadi A. What is the correct form of BET isotherm for modeling liquid phase adsorption? *Adsorption : journal of the International Adsorption Society* 2009; 15: 65-73. DOI: 10.1007/s10450-009-9151-3.

223. Mori S and Barth HG. *Size exclusion chromatography*. Springer Science & Business Media, 2013.

224. Marinsky JA and Marcus Y. *Ion Exchange and solvent extraction: a series of advances*. CRC Press, 1981.

225. Stenholm Å, Lindgren H and Shaffie J. Comparison of amine-selective properties of weak and strong cation-exchangers. *Journal of Chromatography A* 2006; 1128: 73-78.

226. Jandera P and Churacek J. *Gradient elution in column liquid chromatography: theory and practice*. Elsevier, 1985.

227. Fausnaugh J, Kennedy L and Regnier F. Comparison of hydrophobic-interaction and reversed-phase chromatography of proteins. *Journal of Chromatography A* 1984; 317: 141-155.

228. Pitois O, Fritz C and Vignes-Adler M. Hydrodynamic resistance of a single foam channel. *Colloids and Surfaces A: Physicochemical and Engineering Aspects* 2005; 261: 109-114. DOI: https://doi.org/10.1016/j.colsurfa.2004.11.045.

A – Literature Review Supporting Information

A.1 – Filter technology

A.1.1 Filter classifications

The first incarnations of physical filtration systems were sand filters believed to be used by ancient civilisations, but the first documented municipal system was created by Robert Thom in the 1800's[28]. Since this time the improved understanding of how filters were able to purify liquids has enabled innovators to build more sophisticated filters for specialised applications. Modern filters can be created with a controlled pore size to selectively remove contaminants, with pore sizes classified as microfiltration, ultrafiltration, nanofiltration, or reverse osmosis. Particles larger than 1 mm in size are commonly referred to as being "screened" rather than filtered[24]. The typical size capabilities of each filtration technology are summarized in Figure 85. Microfiltration refers to filters with a mean pore ranging from 0.1 µm up to approximately 5 µm. Ultrafiltration targets finer particles, down to a size of approximately 0.01 µm, such as colloids. Each of these classifications typically perform separations based on the particle size, and are readily implemented in industrial applications through various designs. When considering particles that are finer than the capabilities of ultrafiltration, it may be necessary to implement nanofiltration or reverse osmosis.

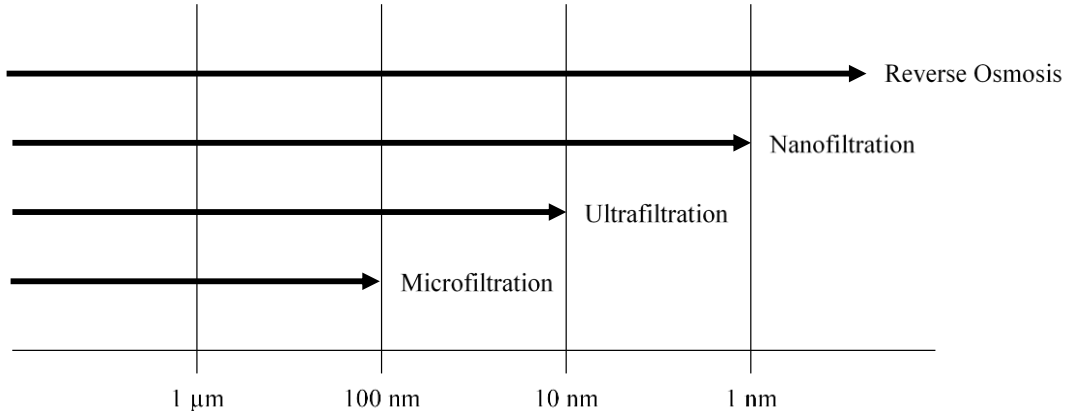

Figure 85, Depiction of filter size regimes and particle size capabilities.

While typically still classified as filtration technologies, nanofiltration and reverse osmosis membranes can perform separations via mechanisms other than size exclusion. This is because when dealing with particles on a scale <0.01 µm, the mixture more closely resembles a solution, with little to no suspended matter. In these cases, the separation occurs when one of the small molecular species from the solution dissolves or diffuses through the filter membrane itself, usually under the influence of a pressure gradient[26]. Membrane materials can be designed to selectively interact with the contaminant and carrier

fluid species, and thus manufacturing highly specialised membrane materials is an area of fervent research. Other specialised filters may selectively bind with specific solute species in processes that more closely resemble chromatography. In any situation where the filtration is required, the correct choice of filter design is critical for obtaining a desired degree of separation for a time and cost efficient optimum[24].

Filters may also be defined by whether they perform surface filtration or depth filtration[219]. In surface filtration a 'cake' builds up on the inlet to the filter medium that requires frequent cleaning or removal to prevent large flow resistance building up, and prevents the target species from penetrating deeper into the media. Depth filtration utilises the entire axial length of the filter to retain the target species through contact with 'collectors'. The collectors can exist as packed particles, fibres, or other structures, but all may be described by empirical models that dictate different mechanisms for collectors to come into contact with target species (straining, diffusion, impaction, sedimentation, interception)[27]. It is important to consider the theory of filter collectors even with chromatography columns, as the collection mechanisms may contribute to blocking of channels and change the operating conditions of the column.

A.1.2 Filter characteristics and measures

A typical measure of a rapid filter's performance is the efficiency, which is broken down into a single collector efficiency comprising of the different particle collection mechanisms. Equation [87] shows the single collector efficiency (η_{filter}) as a sum of the particle interception (η_I), diffusion (η_D), and gravity (η_G) based contact between particles in the solution and the bed media. The single collector efficiency is related to the filtration coefficient (λ), which can be used in a first order relationship between contaminant concentration (C) and the depth (z_{bed}) of the filter bed (Equation [88]), first proposed by Iwasaki in 1937[220].

$$\eta_{filter} = \frac{particles\ contacting\ particle}{particles\ approaching\ particle} = \eta_I + \eta_D + \eta_G \qquad [87]$$

$$\frac{\partial C}{\partial z_{bed}} = -\lambda C \qquad [88]$$

A.2 – Adsorption Models

The simplest adsorption isotherm was developed by Irving Langmuir to describe gas adsorption limited by the formation of a monolayer. The model consists of a fixed concentration of possible adsorption sites (q_s) each with equal bonding potential for one adsorbate molecule, and assumes no interaction between adsorbed species[177,221,38]. In Equation [89], the fraction of occupied sites (θ) is determined by knowing the pressure of the system (P) and the adsorption equilibrium constant (b_{Lang}), which is in turn related to the rates of adsorption (k_{ads}) and desorption (k_{des}) (Equation [90]).

$$\theta = \frac{q}{q_s} = \frac{b_{Lang}P}{1 + b_{Lang}P} \quad [89]$$

$$b_{Lang} = \frac{k_{ads}}{k_{des}} \quad [90]$$

While the Langmuir isotherm is simple, its applications are limited and its accuracy can be insufficient when dealing with processes that include multilayer adsorption. The BET isotherm, developed by Brunauer, Emmett and Teller, was the first isotherm capable of describing multilayer adsorption while still providing information about the monolayer capacity, and thus is one of the most commonly used isotherm models[39]. Brunauer et al. outline several significant assumptions that were made in developing the model, and several more assumptions have been made to improve this model over time. Equation [91] shows one possible form the of the BET isotherm used to describe liquid phase adsorption. The fraction of occupied sites is related to the liquid phase equilibrium concentration (C_{eq}) [N L^{-3}], equilibrium constants of the first adsorbed layer (K_S) and consecutive layers (K_L) of absorbed molecules[222]. This model can describe any number of layers formed on the adsorbent surface, but if it is known that only a limiting number of layers (n_{lim}) may form then Equation [92] may be used.

$$\theta = \frac{K_S C_{eq}}{\left(1 - K_L C_{eq}\right)\left(1 - K_L C_{eq} + K_S C_{eq}\right)} \quad [91]$$

$$\theta = \frac{K_S C_{eq}\left[1 - (n_{lim}+1)\left(K_L C_{eq}\right)^{n} + n_{lim}\left(K_L C_{eq}\right)^{n_{lim}+1}\right]}{\left(1 - K_L C_{eq}\right)\left(1 + \left(\frac{K_S}{K_L} - 1\right)K_L C_{eq} - \left(\frac{K_S}{K_L}\right)\left(K_L C_{eq}\right)^{n_{lim}+1}\right)} \quad [92]$$

Building upon the concept of multilayer adsorption, when considering a material with small pores it is possible for the pore to entirely fill up with a fluid from a vapour phase. This process is known as capillary condensation and occurs due to a lowered saturation vapour pressure within the pore, which can be described using the Kelvin equation[40]. Shown in Equation [93], the apparent vapour pressure for

a species within in a pore (P_{vap}) [M L^{-1} T^{-2}] is directly affected by the surface tension of the fluid (γ) [M T^{-2}] and the radius of the fluid curvature as a droplet within the pore (r_{pore}) [L]. The universal gas constant (R) [$ML^2T^{-2}K^{-1}$], equilibrium vapour pressure (P_{sat}) [M L^{-1} T^{-2}], system temperature (T_K) [], and molar volume of the fluid (V_m) [L^3 N^{-1}] must also be known. This model for describing adsorption is mostly used for determining the pore size distribution of porous solids. In any application, it is important to use the appropriate adsorption model.

$$\ln\left[\frac{P_{vap}}{P_{sat}}\right] = \frac{2\gamma V_m}{r_{pore} R T_K} \quad [93]$$

A.3 – Liquid Chromatography Separation Mechanisms

A.3.1 Size Exclusion

Size exclusion chromatography differs from the other four separation mechanisms as it performs the separation based on the physical size of the solutes, while the other liquid chromatography separation mechanisms use non-covalent interactions[121]. The stationary phase used in size exclusion systems is porous with a pore size distribution tailored to the molecular size of the solutes of interest, such that smaller molecules are able to diffuse into pores and follow a tortuous path through the medium, while larger molecules follow only the main channels through the medium[223]. The end result of the different path lengths is that molecules take different lengths of time to pass through the column (increasing time with decreasing molecular weight), thus resulting in an effective separation without chemical interaction or the manipulation of column conditions to unbind solutes.

A.3.2 Ion Exchange

Ion Exchange Chromatography (IEC) relies on non-covalent bonds to form between the solutes and the stationary phase, which is referred to as the 'ion exchanger'. The stationary phase of the ion exchange column is selected to remove specific solutes based on the charge (positive or negative) and charge strength of the mobile phase species[122]. The charge of the ion exchanger must be counterpart to the solutes that are to be removed, to allow the solute to adsorb to the surface of the ion exchange medium. The strength of an ion exchanger determines whether the adsorption bond is stable over a wide or short pH range; weak ion exchange media will experience desorption when the pH of the system is changed significantly[224]. A change in the pH of the system may be artificially enforced by passing acidic or alkaline solutions through the ion exchanger[225]. This is called an 'elution step' in chromatographic systems that 'fix' solutes at binding sites, and is important for completing a chromatographic separation.

Elution refers to manipulating the conditions of a chromatography system to unbind any bound solutes and allowing them to be captured[226]. In the context of removing trace heavy metals from water, once the target species is bound to the column media it needs to be recovered, and the column regenerated. The contaminated sample would have passed through the column, saturating the stationary phase as the flow front moves through the column, and the effluent would be free of metal solutes. Once the column is saturated and metal solutes being to pass through the column (called the breakthrough), contaminated sample is no longer passed through the column and instead the elution species is introduced. As the elution front moves through the column it unbinds the metallic species, and the eluent and solute exit the column together.

A.3.3 Affinity

Affinity chromatography also involves non-covalent interaction between the solutes in the mobile phase and the surface of the stationary phase, and therefore requires an elution step. The binding between the solutes and stationary phase in affinity separation are highly specific and often the binding site is designed to target a specific molecule. For this reason, the technology is popular for biological and pharmaceutical applications[123], and is currently favoured for applications which require high specificity and low throughput. Molecularly Imprinted Polymers are one example of possible affinity chromatography media.

A.3.4 Reversed Phase

The terminology ‘reversed phase’ and ‘normal phase’ in chromatography refer to the polarity of the mobile phase and the hydrophilic or hydrophobic functionality of the stationary phase. In Reversed Phase Chromatography (RPC) the stationary phases are hydrophobic, and the mobile phases use polar solvents. This enables hydrophilic species to be eluted first, while other hydrophobic species interact with the stationary phase and are eluted second[97]. The eluent species used in RPC are required to be highly non-polar to then cleave the bonds of the hydrophobic solute species.

A.3.5 Hydrophobic Interaction

Hydrophobic Interaction chromatography is very similar to RPC, and is only differentiable by the strength of the bonds between the solute and the stationary phase. Weaker non-polar functionality is used in the stationary phase media, and the mobile phase contains a high salt concentration. The benefit of this technology is that the solutes can be eluted with more ease simply by changing the salt concentration in the mobile phase elution step[227].

A.4 - Definitions of Characteristic Length

It is common practice in the study of fluid flow systems to define a characteristic length (L_c) pertaining the geometry of a flow channel. This characteristic length is used to describe the system of flow channels and is used in dimensionless analysis of the system, such as when calculating the Peclet number. The choice of $L_c$is therefore important to enable the comparison of flow systems at different scales, and between flow channels with different geometries. For a fixed geometry, any choice for the characteristic length is viable to be used in scaling the system as it will relate to a system with the exact same geometric ratios. However, when wanting to compare flow channels with significantly different geometries (such as with sphere particle packing, cylindrical pipes, and TPMS structures), not all characteristic lengths are equal.

By convention, the diameter of a sphere is used as L_c in packed bed analysis[16], even though it relates to the geometry of the solid phase material constructing the channel and not the flow channels themselves. For cylindrical pipes, the diameter of the flow channel is used; thus making it difficult to justify a compare the two systems. There does not yet appear to be a consensus on what the characteristic length for TPMS structures should be, but literature favours the edge length of a repetitive unit cell[111], [8]. This edge length does not necessarily pertain to the flow channel, and TPMS with the same unit cell size may possess vastly different porosities and channel dimensions. For the analysis performed in this work several definitions of characteristic length were investigated to determine the most suitable, and are summarized below.

A.4.1 Particle size in packed beds

For channel networks defined by the interstitial space of repeating particles the L_c chosen relates directly to the geometry of the particles themselves. As mentioned above, this convention makes comparison with other geometries difficult as there is no equivalent 'particle length' for continuous structures. For spheres the L_c used is the sphere diameter, while for other particle shapes the choice for L_c may be the bounding unit cell's edge length, or equated to the circumdiameter (the diameter of a sphere with equal particle volume)[111]. The arrangement of these particles is known to influence the void space distribution and therefore the flow channel morphology, but this effect is not represented by this definition of L_c. For example, the arrangement of spherical particles in a simple cubic structure produces very different porosity and wetted surface area to that of a body centred cubic (BCC) arrangement, but would share the same value of L_c (Figure 86). Without pertaining to the fluid channel properties, and being undefined for continuous structures, particle size was deemed unfit to be used as the L_c in this work.

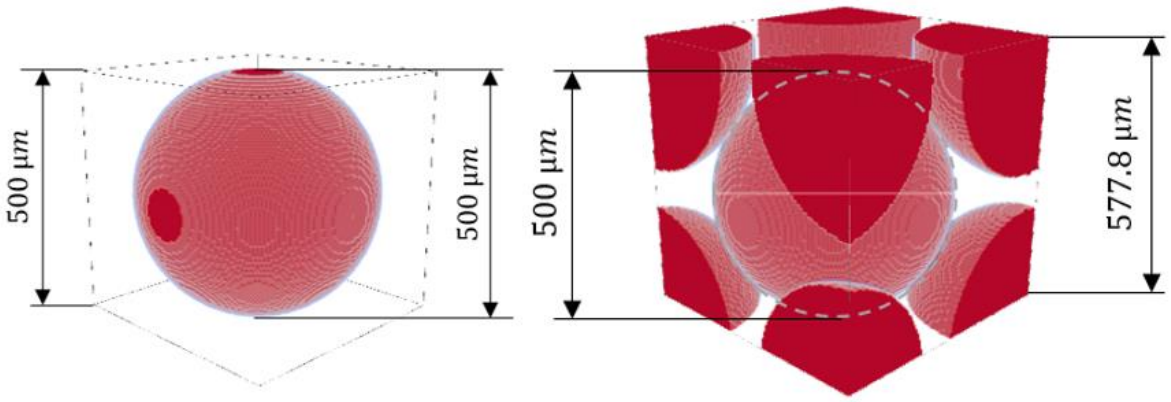

Figure 86. Illustration of how particle orientation can change the size of the periodic unit cell dimensions for same sized particles. Left to right, SC packed sphere and BCC packed sphere unit cell for 500 µm diameter sphere.

A.4.2 Periodic length of the geometry

With the exception of randomly packed media (such as random particle packing, and many naturally occurring materials), all ordered structures may be reduced to a periodically repeating structure in three dimensional Cartesian space. Previous work involving TPMS has defined the L_c as the periodic length of the system[8], which for TPMS is equivalent to the edge length of the unit cell. The periodic length is applicable to many geometries, but there is difficulty in defining a periodic length for a uniform duct, which is theoretically periodic over an infinitely small distance. This definition also lacks a direct relation to the fluid channels, and therefore was not used.

A.4.3 Hydraulic diameter for ducts

For flow channels with uniform cross sections, the characteristic length is most often defined as the hydraulic diameter ($d_{h,channel}$) [L] related to the wetted perimeter (P_w) [L] and flow area (A_{flow}) [L^2] of a regular cross section (Equation [65])[182]. For cylindrical pipes, the hydraulic diameter equation can be shown to be equivalent to the pipe diameter. This definition allows the comparison of many duct-like structures, but is less capable of representing the flow through non-uniform structures such as TPMS.

$$d_{h,channel} = 4 \times \frac{A_{flow}}{P_w} \qquad [94]$$

To calculate an equivalent hydraulic diameter for non-uniform structures, the wetted perimeter and flow area was calculated at several intervals along one periodic length of the media to obtain an average. This definition was therefore unable to be calculated for randomly oriented flow channels, other than

by means of taking several sample lengths and obtaining a mean value. For periodic structures such as TPMS, the average hydraulic diameter for one periodic distance was found by numerically calculating A_{flow} and P_w at n many slices and calculating the average according to Equation [95]. However, this numerical estimate was dependent on which axis the 'slices' were measured along and while this definition showed promise for wide applicability, a simpler definition was preferred.

$$\bar{d}_{h,channel} = 4 \times \left(\frac{\sum_{i=0}^{n} A_{flow,i}}{\sum_{i=0}^{n} P_{w,i}} \right) = 4 \times \left(\frac{\sum_{i=0}^{n} d_{h,i}}{n} \right) \quad [95]$$

A.4.4 Average channel diameter (normal to the channel wall)

This definition was considered for its relation to the fluid channel. The average channel diameter (normal to the channel walls) over a periodic section of the geometry could be defined analytically or found numerically for most structures and would represent the fluid space. This parameter was constructed to represent the average shortest distance between a point in the fluid space and a channel wall, and therefore would give a good indication of the channel dimensions. However, the calculations to determine this parameter for TPMS and ordered particle packing were non-trivial and required numerical techniques to be determined.

A.4.5 Equivalent hydrodynamic resistance

An attempt was made to define a characteristic length that related to the pressure drop and flowrate of the system. The method for doing so was to relate the hydrodynamic resistance[228] (R_H) as defined by Equation [96] to a cylindrical pipe with the equivalent hydrodynamic resistance. For flows in the laminar regime this could be achieved by using a rearrangement of the Hagen-Poiseuille equation[183] (Equation [97]). To relate the two equations, the length over which the pressure drop was observed (z) was used as the length of the pipe with equivalent R_H leaving D_{pipe} [L] as the only unknown.

$$\Delta P = R_H Q, \qquad R_H = \frac{\Delta P}{Q} \quad [96]$$

$$\Delta P_z = \frac{8\mu z}{\pi R_{pipe}^4} Q, \qquad R_H = \frac{\Delta P_z}{Q} = \frac{8\mu z}{\pi R_{pipe}^4} = \frac{128\mu z}{\pi D_{pipe}} \quad [97]$$

While this definition was robust in its handling of periodic and non-periodic geometry, it required a solution to the flow field to calculate the characteristic length. For many structures this is non-trivial

and often computationally expensive, and therefore it was decided the best L_c to use would be dependent solely on geometric properties.

A.4.6 Hydraulic diameter for porous systems

The hydraulic diameter ($d_{h,pore}$) used to describe porous media is given by Equation [98] below, and is dependent only on the porosity (ε) and specific surface area (a) of the porous network[2]. The specific surface area (Equation [99]) is the ratio of wetted surface area (A_w) to the bulk volume (V_{cell}), and is also a useful parameter for estimating the capacity available for surface adsorption phenomena. This definition was found to be able to be applicable to all of the geometries considered and was related to the fluid channels of the system.

$$d_{h,pore} = 4 \times \frac{\varepsilon}{a} \quad [98]$$

$$a = \frac{A_w}{V_{cell}} \quad [99]$$

A.4.7 Preferred characteristic length

The preferred characteristic length was chosen to be the hydraulic diameter as defined for porous media ($d_{h,pore}$), which from this point will be referred to as the hydraulic diameter, d_h. The choice was made based on the need for the L_c to represent the geometry of the flow channel and be applicable to all geometries. This definition was applicable to all periodic systems if defined for the periodic domain, and could approximate random orientations with a large enough sample domain. The problems encountered with infinitely periodic ducts was voided by the fact that the $d_{h,pore}$ took the same value for any length of duct.

It is part of the focus of this work to verify that this definition will finally allow the comparison of starkly different geometries by use of a universal characteristic length definition.

A.4.8 Influence of L_c on reduced plate height

The value of characteristic length used for reducing the Height Equivalent to a Theoretical Plate ($HETP$) [L] to the dimensionless plate height (h) was able to influence the interpretation of the results and therefore was extremely important. When comparing similar geometries (ie, particles with particles) the choice of L_c used to obtain h was consistent and therefore the comparison of dispersion is done so using a valid basis, at least in determining which arrangement performs better relative to the others. When

attempting to compare geometries with different measures of characteristic length, the different characteristic lengths used can have a significant influence on the relative performance of each structure and therefore a consistent definition such as $d_{h,pore}$ is required to ensure the relative performance ranking is valid. To illustrate the effect that using different definition of L_c may have on the outcome, Figure 87 below contrasts several L_c definitions when calculating the minimum reduced plate heights (h_{min}) for the basic TPMS and ordered sphere orientations.

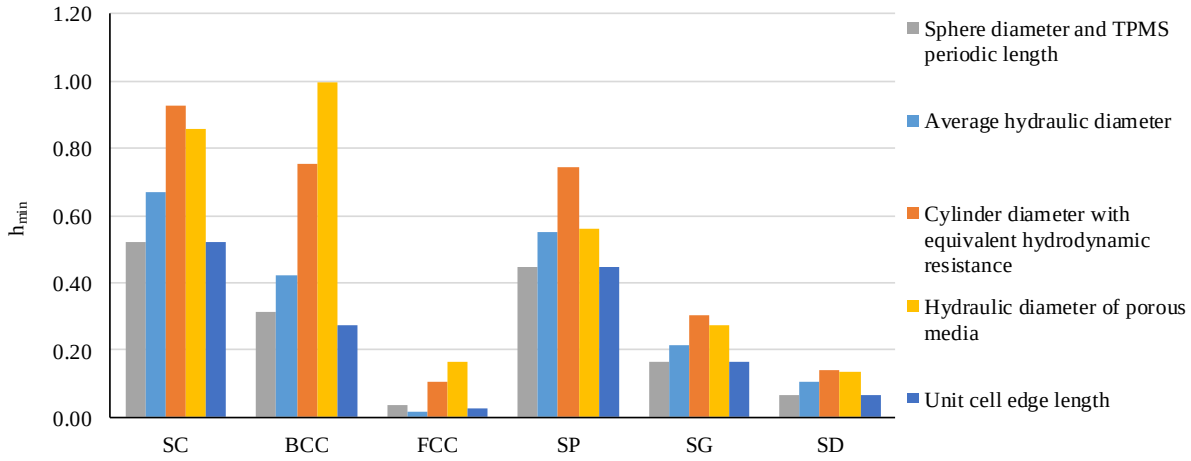

Figure 87. Comparison of reduced plate height for SC, BCC, FCC, SP, SG, and SD geometries when using different definitions of characteristic length in calculation.

The first feature of this graph to be addressed is the change in values for h_{min} for a single geometry. The effect of L_c choice is most pronounced for the BCC and FCC configurations, where there is almost an order of magnitude between the maximum and minimum values found with each definition. The implications this would have include determining how to scale the results of h_{min} when constructing a real column.

The relationship between h_{min} and practical column sizes could be determined empirically. The second consideration is whether the relative performance of different geometries would be consistent for different definitions. At a glance, the relative performance found using each definition appears to have been upheld, but upon closer inspection there are some notable differences. It is found that the 'ranking' of dispersion performance changes dependent on the definition of L_c used, as can be observed with the changing orders of highest to lowest h_{min} in each data set. This occurs because the conversion between different definitions is the ratio of each L_c, which is not a constant factor for all geometries:

$$\frac{L_c(SD, d_{h,pore})}{L_c(SD, d_{axial})} = 0.491 \neq 0.161 = \frac{L_c(FCC, d_{h,pore})}{L_c(FCC, d_{axial})}$$

B – TPMS Level Set Equations

Each of the TPMS structures studied in this report could be represented using nodal approximation equations in three dimensional Cartesian space. The majority of these equations were defined based on space groups identified in a paper by Wohglemuth[15] to approximate triply periodic continuous surfaces. The process for approximating these surfaces and the equations used in this study are given below.

B.1 Defining Space Groups

The method outlined by Wohglemuth for defining the level set equations of triply continuous structures first requires a mathematical description of space groups, which possess similar symmetry. This required expressions for the structure factor ($F_{(hkl)}$), as used in X-ray crystallography, for low values of *h, k* and *l* need to be evaluated from the general form given in Equation [100]. The values for *h, k* and *l* correspond to planes, and *n* is the nodal coordinate within the discretized domain. To obtain equations with only real components, the imaginary components of the result of this expansion are equation to zero, or in the case of the real component equalling zero the imaginary part is used in its place. The expanded and simplified version is shown to be Equation [101].

$$F_{(hkl)} = \sum_{n} \left[\cos\left(2\pi(hx_n + ky_n + lz_n)\right) + isin\left(2\pi(hx_n + ky_n + lz_n)\right)\right] \quad [100]$$

$$\begin{aligned} F_{(hkl)} = {} & \cos(2\pi hx)\left[\cos(2\pi ky)\cos(2\pi lz) + \cos(2\pi ly)\cos(2\pi kz)\right] + \cdots \\ & \cos(2\pi hy)\left[\cos(2\pi kz)\cos(2\pi lx) + \cos(2\pi lz)\cos(2\pi kx)\right] + \cdots \\ & \cos(2\pi hz)\left[\cos(2\pi kx)\cos(2\pi ly) + \cos(2\pi lx)\cos(2\pi ky)\right] \end{aligned} \quad [101]$$

By substituting integer values for *h, k* and *l* the basic structure factor equations are found. Those that were used to construct the level set equations for the TPMS used in this report are given in the simplified forms with Equations [102] to [109] below. The final requirement for defining the surface interface is to equate the level set equation to known value (p). The selectin of this value determines where the interface is located within 3D space, and thus influences the void fractions occupied by the two volumes separated by the interface. The structure factors and values of p required to define the TPMS in this work are defined in the next section.

$$F_{(100)} = \cos(x) + \cos(y) + \cos(z) = p \quad [102]$$

$$F_{(110)} = \cos(x)\cos(y) + \cos(z)\cos(x) + \cos(y)\cos(z) = p \quad [103]$$

$$F_{(111)} = sin(x)\,sin(y)\,sin(z) + \sin(x)\cos(y)\cos(z) + \cos(x)\sin(y)\cos(z) + \cos(x)\cos(y)\sin(z) = p \quad [104]$$

$$F_{(200)} = \cos(2x) + \cos(2y) + \cos(2z) = p \quad [105]$$

$$F_{(211)} = \sin(2x)\cos(y)\sin(z) + \sin(2y)\cos(z)\sin(x) + \sin(2z)\cos(x)\sin(y) = p \quad [106]$$

$$F_{(220)} = \cos(2x)\cos(2y) + \cos(2y)\cos(2z) + \cos(2z)\cos(2x) = p \quad [107]$$

$$F_{(222)} = \cos(2x)\cos(2y)\cos(2z) = p \quad [108]$$

$$F_{(300)} = \cos(3x) + \cos(3y) + \cos(3z) = p \quad [109]$$

B.2 Equations for TPMS

Each of the TPMS observed in this work were defined by either a single structural factor expression or a combination of these factors, and setting the parameter p to specific values. The structure factors and the expanded form of the equations used for each of the basic TPMS structures is given in Equations [110] to [112]. The remaining structures are defined by the structure factors in Equations [113] to [118].

B.2.1 Schwarz Primitive (SP)

$$SP: \quad F_{(100)} = 0 \quad [110]$$

$$\cos(x) + \cos(y) + coz(z) = 0$$

B.2.2 Schoen Gyroid (SG)

$$SG: \quad F_{(110)} = 0 \quad [111]$$

$$\sin(x)\cos(y) + \sin(y)\cos(z) + sin(z)\cos(x) = 0$$

B.2.3 Schwarz Diamond (SD)

$$SD: \quad F_{(111)} = 0 \qquad [112]$$

$$sin(x)\,sin(y)\,sin(z) + \sin(x)\cos(y)\cos(z) + \cos(x)\sin(y)\cos(z) + \cos(x)\cos(y)\sin(z) = 0$$

B.2.4 Schoen I-WP surface (IWP)

$$IWP: \quad F_{(110)} = -0.25 \qquad [113]$$

B.2.5 Schoen F-RD surface (FRD)

$$FRD: \quad 0.8F_{(111)} + 0.1F_{(222)} - 0.1F_{(220)} = 0 \qquad [114]$$

B.2.6 P2-GD surface (P2GD)

$$P2GD: \quad 0.7F^{A}_{(211)} - 0.1F_{(220)} - 0.2F_{(200)} = 0 \qquad [115]$$

B.2.7 Double Schoen Gyroid (DSG)

$$DSG: \quad 0.8F_{(211)} - 0.2F_{(220)} = 0 \qquad [116]$$

B.2.8 Lidinoid surface (L)

$$L: \quad 0.5F_{(211)} - F_{(220)} = -0.15 \qquad [117]$$

B.2.9 The D' surface (D)

$$D: \quad 0.5F_{(111)} - 0.5F_{(220)} = 0.2 \qquad [118]$$

C – Performance Correlations

In studying the performance of various TPMS structures and modified TPMS geometries, several relationships between the geometric properties of a unit cell (ε, Ψ, a), the flow properties of a periodic unit cell (T, $\bar{u}_{dev}$), and the mass transport performance measures (h_{min}, V_D, C_D). Some of the relationships that were identified but not reported in the main body of this document are summarized in Figure 88 to Figure 91 below. Figure 88Figure 87 shows a weak correlation between increase in the velocity deviation ($\bar{u}_{dev}$) and increases in minimum reduced plate height. However, due to the large scatter of data it was decided that the relationship was not strong enough to make predictions for $\bar{u}_{dev}$.

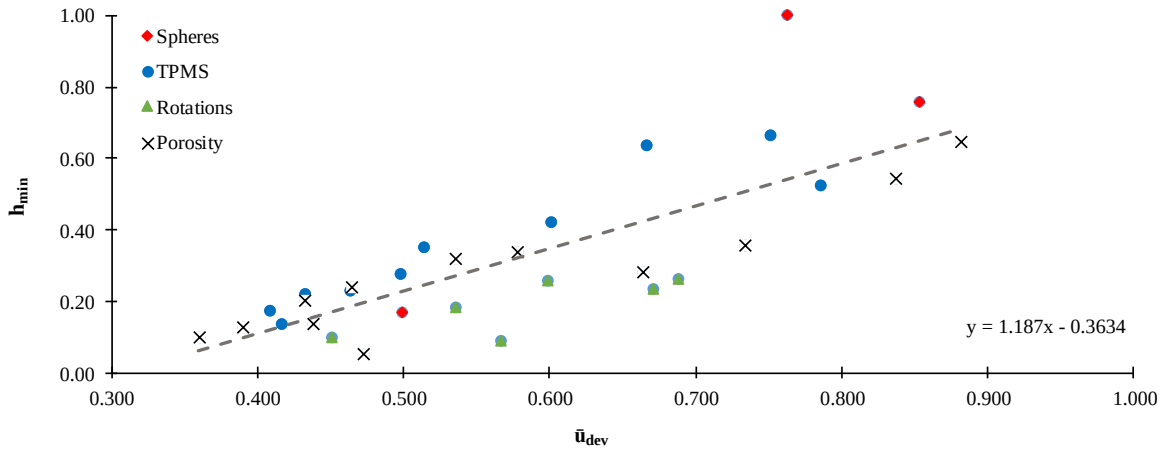

Figure 88. Correlation between reduced plate height and normalized mean deviated velocity.

On the following page Figure 89, Figure 90, and Figure 91 attempt to relate the optimal breakthrough performance ($V_{D,max}$, $C_{D,max}$) to the geometry of each unit cell. The sphere arrangements were again excluded from the trend fitting as they were found to be outliers. The strongest relationship is seen in Figure 90 where the sphericity (Ψ) and porosity squared (ε^2) proved to be a reasonable predictor of dimensionless void volumes in the periodic adsorption tests. It was also seen that the rotated packing structures were the least conforming, due to the changes in sphericity that occurred as a result of redefining the size of the unit cell. Figure 89 also shows that there was a correlation between specific surface area (a) and V_D, but as a does not factor in the distribution of solid phase the correlation is weaker. Figure 91 also related the maximum observed C_D to the geometric parameters, although it was noted the structures with the highest C_D were the ones with noticeably smaller channel diameters (SD ε = 0.25, L, D) indicating that reducing the required diffusive distance was beneficial. As the sphericity and porosity accounted for not only the available surface area, but also how it was distributed within the unit cell (sphericity), they were useful for predicting breakthrough performance.

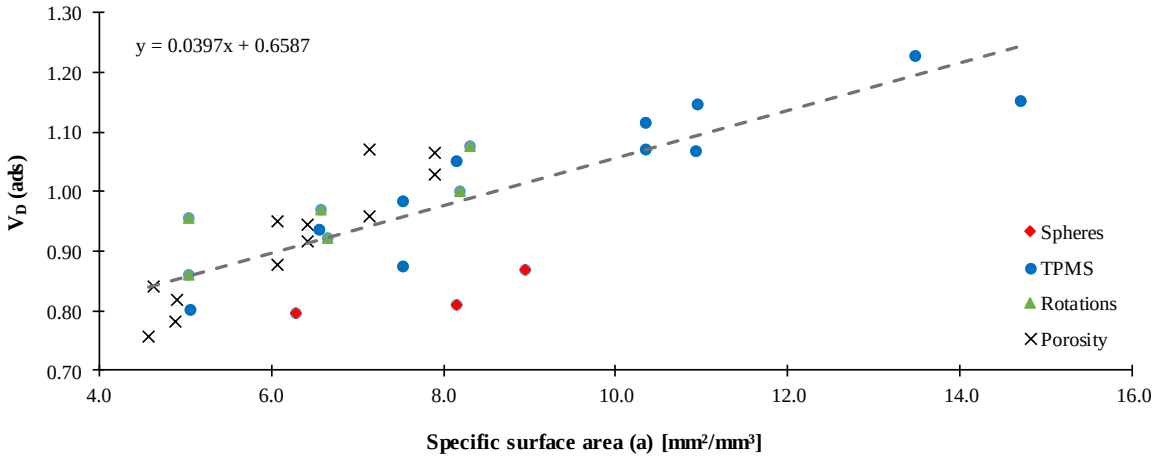

Figure 89. Correlation between specific surface area and the maximum V_D in adsorption simulation. Sphere packing excluded from the fitted trend.

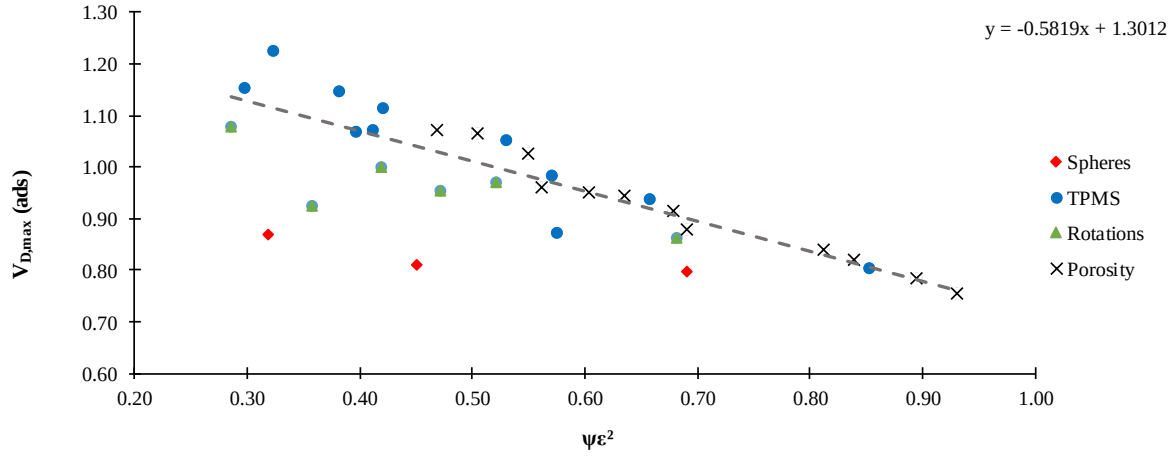

Figure 90. Relating maximum dimensionless volume to the geometric parameters of the unit cell. Sphere packing excluded from the fitted trend.

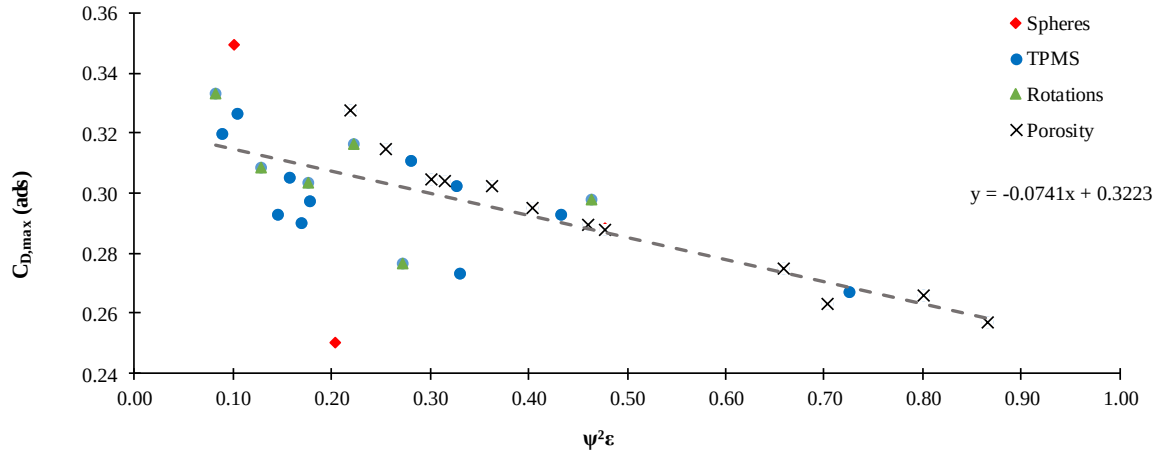

Figure 91. Correlation between maximum adsorption capacity fraction observed and geometric properties of the solid. Sphere packing excluded from the fitted trend.